Stability and Coulomb Fission of Multiply Charged Molecular Clusters

Christopher Harris

Thesis submitted to the University of Nottingham for the degree of Doctor of Philosophy

May 2015

Declaration

I hereby declare that this thesis has not been submitted, either in the same of different form to this or any other university for a degree other than the one I am applying for

Signed

....

Christopher Harris

May 2015

Abstract

The stability of multiply charged clusters under the influence of electrostatic repulsion contained within them is determined by the balance between the cohesive forces holding the cluster together and the repulsion between the charges. Experimentally, the onset of stability is determined through the observation of a critical size, below which the cluster ceases to be observed. There is a region above the critical size in which a multiply charged cluster becomes metastable and the fragmentation into charged fragments can be detected in the experimental time frame. The most interesting pathway is the separation of the precursor into charged fragments which is termed coulomb fission, which if the metastable peaks from the processes are observed, can contain information about the interactions between the charged dielectric fragments and add to our understanding of how like charged species interact in nature.

The work contained presents an investigation of the multiply charged molecular cluster systems: $(C_6H_6)_n^{z+}$, $(CH_3CN)_n^{Z+}$, $(C_4H_8O)_n^{z+}$, $(NH_3)_n^{z+}$ and $(H_2O)_n^{z+}$. Using updated experimental procedures, the critical sizes for multiply charged molecular clusters is determined for charge states of up to z = 8+ and are compared to predictions made with existing theories. The coulomb fission into charged fragments is observed using the mass-analysed kinetic energy (MIKE) scanning technique and by simulating the shape of the experimental peak, the experimental energy release following the separation is determined. This energy is found to agree well with the predictions of a dielectric particle drop model which describes the interactions between dielectric bodies.

Acknowledgements

There are many people who without their help, I would be in no position to finish this doctorate. Firstly, my warmest thanks to my supervisor Prof. Tony Stace FRS, who had the faith in me to take me on, and then was a constant source of experience and inspiration from then on. Especially essential for me was his extensive experience with the ZAB. Any problems that arose, he had seen it all before! His was a reassuring presence, especially at the start of the project, when nothing seemed to click! I also benefitted greatly from his help in some of the more theoretical aspects of this work and from discussions on a range of subjects. My thanks go to Dr Adrian Boatwright, who I initially worked with during my masters project. Working closely with him really imbued me with an enthusiasm for scientific research. I enjoyed discussions with him on a range of topics and I have really learned a lot from him. Also, Dr June McCombie, who goes out of her way to make new postgraduates feel settled, and is always interested to hear about progress - A real unsung hero in the department.

My thanks go to Dr Eleonora Bruzzi, who took the time to teach about the ZAB and looked after me well at the start of the project. Also to other members of the Stace research group, Lifu Ma, Joseph Koka and Gerardo Raggi. My thanks also go to all the project students who I have worked with for their help, and for all the kind people who have helped proof read my theisis.

Without the excellent technical staff in the department everything would grind to a halt very quickly. My thanks go to Neil Barns, who I would inevitably run to first when things turned sour. I am in debt to Electrical technicians James Warren and David Litchfield, pump technician John Whalley and Kevin Hind for their help.

I am blessed with a group of friends in Nottingham who are a constant source of inspiration and fun, and have prevented me from going insane, thus far! Andy, Lauren, Steve, Matt, Katie, Andrew, Ed and Adam, especially have my gratitude!

Without the constant love and support of my parents I would have never have completed my undergraduate degree, let alone this postgraduate course. I owe them everything. My partner Lesley, who has put up with me all this time and has been through so much with me, I don't have the words, I want to thank her for everything.

Contents

Declaration i
Abstract ii
Acknowledgements iii
List of Figures vii
List of Tables xii
List of Abbreviations xiv
Chapter 1 : Introduction 1
1.1 Multiply Charged Molecular Clusters 1
1.2 Stability and Coulomb Fission 3
References 9
Chapter 2 : Experimental Section 1
2.1 Introduction 11
2.2 Experimental setup 13
2.3 Cluster Formation 15
2.4 Supersonic Expansion 18
2.5 Ion Source 20
2.6 Magnetic Sector 23
2.7 Electric Sector 25
2.8 Detection 26
2.9 MIKE Scanning 27
2.10 Dielectric particle model 29
2.11 Peak simulation model 32
References 36
Chapter 3 : Multiply Charged Benzene Clusters 37
3.1 Introduction 37
3.2 Doubly Charged Benzene Clusters 39
3.3 Triply Charged Benzene Clusters 45
3.4 Fourfold Charged Benzene Clusters 51
3.5 Stability of Multiply Charged Benzene Clusters 57
3.6 Conclusions 60
References 61
Chapter 4 : Multiply Charged Acetonitrile Clusters 62
4.1 Introduction 62
4.2 Doubly Charged Acetonitrile Clusters 64

4.3 Triply Charged Acetonitrile Clusters 69
4.4 Fourfold Charged Acetonitrile Clusters 75
4.5 Stability of Multiply Charged Acetonitrile Clusters..........80
4.6 Conclusions..........83
References..........85
Chapter 5 : Multiply Charged Ammonia Clusters..........86
5.1 Introduction 86
5.2. Doubly Charged Ammonia Clusters..........87
5.3. Triply Charged Ammonia Clusters..........96
5.4. Fourfold Charged Ammonia Clusters..........105
5.5. Fivefold Charged Ammonia Clusters..........115
5.6. Sixfold Charged Ammonia Clusters 119
5.7 Sevenfold Charged Ammonia Clusters 126
5.8 Eightfold Charged Ammonia Clusters..........136
5.9 Stability of Multiply Charged Ammonia Clusters..........139
5.10 Conclusions..........142
References..........149
Chapter 6 : Multiply Charged Tetrahydrofuran Clusters..........150
6.1 Introduction 150
6.2 Doubly Charged THF clusters..........151
6.3 Triply Charged THF Clusters 155
6.4. Fourfold Charged THF Clusters 159
6.5 Stability of Multiply Charged THF Clusters..........165
6.6 Conclusions..........169
References..........171
Chapter 7 : Multiply Charged Water Clusters..........172
7.1 Introduction 172
7.2: Doubly Charged Water Clusters 174
7.3 Triply Charged Water Clusters..........179
7.4 Fourfold Charged Water Clusters..........186
7.5 Fivefold Charged Water Clusters..........192
7.6 Stability of Multiply Charge Water Clusters 195
7.7 Conclusions..........198
References..........200
Chapter 8 : Conclusions and Future Work..........201
References..........206

List of Figures

Figure 1.1: Schematic showing the elongation which originates from the electrostatic repulsion of two like charges within a precursor (a). leading to elongation (b,c) and then breakage. A generic representation of coulomb fission 6
Figure 1.2: A potential energy curve for the coulomb fission of the multiply charged cluster $(M)_n^{z+}$ into fragments $(A)_{n-k}^{z-x+}$ and $(B)_k^{x}$........ 7
Figure 2.1: The experimental apparatus: A supersonic nozzle coupled to a VG-ZAB double focusing mass spectrometer with a dynode-photomultiplier detection system. 14
Figure 2.2: A diagram of the solvent reservoir showing the production of a vapour consisting of mixed argon/solvent molecules........ 15
Figure 2.3: The stagnation chamber.. 16
Figure 2.4: The cluster generation chamber 17
Figure 2.5: The supersonic expansion. Not shown is the skimmer which isolates the main beam from the rest of the expansion. 18
Figure 3.1: A mass spectrum showing the onset of doubly charged benzene clusters above n=17 40
Figure 3.2: MIKE spectrum of $(C_6H_6)_{17}^{2+}$ 40
Figure 3.3: MIKE scans showing coulomb fission from mass-selected (a) $(C_6H_6)_{23}^{2+}$, (b) $(C_6H_6)_{24}^{2+}$ clusters. Overlain in blue are the simulated peaks. 43
Figure 3.4: A mass spectrum showing the onset on triply charged benzene cluster peaks. Please note, the peak corresponding to the critical size is not shown, see above text for details 46
Figure 3.5: MIKE spectra showing coulomb fission of (a) $(C_6H_6)_{47}^{3+}$, (b) $(C_6H_6)_{48}^{3+}$ and (c) $(C_6H_6)_{49}^{3+}$. Overlain in blue are simulated peaks........ 48
Figure 3.6: A plot of the electrostatic potential energy as function of surface – surface separation. Shown are the curves calculated following coulomb fission for the fragmentation channels seen for the $(C_6H_6)_{48}^{3+}$ precursor cluster (Figure3.5(b)) 50
Figure 3.7: MIKE spectrum of $(C_6H_6)_{98}^{4+}$ ions in the region of coulomb fission 53
Figure 3.8: Simulated peaks for the two possible pathways for the high energy feature in figure 3.7 54
Figure 3.9: MIKE spectra with simulated peaks overlain for the precursor ions: (a) $(C_6H_6)_{98}^{4+}$ (b) $(C_6H_6)_{100}^{4+}$........ 56
Figure 3.10: Values for critical sizes for benzene charged benzene clusters up to charge state 4+. In blue are the experimental results obtained through experiment in this work, red are the calculated values from the liquid drop model and green are the values obtained in ref 13........ 59

Figure 4.1: The mass spectrum of acetonitrile showing the onset of doubly charged peaks 64
Figure 4.2: MIKE spectrum showing the coulomb fission of the $(CH_3CN)_{31}^{2+}$ ion. Overlain in blue are the simulated peaks 66
Figure 4.3: The potential energy curves for the pathways shown in figure 4.2 67
Figure 4.4: Mass spectrum showing the onset of triply charged acetonitrile peaks 70
Figure 4.5: MIKE spectra showing the coulomb fission from the precursor ions a) $(CH_3CN)_{69}^{3+}$ and b) $(CH_3CN)_{74}^{3+}$. Overlain in blue are the simulated peaks for the pathways observed 72
Figure 4.6: Electrostatic potential energy curves for the pathways shown in Figure 4.5a 74
Figure 4.7: An overlay showing how the characteristic profile from the fission of fourfold charged acetonitrile clusters develops as a function of size 75
Figure 4.8: MIKE spectra from the coulomb fission of $(CH_3CN)_{165}^{4+}$. Overlain is the simulated peaks for a) the 3+/1+ mechanism and b) the 2+/2+ mechanism. 77
Figure 4.9: Potential energy curves for the fragmentation pathways shown in figure 4.8a 78
Figure 4.10: The magnitudes for the critical sizes for acetonitrile determined experimentally (blue)and calculated by the liquid drop model (red) 81
Figure 5.1: Mass spectrum showing onset on doubly charged ammonia cluster peaks 91
Figure 5.2: An expanded view of the $H_x(NH_3)_{55}^{2+}$ region showing the ions that comprise it. p: $(NH_3)_{55}^{2+}$, a: $(NH_3)_{55-1}NH_2^{2+}$, b: $(NH_3)_{54}NH^{2+}$, c: $(NH_3)_{54}NH_4^{2+}$, d: $(NH_3)_{53}(NH_4^+NH_4^+)$, e: $(NH_3)_{53}$ $(NH_5^+NH_4^+)$, f: : $(NH_3)_{53}$ $(NH_5^+NH_5^+)$. 91
Figure 5.3: MIKE spectra for precursor ions (a) $(NH_3)_{51}^{2+}$ and (b) $(NH_3)_{52}^{2+}$ showing coulomb fission. Overlain are the simulated peaks 93
Figure 5.4: Solution to the dielectric particle model for the reaction pathways shown in figure 5.3b 95
Figure 5.5: A mass spectrum showing the onset of triply charged ammonia clusters of the form $H_x(NH_3)_n^{3+}$ 97
Figure 5.6: MIKE spectra showing the characteristic profile from the coulomb fission of triply charged ammonia clusters down to n=117 98
Figure 5.7: Diagram showing the origin of the protonated cluster peaks in the mass spectrum. Taken from [4] 99
Figure 5.8: MIKE spectrum of $(NH_3)_{122}^{3+}$ ions 101
Figure 5.9: MIKE scan of $(NH_3)_{122}^{3+}$ overlain with he predicted energies of E_f for the potential fragments from the protonated precursor cluster 101

Figure 5.10: MIKE spectrum of $(NH_3)_{122}^{3+}$ overlain with the simulated peaks 103
Figure 5.11: The potential energy curves calculated for the three fragmentation pathways observed in the MIKE spectrum (figure 5.10) 104
Figure 5.12: MIKE spectrum showing the signal from coulomb of $(NH_3)_{208}^{4+}$ ions 106
Figure 5.13: A plot of the characteristic signal about 8600 eV in the MIKE spectra for clusters approaching the critical size. $(NH_3)_{205}^{4+}$ is assigned as the critical size 106
Figure 5.14: MIKE spectrum for the fission of $(NH_3)_{210}^{4+}$ ions overlain with the simulated peaks for the pathway producing 3+ and 1+ charged cluster fragments 110
Figure 5.15: MIKE spectrum for the fission of $(NH_3)_{210}^{4+}$ ions overlain with the simulated peaks for the pathway producing 2+ and 2+ charged cluster fragments 111
Figure 5.16: Solution to the dielectric particle model for the fragmentation pathways shown in figure 5.14 112
Figure 5.17: Solution to the dielectric particle model for the fragmentation pathways shown in figure 5.15 113
Figure 5.18: A plot showing the deterioration of the characteristic signal intensity as the precursor cluster approaches the stable size $ncrit(4)$ 114
Figure 5.19: An overlay showing the onset of the characteristic coulomb fission profile around 8500 eV above a critical size of $ncrit = 302$ 116
Figure 5.20: MIKE spectrum showing coulomb fission in $(NH_3)_{385}^{5+}$ ions 117
Figure 5.21: Simulated peaks of the fission pathways labelled for the precursor $(NH_3)_{385}^{5+}$. 117
Figure 5.22: An overlay of MIKE spectra showing the simultaneous onset of 6+ clusters beyond $ncrit = 468$ and the progression towards the stable size of 5+ clusters at $nstab = 410$ 120
Figure 5.23: MIKE spectrum showing the coulomb fission of $(NH_3)_{492}^{6+}$ into the fragments shown overlain with the simulated peak for the process 123
Figure 5.24: An expanded view of the MIKE spectrum showing the coulomb fission of $(NH_3)_{492}^{6+}$ into the fragments shown overlain with the simulated peaks for the pathways 124
Figure 5.25: Solution to the dielectric particle model for the fragmentation pathways shown in figure 5.18 125
Figure 5.26: An overlay of MIKE spectra showing the simultaneous onset of 7+ clusters beyond $ncrit(7) = 630$ and the progression towards the stable size of 6+ clusters at $nstab(6) = 564$ 127
Figure 5.27: Four examples of MIKE spectra from sevenfold charged precursor ions showing degrees of asymmetry towards the low energy side of the peak 128

Figure 5.28: MIKE spectra for $(NH_3)_{679}^{7+}$ cluster ions overlain with the simulated peaks for the 6+/1+ fission mechanism 129
Figure 5.29: MIKE spectrum showing the fission of $(NH_3)_{679}^{7+}$ cluster ions. The simulated peaks for fragments are shown 130
Figure 5.30: MIKE spectrum showing the coulomb fission of $(NH_3)_{679}^{7+}$ cluster ions. The simulated peak in blue is for coulomb fission into the fragments shown; in red is the simulated peak from the coulomb fission of the artefact precursor into a fragment of same symmetry................................ 133
Figure 5.31: MIKE spectrum showing the coulomb fission of $(NH_3)_{665}^{7+}$ cluster ions. The simulated peak in blue is for coulomb fission into the fragments shown; in red is the simulated peak from the coulomb fission of the artefact precursor into a fragment of the same symmetry.......................... 134
Figure 5.32: Electrostatic potential energy curve following coulomb fission of $(NH_3)_{679}^{7+}$ into 6+/1+ charged fragments.. 135
Figure 5.33: Electrostatic potential energy curve following coulomb fission of $(NH_3)_{679}^{7+}$ into 5+/2+ charged fragments.. 135
Figure 5.34: MIKE spectra showing an onset of a characteristic signal originating from eightfold charged ammonia clusters with a simultaneous decrease in intensity in sevenfold charged clusters as the stable size is reached.. 137
Figure 5.35: The MIKE spectra for the fission of the $(NH_3)_{824}^{8+}$ overlain with the simulated peaks for the potential fates of the cluster 138
Figure 5.36: Comparison of the calculated and experimentally determined values of the critical sizes $ncrit(z)$.. 140
Figure 5.37: A graph showing the relationship of average KER to the magnitude of the total charge (q1.q2). In red is the curve av. KER = q1.q2. 148
Figure 6.1: Mass spectrum showing the onset of $(C_4H_8O)_n^{2+}$ ion peaks 151
Figure 6.2: MIKE spectra of $(C_4H_8O)_{25}^{2+}$ overlain in blue by the simulated peaks 153
Figure 6.3: Potential energy curves for the fragmentation pathways shown in figure 6.1 at very short separations 154
Figure 6.4: A mass spectrum showing the critical region of triply charged THF clusters 156
Figure 6.5: MIKE scan showing the fragmentation for the fission of $(C_4H_8O)_{53}^{3+}$.overlain in blue are the simulated peaks.. 157
Figure 6.6: Potential energy curves for the interaction between the fragments for the pathways shown in figure 6.5.. 158
Figure 6.7: MIKE spectra showing fragments resulting from (a) $(C_4H_8O)_{119}^{4+}$ and (b) $(C_4H_8O)_{53}^{2+}$... 162
Figure 6.8: MIKE spectra showing fission from the precursor ion $(C_4H_8O)_{110}^{4+}$ 163
Figure 6.9: Figure 6.9 overlain with the fitted simulated peaks from the fragmentation into 3+/1+ fragments 163

Figure 6.10: Figure 6.7 overlain with the simulated peak for the fission into 65^{2+} and 45^{2+} fragments 164
Figure 6.11: A plot of the experimental and critical sizes as a function of charge *z* 168
Figure 7.1: Mass spectrum showing the onset of doubly charged water clusters 175
Figure 7.2: MIKE spectrum showing the fragments formed from coulomb fission of the $(H_2O)_{37}^{2+}$ ion [7]. Overlain are the simulated peaks from the peak simulation model 176
Figure 7.3: The potential energy curves calculated for the separating fragments for the pathways shown in figure 7.2 177
Figure 7.4: a) Mass spectra showing the region of onset of triply charged water clusters. b) An expanded view showing the peaks that make up the feature........ 181
Figure 7.5: MIKE spectrum in the region of coulomb fission for forms of the $H_x(H_2O)_{86}^{3+}$ precursor. Overlain are the locations of the predicted energies for potential protonated forms of the 2+ charged fragment 183
Figure 7.6: MIKE spectra showing the fission of $(H_2O)_{86}^{3+}$ overlain with the simulated peaks 184
Figure 7.7: potential energy curves for the fragmentation pathways shown in figure 7.6........ 185
Figure 7.8: An overlay of MIKE spectra monitoring the neutral loss pathway for fourfold charged precursors 187
Figure .7.9: MIKE spectrum for the coulomb fission of $(H_2O)_{158}^{4+}$........ 189
Figure .7.10: Figure 7.8 overlain with the predicted peak for the formation of the $(H_2O)_{99}^{2+}$ fragment 189
Figure 7.11: The MIKE spectrum of $(H_2O)_{158}^{4+}$ overlain with simulated peaks for the coulomb fission into 3+ charged fragments........ 190
Figure 7.12: Potential energy curves for the fragments formed from the coulomb fission of $(H_2O)_{158}^{4+}$ into 3+/1+ fragments........ 191
Figure 7.13: MIKE spectrum showing the coulomb fission of the $(H_2O)_{250}^{5+}$ ion 193
Figure 7.14: Figure 7.13 overlain with the simulated peaks for a range of 3+/2+ fragmentation pathways 193
Figure 7.15: Comparison of the experimentally determined critical sizes and the values predicted by the liquid drop model........ 195

List of Tables

Table 3.1: A table comparing the predicted barrier heights U_{max} with the <*KER*> from the simulated peaks of $(C_6H_6)_{23}^{2+}$ and $(C_6H_6)_{24}^{2+}$. Also shown are values of *KER* calculated using the width of the peak [12]. 43
Table 3.2: Calculated values of the barrier heights from the dielectric particle model and <*KER*> from the fitted simulated peaks in figure 3.4. 48
Table 3.3: The fragment size and the barrier height U_{max} for the fragment at 9279 eV in figure 3.6 and the values for <*KER*> in the simulated peaks for each Z_f shown in figure 3.7 54
Table 3.4: The values for the barrier height and the <KER> from the fitted peaks on figure 3.8 56
Table 4.1: Values for $< KER >$ and $Umax$ for the pathways shown in figure 4.2. Also shown are values calculated for the kinetic energy release from the FWHM of the shown as KER using an older method [5]. 66
Table 4.2: Values for $< KER >$ and $Umax$ for the pathways shown in figure 4.5 73
Table 4.3: Values for $Umax$ and $< KER >$ for the pathways shown for the two fission mechanism shown in figure 4.8(a,b) 78
Table 4.4: Experimental and calculated values for $ncrit(z)$ and the percentage difference for multiply charged acetonitrile clusters 81
Table 5.1: Values for $< KER >$ and $Umax$ for the fragmentation pathways shown in figure 5.2 for (a) $(NH_3)_{51}^{2+}$ and (b) $(NH_3)_{52}^{2+}$ 94
Table 5.2: The values for U_{max} and <*KER*> for the channels highlighted in figure 5.10 103
Table 5.3: The values for $Umax$and $< KER >$ for the channels highlighted in figure 5.14 110
Table 5.4: The values for $Umax$ and $< KER >$ for the channels highlighted in figure 5.15 111
Table 5.5: $< KER >$ and $Umax$ values for the fragments that make up the peak in figure 5.21 118
Table 5.6: The identity of the fragment detected at 8520 eV and the value of the barrier height from the separation of the two fragments for charge states $Zf = 4, 3$ 121
Table 5.7: Table showing the values of $< KER >$ and $Umax$ for the pathway shown in figure 5.23. Additional values are given for imaginary neighbouring fragments which are very close in magnitude. 123
Table 5.8: Table showing the values of $< KER >$ and $Umax$ for the pathway shown in figure 5.24 124
Table 5.9: Values for $< KER >$ and Umaxfor the simulated peaks in figure 5.28 129
Table 5.10: Values of $< KER >$ and Umax for the pathways shown on figure 5.29 131

Table 5.11: Values of $< KER >$ and $U\max$ for the pathways shown on figure 5.29 134
Table 5.12: Values of $< KER >$ and $U\max$ for the pathways shown on figure 5.30 134
Table 5.13: Values of $< KER >$ and $U\max$ for the pathways shown on figure 5.26 138
Table 5.14: Values of experimentally determined and calculated $ncrit(z)$ 140
Table 5.15: Values for the critical range, most probable pathway, number of pathways and average KER over the available pathways for multiply charge ammonia clusters 147
Table 6.1: The barrier heights and the <KER> for the fragments detected in figure 6.2 154
Table 6.2: The calculated values of barrier height and <KER> for the $(C_4H_8O)_{53}^{3+}$ cluster fission........ 157
Table 6.3: The calculated values of $Umax$ and $< KER >$ for the pathways shown in figure 6.9 164
Table 6.4: The calculated values of $Umax$ and $< KER >$ for the pathway shown in figure 6.10 164
Table 6.5: Values for the experimental and calculated critical sizes 168
Table 7.1: Values of $< KER >$ from the fitted peaks and $Umax$ for the fragmentation channels shown in figure 7.2. Included for comparison are values of KER calculated using the old methodology [7] 176
Table 7.2: Values for the $< KER >$ for the simulated peaks and $Umax$ for the pathways shown 185
Table 7.3: The values of $< KER >$ and $Umax$ for the pathways shown in figure 7.10........ 190
Table 7.4: Values for $< KER >$ and $Umax$ for the pathways shown in figure 7.11........ 190
Table 7.5: Values for $< KER >$ and $Umax$ for the pathways shown in figure 7.14 194
Table 7.6: Values for the experimentally and theoretically determined critical sizes 196
Table 8.1: Tabulation of the experimentally determined critical sizes of the systems studied 203

List of Abbreviations

MIKE: Mass-analysed kinetic energy scanning

ffr: Field free region

EI: Electron ionisation

ESI: Electrospray ionisation

CRM: Charge residue mechanism

IEM: Ion evaporation mechanism

$n_{crit}(z)$: Critical size for charge state z

$n_{stab}(z)$: Stable size for charge state z

Chapter 1 : Introduction

The purpose of this chapter is to give a selective overview of the research and theory that has facilitated the work contained in this thesis. Where relevant, progress in the field is given up to the current level of understanding.

1.1 Multiply Charged Molecular Clusters

The study of physical chemistry has benefited greatly from the advent of cluster science. Clusters give a researcher a medium that is distinguishable from condensed or gaseous phases, atoms or bulk and one that is controllable in size and composition. An accepted description of a cluster is 'a large stable aggregate of atoms, ions or molecules that are weakly bound [1], with anywhere between 2 and 10^4 – 10^5 aggregates' [2]. Clearly this is a very large range and physical and chemical properties will change significantly within this range. With the application of modern laboratory equipment the study of clusters has turned into an exciting field of research, enabling the study of the development of characteristic properties of compounds. It is possible in many cases to identify the size of a cluster in which the system shows characteristic chemical and physical properties that are identical to the bulk material. With modern laboratory equipment one is able to accurately control the size of the cluster and follow a property of interest as a function of cluster size. A classic example of this type of experiment was published by Buffat *et al.* [3] who by measuring the size dependent melting temperature of gold particles found that the melting point of bulk gold could be reached with a finite number of gold atoms . The evolution of other bulk properties can be measured by stepwise growth of clusters: magnetism [4], ionisation potential, nature of bonding [5], solvation [6-8] being notable examples. Due to the high proportion of constituents on the surface, clusters have also attracted attention for their potential for use in catalysis [9]. Clusters have also been applied widely in spectroscopic experiments due to the cold platform they provide for seeded compounds [10-12].

A size dependent property that has been the focus of interest in the field of cluster science is the ability of a cluster to support charge. It has been known for a long time that there exists a critical size in cluster systems with charge states $z \geq 2$ that below which the cluster ceases to exist, fragmenting by a process termed coulomb fission [13]. This is the point where the cohesive energy brought about by the surface tension is overcome by the electrostatic repulsion of the total charge within the system. The number of n molecules needed to support z charges in a cluster is termed the critical size $n_{crit}(z)$ and has been determined by an onset of 'non-integer' peaks in a cluster mass spectrum [13]. Beyond this size the inter-charge distance is great enough that the cohesive energy of the cluster can withstand the diminished electrostatic repulsion and the cluster becomes metastable.

The study of stability under electrostatic repulsion and coulomb fission from precursors containing a large amount of charge is the focus of this work. Presented are new methods for determining the mechanism and energetics of the coulomb fission process including results showing coulomb fission up to charge state of 8+. Also included is a study of the onset of stability of the multiply charged systems and how it compares to previous theories. Results are presented for benzene -$(C_6H_6)_n^{z+}$, acetonitrile -$(CH_3CN)_n^{z+}$, ammonia – $(NH_3)_n^{Z+}$, Tetrahydrofuran (THF) – $(C_4H_8O)_n^{z+}$ and water – $(H_2O)_n^{z+}$ multiply charge cluster systems.

1.2 Stability and Coulomb Fission

The first relevant description of stability of multiply charged clusters and droplets was proposed by Lord Rayleigh in 1882 [14] where he stated: "In consequence of electrostatic repulsion, a charged spherical mass of liquid, unacted upon by other forces is in a state of unstable equilibrium....when the charge is great the spherical form is unstable...". Theory developed from this describes the stability of a charged droplet under the influence of charge by treating the cluster system as a continuum with a spherical shape of radius r, that being the minimum value of the surface energy. The critical size, or the minimum number of molecules required to stabilise a cluster containing z charges ($n_{crit}(z)$) is given by the Rayleigh equation [15]:

$$n_{crit}(z) = \frac{(ze)^2}{64\pi^2\gamma\varepsilon_0 r_m{}^3} \tag{1.1}$$

Where z is the total charge, e is is the elementary charge constant, ε_0 is the permittivity of free space, γ is the surface tension of the droplet and r_m is the radius of the cluster. Below this size the cluster is unstable with respect to fission, with a lifetime less than 1µs. In the context of the experiments to be presented, this means that if a multiply charged cluster below the critical size was to form during ionisation it would undergo fission before any analysis could occur. An increase in size beyond $n_{crit}(z)$ stabilises the cluster with respect to coulomb fission and the cluster becomes metastable with a lifetime in the region of approximately 50 µs making it observable in the experimental timeframe (see Chapter 2). The molecular radius is calculated *via* the density of the bulk material in liquid phase, the same method that is used to calculate cluster radii in the dielectric particle model. Room temperature values for surface tensions were used. Beyond a certain size the charge is stabilised to a degree where coulomb fission ceases to be observed in the apparatus. This is termed the stable size for charge state z ($n_{stab}(z)$).

On a molecular level, there will be a range of intermolecular forces holding the cluster together against the electrostatic repulsion. Between neutral molecules of any kind random dipole induced-dipole interactions (dispersion interaction) will be present. If the molecules have strong dipole moments there will also be dipole-dipole and dipole-induced dipole interactions. The presence of charge on the molecules will cause charge-dipole (electrostatic interactions) and charge induced-dipole interactions (inductive interactions) depending on the presence of a permanent dipole the molecules. Water and ammonia molecules, due to the presence of lone pairs of electrons on the O and N atoms can also form hydrogen bonds. Comparison between the experimental measurements on the bond dissociation energy of the dimers of neutral water (1105 ± 10 cm^{-1}) [16], ammonia (660 ± 20 cm^{-1}) [17] and benzene (564 ± 81 cm^{-1}) [18] (larger calculated values for the benzene dimer have been reported, but the values are for the well depth D_e rather than the lowest vibrational energy D_0 [18]) show the strength of the dimer bond is determined, to an extent, by the strength of these interactions. The benzene dimer, held together mainly by dispersive interactions has the weakest interaction energy. The water has a higher energy than that of ammonia due to the increased strength of the hydrogen bond between water molecules. The surface tension of the cluster is the cohesive force that holds the cluster together. To minimise surface energy, the cluster will take the form of a sphere or a close approximation of a sphere. Water, having the strongest intermolecular forces, including hydrogen bonds, will have the largest surface tension (0.072 Nm^{-1}) at the cluster interface. Ammonia clusters also have a hydrogen bonding network. However, the strength of the ammonia – ammonia hydrogen bond is weaker than for water, therefore, the magnitude of the surface tension is smaller. A value of 0.038 Nm^{-1} for ammonia is used in this work [19]. Benzene (0.029 Nm^{-1})[20], acetonitrile (0.029 Nm^{-1}) [21] and tetrahydrofuran (0.026 Nm^{-1}) [22]all have smaller surface tensions. This reduction is due to the lower strength of the attractive intermolecular van der Waals interactions in these systems compared to hydrogen bonds present in water and ammonia. The second governing factor in the magnitude of the critical size $n_{crit}(z)$ is the molecular radius, which is calculated from the bulk density of the substance. This results in the benzene system, which has a comparably small surface tension, having a critical size $n_{crit}(2) = 17$ much smaller than water $n_{crit}(2) = 35$. This is due to the increased separation of the charges compensating for the decrease in surface tension. Comparison between water and ammonia ($n_{crit}(2) = 50$) which have similar molecular radii, reveal the effect the stronger hydrogen bonds have on the value of surface tension for water and the resultant decrease of the critical size.

Over the past 30 or so years there have been many attempts observe and model coulomb fission in various systems [13,23-36]. Some of the work concerns metallic clusters, optical molasses, morse clusters and droplet jets which although may have different physical properties to molecular clusters that are the focus of this work, have yielded some good results that have benefited the whole area of study. Coulomb fission is a charge separation process. The simplest description is that of a precursor with more than one charge centre fragmenting into two or more charged fragment ions when under the influence of electrostatic repulsion, carrying portions of the initial mass of the body. Figure 1.1 gives a schematic of the elongation of the precursor followed by the scission into two charged fragments beyond a critical shape (c).

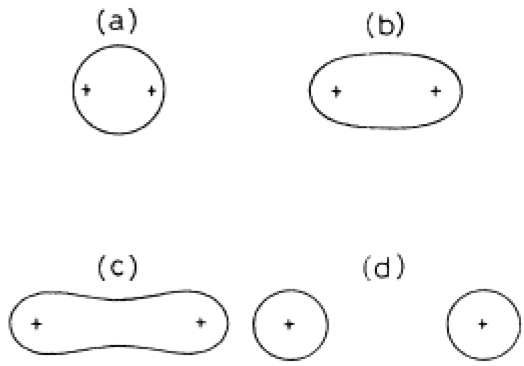

Figure 1.1: Schematic showing the elongation which originates from the electrostatic repulsion of two like charges within a precursor (a). leading to elongation (b,c) and then breakage (d). A generic representation of coulomb fission

A mechanism for describing coulomb fission, starting from ionisation, is a multi-staged process. Firstly, from a double ionisation event from a single electron, a doubly charged ionic cluster of size n is formed with the charged centres separated by m monomers: $(M)^+(M)_m(M)^+(M)_{n-m-2}$ [37]. The next stage comprises rapid electron-hole recombination leading to the repositioning of the charges to opposite sides of the cluster, minimising electrostatic repulsion, giving the cluster ion the form of $(M)^+(M)_{n-2}(M)^+$, a mechanism first proposed by Gay and Berne [37]. Considering a molecular cluster is assumed spherical in shape and dielectric in nature means the charge that is initially gained through the ionisation process is able to move to the surface of the sphere to achieve the most stable configuration. Depending on the number of aggregates in the cluster it will now either be unstable, metastable or thermodynamically stable with respect to fission. The intrinsic energy barrier to fission $E_{barrier}$ is overcome by the residual internal energy in the cluster left over from the ionisation process. This energy is randomly distributed among the many vibrational modes within the cluster, but a portion will be distributed into the collective mode that results in the critical shape before fission and will eventually drive the cluster over the fission barrier. The magnitude of the maximum of potential energy between the fragments with respect to infinite separation (U_{max}) can be derived from the experimental kinetic energy release, KER (see Chapter 2.11). This value can contain information about the position of the charges pre-coulomb fission. Previous work [38] has found that by using a new dielectric particle model (Section 2.10) the interactions between the fragments post-coulomb fission can be analysed. The magnitudes of the calculated U_{max} are found to closely match the experimentally determined KERs for a range of dication cluster systems. Figure 1.2 shows a generic schematic for a potential energy curve for coulomb fission,

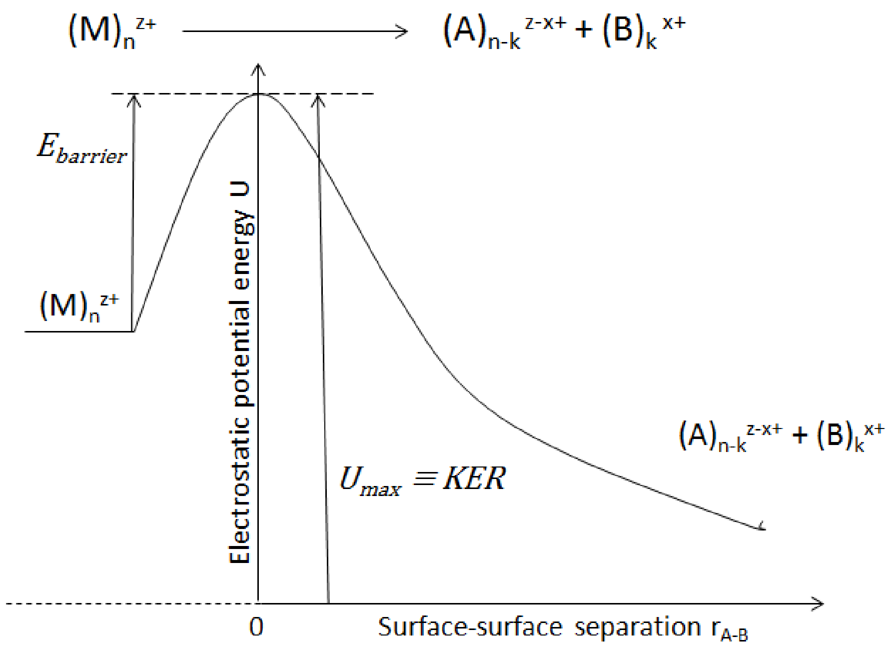

Figure 1.2: A potential energy curve for the coulomb fission of the multiply charged cluster $(M)_n^{z+}$ into fragments $(A)_{n-k}^{z-x+}$ and $(B)_k^{x}$

It has been shown that in some circumstances the force between two like charged dielectric particles can be attractive [39] (Section 2.10). This mirrors observations made in other dielectric mediums. Ocht *et.al.* [40] were able to measure the effect of charge in water droplets in free fall and found a range of interactions between the charged droplets. Attractive potentials have been studied for powder based materials, similar to those used in electrophotographic printers [41]. There are noted similarities between the fragmentation pathways of the multiply charged cluster and the fundamental step of the electrospray ionisation (ESI) technique in which the final analyte is formed [42]. The work presented shows unimolecular fission for clusters much larger and highly charged than previously observed. This affords the opportunity to study molecular clusters that are comparable in size and charge to an ESI droplet.

References

[1] M.R. Hoare, *Adv chem phys* **40** (1979).
[2] J.E. Campana, *Mass Spectrometry Reviews* **6** (1987) 395.
[3] P. Buffat, J.P. Borel, *Physical Review A* **13** (1976) 2287.
[4] I.M.L. Billas, A. Chatelain, W.A. Deheer, *Science* **265** (1994) 1682.
[5] K. Rademann, B. Kaiser, U. Even, F. Hensel, *Physical Review Letters* **59** (1987) 2319.
[6] M. Peschke, A.T. Blades, P. Kebarle, *Journal of Physical Chemistry A* **102** (1998) 9978.
[7] R.R. Wright, N.R. Walker, S. Firth, A.J. Stace, J*ournal of Physical Chemistry A* **105** (2001) 54.
[8] A. Stace, *Science* **294** (2001) 1292.
[9] A.W. Castleman, *Catal. Lett*. **141** (2011) 1243.
[10] H. Cox, A.J. Stace, *International Reviews in Physical Chemistry* **29** (2010) 555.
[11] L. Ma, T. Takashima, J. Koka, H.J. Kimber, H. Cox, A.J. Stace, *Journal of Chemical Physics* **138** (2013).
[12] A.J. Stace, *Journal of Physical Chemistry A* 106 (2002) 7993.
[13] K. Sattler, J. Muhlbach, O. Echt, P. Pfau, E. Recknagel, *Physical Review Letters* **47** (1981) 160.
[14] L. Rayleigh, *Philos. Mag* **14** (1882) 184.
[15] O.E. T.D. Mark, *Clusters of Atoms and Molecules II*, 1994.
[16] B.E. Rocher-Casterline, L.C. Ch'ng, A.K. Mollner, H. Reisler, *Journal of Chemical Physics* **134** (2011).
[17] A.S. Case, C.G. Heid, S.H. Kable, F.F. Crim, *Journal of Chemical Physics* **135** (2011).
[18] H.J. Neusser, H. Krause, *Chemical Reviews* **94** (1994) 1829.
[19] M. Conde-Petit, Thermophysical Properties of NH3 + H2O Solutions for the Industrial Design of Absorption Refrigeration Equipment. *M. Conde Engineering*, 2004.
[20] A.W. Adamson, A.P. Gast, *Physical Chemistry of Surfaces*, 1997.
[21] J. Jasper, *J. Phys. Chem. Ref. Data* **1** (1972).
[22] www.Surface-tension.de.
[23] D. Kreisle, O. Echt, M. Knapp, E. Recknagel, K. Leiter, T.D. Mark, J.J. Saenz, J.M. Soler, *Physical Review Letters* **56** (1986) 1551.
[24] R. Casero, J.J. Saenz, J.M. Soler, *Physical Review A* **37** (1988) 1401.
[25] O. Echt, D. Kreisle, E. Recknagel, J.J. Saenz, R. Casero, J.M. Soler, *Physical Review A* **38** (1988) 3236.
[26] N.G. Gotts, A.J. Stace, *Physical Review Letters* **66** (1991) 21.
[27] N.G. Gotts, P.G. Lethbridge, A.J. Stace, *Journal of Chemical Physics* **96** (1992) 408.
[28] U. Naher, S. Bjornholm, S. Frauendorf, F. Garcias, C. Guet, *Physics Reports-Review Section of Physics Letters* **285** (1997) 245.
[29] C. Brechignac, P. Cahuzac, N. Kebaili, J. Leygnier, *Physical Review Letters* **81** (1998) 4612.
[30] D. Duft, T. Achtzehn, R. Muller, B.A. Huber, T. Leisner, *Nature* **421** (2003) 128.
[31] D. Schroder, *Angew. Chem.-Int. Edit.* **43** (2004) 1329.
[32] I. Last, Y. Levy, J. Jortner, *Journal of Chemical Physics* **123** (2005).
[33] A. Heidenreich, J. Jortner, I. Last, *Proceedings of the National Academy of Sciences of the United States of America* **103** (2006) 10589.
[34] M. Hoener, C. Bostedt, S. Schorb, H. Thomas, L. Foucar, O. Jagutzki, H. Schmidt-Böcking, R. Dörner, T. Möller, P*hysical Review A* **78** (2008) 021201.
[35] I. Last, J. Jortner, *Chem. Phys.* **399** (2012) 218.

[36] M.W. Ross, C. Berkdemir, A.W. Castleman, Jr., *The journal of physical chemistry. A* **116** (2012) 8530.
[37] J.G. Gay, B.J. Berne, *Physical Review Letters* **49** (1982) 194.
[38] X. Chen, University of Nottingham, 2011.
[39] A.J. Stace, A.L. Boatwright, A. Khachatourian, E. Bichoutskaia, *Journal of Colloid and Interface Science* **354** (2011) 417.
[40] H.T. Ochs, R.R. Czys, *Nature* **327** (1987) 606.
[41] J.Q. Feng, *Physical Review E* **62** (2000) 2891.
[42] X. Chen, E. Bichoutskaia, A.J. Stace, *The journal of physical chemistry. A* **117** (2013) 3877.

Chapter 2 : Experimental Section

2.1 Introduction

The experimental measurements of multiply charged molecular clusters presented in this thesis have been carried out using a VG-ZAB double focusing mass spectrometer of Niers-Johnson geometry; that is, with a mass-selecting magnetic sector preceding the energy analyser. The mass spectrometer ionises neutral clusters, and using different operating modes, one is able to isolate both precursor and fragment clusters for study. The mass spectrometer is coupled to a pulsed supersonic nozzle which produces the neutral clusters. Cluster ions of a range of sizes and charge states are produced in the ion source and are focused *via* a magnet into a field free region (*ffr*) where fragmentation of metastable precursors can be measured by scanning an electrostatic analyser (ESA) over a range of energy values. The ion beam must also pass through three sets of focussing slits. One is positioned at the end of the ion source and subsequent ion optics, the intermediate slit is positioned at the end of the 2nd *ffr* and acts to focus in the z-axis, and finally, the collector slit is positioned after the ESA and before the detector. These slits act to align the ion beam and also discriminate against divergence of the ion beam, allowing for more precise measurements of coulomb fission.

This setup allows for the production and ionisation of atomic and molecular clusters and subsequent probing of unimolecular reaction pathways of the ions by using a technique called mass-analysed ion kinetic energy (MIKE) scanning. Additionally, the ZAB can accommodate a collision cell at the end of the 2nd field free region enabling the study of collision-induced fragmentation reactions and has a port to allow a laser to pass into the chamber, allowing laser-induced fragmentation reactions to be performed. There is also an option to include a ‘pick-up’ chamber between the cluster chamber and the ion source enabling the production and study of metal-ligand complexes.

2.2 Experimental setup

The experimental process can be broken down into 6 stages: Cluster production, ionisation, magnetic sector, second field free region, electric sector and detection. Clusters are formed *via* the supersonic expansion of a mixture of the solvent of interest with a carrier gas, which for all results presented was argon gas. For experiments involving ammonia, a pre-seeded gas mixture of 10% ammonia/argon was used. The neutral clusters then travel a short distance to the ion source where they are ionised by electron ionisation. Positive ions are then extracted by charged plates through the first field free region (1st *ffr*) into the magnetic sector. Clusters are isolated by using an electromagnet with a fixed radius of curvature. The value of the magnetic field strength will select a cluster ion with a specific value of mass-to-charge (m/z) and exclude all others. The selected ions travel on to the second field free region (2nd *ffr*) where the fragmentation of precursor ions can be observed. Resulting fragments, and residual precursor ions pass on to the electric sector which separates the ions according to their kinetic energy in the laboratory frame. The reaction fragments then pass through to be detected. Figure 2.1 is a schematic overview of the experimental apparatus.

This basic setup has been used in similar experiments previously [12, 13]. Modifications have been made to maximise the probability of detecting the very small signals resulting from coulomb fission presented in this work. A pick-up cell, between the cluster chamber and ion source chamber was removed. This reduces the distance to ionisation from the nozzle and so reduces the divergence of the collimated molecular beam. This will increase the number density of neutral clusters entering the ion source. This results in additional ionisation in the ion source and consequently, additional multiply charged precursors in the final ion beam. Secondly, in order to maximise dynode conversion and peak separation in the MIKE spectra, higher accelerating energies were used. The increase in kinetic energy of ions in the beam colliding with the dynode results in stronger signals at detection. The resolution of MIKE peaks can be improved by increasing the accelerating energy. The laboratory frame kinetic energy of MIKE peaks is dependent on E_p the kinetic energy of the parent (See Equation 2.10, Section 2.9). This energy is given to it by the accelerating potential. If one was to increase this energy from 5 kV to 7 kV, the peaks would shift in energy by a factor of 7/5, and so too would the spacing of the peaks. It may be assumed that the MIKE spectra presented are performed under 7 kV accelerating potential, unless otherwise stated.

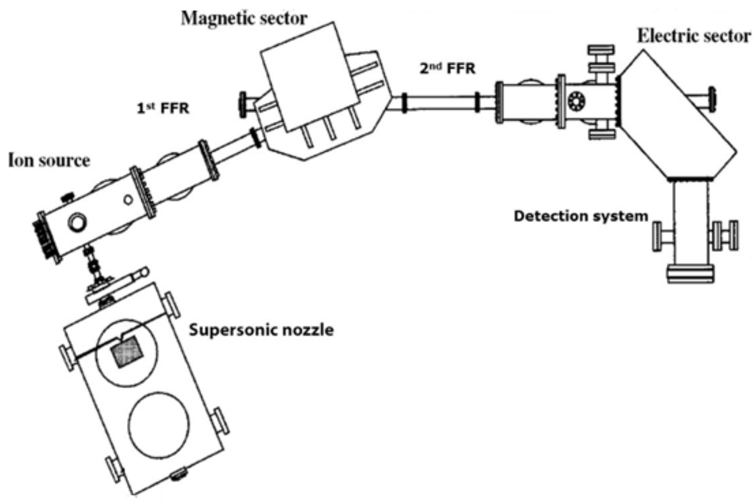

Figure 2.1: The experimental apparatus: A supersonic nozzle coupled to a VG-ZAB double focusing mass spectrometer with a dynode-photomultiplier detection system.

2.3 Cluster Formation

The first stage of cluster formation is to form mixed clusters of the solvent molecules and argon atoms. To achieve this argon gas is passed into a reservoir containing approximately 20 ml of the solvent. The gas enters at the base of the reservoir and passes to the top, mixing with the vapour phase of the solvent above the meniscus. The gas mixture then passes through into the stagnation chamber located behind a nozzle inside the expansion chamber. It is often found to be effective to apply some level of cooling by using an ice bath to lower the vapour pressure of solvent in the reservoir. This can help achieve a balanced mix of solvent/carrier gas that is suitable for supersonic expansion. High amounts of solvent in the stagnation can 'flood' the chamber which can limit the supersonic expansion process as a means of producing molecular clusters (Section 2.4). Figure 2.2 shows a cross section of the reservoir. The only exception to this procedure was during the production of ammonia clusters where a pre-mixed cylinder of 10% ammonia with argon gas is used to pass the mixture directly into the stagnation chamber.

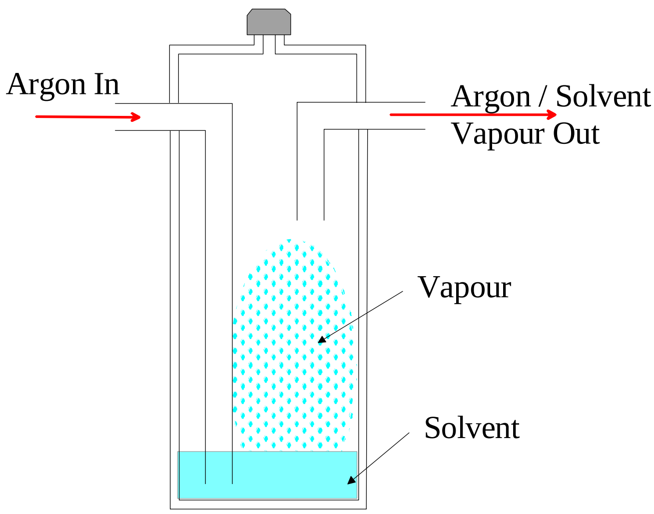

Figure 2.2: A diagram of the solvent reservoir showing the production of a vapour consisting of mixed argon/solvent molecules

The vapour is then passed into the stagnation cell housed inside the cluster generation chamber (figure 2.3). The stagnation chamber is made of aluminium and ~ 8 x 10^{-4} m^3 in volume, the nozzle orifice is part of the front plate with a diameter of 0.2 mm and opens out to a 30° cone angle with a 5 mm channel length. In order to provide a pulsed gas flow a Bosch fuel injector is mounted onto the front plate and is driven by a 12 V square pulse. When switched off the cap and Kalrez disc attached to the fuel injector rests against the nozzle orifice sealing the gas flow off to the cluster chamber. When switched on the cap retracts back a short distance and returns forward to seal the nozzle before the next cycle. This process allows a short burst of gas through the nozzle initiating the first stages of pulsed supersonic expansion (Section 2.4). There is also a mechanism to prevent gas flow into the stagnation chamber, and instead, evacuate the stagnation chamber using a rotary pump.

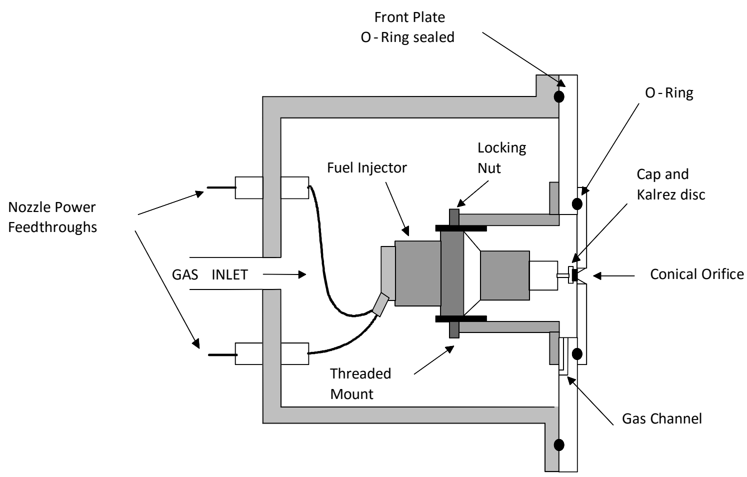

Figure 2.3: The stagnation chamber.

Figure 2.4 shows the location of the stagnation chamber in the main cluster chamber. The skimmer is a fluted cone of diameter 1 mm and length 2.54 cm. The distance between the skimmer and the nozzle is 3 cm. When the supersonic expansion hits the skimmer it is collimated into a narrow beam containing neutral molecular clusters and residual argon atoms.

The cluster generation chamber is divided into two sections by a bulkhead, the expansion chamber and the collimation chamber. The expansion chamber is pumped by 8000 ls^{-1} oil diffusion pump which is backed by an Edwards E2M40 2-stage rotary pump. This configuration achieves a base pressure of approximately 6 x 10^{-7} mbar. When operational, an Edward EH 250 booster pump is used to assist pumping of the region, resulting in a working pressure of approximately 9 x 10^{-4} mbar. The collimation chamber is pumped by a 2000 ls^{-1} Edwards diffstak pump backed by an Edward E2M-40 2-stage rotary pump, achieving a base pressure of approximately 5 x 10^{-7} mbar and a working pressure of 5 x 10^{-5} mbar. The pressure in both sections is monitored continuously by penning gauges.

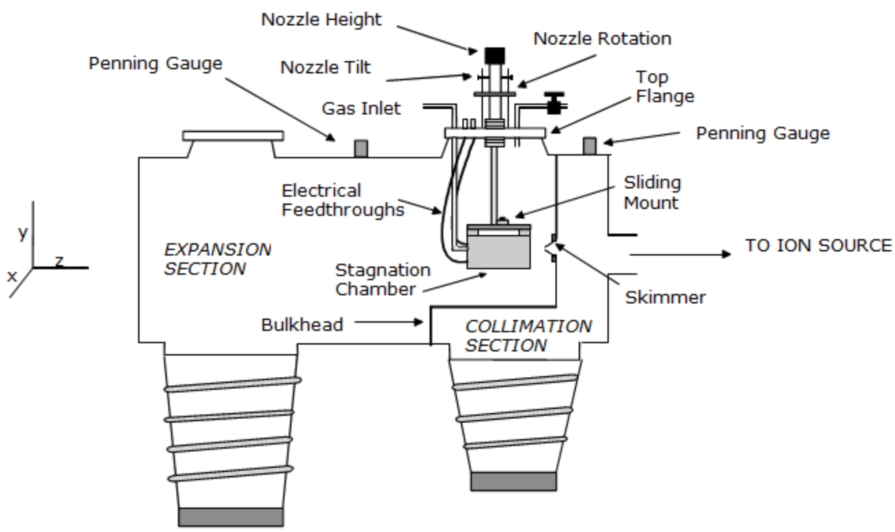

Figure 2.4: The cluster generation chamber

2.4 Supersonic Expansion

Supersonic expansion is a means of producing a beam of uniform molecular clusters for later study. Gas held at constant pressure and temperature is passed through a nozzle of diameter D_0 into an expansion chamber which is under high vacuum. The combination of high backing pressure and a small orifice results in frequent collisions in the region of the nozzle which acts to redistribute the thermal motion of the molecules held in the stagnation chamber into directional kinetic motion in the axis of the jet [1]. As a result the velocity distribution is greatly narrowed giving a very low translational temperature. For supersonic expansion to occur, a Knudsen number (K_n) of <1 is required. K_n is defined by:

$$K_n = \lambda_0 / D_0$$

Where λ_0 is the mean free path of the gas and D_0 is the diameter of the nozzle. If K_n >>1 the resultant expansion is termed effusive where due to the lack of collisions significant reordering of velocities and subsequent cooling is not seen. Figure 2.5 gives a schematic of the supersonic expansion.

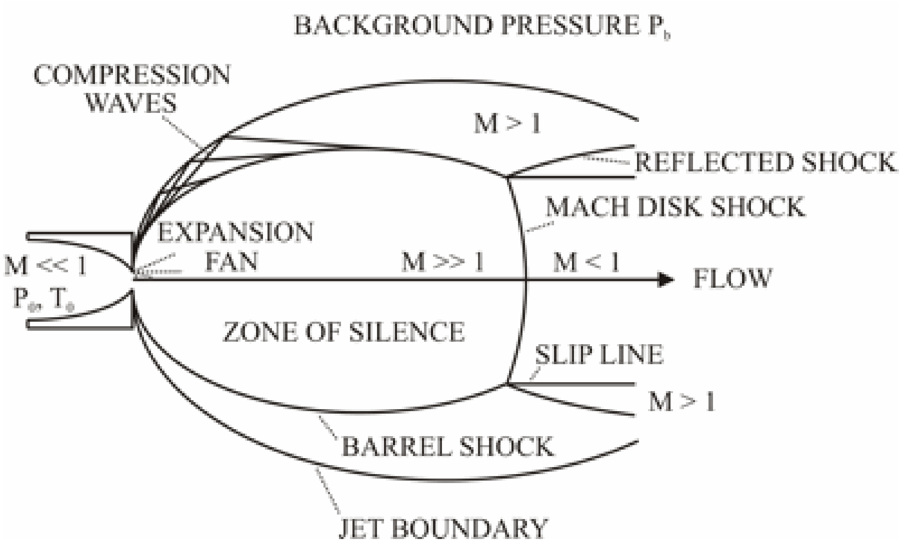

Figure 2.5: The supersonic expansion. Not shown is the skimmer which isolates the main beam from the rest of the expansion.

As the gas mixture leaves the nozzle region it expands until it reaches the jet boundary with background pressure P_b and can expand no longer. This creates shock fronts as reflected waves merge and form a singular front. In the axial direction this is known as the mach disk shock and if allowed to form will interfere with the molecular flow of the expansion. The position of the mach disk is given by [2] :

$$\frac{x_m}{D_0} = 0.67\left({}^{P_0}/_{P_b}\right)^{1/2}$$

Where x_m is the distance from the nozzle and P_0 is the initial pressure in the stagnation chamber. To isolate a molecular beam and avoid interference from the mach disk a skimmer is placed upstream of this position which isolates a molecular beam from the jet.

Collisions of expanding gas in the first few nozzle lengths lead to clustering. During the initial stages of growth three-body reactions are predominant with the energy generated by the process carried away with the third body. When the cluster is large enough for the internal degrees of freedom to accommodate the energy two-body growth reactions will occur [3]. There are also destructive reactions that will reduce the size of the cluster. These are termed sputtering and decay.

$$A_n + A + B \rightarrow A_{n+1} + B \qquad \textit{(Three-body growth)}$$

$$A_n + A \rightarrow A_{n+1} \qquad \textit{(Two-body growth)}$$

$$A_n + A \rightarrow A_{n-1} + 2A \qquad \textit{(Sputtering)}$$

$$A_n \rightarrow A_{n-1} + A \qquad \textit{(Decay)}$$

2.5 Ion Source

The ionisation source of the mass spectrometer consists of a dual EI/CI ion source contained within a housing chamber held at approximately 3 x 10^{-7} mbar. For the experiments reported herein, electron ionisation (EI) is used in the production of charge clusters. Electrons are produced by thermionic emission from a tungsten filament and accelerated towards a trap electrode kept constant at 1 mA, located at the opposite end of the source block. The electrons are forced into a helical path by the presence of two permanent magnets which are fixed on opposite ends of the outside of the source block, this increases the distance the electrons travel through the path of neutral clusters, hence increasing the probability of collisions. Neutral clusters enter perpendicularly to the path of the high energy electrons and the final trajectory of the resulting ions into the spectrometer. The ions are subject to a small repulsive potential from the repeller which is controlled with a variable voltage of – 40V to +40 V which directs the ions into the 1st field free region. The source block is floated at a potential of up to 10 kV which provides the ions with their initial kinetic energy. Several focussing plates act on the ions as they travel into the mass spectrometer. Figure 2.6 shows a top-down photograph of the source block.

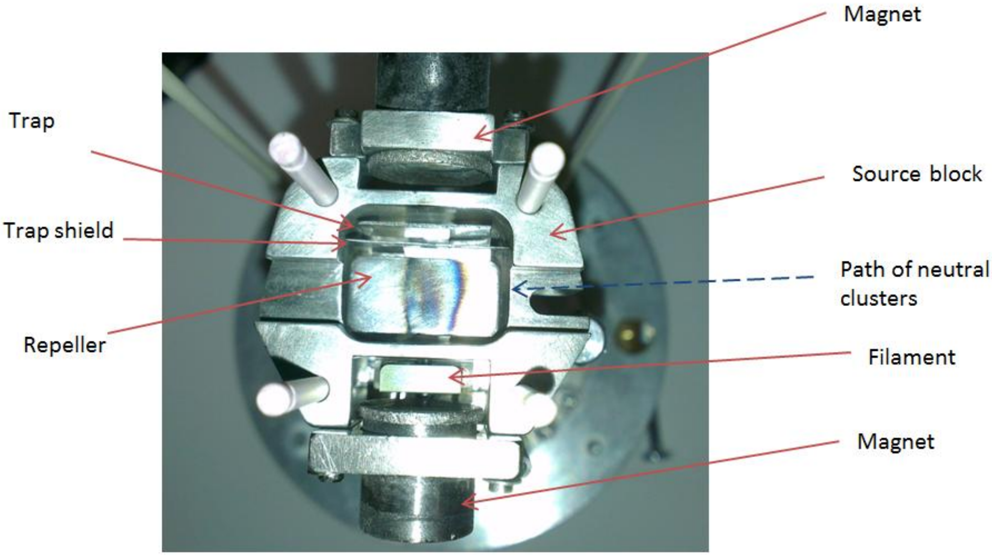

Figure 2.6: A top-down view of the source block. The trajectory of the ionised clusters is out of the page.

In the first stages of the ionisation event the approaching electrons act to distort the electric field of the neutral clusters. If the energy of the electron exceeds a critical point, termed the appearance energy, some of the neutral clusters will be ionised and a secondary electron is ejected from the cluster. Cluster ionisation follows Frank-Condon principles [4], thus the resultant ions will initially take on a range of excited vibronic states. There is likely to be a large internal energy of up to 6 eV [5] which can then be dissipated by the release of monomer units of solvent and the remaining argon atoms, as well as radiative emission [6,7]. The initial ionisation event takes place in the timescale of approximately 10^{-16} s, with subsequent aforementioned processes creating the ions forming the main ion beam entering the mass spectrometer within 10^{-8} s using the current experimental set-up [8].

A general scheme for electron ionisation of atomic clusters has been given [9]:

$$e^- + R_n \rightarrow {R_m}^+ + (n - m)R + 2e^-$$

This process produces two secondary electrons which are then scattered from the initial trajectory of the primary electron. If the energy of the primary electron greatly exceeds the appearance potential then it is possible for the secondary electrons to travel through the cluster and undergo subsequent ionisation events, thus resulting in multiply charged clusters. This mechanism was first proposed based on molecular dynamics simulations by Gay and Berne [10]. It is supported by observing that the appearance potentials of multiply charged atomic clusters correlate to the potential required for single ionisation multiplied by the number of the charge state [11]. One can therefore predict the accessibility of higher-order z-fold charge clusters by only knowing the bare ionisation energy of the solvent.

2.6 Magnetic Sector

In the first field free region the ions experience no external force and are propelled by their initial kinetic energy, obtained from the ion source. The working pressure of the flight tubes from the ion source through the mass spectrometer is kept at approximately $6x10^{-7}$ mbar by four Edward Diffstak mk 2 oil diffusion pumps. It is especially important that the pressure in the mass spectrometer is as low as possible to attempt to eliminate the interference from collision-activated processes. Ions entering the magnet experience a force perpendicular to the direction of their motion of a magnitude proportional to its charge and the strength of the magnetic field. This is called the Lorentz force:

$$F = zvB \tag{2.1}$$

Where F is force, z is charge on the ion, v is initial velocity of the ion and B is the strength of the magnetic field. The magnetic force is balanced by the centrifugal force ($F = \frac{mv^2}{r}$) acting outward of the radius of the circle.

$$F = \frac{mv^2}{r} = zvB \tag{2.2}$$

Equation 2.2 can be rearranged to give a linear relationship between mv and the magnetic field.

$$mv = zBr \tag{2.3}$$

Subsequent rearrangement gives:

$$v = \frac{zBr}{m} \tag{2.4}$$

The ions produced in the ion source will have energy kinetic energy given by the accelerating voltage ($mv^2/2 = zV$) which can be rearranged to mv^2 =

2zV. When the equation above is put into this a relationship between mass and charge and magnetic field strength is obtained:

$$\frac{m}{z} = \frac{B^2 r^2}{2V} \qquad (2.5)$$

The ions are transmitted through a curvature of radius *r* if the mass to charge ratio (*m/z*) of the ion cluster is in keeping with the expression above. Those ions which do not have the required *m/z* ratio impact the walls of the magnet are not transmitted. It is possible to manually select ions of known *m/z* by adjusting the value of *B*. Upon leaving the magnetic sector the selected cluster ions enter the second field free region (2^{nd} *ffr*) situated before the electric sector. It is in this region where coulomb fission of selected multiply charged cluster ions occurs, as well as other unimolecular processes.

2.7 Electric Sector

The second half of the double focusing functionality of the ZAB is the electric sector which is comprised of an electrostatic analyser (ESA). The role of the ESA is to separate the charged fragments formed in the *2nd ffr* by their kinetic energies in the laboratory frame. For ions to travel the length of the electric sector they must follow a trajectory along the curvature of the electric plates which has radius r. The electrostatic force (zE) felt by the ions is balanced by the centrifugal force acting outwards of the radius of the circle:

$$\frac{mv^2}{r} = zE \tag{2.6}$$

Where z is the charge on the ion and E is the voltage on the electric sector plates. The kinetic energy of the ions is given by the accelerating potential (V) of the source is given by:

$$\frac{1}{2}mv^2 = zV \tag{2.7}$$

Substituting for mv^2 into Equation 2.6 and rearranging to give an expression for the value of curvature of radius r is derived:

$$\frac{2zV}{r} = zE \tag{2.8}$$

$$\frac{2V}{E} = r \tag{2.9}$$

The implication of this is that all ions accelerated by the same voltage at the source will be transmitted at field strength, E, irrespective of their mass or charge. So in effect the ESA is kinetic energy analyser and not a mass analyser. If the accelerating voltage is decoupled from electric field (by scanning E and holding V constant) one can search for fragments of the mass selected precursor ions. This technique is known as mass analyser ion kinetic energy (MIKE) scanning and is described fully in Section 2.9.

2.8 Detection

The detection system used in this work is a Daly scintillation detector combined with a photomultiplier tube allowing detection of weak signals. Ions leaving the ESA are attracted to a dynode off-axis to the ion beam which is held at a potential of -15 kV. The collision of the ions with the dynode results in an electron cascade. Following which, the electrons are repelled by a negative voltage towards a phosphor screen. Collisions with the phosphor screen release photons which are passed into a sealed photomultiplier tube (Thorn EMI 9324B) which acts to amplify the electron count creating a current pulse at the end dynode. This signal is delivered into a preamplifier and then into a Stanford Instruments SR850 lock-in amplifier that is able to distinguish between pulses originating from the nozzle and background signal.

2.9 MIKE Scanning

It is possible with the experimental set up previously discussed to decouple the accelerating voltage from the electric sector and scan the voltage on the plates. This technique is called mass-analysed ion kinetic energy (MIKE) spectrometry and enables fragments of the mass-selected precursor ion formed in the *2nd ffr* to be detected. When a precursor fragments into daughter ions, their kinetic energy is partitioned as a ratio of their masses (laboratory-frame velocity will be the same). As the initial kinetic energy is given by the accelerating voltage (E_0) at the ion source the kinetic energy of the fragment (E_f) will be a multiple of that dependent on the ratio of masses. The full expression is given by equation 2.10.

$$E_f = \frac{M_f Z_p}{M_p Z_f} E_0 \tag{2.10}$$

Where M_f and M_p is the mass of the fragment and precursor ions respectively and Z_f and Z_p are the charges on the fragment and precursor ions respectively. In the experimental data presented, only the heavier of the two fragments from coulomb fission is detected. This is due to less experimental discrimination experienced by the heavier ion. MIKE scanning is an effective technique for observing fragmentation as the magnetic sector allows the mass selection of a particular precursor ion, and the subsequent separation of fragment ions by their kinetic energies allows different reaction pathways to be seen in the same scan. Interference from additional processes from other precursors is minimised due to the mass filtering of the magnetic sector. The ESA can transmit at voltages between 0 – 10kV which can be adjusted to allow for additional resolution in the MIKE spectrum or to accommodate additional features at energies not accessible with a particular initial energy. A MIKE spectrum shows the variance of the ion count at the detector as the magnitude of the electronic signal relayed from the detection system.

What has been observed in MIKE spectra of coulomb fission of dication molecular clusters is the appearance of 'dish shaped' peaks [12-14]. The dishing of the peaks is characteristic of charge separation has occurred with a large release of kinetic energy in three dimensions [15]. Figure 2.7 shows a schematic of the precursor ion in the *2nd ffr*, prior to coulomb fission, travelling along the x-axis. Highlighted are the three dimensions that the fragment can follow post-coulomb fission in relation to the walls of the flight tube.

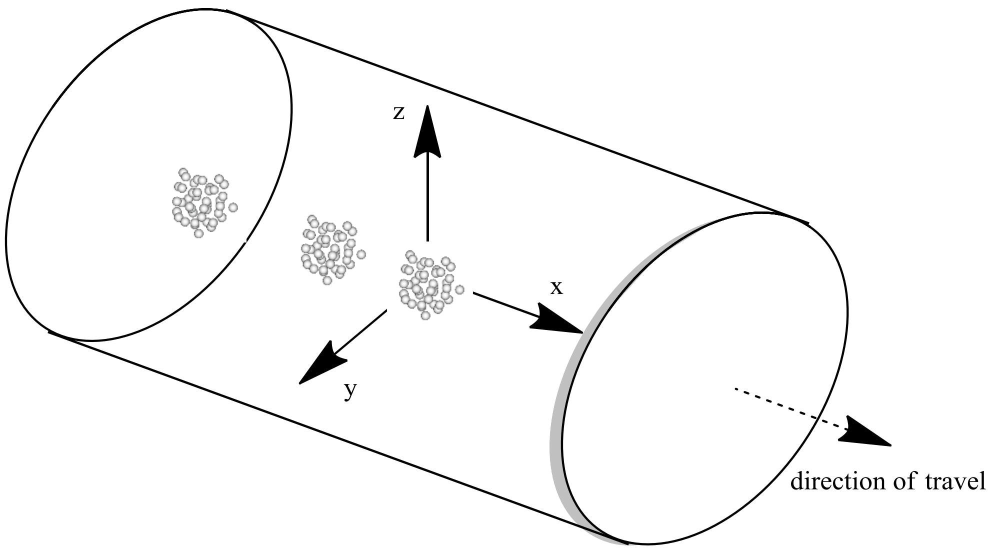

Figure 2.7: Schematic of the 2nd *ffr* showing the direction of fragmentation with respect to the initial velocity of the precursor ion

Clearly the fragment can leave the precursor at any trajectory. The trajectory exactly co-axial to the x-axis will gain the greatest amount of kinetic energy in the laboratory frame, and the trajectory 180^{o} in the opposite direction will lose the greatest amount. In a disk shaped MIKE peak this will correspond to the two extremes in the energy spread of the peak. Those ions with trajectories with large velocity components in the y or z plane will represent the diminished intensity seen in the middle of the peak as some of these ions will collide with the walls of the flight tube before reaching the slits at the end and so will be lost to detection. 'Dishing' of MIKE peaks is typically seen following processes with a large *KER*. The mass of the detected fragment is also crucial as it determines the magnitude of the change in velocity brought about by the *KER* post coulomb fission. Example of dishing are seen in the coulomb fission of dication molecular clusters (see Figure 3.3 for a good example of these features)

The detection of fragments observed in a MIKE spectrum is subject to timeframe constraints. Only fragments formed in the 2^{nd} *ffr* will be detected, this corresponds to a time interval of 38-60 μs under a 5 kV accelerating potential. Fragmentation pathways with lifetimes outside of this window will be followed either before or after the precursor ions are in the 2^{nd} *ffr* and will not be detected. Lifetimes of the detected pathways can be compared from the heights of the fragment peaks. In general, the closer the fragmentation is to the middle of the flight tube of the 2^{nd} *ffr,* the stronger the peak will appear in the resultant MIKE spectrum, as it agrees more closely with the experimental constraints. A recent publication showed how the trend in intensity of fragment peaks from fission of the $(NH_3)_{52}^{2+}$ precursor can be reproduced using a simple kinetic model [14]. The lifetimes for a range of energies corresponding to the barrier to fission ($E_{barrier}$) were compared to the time interval for the 2^{nd} *ffr*. The resultant trend in intensity implies that when the lifetime is too short the majority of ions undergo fission before the 2^{nd} *ffr*. The sharp rise to a peak in intensity corresponds to ions with a lifetime towards the middle of the time interval, and the long tailing off in intensity corresponds to the ions undergoing fission along the long path length of the 2^{nd} *ffr*.

2.10 Dielectric particle model

The simplest treatment of interacting charges considers two totally polarising spheres or point charges. The electrostatic energy between two charges Q_1, Q_2 at distance d can be derived from coulombs law. Including a correction to account for the dielectric nature of the spheres by including the relative dielectric constant (ε_r) of the bulk substance in the denominator term will give equation 2.11.

$$U^0 = \frac{1}{4\pi\varepsilon_0} \frac{Q_1 Q_2}{(\varepsilon_r)d} \tag{2.11}$$

Solving equation 1 for any of the dication clusters that have previously been studied, assuming the charges will be as far apart as possible in the cluster, to take account of the observation of a minimum size, the value of U^0 will be much smaller than that observed experimentally [12]. To account for the measured energy, the charges would have to be located on neighbouring molecules. The dielectric particle model [16] provides a solution to the problem by treating the charged fragments as dielectric spheres. The total charge is a combination of free and bound charge: ($\sigma_t = \sigma_f + \sigma_b$), which is dynamic and located on the surface of the sphere. The free charge is taken to be fixed and uniform across the surface of the particle and is not influenced by the dielectric nature of the particle or any external electric field. The bound charge is also initially distributed evenly on the surface of the particle, however, under the influence of an electric field it will become polarised. In the case of a small particle in close proximity to a larger one, the degree of attenuation of the electrostatic potential is great enough to produce attraction between the particles at short distances [17]. Equation 2.12 [18] gives the magnitude of the electrostatic interaction energy of a dielectric sphere of charge Q_1, radius a_2 and dielectric constant k_2 at a distance h from the surface to a point charge Q_2. The redistribution of the bound charge is represented by the multipole terms in equation 2.12 Taking m = 1-3, the three leading terms become $1/_{h^4}$, $1/_{h^6}$ and $1/_{h^8}$ which represent ion induced -dipole, -quadrupole and -octupole terms of a multipole expansion.

$$U^1 = \frac{Q_1 Q_2}{4\pi\varepsilon_0 h} - k_1 {Q_1}^2 \sum_{m=1}^{\infty} \frac{(k_2 - 1)m}{[(k_2+1)m+1]} \frac{a_2^{2m+1}}{h^{2m+1}} \quad (2.12)$$

It is the balance between the first and second terms of the expression that determine the magnitude of the total interaction. The interactions of dielectric spheres with an external point charge within the dielectric particle model are summarized in Eq. 2.12. Agreement between calculated interaction energies using equation 2.12 and experimental *KER* support this treatment of dynamic surface charge [12].

2.11 Peak simulation model

A new methodology has been developed to improve the measurement of *KER* following coulomb fission. Previous measurements use the full width at half maximum (FWHM) of the peak assuming a Gaussian shaped curve to calculate a single energy release for the process. This method has several issues associated with it. Firstly, it relies quite heavily on the quality of the experimental data as the measured *KER* value is very sensitive to the width of the peak. This can be obscured by poor signal-to-noise levels, which towards the upper end of the size and charge range in the experimental data becomes a significant issue. Additional broadening may originate from artefact peaks as a result of the fragmentation of precursor ions that are formed in the 1st *ffr*. Elucidating the magnitude of the components of the width originating from the artefact and precursor is problematic. Secondly, this methodology assumes that all ions that fragment to make up the peak release the same amount of kinetic energy upon fragmentation. This is slightly erroneous as there will certainly be a range of energy releases in three dimensions, with the peak made up of these individual energy releases.

A method by Beynon and colleagues seeks to address this [19,20] by computing a distribution of *KER*s from a simulated peak and subsequently finding an average *KER*. The calculations take account of the fact that from the centre of mass frame, fragmentation is equally probable in every direction, which assuming an equal distribution of charge on the surface of multiply charged clusters in these experiments, is a valid assumption. A distribution $n(T)$ of kinetic energies is calculated and is used to construct the peak. Additionally, restrictions in the z-axis due to the height of the intermediate slit can be incorporated. In the case of a small kinetic energy release and if the length of the intermediate slit is large in the z-axis a single kinetic energy release will be very close in shape to a rectangle and a multiple releases of equal probability will take the form of multiple rectangles of equal areas.

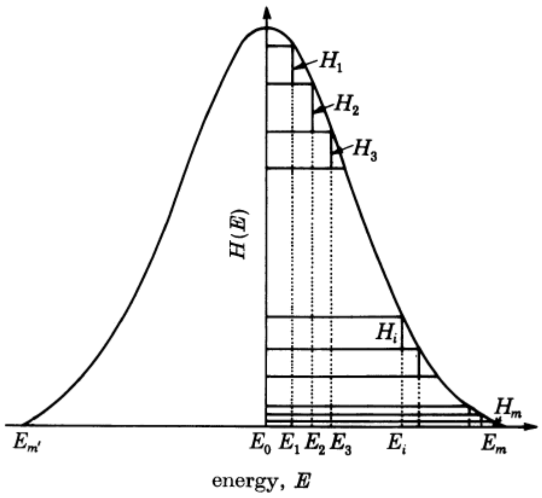

Figure 2.8: A visualisation of the construction of the metastable peak from single energy releases [20].

Figure 2.8 shows the division of a MIKE peak into a finite number of rectangles. The average translational energy is labelled as E_0 on the x-axis and the maximum translational energies are labelled as E_m and $E_m{}'$. E_0 corresponds to the predicted laboratory-frame kinetic energy of the detected fragment, E_f Equation 2.10. From the maximum spread $(E_m - E_0)$ one can calculate the maximum *KER* (denoted as T_m) [15].

$$T_m = \frac{m_2 eV}{16 m_3}\left(\frac{2(E_m - E_0)}{E_0}\right)^2 \qquad (2.13)$$

Where m_2 and m_3 are the masses of the two fragments, e is the elementary charge constant and V is the accelerating potential. From the value of T_m the peak is subdivided into m number of rectangles. The rectangles correspond to *KER*s (T_i) given by eq. 2.14:

$$T_i = \frac{iT_m}{m} \; (i = 1,2 \ldots m) \qquad (2.14)$$

It is found that a value of m ≈ 25 is sufficient to accurately produce a distribution to simulate most experimental peaks [20]. The high energy value of the translational energy for each rectangle E_i is determined and the corresponding value of the height H_i is determined using the equation for the area of a rectangle. If we consider that the height of each rectangle contributing to the peak is $h_i n(T_i)$, then the distribution of *KER*s can be determined by considering the height of ordinate H_i which can be expressed as a function of the height of the rectangle $h_i n(T_i)$ added to the height of the ordinate 'underneath' it, H_{i+1}.

$$H_i = h_i n(T_i) + H_{i+1} \tag{2.15}$$

From eq. 2.15 the final distribution function $n(T)$ is determined and the average kinetic energy release <*KER*> is calculated.

$$< KER > = \frac{\sum T_i n_i}{\sum n} \tag{2.16}$$

The model can incorporate parameters which account for large z discrimination, which leads to discrimination against some of the ions that would contribute to the central region of the peak, resulting in dishing of the peak. The degree of dishing will depend on the position of fragmentation, the length of the intermediate slit in the z direction and the magnitude of *KER*.

This methodology is used to construct simulated peaks that fit the experimental peaks in the MIKE spectra presented in this work and thus giving the magnitude of <*KER*> for the fission pathway. In most cases the simulated peaks are regarded as 'fitted' if the width and shape match the experimental peak well. It is also used to determine which fission mechanisms are being followed as the simulated widths for different mechanisms typically show large differences, due to significant changes in the parameters of mass and *KER* in the calculation. However, this methodology cannot account for the heights of the peaks for the experimental pathways. All fragmentations are assumed to occur at the same position in the flight tube and therefore the lifetime factors in determining the peak intensity for the pathways are not accounted for. The simulated features are therefore manually modified to match the heights of the experimental profile. No attempt has been made to correct for additive effects from close lying simulated peaks to the total profile as this will not contribute to the simulated width.

References

[1] H. Pauli, Atomic and Molecular Beam Methods, *Oxford University Press*, 1998.
[2] R. Campargue, *Journal of Physical Chemistry* **88** (1984) 4466.
[3] E.L. Knuth, *Journal of Chemical Physics* **66** (1977) 3515.
[4] T.D.E. Mark, O., I*nternal Reactions and Metastable Dissociations After ionisation of van der Waals Clusters*, Springer - Verlag, 1994.
[5] R.A.W.J. M.E. Rose, *Mass Spectrometry for Chemists and Biochemists*, Cambridge University Press, 1982.
[6] C.Y. Ng, *Adv. Chem. Phys*. **L2** (1983).
[7] O.F. Hagena, *Molecular Beams and Low Density Gasdynamics*, Marcel Dekker, Inc., New York, 1974.
[8] P.G. Lethbridge, (1989).
[9] H. Haberland, *Surface Science* **156** (1985) 305.
[10] J.G. Gay, B.J. Berne, *Physical Review Letters* **49** (1982) 194.
[11] P. Scheier, T.D. Mark, *Chemical Physics Letters* **136** (1987) 423.
[12] X. Chen, E. Bichoutskaia, A.J. Stace, T*he journal of physical chemistry. A* **117** (2013) 3877.
[13] X. Chen, University of Nottingham, 2011.
[14] G.H. Wu, X.J. Chen, A.J. Stace, P. Linse, *Journal of Chemical Physics* **134** (2011) 4.
[15] J.H.B. R.G. Cooks, R.M. Capropli, G.R Lester, *Metastable ion*s, 1973.
[16] E. Bichoutskaia, A.L. Boatwright, A. Khachatourian, A.J. Stace, *Journal of Chemical Physics* **133** (2010).
[17] A.J. Stace, A.L. Boatwright, A. Khachatourian, E. Bichoutskaia, *Journal of Colloid and Interface Science* **354** (2011) 417.
[18] A.J. Stace, E. Bichoutskaia, *Physical Chemistry Chemical Physics* 13 (2011) 18339.
[19] J.E. Szulejko, A.M. Amaya, R.P. Morgan, A.G. Brenton, J.H. Beynon, Proceedings of the Royal Society of London Series a-Mathematical Physical and Engineering Sciences **373** (1980) 1.
[20] A. Mendezamaya, A.G. Brenton, J.E. Szulejko, J.H. Beynon, Proceedings of the Royal Society of London Series a-Mathematical Physical and Engineering Sciences **373** (1980) 13.

Chapter 3 : Multiply Charged Benzene Clusters

3.1 Introduction

Benzene, first observed as a by-product of working with oil and coal, is a common and important molecule in the study of chemistry. It has intrigued scientists due to its uncommon molecular structure, eventually realised to be a ring of carbon and hydrogen atoms with a delocalised ring of electrons above and below the plane of atoms. The understanding of the delocalised pi-system changed perspectives on the nature of chemical bonding [1-6]. In the field of physical chemistry, benzene is a common solvent used as a ligand in gas phase metal-ligand systems. This is due to its ability to donate some of the electron density in the ring to the electronically unsaturated metal ion centre. It also has a suitable vapour pressure in the liquid state, under mild cooling, to be used effectively in the cluster formation step in pick-up type experiments [7, 8] .

Work by Gotts *et al*. [9] focused on the collision induced dissociation (CID) of multiply charged benzene clusters. It was found that by activating the clusters via collisions with a background gas, charged fragments originating from coulomb fission were detected for doubly and triply charged clusters. However, due to the large exchange of energy upon collisions many monomer units will leave the mass-selected charged cluster before fission. This can cause complications in identifying the precursor cluster ion that undergoes fission and hence assignments of the energetics involved.

More recently, data showing the unimolecular Coulomb fission in doubly charged benzene clusters has been presented [10]. The resolved peaks in the MIKE spectra were shown to be from coulomb fission. By analysing the potential energy between the fragments for the observed fragmentation pathways using a dielectric discontinuity model [11, 12], also with the more sophisticated dielectric particle model described in section 2.3 [10], the calculated electrostatic barrier was shown to be in close agreement with the experimentally determined kinetic energy release (*KER*).

The work presented in this chapter seeks to build on these results by applying the peak simulation model to the older data, showing how by using this methodology more accurate <*KERs*> are obtained from the fitted peaks which are more closely matched to the barrier heights predicted by the dielectric particle model (U_{max}) for the pathways seen experimentally. Additionally, presented is the identification and coulomb fission of triply and fourfold charged benzene clusters. By using the described experimental techniques and analysis, the identification of the fragments and the magnitude of the energy release following coulomb fission are accurately determined.

3.2 Doubly Charged Benzene Clusters

The detection of the critical size of doubly charged benzene clusters ($n_{crit}(2)$) can be accomplished using mass spectrometry. Figure 3.1 shows the onset of these species above $(C_6H_6)_{17}^{2+}$. Below this size there are peaks coincident to the doubly charged species, these are possibly due to internal fragmentation of molecules in the singularly charged cluster post ionisation. The observed critical size of $n_{crit}(2)$ =17 is smaller than previous assignments of 23 [13] and 22 [12]. This is possibly due to the increased number density of the small dication clusters brought about by modification to the experimental apparatus from ref [12]. As noted in Chapter 2 the removal of the pick-up cell between the cluster chamber and the ion source will reduce the distance of cluster formation to the point of ionisation and hence decrease the divergence of the molecular beam, allowing more neutral clusters into the ion source. This increase in neutral clusters entering the source is reflected linearly in the final ion count at detection. Additionally, it should be noted that the experiments in ref [12] were performed with an accelerating potential of 5 kV, where as these experiments were carried out at 7 kV. As mentioned in Chapter 2, this has two advantages over the former: Improvement in the dynode conversion efficiency and improvement of the resolution of the MIKE peaks. Particularly relevant to this new observation, using a higher accelerating voltage will increase the velocity of the ions and reduces the time frame of the experiment. In the case of ions very close to the critical size the barrier to fission will be close to zero and therefore the time constant for fission will be comparatively very small. By reducing the timeframe of the experiment it is possible that the smaller ions that previously were decaying before reaching the detector will now reach the 2nd *ffr* before fragmenting, and can now be detected. To verify that clusters as small as n=17 are being produced, presented in Figure 3.2 is the MIKE spectrum following coulomb fission of $(C_6H_6)_{17}^{2+}$.

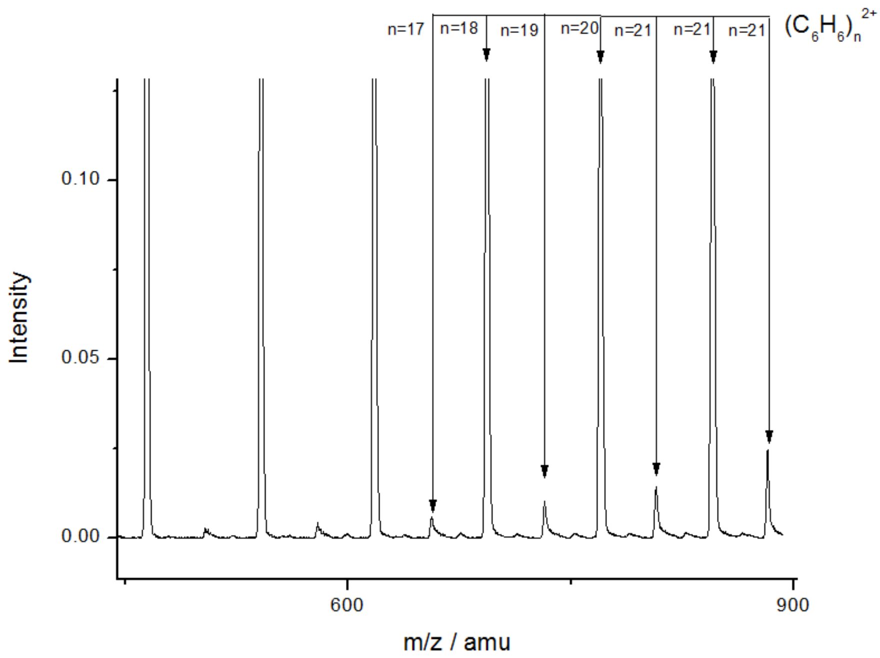

Figure 3.1: A mass spectrum showing the onset of doubly charged benzene clusters above n=17

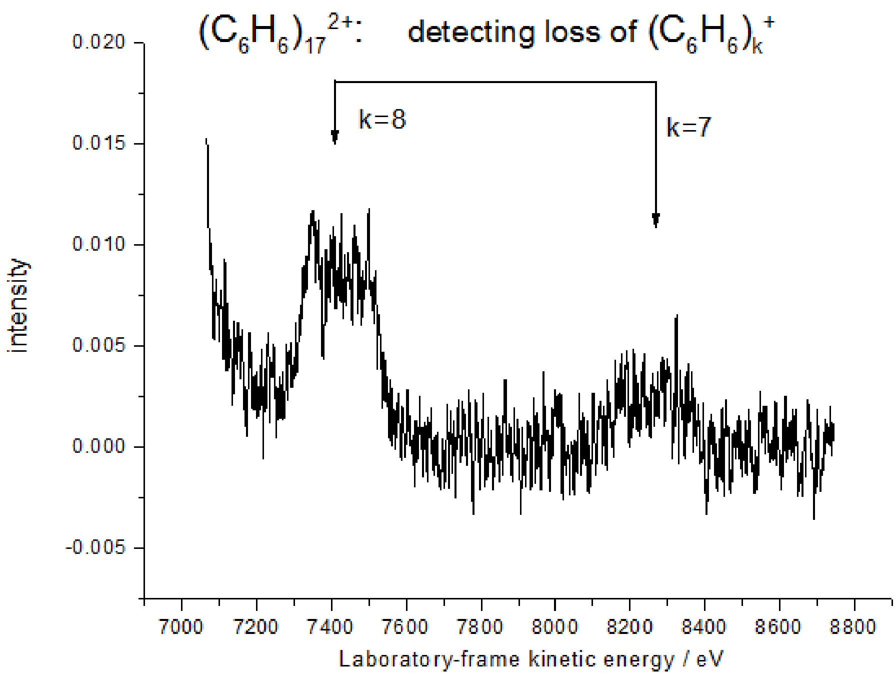

Figure 3.2: MIKE spectrum of $(C_6H_6)_{17}^{2+}$

It has been shown that the dielectric particle model predicts the KER following coulomb fission of doubly charged benzene clusters accurately [10]. Therefore, in this methodology that value is used as a guide to the range of *KERs* that will go into simulating the peak using the peak simulation model. It is found that in conjunction with the barrier height, using the same basic input parameters representing instrumental settings, i.e. slit height, precursor width, one can reproduce the experimental data accurately. The average kinetic energy release (<*KER*>) which is made up of the allowed *KERs* that form the peak give a more accurate description of the energy of the ejected fragments and agrees more closely with the values of U_{max}.

Figure 3.3 (a,b) show the coulomb fission of $(C_6H_6)_{23}^{2+}$ and $(C_6H_6)_{24}^{2+}$ precursors. Overlain over the MIKE spectra are the simulated peaks for each pathway from the peak simulation model. As in every case of MIKE spectra presented in this work, only the larger of the two ions is detected due to less experimental discrimination experienced on that ion. Most features of the experimental data are reproduced accurately, the width and the degree of 'dishing' to the simulated peaks shows strong agreement to the experimental MIKE peaks. The peaks are therefore considered 'fitted' and the values for the <*KERs*> for the pathways are used in subsequent analysis. The only exceptions to this are the peaks for the k=11 channels in both clusters where the experimental peak is narrower and resembles a full Gaussian-like peak. This observation is evidence for neutral evaporation following an initial coulomb fission reaction to produce the final cluster. Since the *KER* following neutral evaporation is significantly smaller than the approximate 0.85 eV observed following coulomb fission the fragments will undergo less divergence from the main ion beam, so experience little to no discrimination in the z-axis from the focussing slit. This results in a full, Gaussian-like profile. There is a peak in the intensity of the fragment peaks corresponding to loss of approximately 35% mass for both spectra. The intensity trends are due to the different lifetimes of fragment channels with respect to coulomb fission and how closely this value is to the average time spent in the 2nd *ffr* of the mass spectrometer as shown in a recent publication [14].

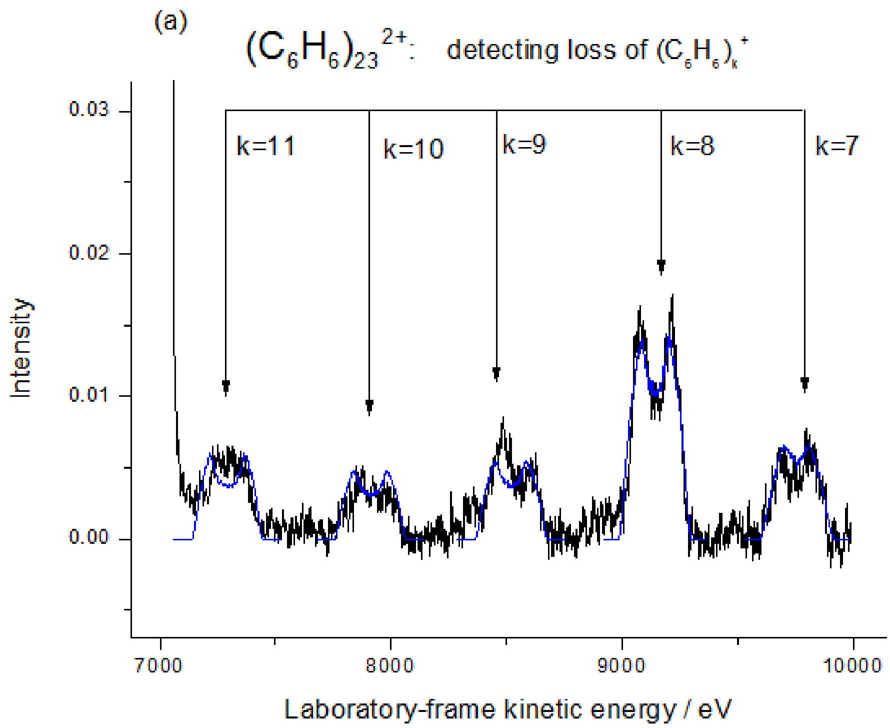

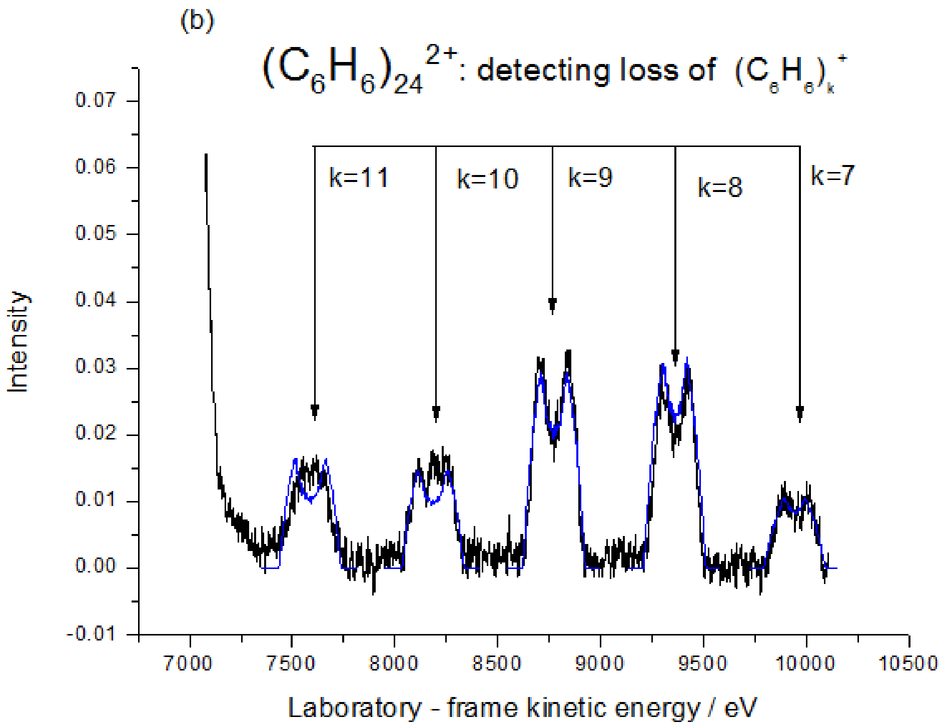

Figure 3.3: MIKE scans showing coulomb fission from mass-selected (a) $(C_6H_6)_{23}^{2+}$, (b) $(C_6H_6)_{24}^{2+}$ clusters. Overlain in blue are the simulated peaks.

Precursor	Fragment	*KER* from FWHH/ eV	U_{max} / eV	<*KER*> / eV
$(C_6H_6)_{23}^{2+}$	K=10	0.73	0.93	0.86
	K=9	1.10	0.93	0.86
	K=8	0.95	0.93	0.86
	K=7	0.94	0.94	0.84

Precursor	Fragment	*KER* from FWHH / eV	U_{max} / eV	<*KER*>/eV
$(C_6H_6)_{24}^{2+}$	K=11	0.42	0.91	0.86
	K=10	0.92	0.91	0.86
	K=9	0.98	0.92	0.86
	K=8	0.91	0.92	0.86
	K=7	-	0.92	0.86

Table 3.1: A table comparing the predicted barrier heights U_{max} with the <*KER*> from the simulated peaks of $(C_6H_6)_{23}^{2+}$ and $(C_6H_6)_{24}^{2+}$. Also shown are values of *KER* calculated using the width of the peak [12].

Table 3.1 shows the predicted barrier heights (U_{max}) against the <KER> from the simulated peak for each fragmentation pathway. Also shown are values of KER that have been calculated from the older method of using the FWHH of the experimental peak [12]. The values of U_{max} and <KER> are closely matched for each channel with the values of U_{max} fall consistently below the values of <KER> in energy. This is likely due to the partitioning of energy into internal modes of the fragment as the fragments separate, hence, the energy is 'lost' [10, 14] which may correspond to partition of energy into the compression modes proposed by Gay and Berne [15] .

3.3 Triply Charged Benzene Clusters

Presented are the first observations showing direct, unimolecular coulomb fission of triply charged benzene clusters. Triply charged benzene clusters were produced and detected as described in Chapter 2. Figure 3.4 shows the onset of triply charged cluster ions in a mass spectrum. The 3+ peaks can coincide with a singularly charged ion possessing 1/3 of the mass, and hence the large cluster peak will contain a component of a triply charged cluster, provided it is above $n_{crit}(3)$. The peak corresponding to of $n_{crit}(3)$ is completely obscured by the presence of background peaks in the mass spectrum, and is not seen in Figure 3.4. To reach a definitive value it is necessary to perform MIKE scans on the cluster peak of interest to determine if the feature is a 3+ peak or a background feature. Following this analysis, a value of $n_{crit}(3)$ = 43 is assigned. This value is well below previously reported values of 52 [13]. The discrepancy is possibly due to the likely presence of background peaks in previous mass spectral studies into benzene clusters obscuring the measurements. It is only by performing MIKE scans on the features that fragments from triply charged benzene clusters are found.

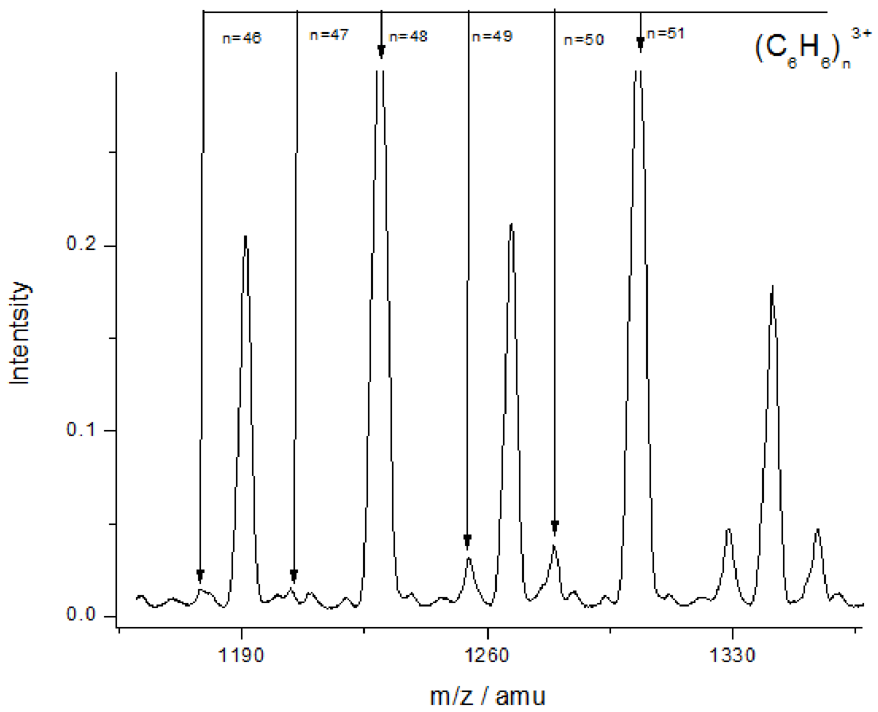

Figure 3.4: A mass spectrum showing the onset on triply charged benzene cluster peaks. Please note, the peak corresponding to the critical size is not shown, see above text for details

Figure 3.5 shows MIKE spectra of the coulomb fission of triply charged $(C_6H_6)_{47}^{3+}$, $(C_6H_6)_{48}^{3+}$ and $(C_6H_6)_{49}^{3+}$ cluster ions into two charged fragments. The heavier of the two contains roughly 85% of the initial mass and two of the three charges, the remaining mass and charge is accommodated in the smaller of the two fragments. As before, only the larger of the two fragments is detected. The fragment peaks resemble a full profile opposed to the examples presented in Section 3.2, this is due to the mass of the fragments being significantly larger and hence undergoing less divergence from the main ion and therefore experiencing less discrimination by the apparatus. The simulation model predicts an onset of dishing to the peaks as the fragment reduces in size, see k=7, 8 in figure 3.5(a). This is less apparent in the experimental data, possibly because the degree of loss of signal predicted from the centre of the peak is slight, and is smaller than the noise level in the spectrum. The exception is figure 3.5b where there is a detectable degree of dish shape in the k=9, 10 fragment peaks.

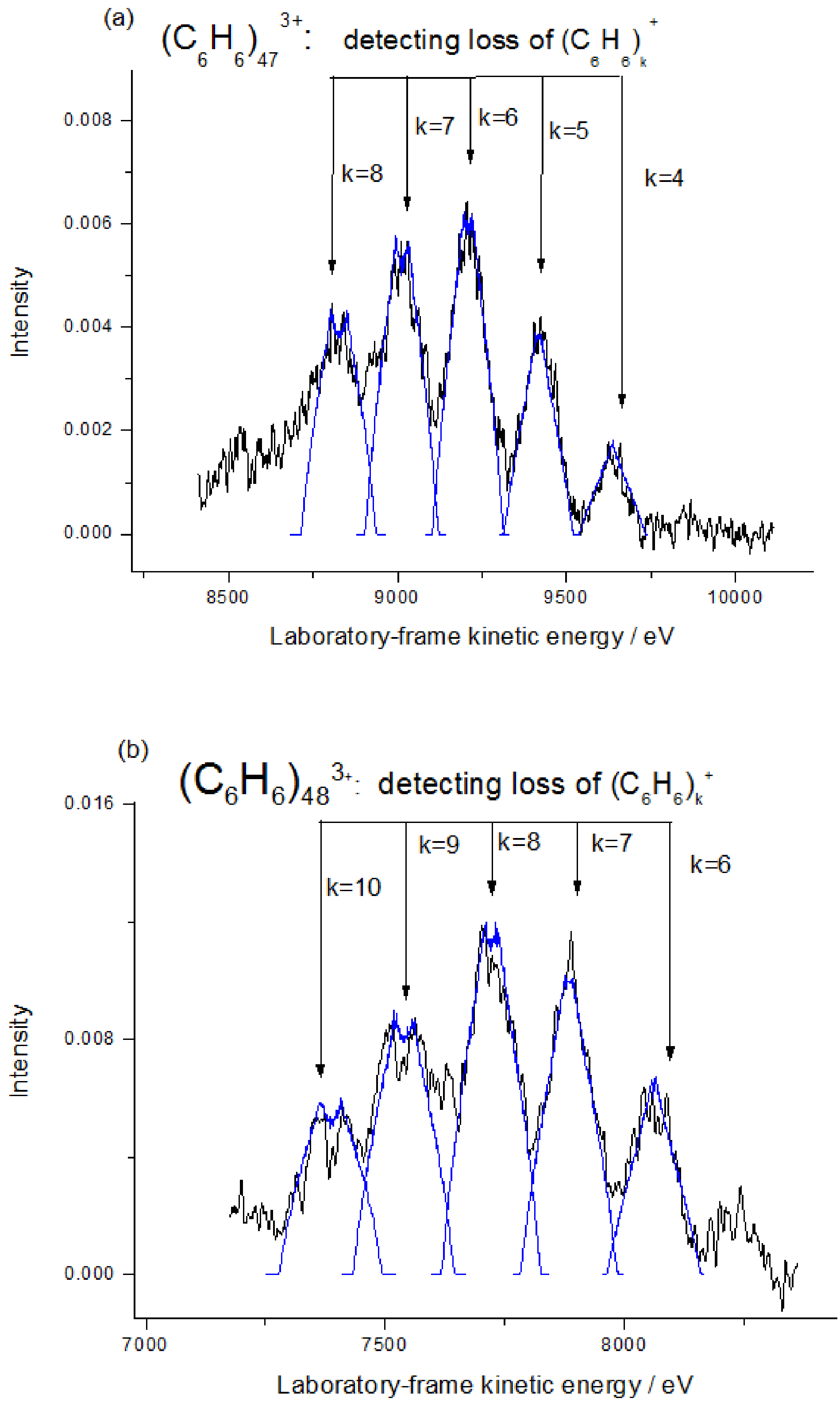

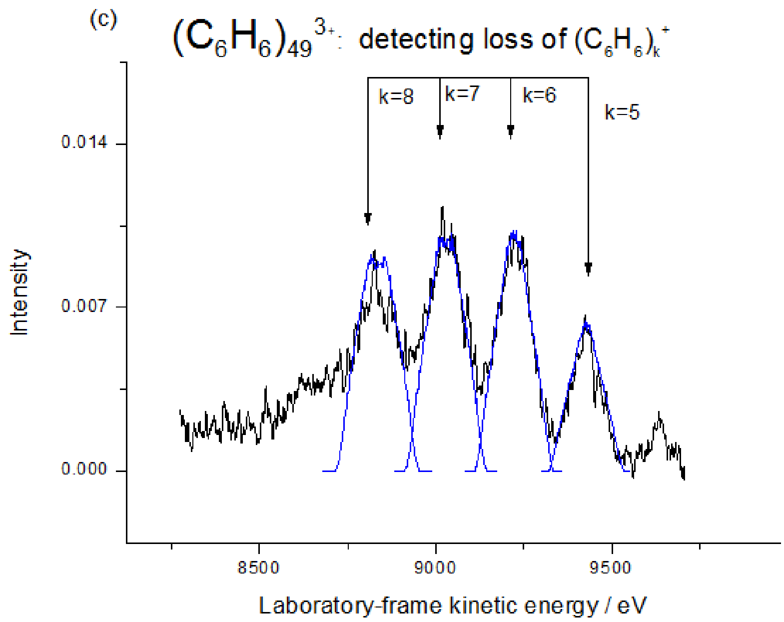

Figure 3.5: MIKE spectra showing coulomb fission of (a) $(C_6H_6)_{47}^{3+}$, (b) $(C_6H_6)_{48}^{3+}$ and (c) $(C_6H_6)_{49}^{3+}$. Overlain in blue are simulated peaks for the processes detected.

Precursor	Fragment	U_{max} / eV	*<KER>* / eV
$(C_6H_6)_{47}^{3+}$	K=4	1.62	1.57
	K=5	1.60	1.57
	K=6	1.58	1.56
	K=7	1.56	1.56
	K=8	1.55	1.56

Precursor	Fragment	U_{max} / eV	<KER> / eV
$(C_6H_6)_{48}^{3+}$	K=5	1.59	1.56
	K=6	1.57	1.56
	K=7	1.56	1.56
	K=8	1.54	1.56
	k=9	1.53	1.56

Precursor	Fragment	U_{max} / eV	*<KER>* / eV
$(C_6H_6)_{49}^{3+}$	K=5	1.58	1.57
	K=6	1.56	1.57
	K=7	1.55	1.55
	K=8	1.53	1.53

Table 3.2: Calculated values of the barrier heights from the dielectric particle model and *<KER>* from the fitted simulated peaks in figure 3.4.

Figure 3.6 show the electrostatic potential energy curve calculated by the dielectric particle model following the coulomb fission of the $(C_6H_6)_{48}^{3+}$ precursor. The six channels k=5–10 are plotted from centre–centre separation = 0 to around 0.5 nm. As can be seen, the interaction is repulsive over all channels. This is due to the relatively low value of the dielectric constant of benzene (ε_r=2.3). The consequent lack of polarisability in the charged cluster fragments means that even in the case of large mass asymmetry (88%), electrostatic repulsive interactions dominate over induced polarisation interactions. Conversely, because of the increased charge density in the smaller fragment for the more asymmetric fragmentation pathways, repulsive forces become more effective, and hence, the maximum in electrostatic potential energy is seen to be raised relative to more symmetric fragmentation

.

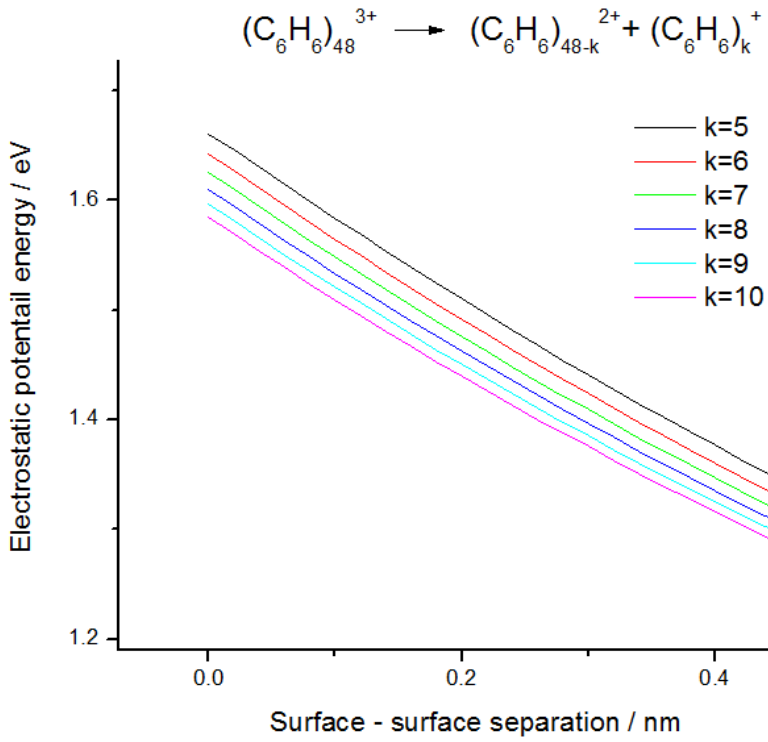

Figure 3.6: A plot of the electrostatic potential energy as function of surface – surface separation. Shown are the curves calculated following coulomb fission for the fragmentation channels seen for the $(C_6H_6)_{48}^{3+}$ precursor cluster (Figure3.5(b))

3.4 Fourfold Charged Benzene Clusters

Results are presented showing the coulomb fission of fourfold charged benzene clusters. Due to the weak signals in the mass spectrum from these large ions no success was found in the identification an accurate critical size $n_{crit}(4)$ from mass spectral investigation. However, coulomb fission was detected for two cluster ions giving a rough estimate of the critical size. Analysis performed on these spectra reveal the barrier height and the <KER> values from the fragment peaks agree well. Fourfold charged cluster peaks above the critical size are predicted to appear every $M_r/4$ = 19.5 amu in a mass spectrum. This means they can be coincident with singly charged peaks and doubly charged peaks, both of which possess a peak intensity of a magnitude much greater than a fourfold cluster peak close to $n_{crit}(4)$. Due to this it is found to be preferable to 'sit' on a singly or doubly charged peak corresponding to a fourfold charge cluster of interest to ensure correct mass selection for the ensuing MIKE scan. There will be little interference from processes from these clusters in the MIKE spectrum as the coincident clusters (roughly $(C_6H_6)_{50}^{2+}$ and $(C_6H_6)_{75}^{3+}$) will exceed the stable sizes for these charge states and will not undergo coulomb fission. Due to lack of mass spectral data and acknowledging the above, assignment of an accurate value of $n_{crit}(4)$ is difficult, an approximate value of 96 molecules is assigned as no evidence for fission is found below this number. The magnitude of the stable size is found to be 100 molecules giving a critical range of 4 molecules. This is out of step with observations on other fourfold-charged molecular clusters (see subsequent chapters) which all show a significantly larger critical range. There is no apparent reason why benzene should possess such a narrow range compared to other molecules, so this and the weak signals observed lead to the conclusion that the absolute critical size under our experimental conditions is lower than the stated value by a margin. This is supported by the predicted critical size given by the liquid drop model being the order of 20 molecules smaller (see Section 3.5).

The assignment of fragments from the MIKE spectra becomes more problematic for fourfold-charged clusters due to there being two possibilities for the charges to partition between fragments. For instance, the fragments detected could be triply charged, leaving the smaller cluster with one charge, or, it could be doubly charged leaving the second fragment also doubly charged. Application of Equation 2.10 on its own will give the two potential identities of the larger fragment for the charge states Z_f = 3, 2, but no way of determining which (or both) is being detected. The solution to this is to use the peak simulation model to predict the peak profiles for both. It is expected that the two mechanisms will have visibly differing profile due to the discrepancy in size and charge. A general methodology for this would be:

1) Use equation 2.10 to work out the identity of fragments to be tested for a value of Z_f
2) Calculate the predicted barrier for the fission process *via* the dielectric particle model for the first set of fragments
3) Use this information to simulate the experimental peak and compare with MIKE scan
4) Repeat for second fission mechanism

Following this methodology will reveal the coulomb fission mechanism and give a good account of the shape of the experimental peaks for most instances.

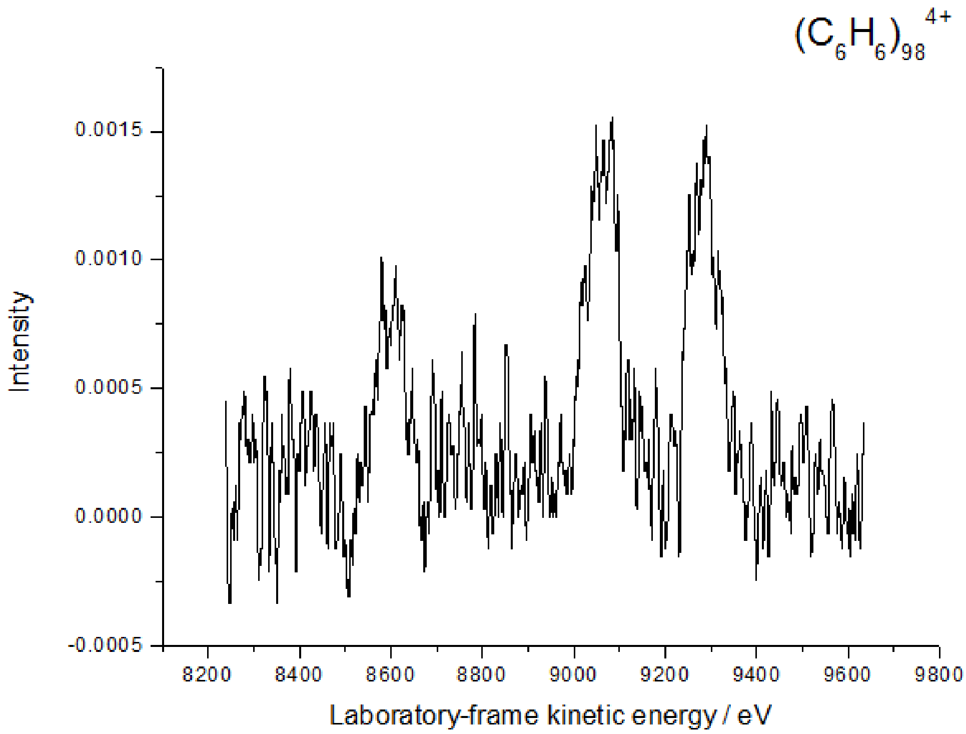

Figure 3.7: MIKE spectrum of the coulomb fission of $(C_6H_6)_{98}^{4+}$

Figure 3.7 shows the MIKE spectrum following coulomb fission of mass selected $(C_6H_6)_{98}^{4+}$ clusters. Following the methodology above, Figure 3.8 gives the simulated peaks for Z_p =3, 2 for the peak at approximately 9300 eV. Table 3.3 gives the outputs from the calculations, the simulated peaks have a <*KER*> close to the predicted barrier height for both fission mechanisms, but it is immediately apparent that the Z_f= 3 pathway is being observed. The peak is roughly the same width and general shape as the experimental MIKE peak. Whereas, the peak simulated for Z_f = 2 shows the effect of large divergence and instrumental discrimination on a lighter fragment (and larger *KER* for fission), and hence is much more wide and dish shaped.

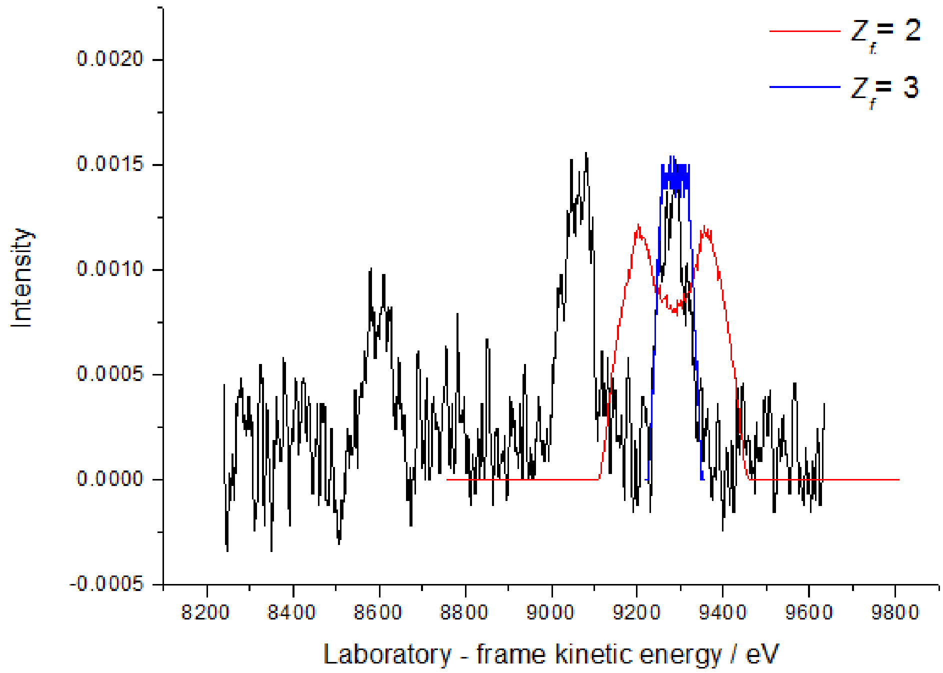

Figure 3.8: Simulated peaks for the two possible pathways for the high energy feature in figure 3.7

Z_f	3+	2+
Molecules in Fragment	97	63
U_{max} / eV	2.11	2.30
<*KER*> / eV	2.00	2.18

Table 3.3: The fragment size and the barrier height U_{max} for the fragment at 9279 eV in figure 3.6 and the values for <*KER*> in the simulated peaks for each Z_f shown in figure 3.7

Figure 3.9 shows the complete assignment of the fitted simulated peaks for the MIKE spectra of $(C_6H_6)_{98}^{4+}$ and $(C_6H_6)_{100}^{4+}$ clusters. It is apparent that each fragment peak is from a triply charged fragment due to the consistent fitting to the simulated data. One curiosity is the break in the trend for a continuous range of fragments to be detected that is seen in lower order charged clusters. In the instance of fourfold charged clusters there is a difference of 2-5 molecules between successive fragment peaks in the MIKE spectra. The difference in the energy of the barriers for fission will not be considerable for two adjacent pathways, so there is no apparent kinetic reason why one fragment should be resolved relative to the other. The observation of pathways may be due to a specific stability of either the detected fragment or the small singularly charged fragment that is ejected.

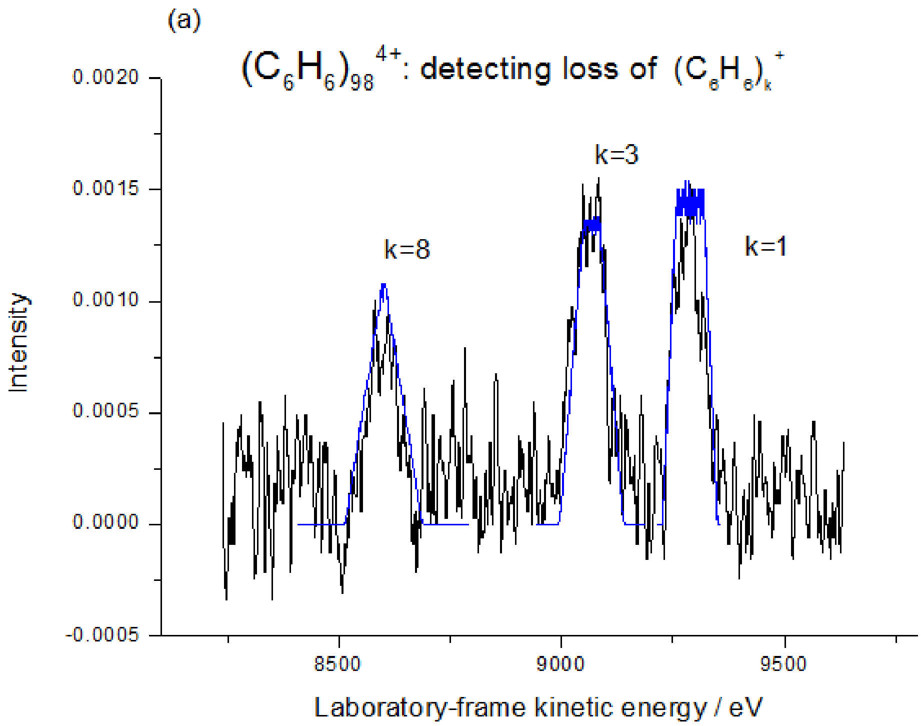

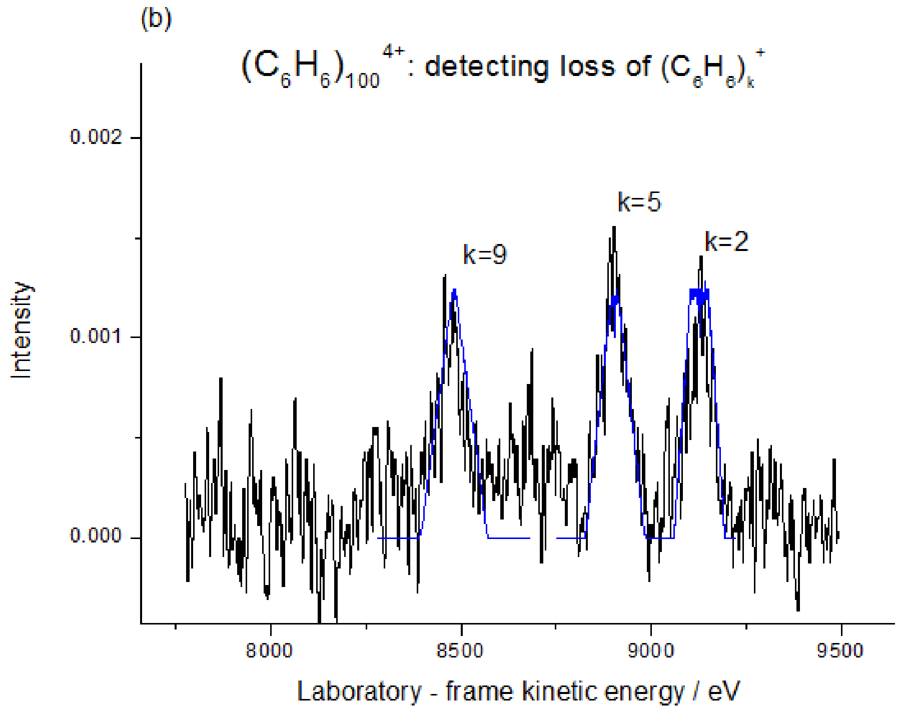

Figure 3.9: MIKE spectra with simulated peaks overlain for the precursor ions: (a) $(C_6H_6)_{98}^{4+}$ (b) $(C_6H_6)_{100}^{4+}$

precursor cluster	Fragment	U_{max} / eV	<KER>
$(C_6H_6)_{98}^{4+}$	k=1$^+$	2.12	2.00
	k=3$^+$	2.01	2.00
	k=8$^+$	1.94	1.98

Precursor cluster	Fragment	U_{max} / eV	<KER>
$(C_6H_6)_{100}^{4+}$	k=2$^+$	2.07	2.00
	k=5$^+$	1.99	1.99
	k=9$^+$	1.91	1.98

Table 3.4: The values for the barrier height and the <KER> from the fitted peaks on figure 3.8

3.5 Stability of Multiply Charged Benzene Clusters

With experimental data for the determination of critical sizes of multiply charged benzene clusters of charge state up to Z_p = 4 it is possible to compare and assess the suitability of the liquid drop (LD) model for predicting the stability of multiply charged benzene clusters. The Rayleigh equation is given as (Equation 1.1):

$$n_{crit}(z) = \frac{(ze)^2}{64\pi^2\gamma\varepsilon_0 {r_m}^3}$$

Where z is the charge state of the cluster, e is the elementary charge constant, γ is the surface tension, ε_0 is the permittivity of free space and r_m is the molecular radius. Previous calculations have been performed [16] using Lennard-Jones potentials to calculate the point at which the calculated barrier to fission becomes equal to 0. This point is taken as the critical size. These values along with the calculated values using Equation 1.1 and the experimental results are plotted on figure 3.10 and tabulated in table 3.5. There is an increasing divergence between the values of the experimental critical size and what is predicted by the LD model as the charge state increases. This could be due to general concerns regarding the LD model. Firstly, surface tension is strongly size dependent, this has been shown for a number of different droplets [17] and in some research, attempts have been made to correct for this [13]. In general, the value of the surface tension decreases exponentially from the bulk value with decreasing radius of the droplet. In the case of small clusters the difference between the size dependent surface tension and the bulk value used in the calculation is greatest. However, reference to figure 3.9 shows a close agreement in the two values for $n_{crit}(2)$ and $n_{crit}(3)$ and a marked disagreement for $n_{crit}(4)$. This would apparently rule out a major contribution from the value of the surface tension to the observed stability.

Another crucial aspect of the LD model is that the symmetry of the cluster is assumed to be spherical and will undergo deformations from that starting configuration. When the initial structure deviates strongly from this symmetry it could impact on the accommodation of charge, and therefore, the stability of the cluster. There is evidence to suggest that benzene dimer ions can exist in multiple configurations. Lee and co-workers [18] performed *ab-initio* calculations that showed as well as pi-pi stacking, 'T-shaped' conformations were also accessible. If these directing forces are present in the cluster system the final structure may not 'add up' to a perfectly spherical structure. If this is the case then as the structure becomes larger, the deviation from a spherical shape will increase.

It is accepted that there is considerable uncertainty in the assignment in the experimental value of $n_{crit}(4)$ for the reasons set out in the text. This is understandable as the signal strengths in the two clearest examples in figure 3.10 are comparatively weak relative to examples of fission in lower ordered charged clusters. This would suggest that clusters with weaker signals approaching the smaller critical size are not being resolved. It might be that large neutral benzene clusters are not being produced at great numbers. It is accepted that a highly excited charged clusters will lose energy after ionisation by the ejection of a number of neutral molecules [19]. To compensate for this, there is a requirement for neutral clusters larger than the multiply charged precursor to from. Insufficient energy supplied by the ionising electrons is another potential factor. The ionisation energy of benzene is 9.24 eV, so following the ionisation mechanism outlined in section 2.5, at least 36.96 eV will need to be supplied for four ionisation events to be accessible. This is well within the limit of the ion source which is has a maximum electron energy of 100 eV.

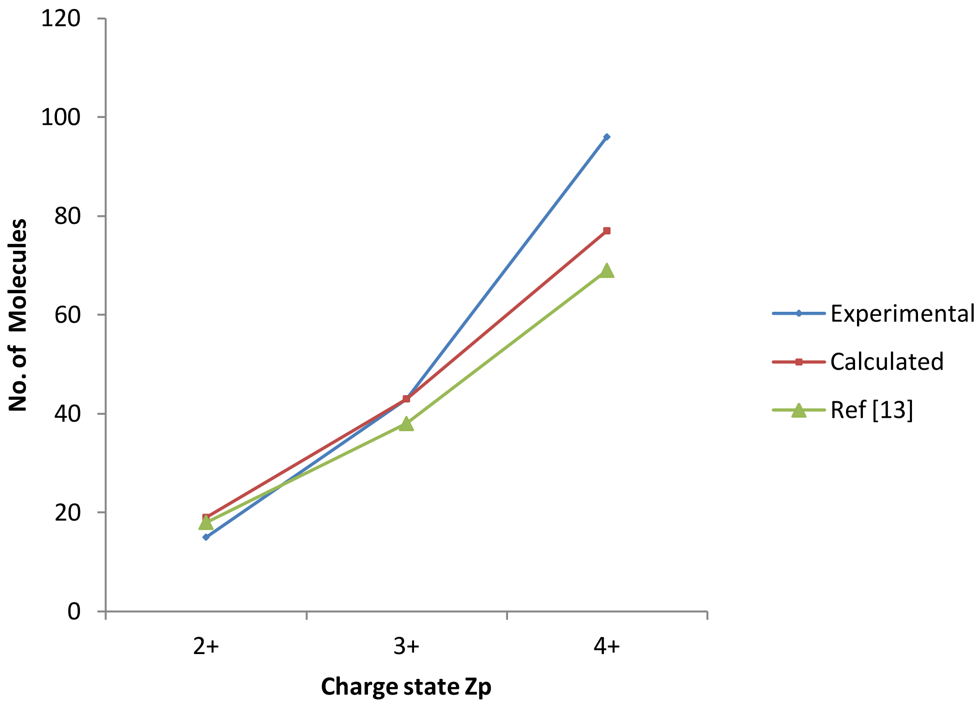

Figure 3.10: Values for critical sizes for benzene charged benzene clusters up to charge state 4+. In blue are the experimental results obtained through experiment in this work, red are the calculated values from the liquid drop model and green are the values obtained in ref 13

Charge state z	Experimental $n_{crit}(z)$	Calculated $n_{crit}(z)$	% difference
2+	28	30	7
3+	66	69	4
4+	161	122	2

Table 3.5 Values for the experimental and calculated critical sizes using the liquid drop model for benzene

3.6 Conclusions

Well resolved data showing the critical sizes for multiply charged benzene clusters up to charge state 4+ have been presented and discussed with comparison to the predictions from the established liquid drop model. It is found that the model accurately predicts the critical sizes for 2+ and 3+ charged clusters, but disagreement is seen for 4+ charged clusters. Generally speaking the general form of the liquid drop model more accurately predicts the experimental sizes than the model used in reference 13, which uses a slightly more involved methodology to calculate the critical size.

It is found that by using the peak simulation model, accurate accounts of the peak shapes and energy releases are obtained for the fission of the dication precursors. By comparing the values of <*KER*> to previously reported values [10, 12] better agreement is found with the barrier heights given by the dielectric particle model for dication benzene clusters. The experimental parameters used in the peak simulation for the dication species are kept constant in the analysis of the higher ordered charged clusters (Section 3.3, 3.4) and again, good accounting of the peak shapes is seen. Dishing of the peak at reduced fragment size is predicted for all species and is seen experimentally in one MIKE spectrum (figure 3.5b). The values of the <*KER*> are compared to the predicted barrier heights and good agreement is seen.

For fourfold charged benzene precursors, it has been determined through the methodology set out in Section 3.4 that the fragments following fission are 3+ and 1+ charged. The ejected singularly charged clusters contains less than 10 molecules. This resembles the loss of highly charged solvent clusters from ESI droplets (alongside neutral evaporation). The resolved fragmentation pathways do not follow an inclusive range as seen in lower order charged clusters as there is a difference of at least two molecules between successive peaks.

References

1. L. Pauling, *Nature* **325**, 396 (1987).
2. R. P. Messmer, P. A. Schultz, *Nature* **329**, 492 (1987).
3. R. D. Harcourt, *Nature* **329**, 491 (1987).
4. J. Gerratt, M. Raimondi, D. L. Cooper, *Nature* **329**, 492 (1987).
5. D. L. Cooper, J. Gerratt, M. Raimondi, *Nature* **323**, 699 (1986).
6. P. V. Schleyer, *Chemical Reviews* **105**, 3433 (2005).
7. R. R. Wright, N. R. Walker, S. Firth, A. J. Stace, *Journal of Physical Chemistry A* **105**, 54 (2001).
8. L. Ma *et al.*, *Journal of Chemical Physics* **138**, (2013).
9. N. G. Gotts, A. J. Stace, *Journal of Chemical Physics* **95**, 6175 (1991).
10. X. Chen, E. Bichoutskaia, A. J. Stace, *The journal of physical chemistry. A* **117**, 3877 (2013).
11. P. Linse, *Journal of Chemical Physics* **128**, (2008).
12. X. Chen, *University of Nottingham*, (2011).
13. O. Echt *et al.*, *Physical Review A* **38**, 3236 (1988).
14. G. H. Wu, X. J. Chen, A. J. Stace, P. Linse, *Journal of Chemical Physics* **134**, 4 (2011).
15. J. G. Gay, B. J. Berne, *Physical Review Letters* **49**, 194 (1982).
16. D. Kreisle *et al.*, *Physical Review Letters* **56**, 1551 (1986).
17. H. M. Lu, Q. Jiang, *Langmuir* **21**, 779 (2005).
18. E. C. Lee *et al.*, *Journal of Physical Chemistry A* **111**, 3446 (2007).
19. T. D. Mark, in *Gaseous Ion Chemistry and Mass Spectrometry,* J. H. Furtrell, Ed. (J. Wiley, New York, 1986).

Chapter 4 : Multiply Charged Acetonitrile Clusters

4.1 Introduction

Multiply charged acetonitrile clusters are produced as described by the experimental procedure in Chapter 2 and are studied to gain insight into the stability of these clusters under the influence of charge. The coulomb fission reactions close to the critical size are monitored using the MIKE scanning techniques. The resolution and subsequent analysis of these peaks reveals information about the energetics of the processes. Acetonitrile is a simple organic nitrile with the formula CH_3CN. It has a dielectric constant of $\varepsilon_r =$ 36.6 exists as a liquid at temperatures 227-354K, properties which make acetonitrile ideal for use as a solvent. Acetonitrile is extensively used as a solvent in the production of butadiene [1] and is often used as a building block in organic synthesis [2], Acetonitrile is also used extensively as a solvent in electrospray ionisation (ESI) in mass spectrometry. As mentioned in Section 1.1, there are noted similarities in study of the mechanics of the initial stages of ESI and the processes observed in the study of coulomb fission in molecular clusters [3].

Dication acetonitrile clusters have also been the subject of a study into collision induced fission reactions, where a large range of fragments were detected [4]. As mentioned previously, detailed analysis of collision-induced fragmentations is difficult due to the uncertainty of the identity of the final precursor formed prior to coulomb fission. Dication acetonitrile clusters have been a subject of recent publications which presented the observation of fragment peaks resulting from unimolecular coulomb fission [3,5]. The *KERs* were determined from the FWHM of the Gaussian fitting of the experimental peak, and was found to agree to within approximately 20% of the values of U_{max} predicted by the dielectric particle model [6]. The work presented applies the improved experimental setup and methodology for measurements on dication acetonitrile clusters. The measurements and analysis is then taken forward to charges states of up to $Z_p = 4$.

4.2 Doubly Charged Acetonitrile Clusters

The identification of doubly charged acetonitrile clusters is achieved by the observation of non-integer peaks in the cluster mass spectrum and the onset of these peaks corresponds to the critical size $n_{crit}(2)$. Figure 4.1 shows the mass spectrum of acetonitrile. Above a size of n=28, peaks approximately 20.5 amu from the main cluster peaks appear. These peaks reveal the presence of doubly charged clusters in the ion beam at detection. The critical size of $n_{crit}(2) = 28$ is coincident with the smaller singularly charged $(CH_3CN)_{14}^+$ ion which comprises the majority of the peak. The presence of the doubly charged ion is determined from using the MIKE scanning technique to detect the resultant fragments from this ion. The clusters grow in stability with an increase in size, which is reflected in the heights of the doubly charged peaks in the mass spectrum reaching a consistent height beyond a size of n=31. The intensity of the peaks makes the cluster ions very suitable for the MIKE scanning technique.

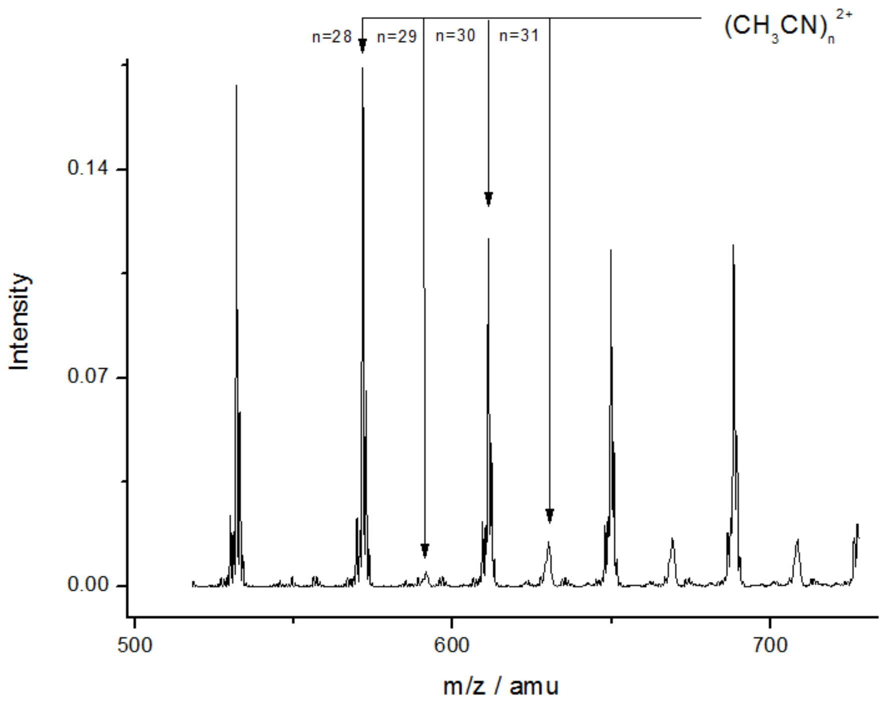

Figure 4.1: The mass spectrum of acetonitrile showing the onset of doubly charged peaks

Figure 4.2 shows an expanded view of the MIKE spectrum in the region of coulomb fission for the precurosr ion $(CH_3CN)_{31}^{2+}$. The centres of the three main dish-shaped peaks rising fom the baseline are at energies that correspond to the loss of a singularly charged cluster containing between 6 and 8 molecules. The noise levels in the peaks are quite high, however, analysis can still be performed. The partially resolved peak which would correspond to the k=5 fragment is observable, however, the remainder of the peak exceeds the energy limit of the ESA and is therefore, not resolved. A more complete specrum has been presented at a lower accelerating energy (E_p=5000 eV) [5] which presents a complete range of detectable fragments. Figure 4.2 was peformed at 6000 eV in order to maximise the signal intensity of the peaks, whilst allowing for resolution of the majority of the fragments inside the ESA limit of 10 kV. What can be seen is that the maximum of intensity is seen at the k=6 fragment, corresponding to roughly 20% loss of mass, indicating this pathway has a lifeime that most closely agrees with the timeframe of the experiment. The simulated peaks are overlain in blue, acceptable fitting to the experimental data is seen, allowing for a small degree of discrepancy in the shape. When compared to the raw data, the simulated peaks appear to be too wide at the base of the peak and too narrow at the top. When the relatively high levels of noise in the spectrum is considered, the discrepency is acceptable and the simulated peaks are considered fitted. The $< KERs >$ from the fragments that make up the peaks agree well with what is predicted by the barier model (Table 4.1). Also shown are the values of the $KERs$ calculated from the measured FWHM of the experimental peaks from the previous analysis. As can be seen, the agreement using the newer method, within 95%, far exceeds the 85% agreement seen using the older method.

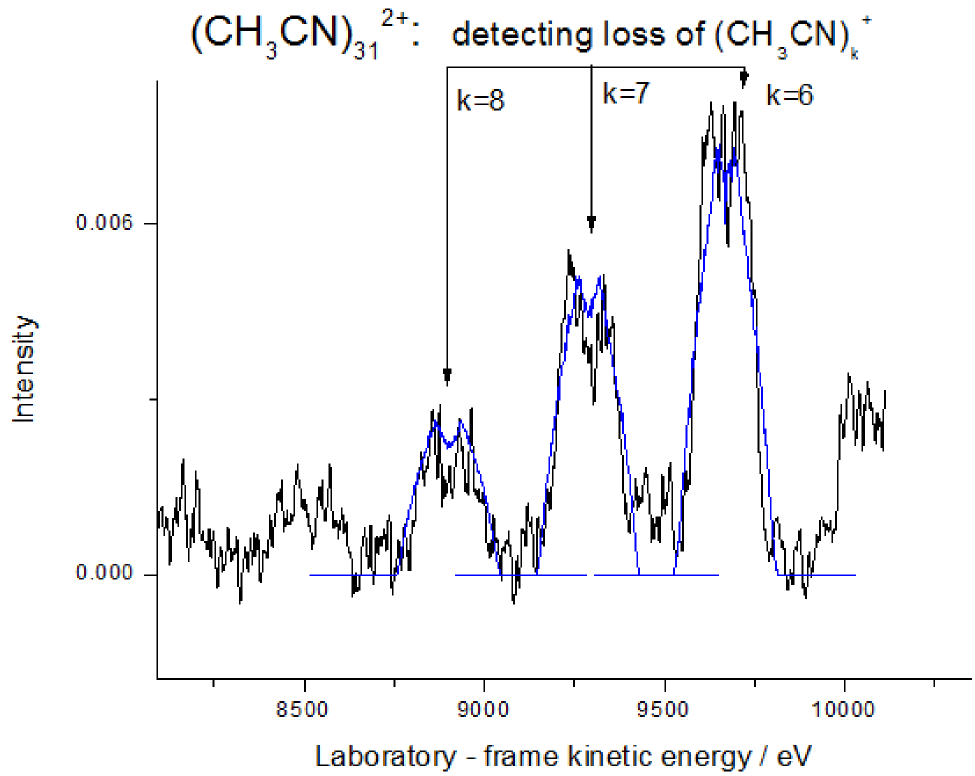

Figure 4.2: MIKE spectrum showing the coulomb fission of the $(CH_3CN)_{31}^{2+}$ ion. Overlain in blue are the simulated peaks

Precursor cluster	Fragment	$< \boldsymbol{KER} >$ / eV	$\boldsymbol{KER}$ / eV	$\boldsymbol{U_{max}}$ / eV
$(CH_3CN)_{31}^{2+}$	k=6+	0.89	0.76	0.89
	k=7+	0.86	0.77	0.90
	k=8+	0.86	-	0.90

Table 4.1: Values for $< KER >$ and U_{max} for the pathways shown in figure 4.2. Also shown are values calculated for the kinetic energy release from the FWHM of the shown as KER using the older method [5].

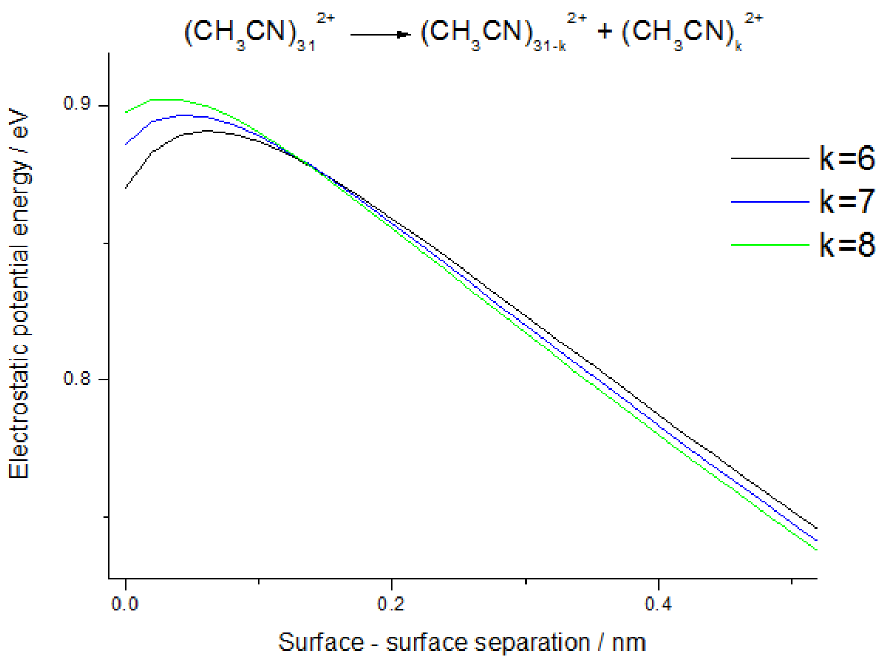

Figure 4.3: The potential energy curves for the pathways shown in figure 4.2

Figure 4.3 shows the electrostatic potential energy curves calculated by the dielectric particle model for the fragmentation pathways seen. Each pathway shows the characteristic shape resulting from the effects of polarisation of the dielectric fragments. This is to the degree that a short range attractive barrier at separations < 0.8 nm is apparent. Due to the asymmetry in charge density, the charge on the larger fragment is distorted by the smaller fragment resulting in polarisation of the larger fragment. The resultant induced attractive forces attenuate the electrostatic repulsion of the charge at short separations, causing attraction between the acetonitrile fragments. The magnitude of attraction is large enough to affect a trend in the maximum in electrostatic energy (U_{max}) between the fragments. The value of U_{max} is seen to be brought down by asymmetry, due to the increase effectiveness of polarisation of the larger fragment from the increasingly charge dense smaller fragment. At approximately 0.7 nm the curves switch ordering due to the reduced influence of the induced potentials at increased separations. Therefore, the asymmetric k=6 pathway has the largest potential energy as the fragments separate. This now reflects the increase in the effectiveness of electrostatic repulsion from a higher charge density on the smaller fragment.

4.3 Triply Charged Acetonitrile Clusters

Triply charged acetonitrile cluster peaks are observed in a mass spectrum. Figure 4.4 shows a mass spectrum in the region where the onset of peaks is observed. The presence of background signals occurring where the onset of peaks is expected obscures the observation somewhat. The loss of HCN and CH_2 are expected fragmentation routes in the acetonitrile mass spectrum under electron ionisation [7] and the peaks seen in Figure 4.4 that are 27 and 14 amu below the singularly charged ion $(CH_3CN)_n^+$ peak will correspond to the $(CH_3CN)_{n-1}CH_2^+$ and $(CH_3CN)_{n-1}HCN^+$ ions respectively, the result of internal fragmentation of the precursor cluster. The spectrum is further complicated by the presence of the large, stable doubly charged acetonitrile clusters undergoing the same fragmentations, resulting in peaks 13.5 and 7 amu down from the doubly charged peaks. However, beyond a size of n=67 peaks corresponding to triply charged acetonitrile rise above the baseline and grow in intensity with the stepwise increase in size of the cluster. The presence of the $(CH_3CN)_{66}^{3+}$ ion which lies underneath the intense $(CH_3CN)_{22}^+$ ion is resolved using the MIKE scanning technique to detect fragments from that triply charger precursor.

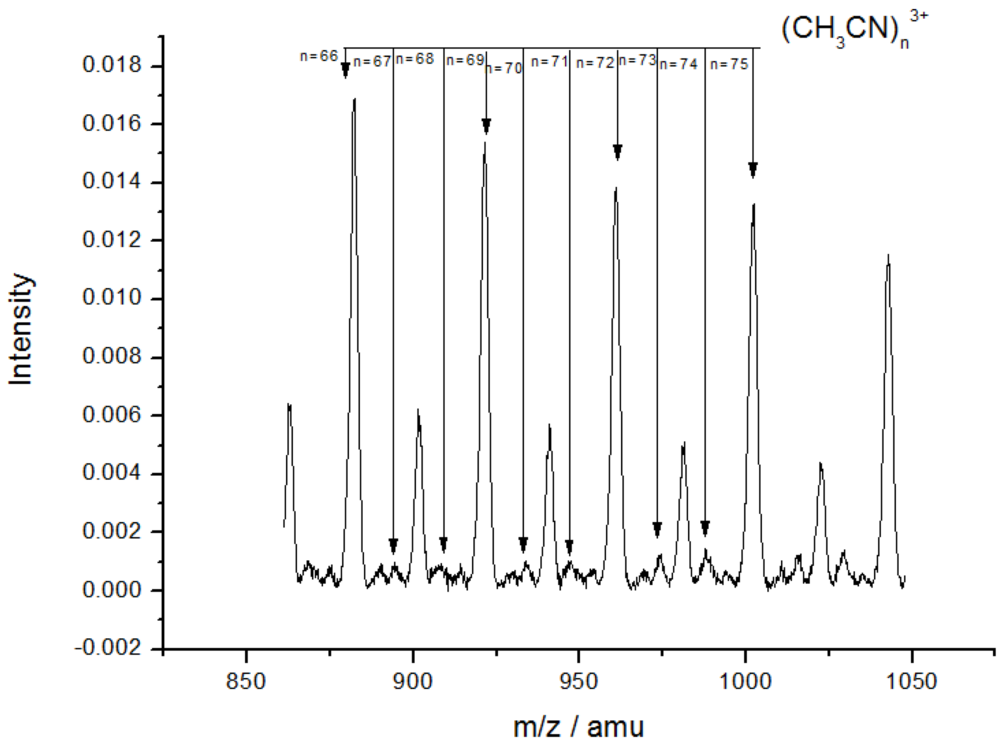

Figure 4.4: Mass spectrum showing the onset of triply charged acetonitrile peaks

Coulomb fission is observed by sitting on a peak containing a component of triply charged acetonitrile clusters and scanning over a range of energies corresponding to expected fragments. This was performed for the $(CH_3CN)_{69}^{3+}$ and $(CH_3CN)_{74}^{3+}$ precursor ions. The resultant MIKE spectra are shown in Figure 4.5. A range of 6 fragmentation pathways are seen for both precursors, with the trends in intensity corresponding to the degree of the agreement of the lifetime of the pathway to experimental constraints. Both precursors are seen to eject a singly charged cluster containing between 5 and 10 molecules corresponding to around 10% mass loss. Figure 4.5(a) shows the profile from the fission of $(CH_3CN)_{69}^{3+}$, where 5 strong peaks from the k=5-9 channel are observed. The presence of the k=10 channel inferred from the slow tailing off of the profile at low energy. The peaks are sufficiently resolved to perform peak analysis on and the shape of the simulated peaks reproduces the experimental profile well. The width of the k=7 peak does not quite account for the full width of the experimental feature. However, broadening of MIKE peaks can occur from additional processes happening in the 2nd *ffr*, for example fragmentation from artefacts or component clusters i.e. protonated species. The remainder of the profile is accounted for well by the simulations. Figure 4.5(b) shows the fission of the $(CH_3CN)_{74}^{3+}$ cluster, where all 6 fragmentation channels are observed from peaks in the MIKE spectrum. There is a large broadening in the k=8 fragment peak which makes the total peak width much wider than what is simulated. This feature may be the result of a significant contribution from artefacts.

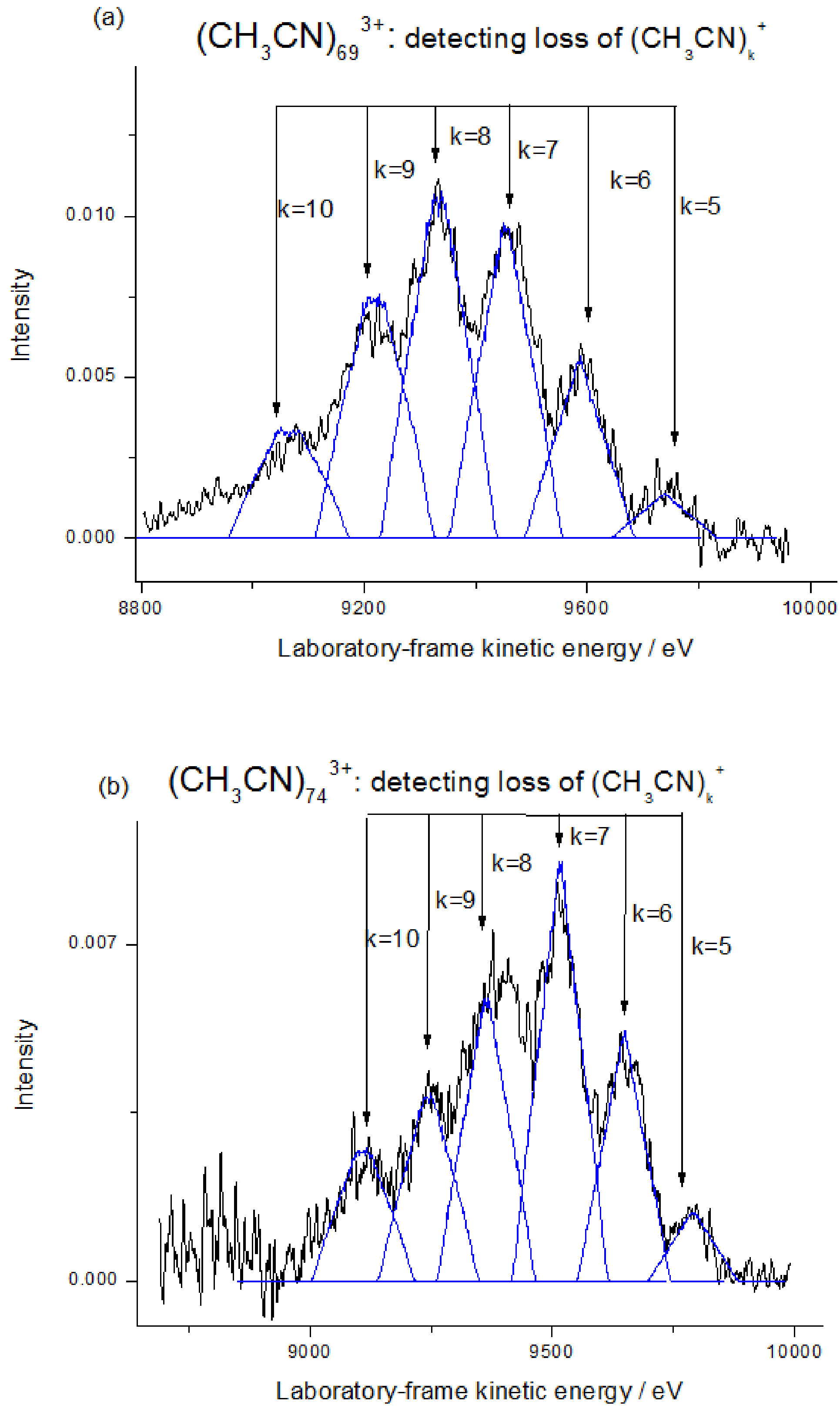

Figure 4.5: MIKE spectra showing the coulomb fission from the precursor ions a) $(CH_3CN)_{69}^{3+}$ and b) $(CH_3CN)_{74}^{3+}$. Overlain in blue are the simulated peaks for the pathways observed

a) Precursor cluster	Fragment	$< KER >$ eV	U_{max} / eV
$(CH_3CN)_{69}^{3+}$	K=5	1.53	1.52
	K=6	1.53	1.52
	K=7	1.53	1.52
	K=8	1.52	1.52
	K=9	1.52	1.52
	K=10	1.52	1.51

b) Precursor cluster	Fragment	$< KER >$ eV	U_{max} / eV
$(CH_3CN)_{74}^{3+}$	K=5	1.43	1.49
	K=6	1.43	1.49
	K=7	1.43	1.49
	K=8	1.42	1.48
	K=9	1.42	1.48
	K=10	1.42	1.48

Table 4.2: Values for $< KER >$ and U_{max} for the pathways shown in figure 4.5

The values for the barrier heights U_{max} and the average kinetic release $< KER >$ for the observed pathways are tabulated in Table 4.2. In general the agreement is better for the $(CH_3CN)_{69}^{3+}$ precursor, possibly a reflection on the better quality of the experimental data, hence allowing a more realistic fitting for the simulated peaks. Figure 4.6 shows the electrostatic potential energy curves for the fragmentation pathways shown in Figure 4.5(a) in the region of short separation. The changing degree of the short range barriers to fission at close separations is apparent, from a relatively large short range barrier for the most asymmetric pathway to almost 0 for the most symmetric. This reveals how sensitive the charge on the larger doubly charged fragment is to the effect of the electric field from the smaller fragment. The values of U_{max} do not decrease with the magnitude of asymmetry as seen previously and there is no cross-over of the curves at larger separations. This demonstrates the joint effectiveness of the polarisation of the larger cluster from the smaller fragment and the effectiveness of the electrostatic repulsion at beyond 0.5 nm separation at large asymmetry.

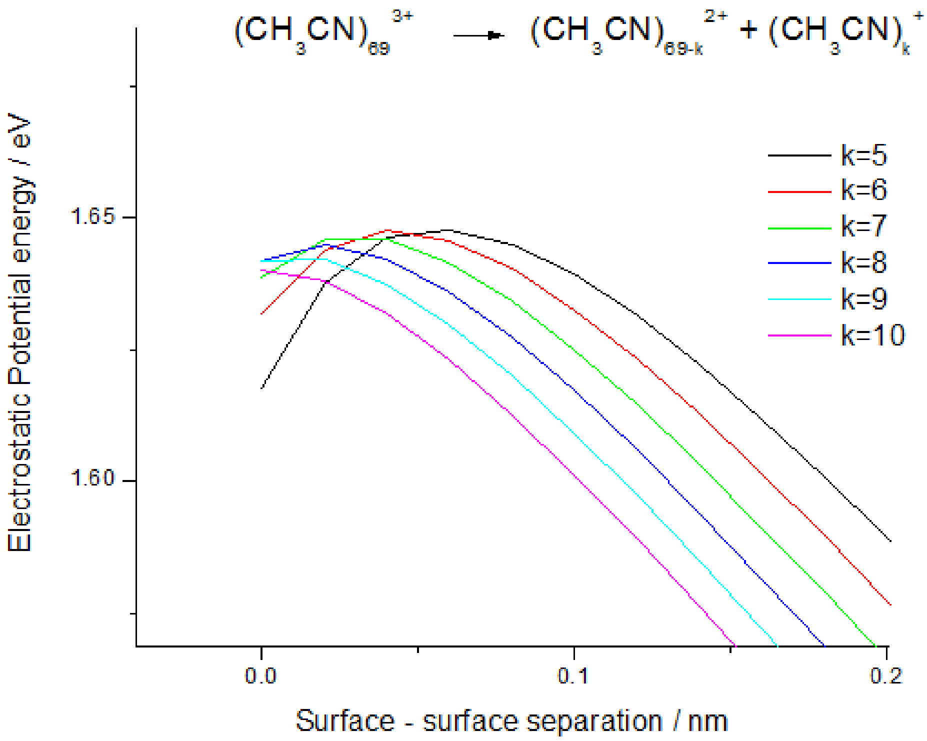

Figure 4.6: Electrostatic potential energy curves for the pathways shown in Figure 4.5a

4.4 Fourfold Charged Acetonitrile Clusters

Distinct peaks corresponding to fourfold charged acetonitrile clusters $(CH_3CN)_n^{4+}$ are not resolved in a mass spectrum. The identification of fourfold charged clusters and the determination of the critical size is achieved via the MIKE scanning technique. A profile of 3 strong peaks resulting from coulomb fission of $(CH_3CN)_{165}^{4+}$ is resolved in a MIKE spectrum. This profile was monitored as a function of decreasing precursor size until it disappears completely a critical size of $n_{crit}(4) = 161$. Figure 4.7 shows an overlay of 4 MIKE spectra from precursors in the size range of n=161 to n=165. For the precursors that do not coincide with a strong cluster peak in the mass spectrum (i.e. a singly or doubly charged peak) the nominal position on the m/z scale was determined from the difference in m/z for the cluster relative to a strong cluster peak.

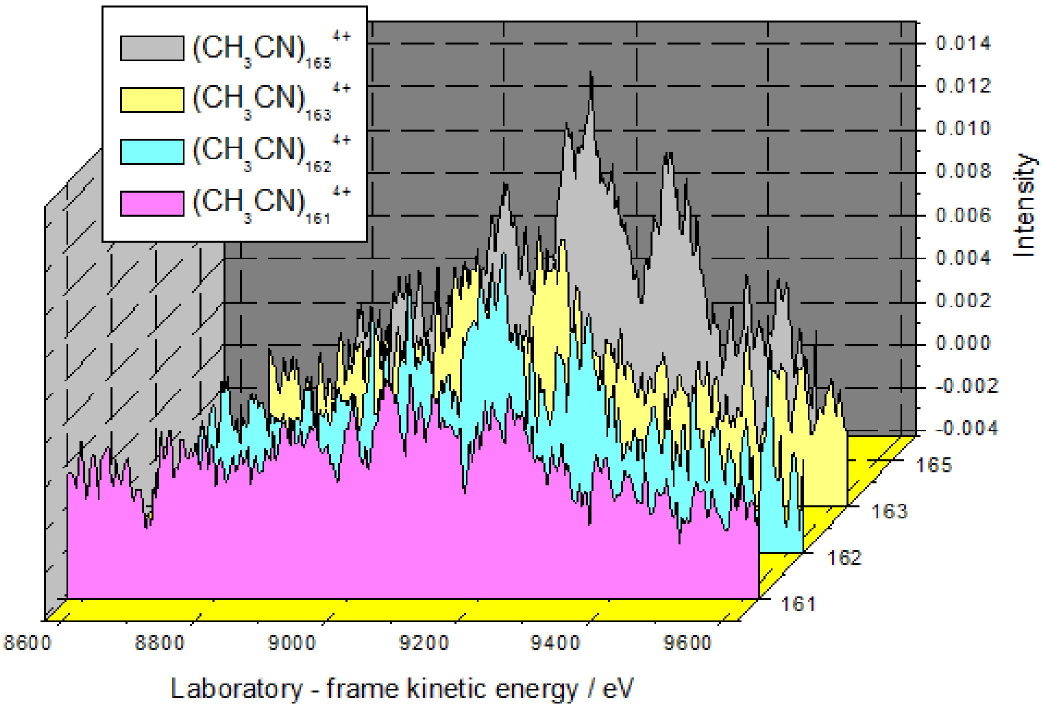

Figure 4.7: An overlay showing how the characteristic profile from the fission of fourfold charged acetonitrile clusters develops as a function of size

The possible fission mechanisms are either the fragmentation into 3+/1+ or 2+/2+ charged fragments. To determine which, the peak simulation methodology is employed in conjunction with the dielectric particle model. Figure 4.8 shows the MIKE spectrum for the fission of $(CH_3CN)_{165}^{4+}$. Using equation 2.10 for $Z_f = 3$, the three peaks are found to correspond to highly asymmetric coulomb fission. The loss of singly charged clusters containing 1, 3 and 5 molecules is determined. Overlain in Figure 4.8(a) are the simulated peaks for the two low energy peaks of the spectrum. The *KER* range used in the simulations is directed by the values for U_{max} which is calculated using the dielectric particle model. The peaks are seen to match the general shape of the experimental peaks. To confirm that these features are not from the 2+/2+ mechanism the analysis was repeated at the energy for the central peak for the fragment in charge state $Z_f = 2$ and the resultant simulation is shown in Figure 4.8(b). The comparative lightness of the fragment in addition to the large magnitude of the *KER* (predicted from $U_{\max}$ = 2.10 eV) result in a wide and highly dished peak that far exceeds the width of the experimental feature. The values for $< KER >$ and U_{max} are given in Table 4.3

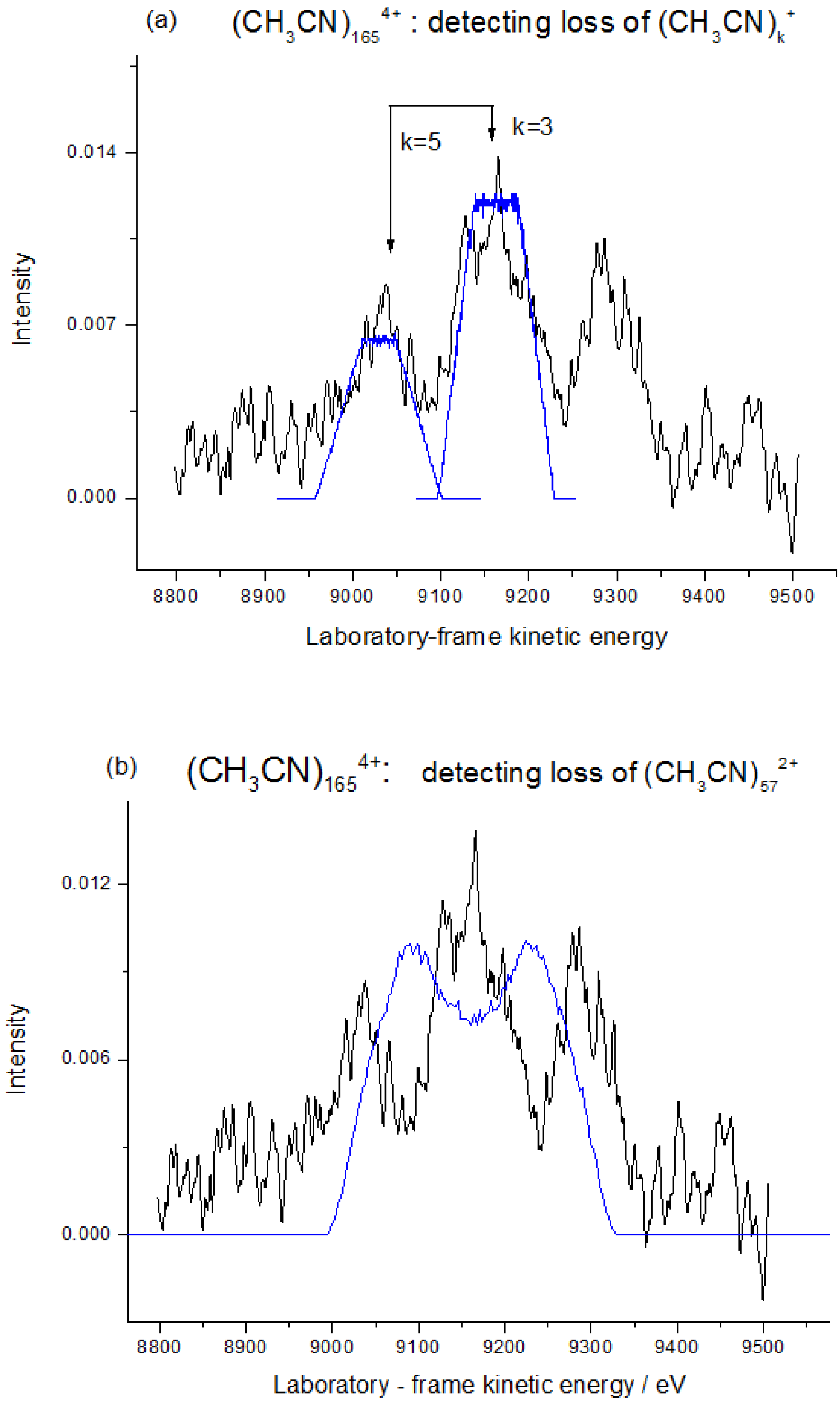

Figure 4.8: MIKE spectra from the coulomb fission of $(CH_3CN)_{165}^{4+}$. Overlain is the simulated peaks for a) the 3+/1+ mechanism and b) the 2+/2+ mechanism.

a) Precursor cluster	Fragment	$< KER >$ / eV	U_{max} / eV
$(CH_3CN)_{165}^{4+}$	$K=1^+$	-	1.83
	$K=3^+$	1.90	1.83
	$K=5^+$	1.90	1.82

b) Precursor cluster	Fragment	$< KER >$ / eV	U_{max} / eV
$(CH_3CN)_{165}^{4+}$	$K=67^{2+}$	1.96	2.10

Table 4.3: Values for U_{max} and $< KER >$ for the pathways shown for the two fission mechanism shown in figure 4.8(a,b)

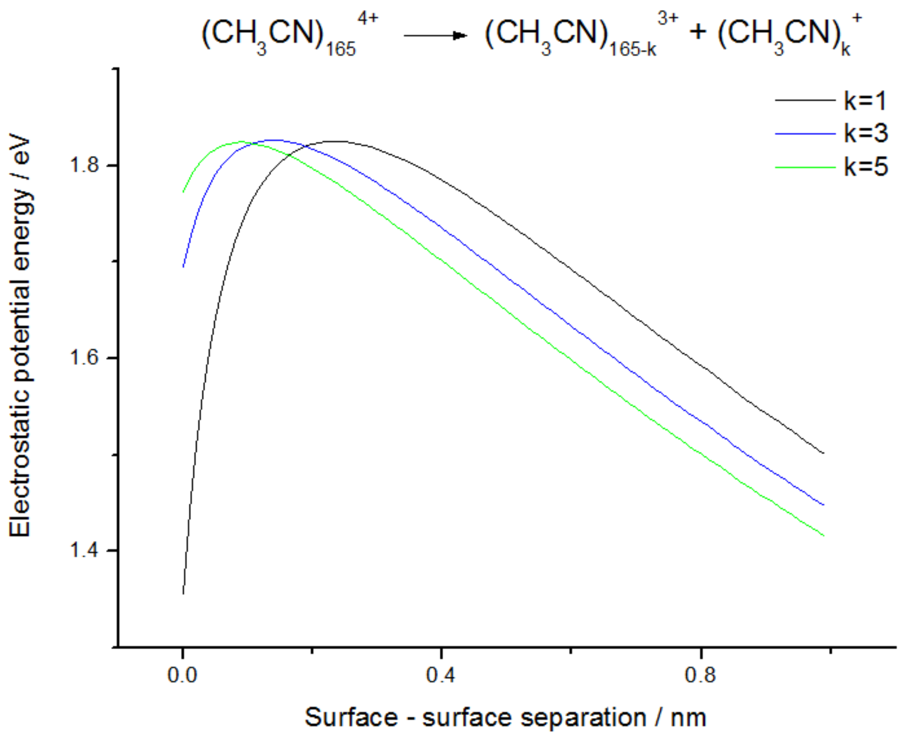

Figure 4.9: Potential energy curves for the fragmentation pathways shown in figure 4.8a

Figure 4.9 shows the calculated potential energy curves for the fission pathways producing 3+/1+ charged fragments from the precursor $(CH_3CN)_{165}^{4+}$. A short range barrier to fission is evident for the k=1 pathway which becomes smaller in magnitude at the k=5 pathway. This is a reflection of the change in charge density from one molecule to 5 molecules in the smaller fragment, and the resultant change in polarising ability. The most asymmetric pathway has the largest values of electrostatic potential energy as the fragments separate, as for triply charged precursors (Figure 4.6), the electrostatic repulsion has a demonstrably large effect.

4.5 Stability of Multiply Charged Acetonitrile Clusters

With the collection of data on multiply charged acetonitrile clusters it is possible to compare the experimentally determined critical sizes with what is predicted by the liquid drop model. Table 4.4 gives the values of experimental $n_{crit}(z)$ collected by the methods described in the preceding sections. The values of the calculated $n_{crit}(z)$ are determined from the solution to the Rayleigh equation (equation 1.1):

$$n_{crit}(z) = \frac{(ze)^2}{64\pi^2\gamma\varepsilon_0{r_m}^3}$$

Where z is the charge state of the cluster, e is the elementary charge constant, γ is the surface tension ε_0 is the permittivity of free space and r_m is the molecular radius. The % difference in the assignments of doubly and triply charged clusters is small, however, the assignments for fourfold charged clusters show a 27% increase from the theoretical size. This observation could be caused from two potential situations. Firstly, if beyond a certain size the acetonitrile cluster becomes deformed significantly from the theoretically assumed spherical shape, it could cause the charges to come into closer proximity, hence, requiring additional molecules to increase the inter-charge distance. This is a tempting conclusion to draw as the acetonitrile cluster does not have the hydrogen bond network that is shown to contribute to the spherical shape of molecular cluster, particularly water and ammonia [9,10]. As previously mentioned acetonitrile is found to favour stacking in anti-parallel conformations [8], DFT calculations performed by Remya *et. al.* [11] show how the structures of acetonitrile cluster up to a size of n=27 are determined by the cooperativity between adjacent molecules that favours a stacking configuration. This is shown to produce clusters that are irregular in shape and definitely non-spherical. The cluster size for $n_{crit}(2)$ and $n_{crit}(3)$ exceed the limits of this study but one might assume that at that size the multiply charged cluster will deviate significantly from the spherical shape assumed by the liquid drop model. However, it would seem that the liquid drop model is capable of predicting the correct sizes for charge states Z_p = 2 and 3. Therefore it is possible that the deviation observed is due to experimental factors.

Charge state z	Experimental $n_{crit}(z)$	Calculated $n_{crit}(z)$	% difference
2+	28	30	7
3+	66	69	4
4+	161	122	27

Table 4.4: Experimental and calculated values for $n_{crit}(z)$ and the percentage difference for multiply charged acetonitrile clusters

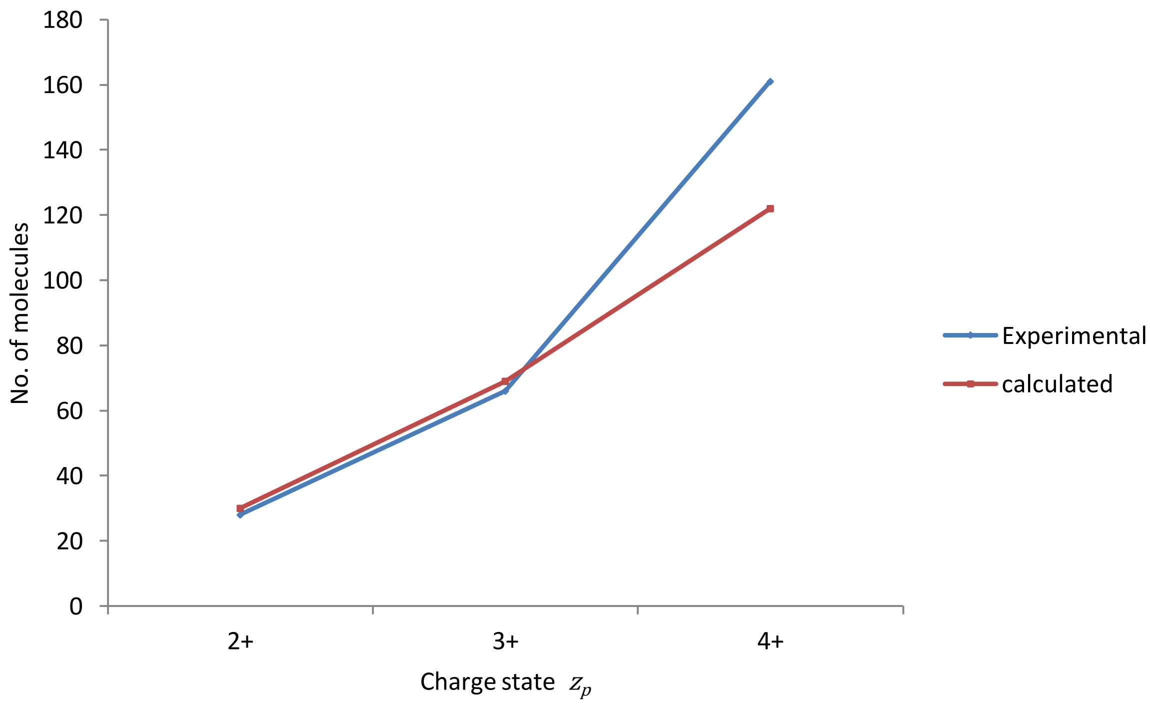

Figure 4.10: The magnitudes for the critical sizes for acetonitrile determined experimentally (blue)and calculated by the liquid drop model (red)

The identification of the onset for fourfold charged precursors is determined from the evolution of a characteristic fission profile in the MIKE spectrum above critical size. However, a measurable MIKE signal from coulomb fission is dependent on the number of precursors in the 2nd *ffr,* and also if they are undergoing fission in the correct timeframe. The magnitude of observed coulomb fission signal can be strongly dependent on the size of the precursor, for instance, many of the cluster systems presented in this work have a certain size range within the critical range that show particularly strong signals from coulomb fission. It is likely that this is determined by the magnitude of the barrier to fission ($E_{barrier}$) over all available pathways. As the cluster gets larger so too does $E_{barrier}$ as the cluster becomes more stable, and so the lifetimes for all available fission pathways will increase. This could ensure a sufficient number of precursors are able to enter the 2nd *ffr* before undergoing coulomb fission, producing a measurable signal. Furthermore, the values of U_{max} observed for the fission of $(CH_3CN)_{165}^{4+}$ show a maximum for the k=1+ pathway. This could be an indication that the magnitude of ($E_{barrier}$) is so small that only the pathways with the largest value of U_{max} (and hence $E_{barrier}$) for the n=165 precursor, (i.e. the k=1+ pathway), live long enough to be detected. In this instance, it does not mean that fourfold charged clusters below the measured critical size do not exist, only that the lifetimes with respect to all coulomb fission pathways are not great enough to be detected using the experimental setup.

4.6 Conclusions

The work presented in this chapter builds on previous measurements on dication acetonitrile clusters and extends measurements on both the stability of the precursor clusters and the measurements of the coulomb fission reaction up to precursor charge states of Z_p =4. The measurements on the dication system confirmed initial measurements showing how the magnitude of the kinetic energy release following the coulomb fission reactions is accurately predicted by the dielectric particle model [3]. Using the peak simulation methodology more accurate measurements of the kinetic energy release are possible, which takes the agreement closer to the predicted values of U_{max}.

Strong peaks in the mass spectrum are observed for triply charged acetonitrile clusters, which show an onset close to what is predicted by the liquid drop model. The fact that the peaks are strong enough to rise above the significant background signals in the mass spectrum is an indication of the large number of the precursor species in the ion beam at detection. The coulomb fission reactions show ejection of a singularly charged cluster containing between 5 and 10 molecules corresponding to approximately 10% mass loss from the precursor cluster. The fitted simulated peaks match the predicted barrier heights quite closely, although there are a few instances where the shape of the simulated peak does not account for the full width of the experimental feature. This is likely a result of broadening of the experimental peaks from artefacts in the spectrum.

Fourfold charged clusters were detected from the presence of fragment signals in the MIKE spectrum from the fission from the fourfold charged cluster. The characteristic profile is seen to rise from the baseline above the critical size and take the form of three peaks corresponding to the loss of a singularly charge cluster containing up to 5 molecules. The large experimental value of $n_{crit}(4)$ compared to the liquid drop prediction could be due to not enough small precursors making it into the 2nd *ffr* to produce a measurable fission signal. Or alternatively, a strongly non-spherical structure in the $n_{crit}(4)$ size regime, not accounted for by the liquid drop model. A question remains as to why there is a difference in two molecules between the fragments peaks in the MIKE spectrum. Acetonitrile has been shown to form stable anti-parallel pairs [8], which might lead to the large fragment requiring an even number to ensure pair formation.

References

[1] H.P. Sun, J.P. Wristers, Butadiene *Encyclopedia of Chemical Technology, 4th ed.*, 1992.
[2] S.A. DiBiase, J.R. Beadle, G.W. Gokel, *Org. Synth*. **62** (1984).
[3] X. Chen, E. Bichoutskaia, A.J. Stace, *The journal of physical chemistry. A* **117** (2013) 3877.
[4] N.G. Gotts, P.G. Lethbridge, A.J. Stace, *Journal of Chemical Physics* **96** (1992) 408.
[5] X. Chen, University of Nottingham, 2011.
[6] E. Bichoutskaia, A.L. Boatwright, A. Khachatourian, A.J. Stace, *Journal of Chemical Physics* **133** (2010).
[7] http://webbook.nist.gov/cgi/cbook.cgi?ID=C75058&Mask=200#Mass-Spec.
[8] G. Delmistro, A.J. Stace, *Journal of Chemical Physics* **99** (1993) 4656.
[9] T. James, D.J. Wales, J. Hernandez-Rojas, *Chemical Physics Letters* **415** (2005) 302.
[10] T.A. Beu, U. Buck, Journal of *Chemical Physics* **114** (2001) 7848.
[11] K. Remya, C.H. Suresh, *Journal of Computational Chemistry* **35** (2014) 910.

Chapter 5 : Multiply Charged Ammonia Clusters

5.1 Introduction

Multiply charged ammonia clusters have been the subject of recent attempts to model unimolecular coulomb fission reactions in molecular clusters. From the Stace research group, Wu *et al.* [1] published results showing the delayed asymmetric coulomb fission of ammonia dication clusters. These were the first observations of unimolecular coulomb fission in molecular clusters, i.e. the precursors are isolated and the fragmentation pathways can be assigned from clear signals in a MIKE spectrum. From the same group it was shown that by modelling the charged fragments as dielectric spheres, the calculated maximum in electrostatic potential energy U_{max} (barrier height) gives a good account of the measured kinetic energy release (KER) [2].

Using the same experimental techniques, the current work extends these observations to higher charge states, and precursor charge states of up to 8+ are identified and studied with respect to coulomb fission. Precursor identification is achieved by using the MIKE scanning technique to identify the onset of multiply charged cluster ions from the resulting coulomb fission signals. The exception to this are doubly and triply charged clusters which can be identified by an onset of non-integer peaks in a mass spectrum. The mass spectra of both systems are known and have been published previously [3, 4]. The work presented analyses the previous data using current theoretical and methodological techniques, showing more accurate assignments of the energetics and extending this work onto higher ordered charged ammonia clusters. As before, in MIKE scanning techniques, only the larger of the two fragment ions is detected.

5.2. Doubly Charged Ammonia Clusters

The identification and coulomb fission of dication ammonia clusters was achieved from observation of resolved peaks in a MIKE spectrum corresponding to charged fragments [1]. The *KERs* of the processes were determined from the FWHM of the experimental peaks, which in general were found to agree well with the predictions of a dielectric discontinuity model [5] and subsequently the more advanced dielectric particle model that is also used in this work [6]. Improvement in the assignments of the *KER* values is sought by application of the peak simulation model. By simulating the fragment peaks, using the known barrier heights as a guide to the expected values of *KER*, simulated peaks can be fitted to the experimental data, thus resolving more accurate $< KER >$ values for the processes. The improvements this methodology brings may be considered especially important for the study of doubly charged (and higher order charged states) ammonia as the peak signal strengths are characteristically weak. This is due to the relatively small molecular mass of ammonia meaning the peaks are closely spaced together in energy, making resolution difficult. This makes energy analysis using the FWHM of the peaks difficult. It is also shown that for the cases of higher order charge states, this methodology can be used to determine the charge state of the fragments when the assignments of the observed pathways are ambiguous and hence the mechanism of coulomb fission that is observed.

The improvements in the experimental method, as explained in Chapter 2, reducing the distance between the supersonic nozzle and ion source and increasing the accelerating voltage from 5 kV to 6 kV post-ionisation will improve overall signal strength at the detector. This will also allow an improvement in the resolution of the individual MIKE peaks in the spectrum as the energy spacing of fragment peaks increases by a factor of 6/5

(Equation 2.10). In light of these changes, the MIKE spectra that are presented are under new experimental conditions.

Figure 5.1 shows a mass spectrum in which the onset of doubly charged ammonia cluster peaks is observed beyond a critical size of $n_{crit}(2)=50$. The resolution of the mass spectrometer is such that peaks originating from both the fragmentation of the clusters and intra-cluster ion-molecule reactions are resolved. These reactions were the subject of a paper by Garvey *et al.* [3], who were able to assign the mass spectra peaks as products of the following intra-cluster reactions. The dominant ion-molecule reaction inside a charged ammonia cluster is the formation of the NH_4^+ ion via Reaction 1:

$$(NH_3)_n{}^+ \quad \rightarrow \quad (NH_3)_{n-2}NH_4{}^+ + NH_2 \qquad (1)$$

In a doubly charged cluster with two charge centres Reaction 1 can occur up to two times inside the cluster producing 2 additional peaks separated by ½ amu, these are labelled as *c* and *d* in figure 5.2. Also observed are the fragmentation reactions of the cation in the un-reacted precursor cluster [7]:

$$(NH_3)_n{}^+ \rightarrow \ (NH_3)_{n-1}NH_2{}^+ + H \qquad (2)$$

Reaction 2 is responsible for peaks *a* and *b* in figure 5.2, as before, the number of charge centres determines the number of times reaction 2 can occur. A loss of up to two hydrogen atoms is possible from the dication cluster resulting in peak *a,* 1 amu below the precursor peak *p* in the mass spectrum.

The peaks to the right of *d* are from further intra-cluster reactions producing the NH_5^+ cation solvated in the cluster. The additional proton is inferred to be 'donated' by the bulk of the cluster. This ion can form by two possible mechanisms [3, 8]:

$$(NH_3)_n{}^+ \rightarrow \ (NH_3)_{n-2}NH_5{}^+ + NH \tag{3}$$

$$(NH_3)_n{}^+ \rightarrow \ (NH_3)_{n-3}NH_5{}^+ + N_2H_4 \tag{4}$$

It is interesting to note the relative intensities of peaks seen in figure 5.2. Peaks a-f all show increased intensity relative to the precursor peak compared to the previous work [3]. To account for this it is worth considering that the size of the cluster (n=55) is smaller than the examples show in Garvey's work (n=59-85) which will have additional degrees of freedom to accommodate the excess energy in the cluster, hence effectively quenching these reactions. Additionally, the electron energy of the ion source used in this work can go up to 100 eV, making it possible for the cluster to contain additional excess energy post-ionisation. This energy can drive the inter-cluster reactions. The work by Garvey and colleagues only shows data collected up to 90 eV.

Figure 5.3 shows MIKE spectra recorded for two dication ammonia clusters $(NH_3)_{51}{}^{2+}$ and $(NH_3)_{52}{}^{2+}$ where the cluster is losing a $(NH_3)_k{}^+$ fragment. The fragment peaks all show a degree of dishing. In the MIKE spectrum in figure 5.1a peak corresponding to the k=11 pathway, which corresponds to the largest cluster fragment in the range detected, has the least degree of dishing. This is not unsurprising due to the reduced divergence the fragment will experience post coulomb fission due to its larger mass relative to the other fragments. The peak simulation model does not reproduce this entirely; a small degree of dishing is predicted, reduced in magnitude to the simulated peaks for smaller fragments. The peaks for the k=12 and k=13 channels show a high degree of dishing in the experimental MIKE spectrum which is not completely accounted for by the simulation model. Possibly the fragmentations are happening, on average, further away from the electric sector than the model predicts, due to having a relatively short lifetime. This will therefore increase the total amount of divergence of the ions that is possible before the focussing slit at the end of the flight tube, and hence the dishing of the peak.

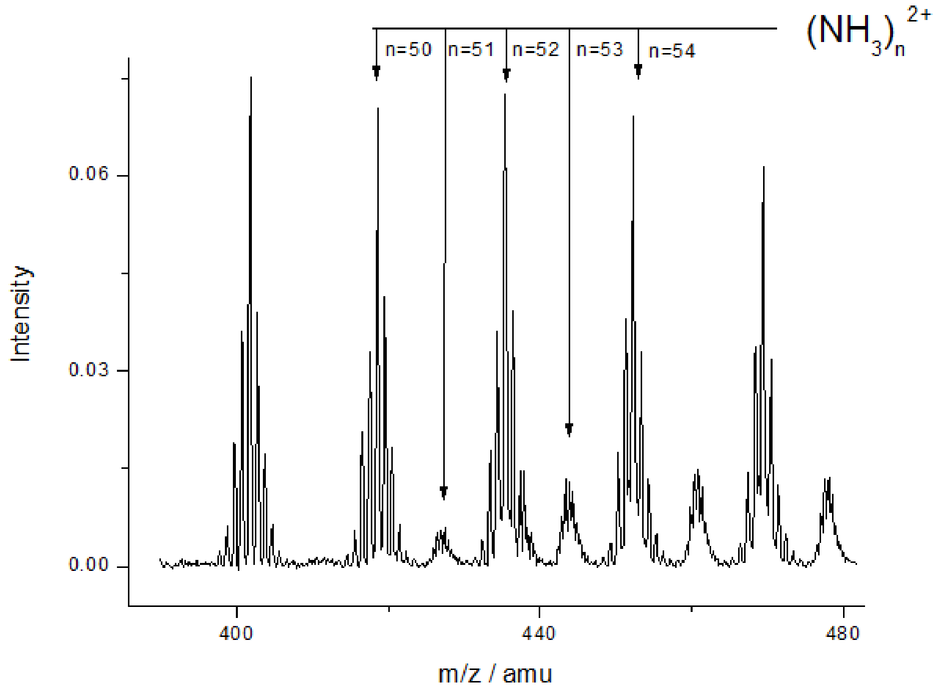

Figure 5.1: Mass spectrum showing onset on doubly charged ammonia cluster peaks

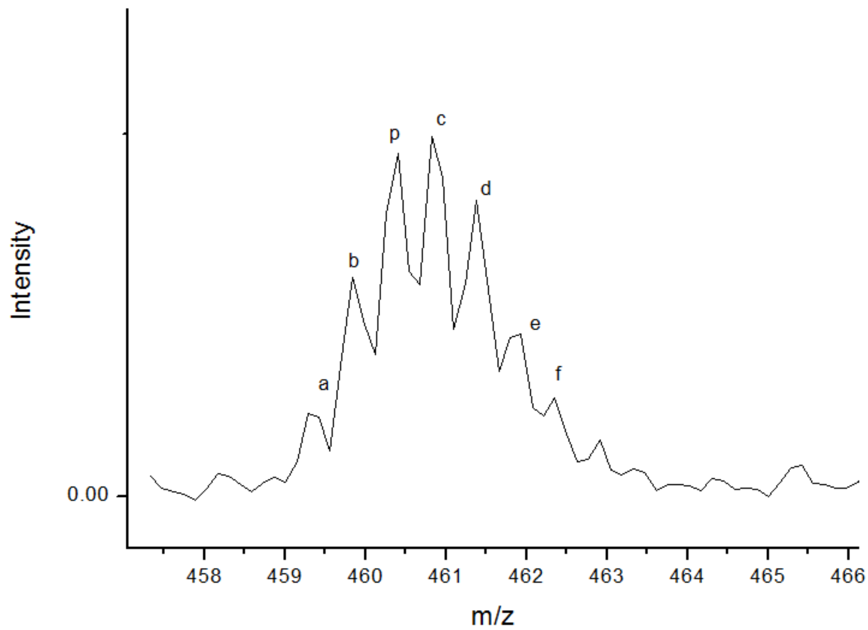

Figure 5.2: An expanded view of the $H_x(NH_3)_{55}^{2+}$ region showing the ions that comprise it. p: $(NH_3)_{55}^{2+}$, a: $(NH_3)_{55\text{-}1}NH_2^{2+}$, b: $(NH_3)_{54}NH^{2+}$, c: $(NH_3)_{54}NH_4^{2+}$, d: $(NH_3)_{53}(NH_4^+NH_4^+)$, e: $(NH_3)_{53}$ $(NH_5^+NH_4^+)$, f: : $(NH_3)_{53}$ $(NH_5^+NH_5^+)$.

Overall, the experimental peaks are better resolved in the MIKE spectrum of $(NH_3)_{52}^{2+}$. This could be due to the increased size of the cluster the charges are accommodated more efficiently and therefore the total energy of the cluster is reduced. This stabilises the cluster against fragmentation with respect to coulomb fission, therefore, more cluster ions will have a lifetime long enough to pass through the magnet and undergo coulomb fission. It is interesting to note that the dishing of experimental peaks is more accurately described by the peak simulation model than in the previous example. There is less dishing in the peaks of the MIKE spectrum. This may be due, in part, to an increase in quality in the experimental data. With reference to the values in Table 5.1a and 5.1b, the values of $< KER >$ and U_{max} are in close agreement, approximately 1%. This is much closer than what has been reported previously where the agreement was within approximately 25%.

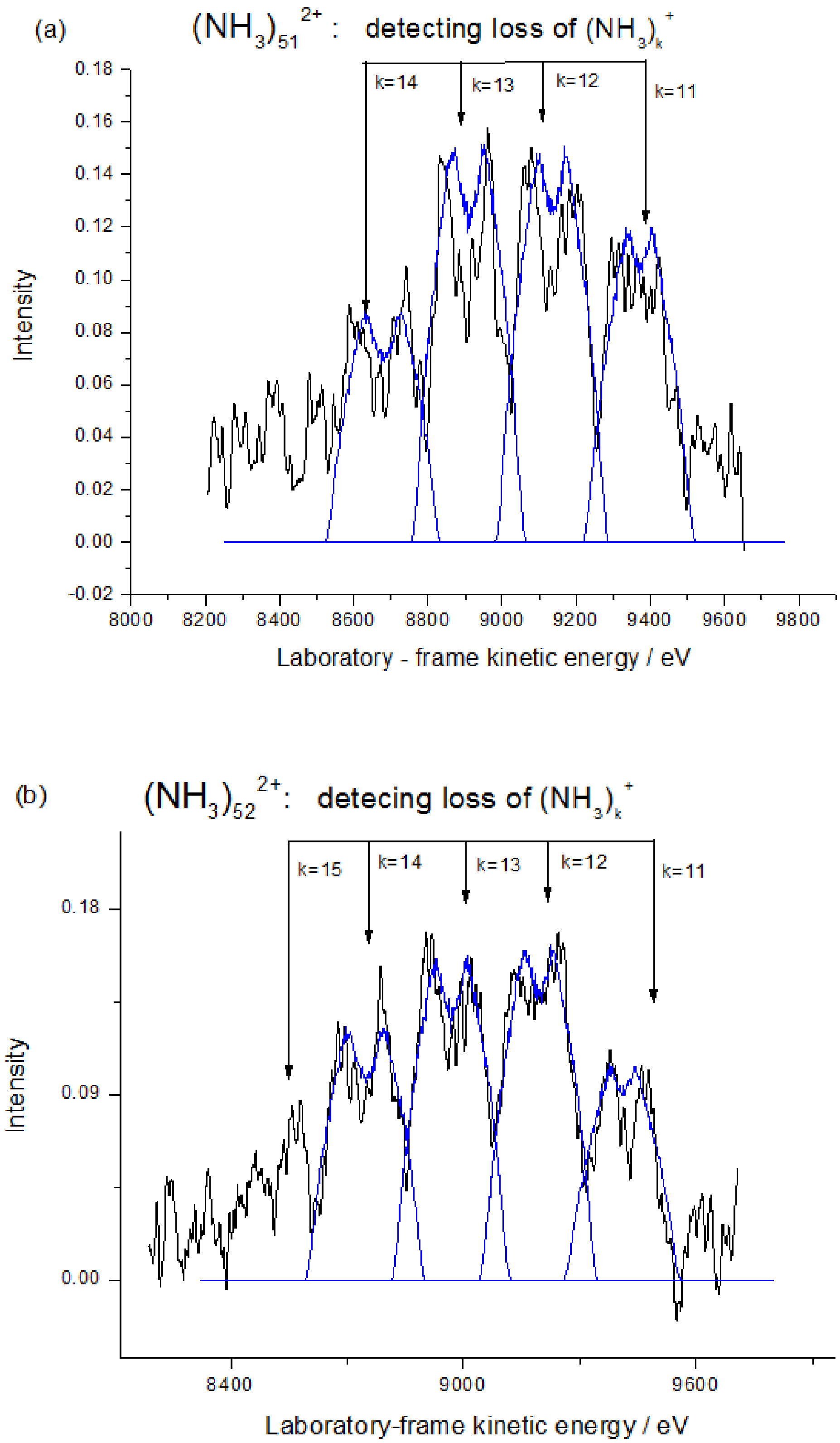

Figure 5.3: MIKE spectra for precursor ions (a) $(NH_3)_{51}^{2+}$ and (b) $(NH_3)_{52}^{2+}$ showing coulomb fission. Overlain are the simulated peaks

(a) Precursor cluster	Fragment pathway	$< KER >$ /eV	U_{max} /eV
$(NH_3)_{51}^{2+}$	k=11^{+}	0.99	0.98
	k=12^{+}	0.99	0.98
	k=13^{+}	0.99	0.99
	k=14^{+}	0.99	0.99

(b) Precursor cluster	Fragment pathway	$< KER >$ /eV	U_{max} /eV
$(NH_3)_{52}^{2+}$	k=11^{+}	0.99	0.97
	k=12^{+}	0.99	0.98
	k=13^{+}	0.99	0.98
	k=14^{+}	0.99	0.98

Table 5.1: Values for $< KER >$ and U_{max} for the fragmentation pathways shown in figure 5.2 for (a) $(NH_3)_{51}^{2+}$ and (b) $(NH_3)_{52}^{2+}$

Figure 5.4 shows the potential energy curves for the separation of charged fragments produced from the coulomb fission of $(NH_3)_{52}^{2+}$ in the range of k=11–14. It is apparent, the most asymmetric pathways produce a curve that is strongly attenuated by attractive potentials, producing a short range barrier to fission at surface-surface separation less than 0.5 nm. A reduction in the magnitude of the maximum of electrostatic potential energy (U_{max}) is seen as asymmetry increases. This observation is due to the high polarisabilities of the larger of the ammonia cluster fragments, with respect to distortion caused by the external electric field originating from the smaller fragment. This results in significant attractive potentials which attenuate the electrostatic repulsion of the total charge in the two fragments. At approximately 0.1 nm there is a crossover in the trend in the potential energy for the pathways. Now the pathway that is most asymmetric has the greatest potential energy between fragments. This is due to the reduced influence of the short range attractive potentials at larger separations. Additionally, the electrostatic repulsion becomes more effective when the electric field originates from a small sphere.

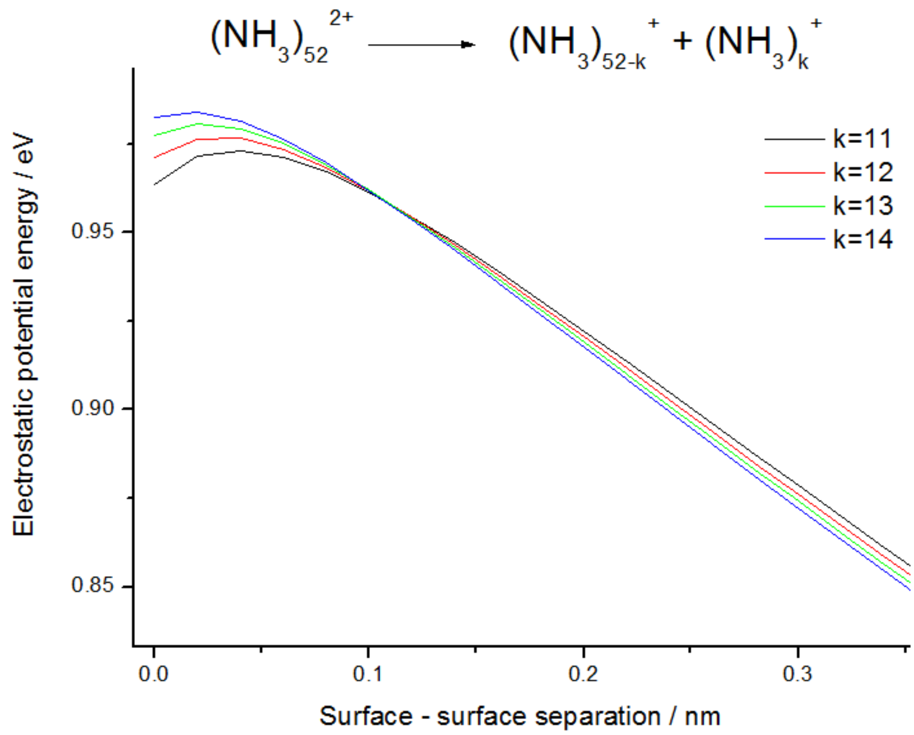

Figure 5.4: Solution to the dielectric particle model for the reaction pathways shown in figure 5.3b

5.3. Triply Charged Ammonia Clusters

The onset of triply charged ammonia clusters may be identified, in part, through a mass spectrum. Figure 5.5 show the mass spectrum with the onset of non-integer peaks at around 690 amu corresponding to the ion $(NH_3)_{121}{}^{3+}$. This however is not found to be the critical size, fragments originating from coulomb fission are observed down to a precursor size of $(NH_3)_{116}{}^{3+}$. These measurements are achieved by tuning the magnet to the m/z value of the triply charged ion and performing a MIKE scan which reveals the presence of the characteristic signal arising from coulomb fission which diminishes in intensity towards the critical size. One can rule out any possibility that these signals are from close lying or coincident doubly charged cluster peaks as the corresponding sizes of these clusters (approx. $(NH_3)_{77}{}^{2+}$) would far exceed the stable size ($n_{stab}(2) = 54$). The fact that these precursor ions are not resolved in the mass spectrum highlights the necessity to verify observations from mass scanning experiments with corresponding MIKE spectra if possible. The observation of a lack of mass spectral precursor ion peaks and the presence of reasonably strong fragment signals may indicate that the majority of the ions passing through the magnet undergo fission before reaching the detector. Figure 5.6 shows a collection of MIKE spectra showing diminishing coulomb fission profiles approaching the critical size.

This value of the critical size $n_{crit}(3)$=116 is smaller than previous assignments of 121 [9]. The variance in these observations can possibly be explained as due to the differences in experimental set-up. A time-of-flight mass spectrometer was used in the previous work which does not have the same resolving power to that of the current experimental set up (maximum $\frac{m}{\Delta m} = 125\,000$) thus peaks corresponding to clusters below a size of n=121 may have been unidentifiable. Additionally, a time of flight mass spectrometer is not able to perform the mass selection necessary for corroborating MIKE spectra.

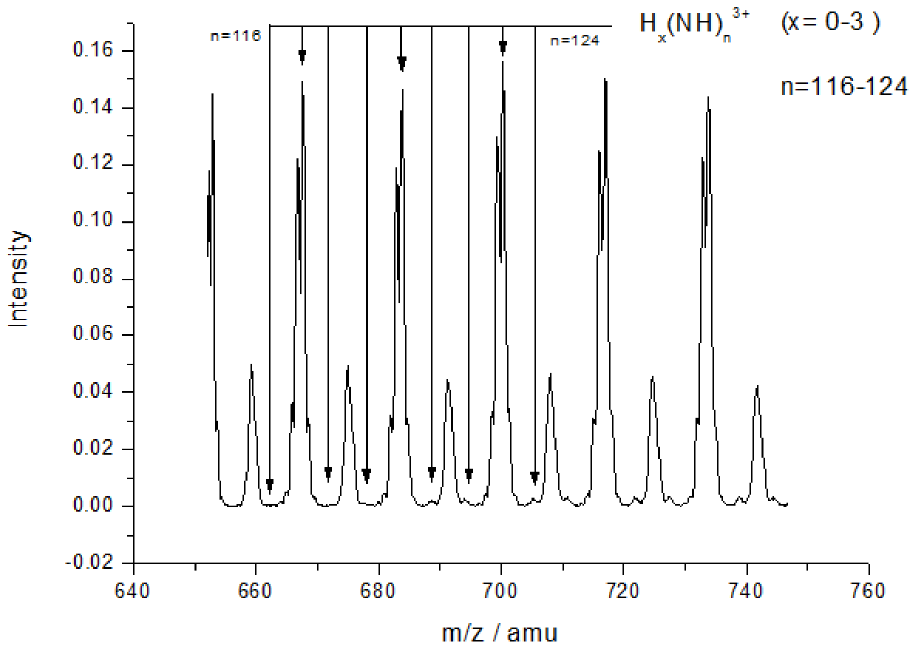

Figure 5.5: A mass spectrum showing the onset of triply charged ammonia clusters of the form $H_x(NH_3)_n^{3+}$

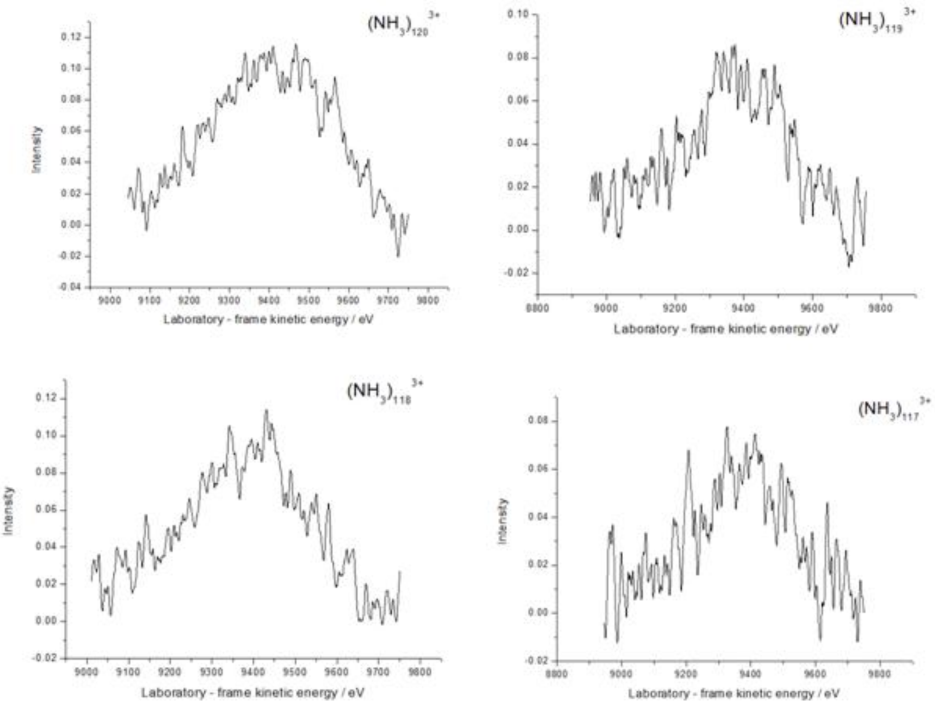

Figure 5.6: MIKE spectra showing the characteristic profile from the coulomb fission of triply charged ammonia clusters down to n=117

Figure 5.5 shows slight branching of the singly charged peaks in the mass spectrum, with two sub peaks 1 amu apart. These peaks are from the protonated forms of the cluster produced by ion-molecule protonation Reaction 1. These reactions have been studied in triply charged ammonia clusters by Garvey *et al.* [4], in the experiments, performed under significantly higher resolution than the example shown, additional peaks are found [4]. Reaction 1 can occur at any charge state, so in the case of a triply charged cluster there is the ability for un-protonated, protonated, doubly protonated and triply protonated precursor species to form. These peaks are separated by 1/3 amu and when resolved, the intensities can give an indication of the relative number densities of the clusters at the detector. Figure 5.7 shows a region of the mass spectrum populated solely with triply charged ions, $M_r/_Z = 17/3$ amu from the main cluster peaks. Shown in the figure 5.7 is a schematic of the three successive ion-molecule reactions and the contribution of each to the 3+ feature of the mass spectrum. It is notable that the precursor peak is significantly smaller in magnitude that the 1st protonated peak which is not seen in singly or doubly charged ammonia clusters. This observation has been attributed to the decrease in distance between the charge centres within the cluster which can be balanced in pure energetic terms by the additional solvation of NH_4^+ over NH_3^+ by neutral ammonia molecules [4, 10], hence favouring the formation of the protonated species.

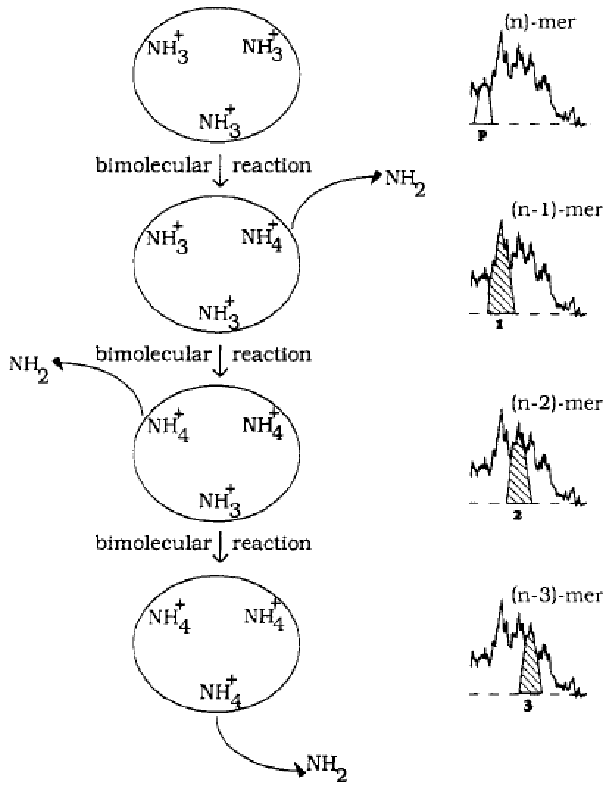

Figure 5.7: Diagram showing the origin of the protonated cluster peaks in the mass spectrum. Taken from [4]

As is seen by the difference in resolution in the 3+ peaks in figures 5.5 and 5.7 the protonated forms are not being individually resolved by our experimental set-up, even in relatively high resolving conditions. As mentioned previously reduction in resolving power is required to achieve the required ion count for detection, consequently, the magnetic sector is not able to select individual ion species 1/3 amu apart for investigation. Therefore, it is assumed that the resultant fission signals have contributions from all protonated forms of the precursor cluster, the relative numbers of which entering the 2nd *ffr* are assumed to be proportional to the heights of the peaks in the mass spectrum. This could potentially produce broadening of the features in the MIKE spectrum due to the proximity in energy of the four potential precursor types fragmenting into the four potential fragment types. Taking the most intense precursor ion in the mass spectrum at n=122: $(NH_3)_{121-1}(NH_4)^{3+}$, losing approximately 10% of its mass after fission to produce the two protonated forms of doubly charged fragment: $(NH_3)_{121-k-1}(NH_4)^{2+}$ and $(NH_3)_{121-k-2}.(NH_4)_2{}^{2+}$. These ions will cover a range of 10 eV in laboratory frame kinetic energy in the MIKE spectrum, thus making both peaks un-resolvable in the MIKE spectrum. Far more likely is that both will appear as part of one broad feature. Figure 5.8 shows the resulting MIKE scan of the $(NH_3)_{122}{}^{3+}$ precursor, in which there would appear to be four faintly resolved features. To illustrate the previous point, in figure 5.9 the MIKE scan is overlaid with predicted energies of the most abundant, singly protonated precursor undergoing fission for the three high energy pathways. The doubly charged ion that is detected can take one of three potential forms. It can either be un-protonated, singly, or doubly protonated. The lines on the spectrum indicate the energies at which the fragments will be detected. The dashed lines indicate the energy which the unprotonated precursor cluster fragments into an un-protonated doubly charged fragment.

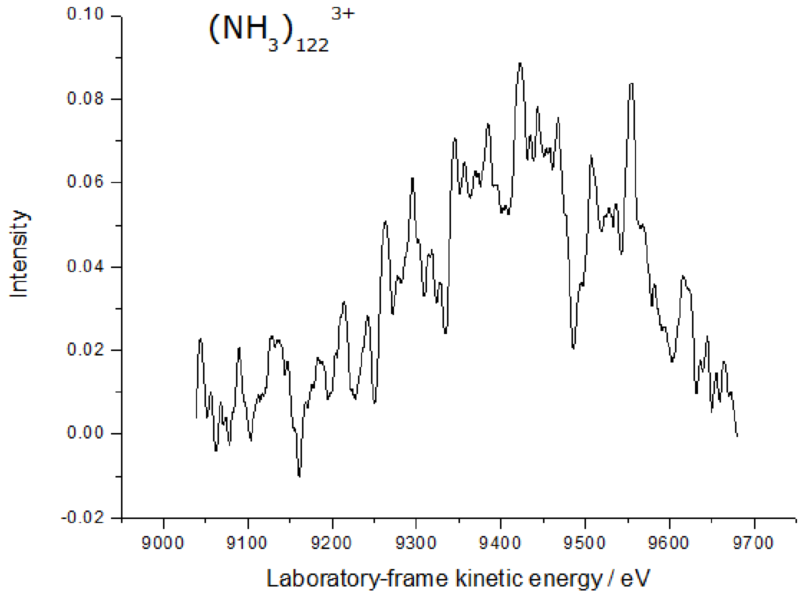

Figure 5.8: MIKE spectrum of $(NH_3)_{122}^{3+}$ ions

$$(NH_4)(NH_3)_{121}^{3+} \longrightarrow (NH_3)_{122-k}^{2+} + (NH_3)_{k-1}(NH_4)^{+}$$

$$\longrightarrow (NH_3)_{122-k-1}(NH_4)^{2+} + (NH_3)_{k}^{+}$$

$$\longrightarrow (NH_3)_{122-k-2}(NH_4)_2^{2+} + (NH_3)_{k-2}(N_2H_5)^{+} + (NH_3)_{k-1}(NH_2)^{+}$$

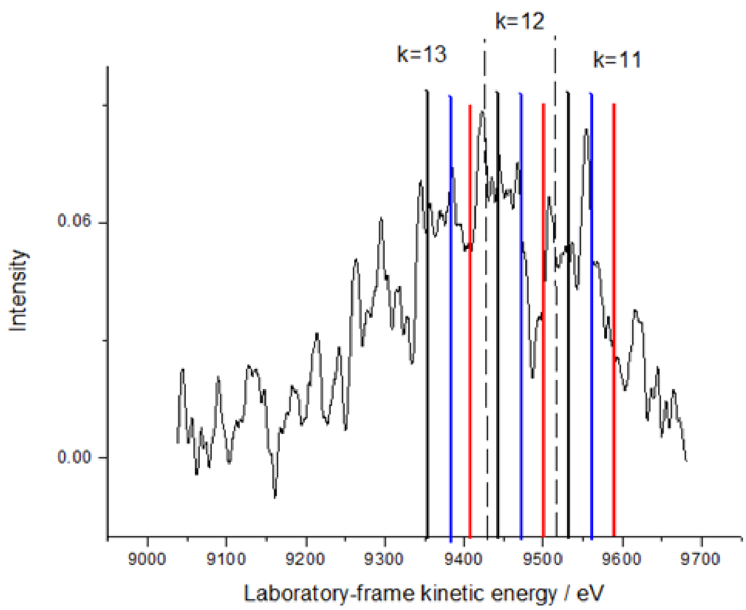

Figure 5.9: MIKE scan of $(NH_3)_{122}^{3+}$ overlain with he predicted energies of E_f for the possible fragments from the protonated precursor cluster

Figure 5.9 shows that it is possible that each feature may be comprised of more than one possible fission reaction. The resulting fragments are close together in energy. Only peaks resulting from the singly protonated form have been considered in figure 5.9, there will likely be a contribution to the fission profile occurring from the less abundant protonated forms of the triply charged precursor. Additionally, there is expected to be overlap from peaks from neighbouring channels (i.e. different value of k). These factors all contribute to the poor resolution of the individual features.

In terms of the energetics of the processes observed, the differences in the ammonia forms can be considered to be negligible. The increase in radius from the addition of 3 hydrogen atoms is minute, so too is any difference in how the charge is accommodated in the cluster. Therefore, the magnitudes of U_{max} will not vary significantly. The increase in mass is again negligible, therefore, in the simulation of the MIKE peaks no significant reduction divergence will be experienced by fragments containing additional protons and no differences are expected in the lifetimes of the pathways concerned. Therefore, analysis of the energetics of the process and assignments of simulated peaks will be done on the un-protonated forms of precursor and fragment ions only. Figure 5.10 shows the simulated peaks overlain on the MIKE spectrum and table 5.2 gives the calculated barrier heights for each channel and the average kinetic energy release associated with each fitted simulated peak. The agreement of the simulated peaks to the experimental data is not as close as in previous cases, probably due to the resolution of the peaks in the MIKE spectrum, making the fitting of the simulated peaks difficult. The simulated peaks possess a value for $<KER>$ that is smaller than the barrier heights by around 0.25 eV.

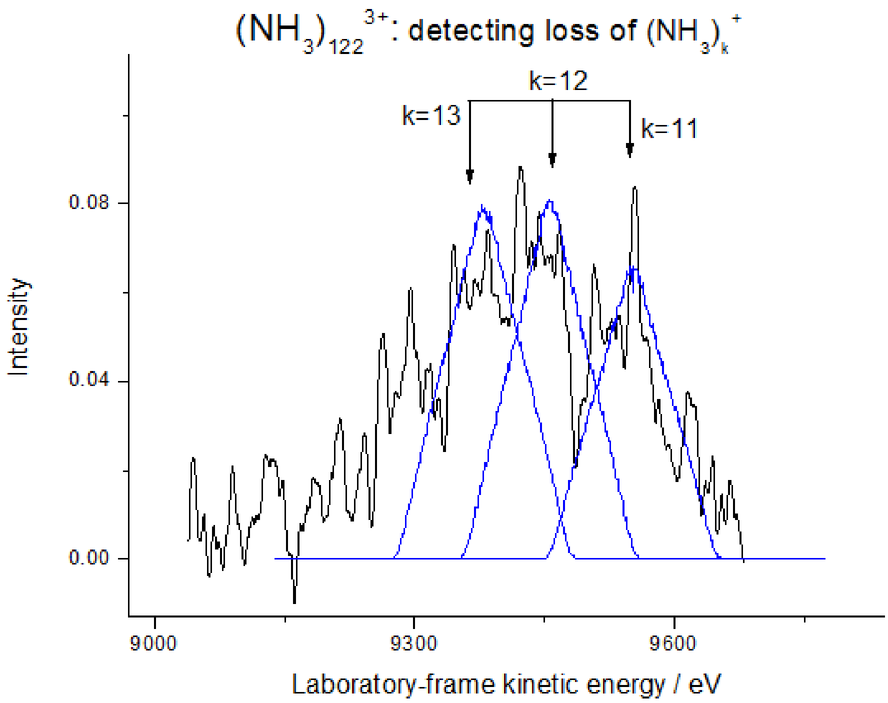

Figure 5.10: MIKE spectrum of $(NH_3)_{122}^{3+}$ overlain with the simulated peaks

Precursor Cluster	Fragment channel	$< KER >$/ eV	U_{max}/ eV
$(NH_3)_{122}^{3+}$	k=11	1.38	1.62
	k=12	1.38	1.62
	k=13	1.38	1.62

Table 5.2: The values for U_{max} and <*KER*> for the channels highlighted in figure 5.10

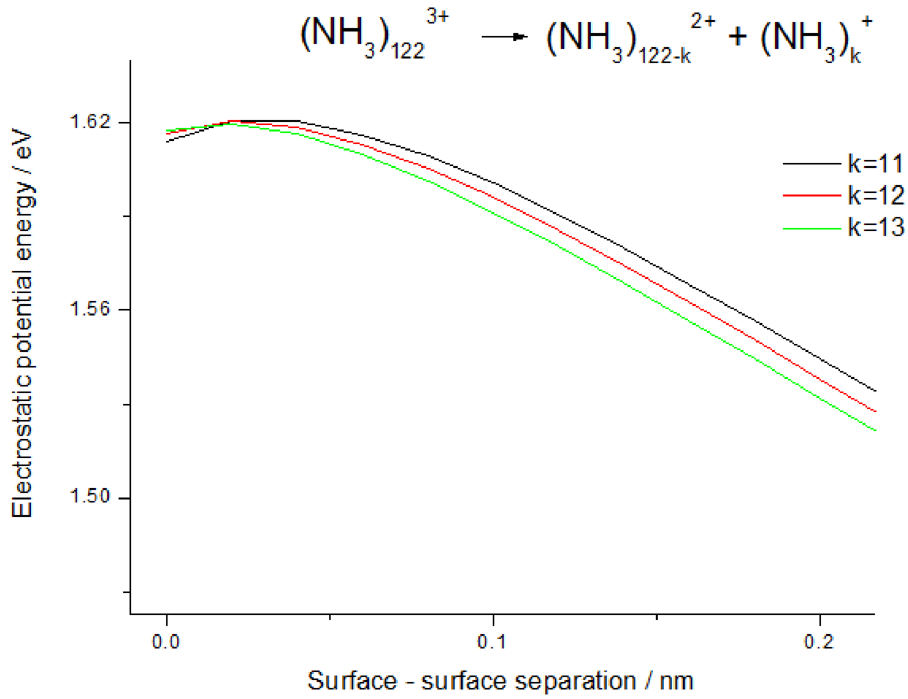

Figure 5.11: The potential energy curves calculated for the three fragmentation pathways observed in the MIKE spectrum (figure 5.10)

Figure 5.11 shows the electrostatic potential energy curves at short surface-surface separations calculated by the dielectric particle model. There is a degree of attenuation of the repulsive force between the two fragments, this is seen by the slight short range barrier of the k=11 pathway. However, unlike the calculated curves for the fragments following dication fission, there is no observed reduction in the value of U_{max} with increased asymmetry. There is a cross over at approximately 0.2 nm where increasing asymmetry between the fragments produces a greater potential energy. This is due to the reduced influence the short range attractive forces have on the value of the potential energy, which is now dominated by the long range repulsive electrostatic interactions. The increase in charge density on the smaller fragment and consequent increase in the effectiveness of the electrostatic repulsion is what causes this to occur.

5.4. Fourfold Charged Ammonia Clusters

The identification of fourfold charged ammonia clusters using mass spectral techniques presented earlier is not achievable. A combination of the narrow mass band between peaks brought about by the small M_r of ammonia and the expected reduction in mass resolution with increasing mass means that the individual 4+ peaks remained un-resolved. Indeed further increases of charge state and cluster size mean that none of the higher order systems presented in subsequent sections show discrete peaks in a mass spectrum. The identification of $n_{crit}(4)$ for the ammonia system has been achieved by the observation of a reduction and eventual loss of a characteristic coulomb fission signal originating from the charged fragments as the cluster size decreases. Figure 5.12 shows the strong broad signal that is observed when performing a MIKE scan for the fission of $(NH_3)_{208}^{4+}$ precursor ions. This is achieved by 'sitting' on the coincident $(NH_3)_{52}^{+}$ peak in the mass spectrum. This singularly charged cluster is easily identified due to the high signal intensities of the series of singularly charged peaks in the mass spectrum. From there a reduction in size by two molecules was tested by sitting on the intense $(NH_3)_{103}^{2+}$ peak, coincident with $(NH_3)_{206}^{4+}$ precursor of interest. The resultant signal is diminished with respect to the $(NH_3)_{208}^{4+}$ peak indicating proximity to the critical size. Further mass selection is completed by reducing the m/z ratio by increments equal to $M_r/4$; hence, producing MIKE spectra for decreasing single monomer increments. The critical size is identified as $(NH_3)_{205}^{4+}$, as it is the smallest size showing a characteristic signal in the MIKE spectrum. Figure 5.13 shows an overlay of all the signals in the MIKE spectra in the range n = 205-208 and the signal from what would be n = 204 but falls below the critical size, and thus, shows no apparent signal.

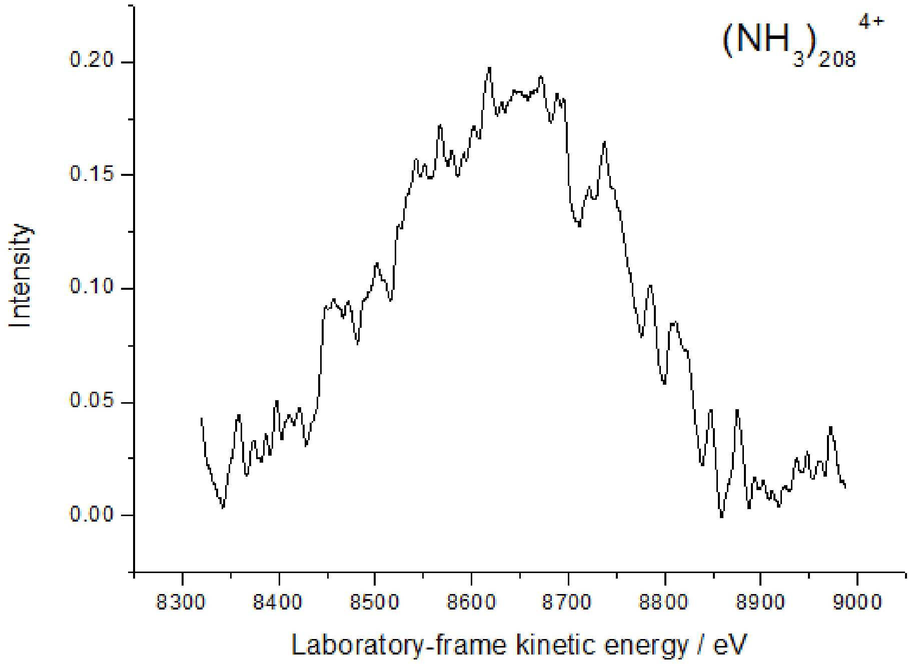

Figure 5.12: MIKE spectrum showing the signal from coulomb of $(NH_3)_{208}^{4+}$ ions

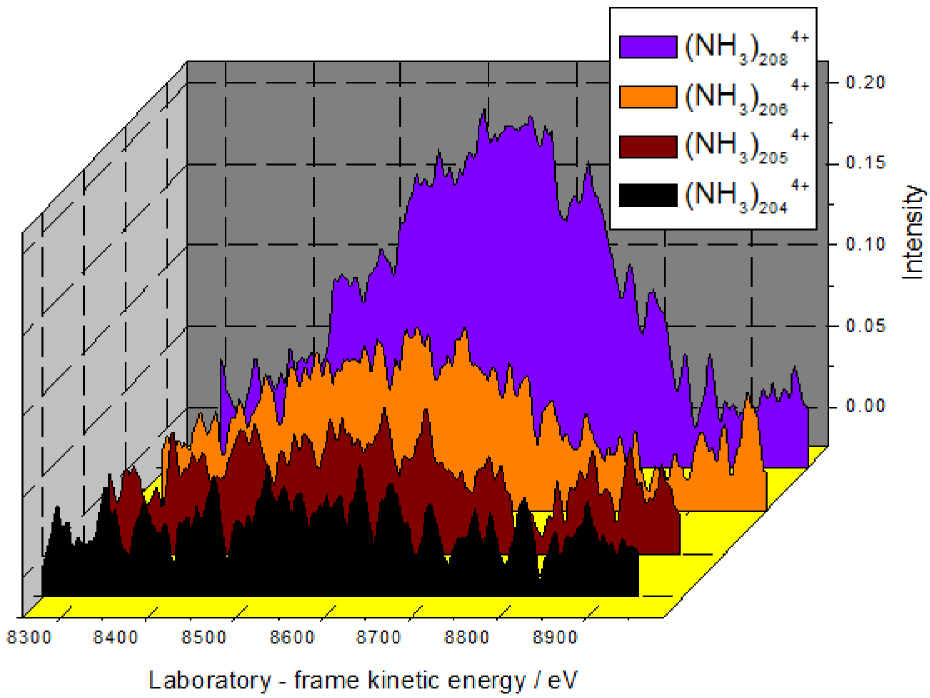

Figure 5.13: A plot of the characteristic signal about 8600 eV in the MIKE spectra for clusters approaching the critical size. $(NH_3)_{205}^{4+}$ is assigned as the critical size

The same general MIKE profile is observed for all precursor clusters from n=206 upwards. It is assumed that a number of fission pathways will be accessible due to the multitude of potential precursor forms for a fourfold charged precursor. In relation to the protonation reaction, an ammonia cluster with 4 charge centres is predicted to be able to form 4 protonated forms of the cluster alongside the unprotonated form and will all be able to undergo distinct coulomb fission fragmentations. However, it is worth noting with reference to figure 5.7 that beyond single protonation, further protonated forms are seen to be diminished, demonstrated by the relative heights of the mass spectral peaks. It is assumed that in charge states beyond $z = 3$ this trend will continue and therefore the number of fourfold-charged, fourfold-protonated ammonia clusters will be considerably diminished relative to the other forms of the cluster. As will the relative number of un-protonated precursors due to the increased solvation of the charge from protonation NH_4^+ [8]. The multitude of fragmentations causes a broadening of the spectral features, and can in part explain why only a single feature is resolved.

As noted in previous chapters, the charge state of the larger detected from fission of a fourfold charged precursor can be either 3+ or 2+ charged. Consideration will be given to both possibilities. Using equation 2.10 and the methodology set out in section 3.4, 3+ charged fragments are simulated in the range of k=12-21 that encompass the energy range of the MIKE signal produced for the fission of $(NH_3)_{210}^{4+}$ cluster ions, this is shown in figure 5.14. As can be seen the width of the feature can be adequately reproduced with 10 simulated peaks. Table 5.3 gives the energetic information for each pathway and good agreement is seen in the values for U_{max} and $< KER >$. It is noted that the 'jagged' shaped to the top of the feature could be caused by the partial resolution of the tips of the 3+ peaks. These observations, however, are at odds with other measurements on 4+ clusters presented in other chapters of this work which typically show a difference of two molecules between separate peaks from fragments that are 3+ charged. It may be due to the spherical geometry of the large ammonia cluster that single molecules are more able to be accommodated between the two fragments, rather than pairing up.

To consider the alternative fragmentation mechanism, Z_f=2, use of Equation 2.10 reveals that the centre of the feature corresponds to loss of a doubly charged cluster fragment containing 80 molecules. Simulation of this pathway with guidance from the value of U_{max} (2.51 eV) reveals a strongly dish-shaped peak that almost satisfies the full width of the experimental feature. To account for the whole shape of the peak it is worth considering the possibility that more than one fragmentation pathway is being detected. By changing the size of the fragment it is possible to reproduce the entire shape of the peak with four pathways, these are shown in figure 5.15. The difference between the dishing seen in the simulated peaks and those observed in the experimental data are attributed to several factors. It is assumed that the final detected cluster fragment retains a degree of energy post coulomb fission, from both the electrostatic repulsion of the charge centres and residual excess energy that is partitioned into internal modes during the ionisation step. This energy can drive the evaporation of neutral molecules and the *KER* associated with this process is much smaller than the ~2.5 eV predicted following coulomb fission. Therefore, the resultant peaks do not show the dishing that is characteristic of the experimental discrimination of strongly divergent ions. As previously, the fragmentation profile is expected to be composed from fragments of various protonated states, originating from up to five forms of the precursor. These fragments will have discrete peaks in the MIKE spectrum very close together in laboratory-frame kinetic energy. However, due to limitations in the energy resolution of the MIKE scanning technique, individual components cannot be resolved.

In the case of fourfold charged molecular clusters it has been found that the 2+ fragment is not observed and the profile shape can be reproduced adequately with peaks from the 3+/+ fission mechanism. Due to the poor peak resolution in Figure 5.14 and 5.15 it is difficult to assign a definite mechanism to the feature, and therefore impossible to rule out a contribution from both mechanisms to the overall profile.

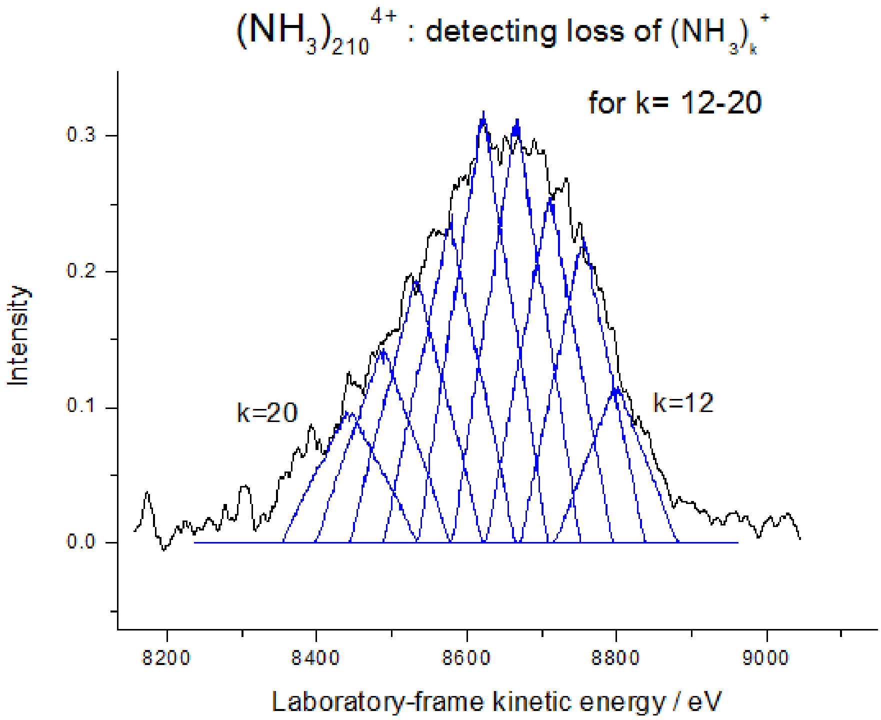

Figure 5.14: MIKE spectrum for the fission of $(NH_3)_{210}^{4+}$ ions overlain with the simulated peaks for the pathway producing 3+ and 1+ charged cluster fragments

Precursor cluster	Fragment channel	$< KER >$/eV	U_{max} / eV
$(NH_3)_{210}^{4+}$	k=12$^+$	2.16	2.15
	k=13$^+$	2.16	2.15
	k=14$^+$	2.16	2.15
	k=15$^+$	2.16	2.15
	k=16$^+$	2.16	2.14
	k=17$^+$	2.16	2.14
	k=18$^+$	2.16	2.13
	k=19$^+$	2.16	2.13
	k=20$^+$	2.16	2.12

Table 5.3: The values for U_{max} and $< KER >$ for the channels highlighted in figure 5.14

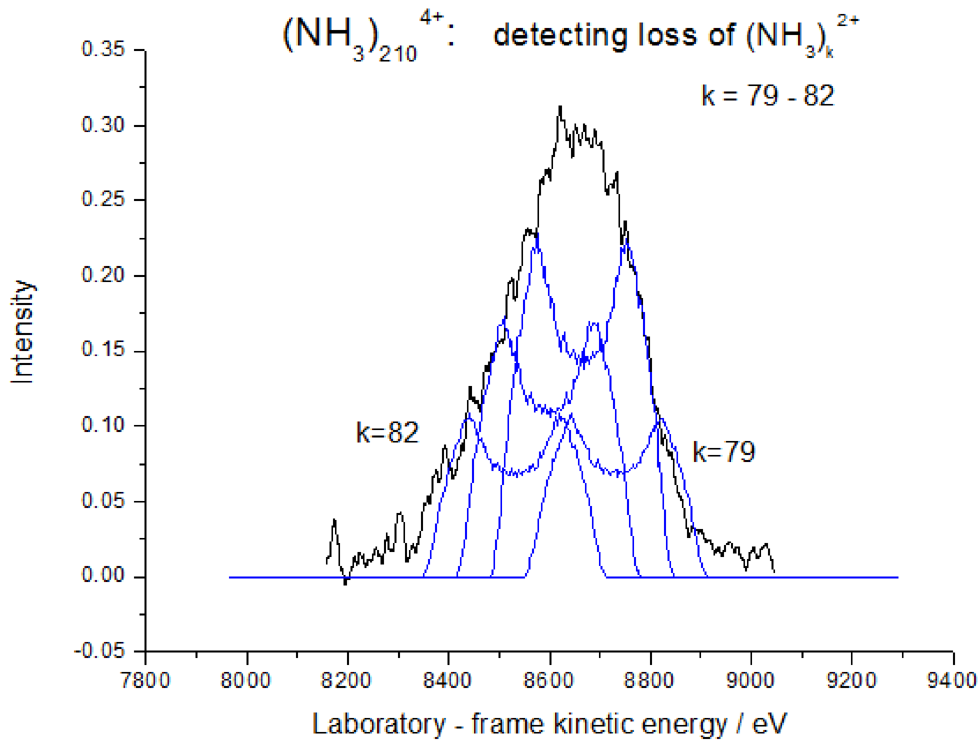

Figure 5.15: MIKE spectrum for the fission of $(NH_3)_{210}^{4+}$ ions overlain with the simulated peaks for the pathway producing 2+ and 2+ charged cluster fragments

Precursor cluster	Fragment channel	$< KER >$ /eV	U_{max} /eV
$(NH_3)_{210}^{4+}$	$k=79^{2+}$	2.47	2.51
	$k=80^{2+}$	2.47	2.51
	$k=81^{2+}$	2.47	2.52
	$k=82^{2+}$	2.47	2.52

Table 5.4: The values for U_{max} and $< KER >$ for the channels highlighted in figure 5.15

Figure 5.16 shows the electrostatic energy curve calculated by the dielectric particle model for the fragmentation pathways shown in figure 5.14. In the case of high asymmetry, especially k=12, the solution shows a moderate attractive attenuation of the electrostatic repulsion. The fact that it requires 94% mass asymmetry in the 3+/1+ system to achieve this is due to the dominating effect of the electrostatic repulsion of the four charge centres over the induced potentials attenuating the electrostatic potential energy.

Figure 5.17 shows the potential energy curve for the 2+/2+ fission mechanism. It can be seen that the values of U_{max} are typically 0.4 eV larger than the more asymmetric mechanism. This can be seen as an effect of the general reduction in the ability of the smaller of the two fragments to polarise the larger and attenuate the electrostatic repulsion. However, the solution shows a reversal in the trend in U_{max}, the value decreases with asymmetry. This indicates that some polarisation is occurring.

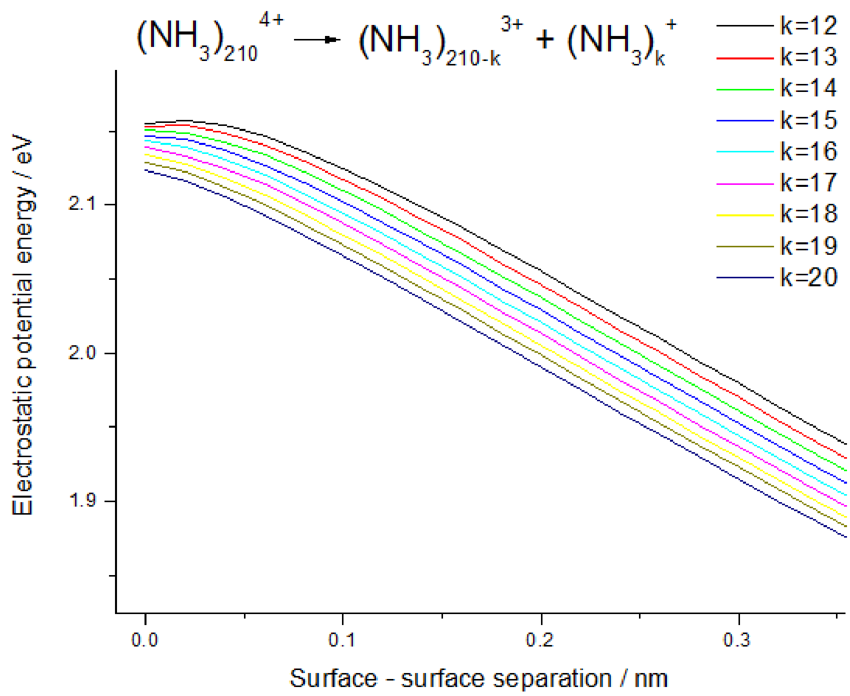

Figure 5.16: Solution to the dielectric particle model for the fragmentation pathways shown in figure 5.14

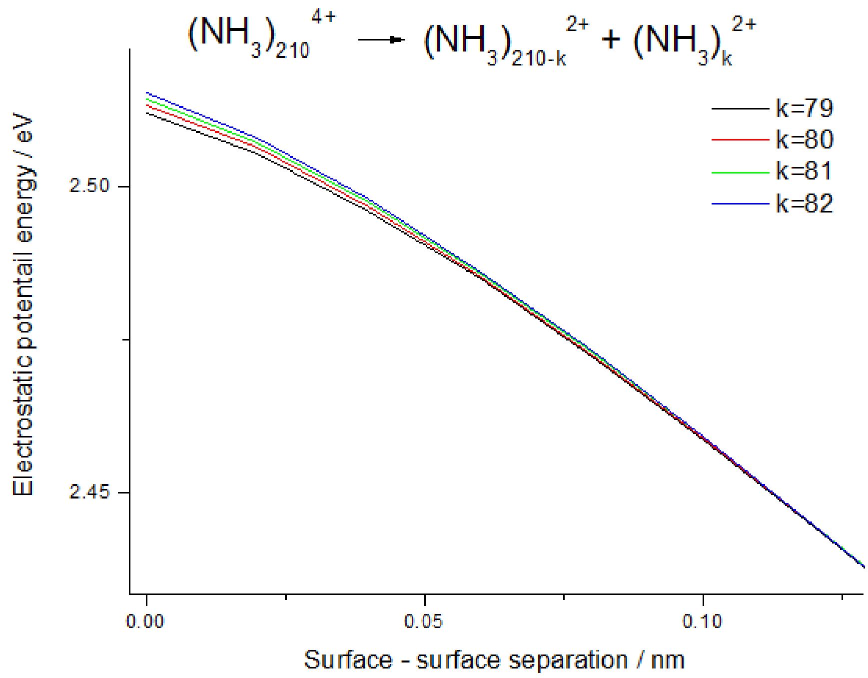

Figure 5.17: Solution to the dielectric particle model for the fragmentation pathways shown in figure 5.15

The upper limit to instability of multiply charged precursor clusters can be determined by performing similar experiments and hence determining the size of cluster required to stabilise the cluster against coulomb fission occurring in the timescale of the experiment, termed the stable size (n_{stab} (4)). The MIKE scanning technique was used to monitor the diminishing intensity of the fission signal as the cluster size increases and the stable size is approached and then met. Figure 5.18 shows an overlay of MIKE spectra which demonstrates that beyond the precursor $(NH_3)_{226}^{4+}$ the signal strength becomes increasingly weak, with the stable size being assigned as $(NH_3)_{234}^{4+}$ where no remnants of the fission profile remain. For comparison, the fission profile from the $(NH_3)_{210}^{4+}$ precursor ion is included in the overlay.

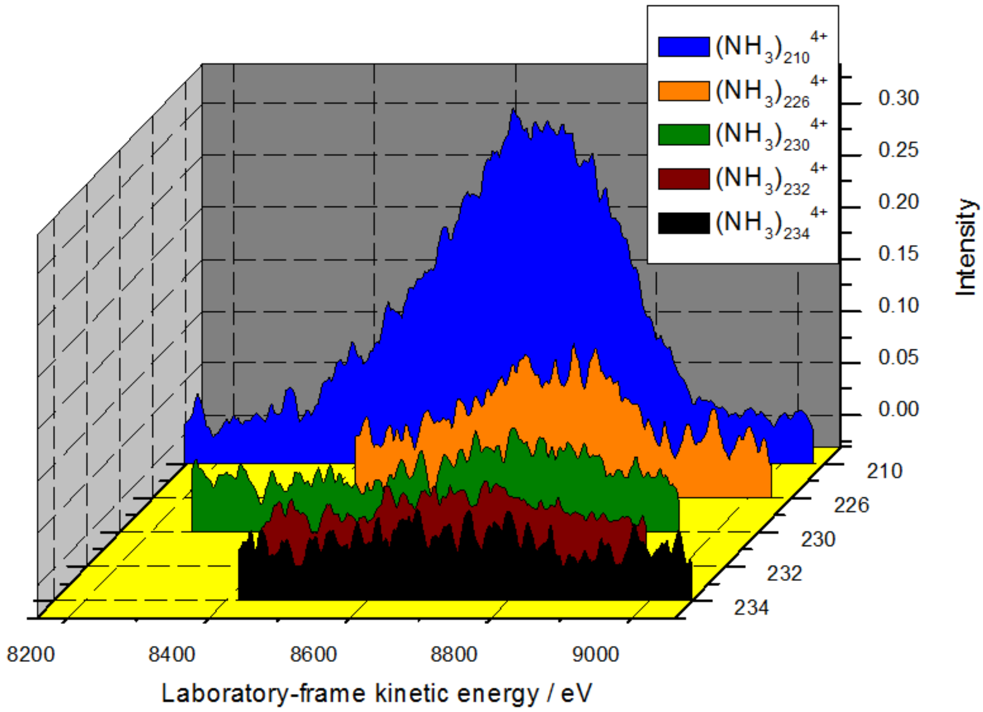

Figure 5.18: A plot showing the deterioration of the characteristic signal intensity as the precursor cluster approaches the stable size $n_{stab}(4)$

5.5. Fivefold Charged Ammonia Clusters

Fivefold charged ammonia clusters are observed above a critical size of $n_{crit}(5) = 302$. Figure 5.19 shows an overlay of MIKE spectra showing a gradual onset of a characteristic fission profile beyond n=320 at laboratory-frame kinetic energy centred around 8700 eV. The reason for such a gradual onset is likely dictated by a small barrier to fission for the smaller clusters, which in turn dictates a short lifetime. This can result in the majority of the clusters undergoing fission before the 2nd *ffr*. To reach a size where the profile intensity is large enough for analysis to be performed, one has to go to the $(NH_3)_{385}^{5+}$ precursor, the MIKE spectrum of which is shown in figure 5.20.

Charge can be partitioned in two ways in the resulting fragments: 4+/1+ and 3+/2+ with the larger of the two fragments retaining the majority of the charge. Using equation 2.10 we can immediately rule out the first possibility, as at charge state $Z_f = 4$, the fragment corresponding to the peak maximum of 9400 eV would contain more molecules than the precursor cluster. The possibility of a cluster capturing additional molecules from collisions with the background gas is remote as the operating pressure is kept at below approximately 10^{-7} mbar. Consideration will therefore only be given to the formation of 3+ and 2+ fragments.

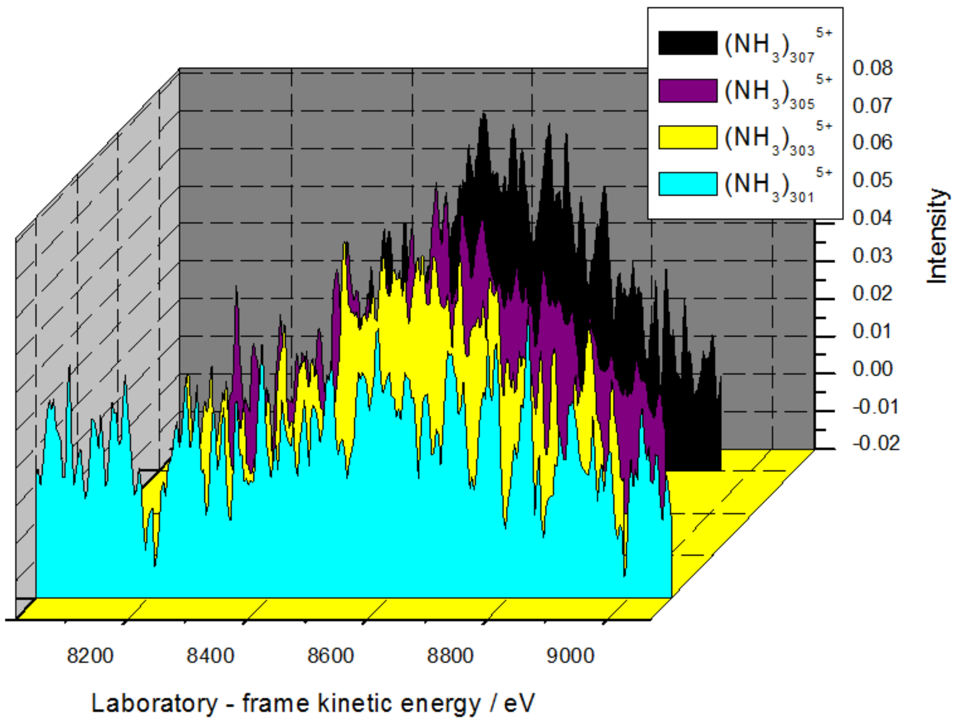

Figure 5.19: An overlay showing the onset of the characteristic coulomb fission profile around 8500 eV above a critical size of $n_{crit} = 302$

The MIKE profile for the fission of the $(NH_3)_{385}^{5+}$ precursor is shown in figure 5.20. The base of the feature is approximately 700 eV wide, therefore, it is reasonable to suggest that the profile is comprised of more than one fragment peak. Figure 5.21 shows how the complete profile can be made up of nine 3+ fragment peaks. As before, a combination of large values of *KER* and the mass of the detected fragment ion combine to produce peaks that are predicted to be strongly dish-shaped. However, there is little evidence of dishing of the peaks seen in the experimental data. This is in part because the individual peaks are un-resolved and also because of the potential in an excited multiply charged cluster to increase achieve an increase in stability by the evaporation of neutral monomers. This, as previously explained, leaves the resultant peak 'filled in'. As seen, the magnitudes of U_{max} do not vary to 2 d.p over the pathways shown. It could be that relative to the fragment size, a change of 9 molecules is not enough to effect a change in the charge density of the fragments, and therefore, the magnitude of the component interactions between the fragments.

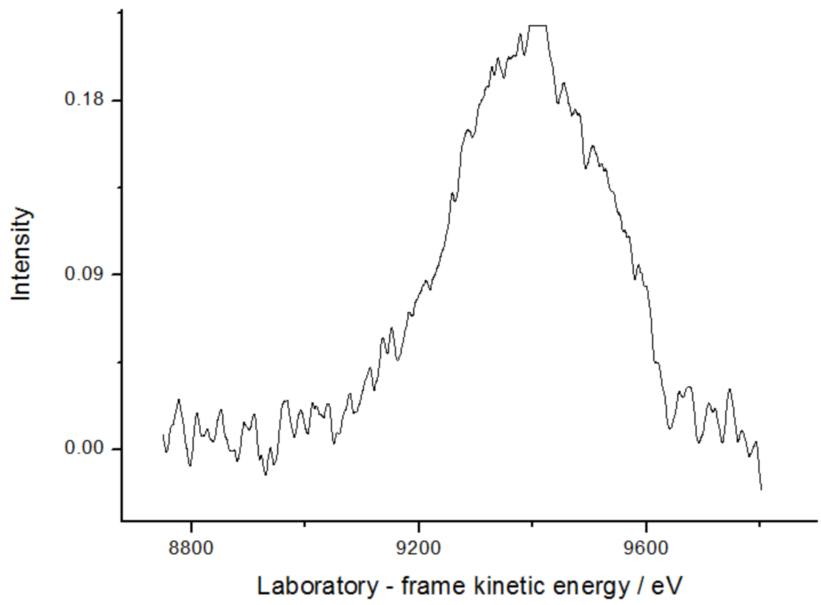

Figure 5.20: MIKE spectrum showing coulomb fission in $(NH_3)_{385}{}^{5+}$ ions

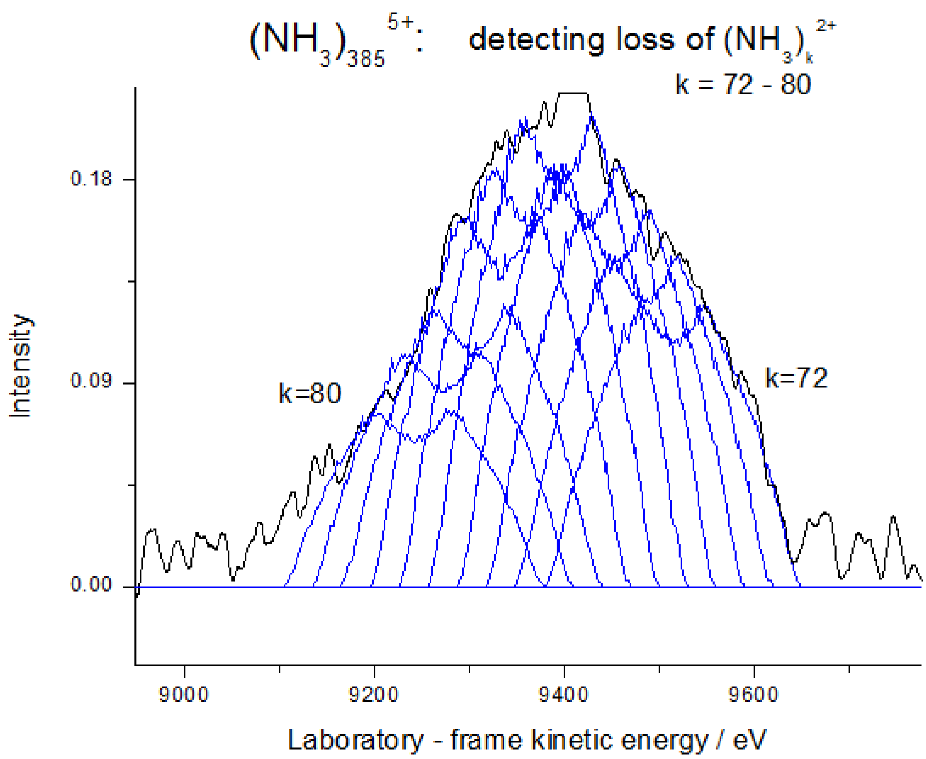

Figure 5.21: Simulated peaks of the fission pathways labelled for the precursor $(NH_3)_{385}{}^{5+}$.

Precursor cluster	Fragment channel	$< KER >$/eV	U_{max} / eV
$(NH_3)_{385}^{5+}$	$k=72^{2+}$	2.97	3.18
	$k=73^{2+}$	2.97	3.18
	$k=74^{2+}$	2.97	3.18
	$k=75^{2+}$	2.97	3.18
	$k=76^{2+}$	2.97	3.18
	$k=77^{2+}$	2.97	3.18
	$k=78^{2+}$	2.97	3.18
	$k=79^{2+}$	2.97	3.18
	$k=80^{2+}$	2.97	3.18

Table 5.5: $< KER >$ and U_{max} values for the fragments that make up the peak in figure 5.21

5.6. Sixfold Charged Ammonia Clusters

There is an overlap in the m/z range above $n_{crit}(5)$ in which both six and fivefold charged ammonia clusters exist. This is due to the large critical range seen for five–fold charged ammonia clusters undergoing fission (83 molecules). Fortuitously, the characteristic MIKE profiles for fragments originating from 6+ and 5+ precursors are observed at different energy ranges and are therefore separately resolvable. The shifting intensities of the two signals can be observed by performing MIKE scans on a range of m/z signals in a mass spectrum that comprise mainly singularly charged ions, but will contain a component from both five and sixfold charged ammonia clusters. Figure 5.22 gives an overlay of the MIKE spectra that have been used to identify the values of $n_{crit}(6)$ and $n_{stab}(5)$. The stable size for the corresponding lower order precursors components is exceeded and so one can rule out contributions from these to the fission profiles. The fission profile for the $(NH_3)_{385}^{5+}$ precursor ion is filled in black and is presented at the back of the overlay. As the precursor size increases in Figure 5.22 there is a noticeable diminishing of the characteristic signal 5+ at around 9500 eV until a size of n =410 is reached. From there onwards there is no detectable signal originating from the 5+ component, hence an assignment of $n_{stab}(5) = 410$ is made. The onset of a fission profile from 6+ precursor ions is observed above a critical size of $n_{crit}(6) = 468$. A characteristic profile at around E_f= 8600 eV is seen to grow with increasing size of precursor cluster until at $(NH_3)_{492}^{6+}$ where profile becomes similar in magnitude and shape to $(NH_3)_{385}^{5+}$.

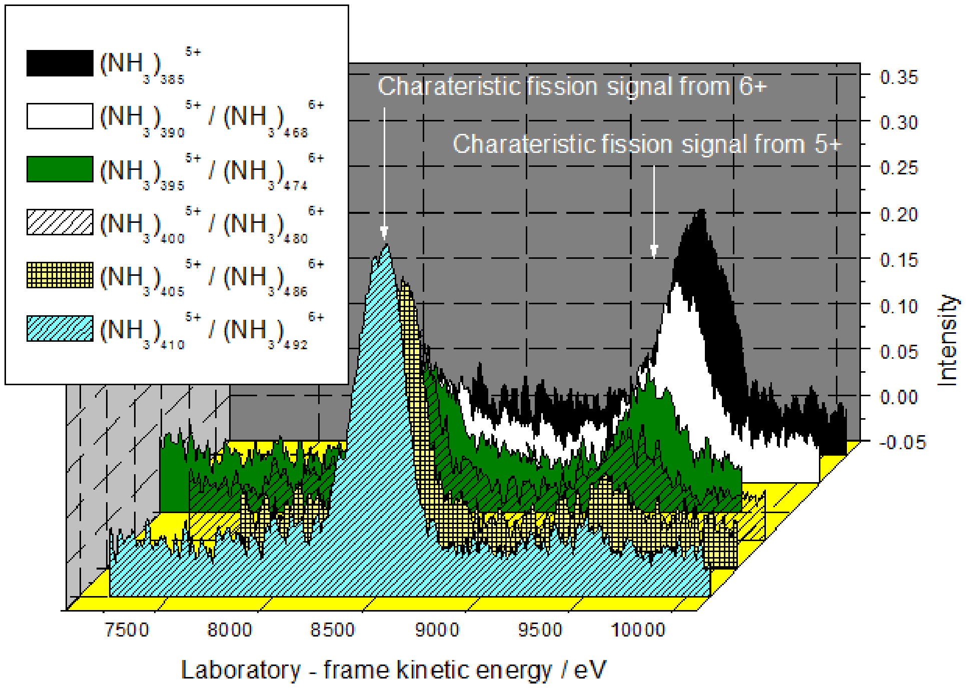

Figure 5.22: An overlay of MIKE spectra showing the simultaneous onset of 6+ clusters beyond $n_{crit} = 468$ and the progression towards the stable size of 5+ clusters at $n_{stab} = 410$

For this charge state the large fragment ion from fission of a $(NH_3)_n^{6+}$ ion potentially can be any of $Z_f = 5, 4, 3+$. As before, the location of E_f on the MIKE spectrum will inform us of which charge states are possible. Taking the centre of the fission profile for $(NH_3)_{492}^{6+}$ and using eq. 2.10 with a value $Z_f = 5$ and 8520 eV will correspond to the fragment $(NH_3)_{499}^{5+}$ that is larger than the precursor. Therefore, the fission into 5+/+ fragments is ruled out as being detected in these experiments. Considering the remaining two possible mechanisms of coulomb fission, the identities of the fragment at 8520 eV for charge states $Z_f = 4, 3$ are considered (see Figures 5.23 and 5.24) and the values for U_{max} are given in table 5.6.

Fragment charge state Z_f	Fragment at 8520 eV	U_{max}/ eV
4+	$(NH_3)_{399}^{4+}$ + $(NH_3)_{93}^{2+}$	4.10
3+	$(NH_3)_{300}^{3+}$ + $(NH_3)_{192}^{3+}$	4.26

Table 5.6: The identity of the fragment detected at 8520 eV and the value of the barrier height from the separation of the two fragments for charge states $Z_f = 4, 3$

As might be expected the lower charge density in the smaller fragment of the $Z_f = 3$ mechanism the maximum potential energy is larger due to reduced attenuation of the long range electrostatic potentials that is brought about from polarisation. This is brought about by the reduction of asymmetry in the charge density between the two fragments. The $(NH_3)_{300}^{3+}$ fragment is a similar mass to those fragments seen in the fission of 5+ ammonia clusters (Figure 5.21 and Table 5.5) but with a larger *KER* predicted from the magnitude of the barrier U_{max}. Therefore, a wide dish shaped peak typical of large divergence is expected. Figure 5.23 shows the simulated peak overlaid on the MIKE spectra for $(NH_3)_{492}^{6+}$. A single fragmentation pathway following this fission mechanism is all that is required to fill the whole width of the experimental peak. This is an unusual observation, as every previous example a range of fragments is observed, the intensity of the associated peak an indication of how closely the lifetime matches the experimental constraints. The observation of an absence of dishing in the experimental peak implies that the potential $(NH_3)_{300}^{3+}$ fragment is formed in a multiple step process. Firstly, by coulomb fission to produce a cluster of size 300+x molecules, followed by neutral evaporation of x molecules to form the final fragment. The small *KER* following neutral evaporation results in in-filling of the peak. There is no obvious reason for $(NH_3)_{300}^{3+}$ to be the only detected fragment as the barrier heights for the two neighbouring fragments are comparable in magnitude. This implies that the lifetimes for these pathways are very similar (the energies for the barrier heights mentioned are given in Table 5.7). It is seen that the agreement in *KER* of the fitted peak and U_{max} for the pathway is not as close as for other cases.

To address the other type of fragmentation, when $Z_f = 4$ (4+/2+ mechanism), the fragmentation is much more asymmetric (see table 5.6). This leads to a smaller value of U_{max}. This predicts a smaller *KER* and therefore a narrower peak shape. This would be aided by the additional mass of the detected fragment relative to the alternative mechanism. Figure 5.24 shows the MIKE spectrum for $(NH_3)_{492}^{6+}$ overlaid with the simulated peaks where the width of the experimental profile is accounted for by the 10 simulated peaks. As before, the absence of any dishing in the final profile is attributed to the reasons set out in Section 5.4. It is seen from other sections in this work that there is an obvious preference for a range of fragments to be detected. This, as mentioned is due to the lifetimes for the range of fragmentation pathways matching the experimental constraints to differing degrees. Additionally, the agreement between the *KER* of the fitted peak and U_{max} is closer than for the single fitted peak simulated for the 3+/3+ mechanism. Therefore, based on these observations, it is concluded that the experimental profile is formed solely from fragmentation following the 4+/2+ fission mechanism.

Figure 5.25 shows the electrostatic potential energy curve following the fission of the $(NH_3)_{492}^{6+}$ ion into 4+/2+ fragments. The trend of the curves indicates that the electrostatic interaction is dominating. The added effectiveness of the repulsion from a smaller fragment is shown by the asymmetric pathways having the highest potential energy.

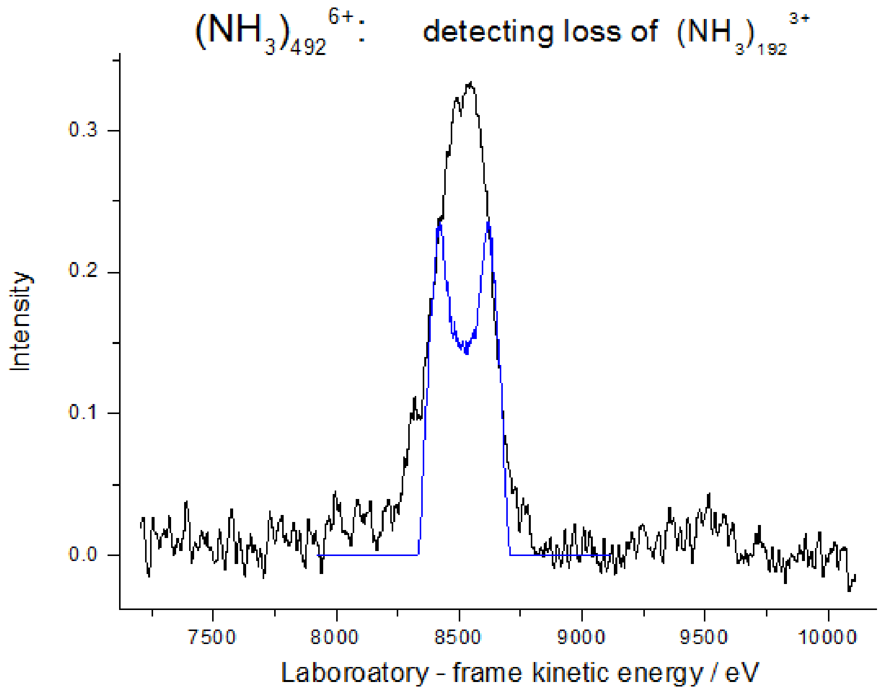

Figure 5.23: MIKE spectrum showing the coulomb fission of $(NH_3)_{492}^{6+}$ into the fragments shown overlain with the simulated peak for the process

Precursor cluster	Fragment channel	$< KER >$/eV	$\boldsymbol{U_{max}}$/ eV
$(NH_3)_{492}^{6+}$	k=192^{3+}	3.92	4.26
	'k=191^{3+}'	-	4.26
	'k=190^{3+}'	-	4.26

Table 5.7: Table showing the values of $< KER >$ and U_{max} for the pathway shown in figure 5.23. Additional values are given for imaginary neighbouring fragments which are very close in magnitude.

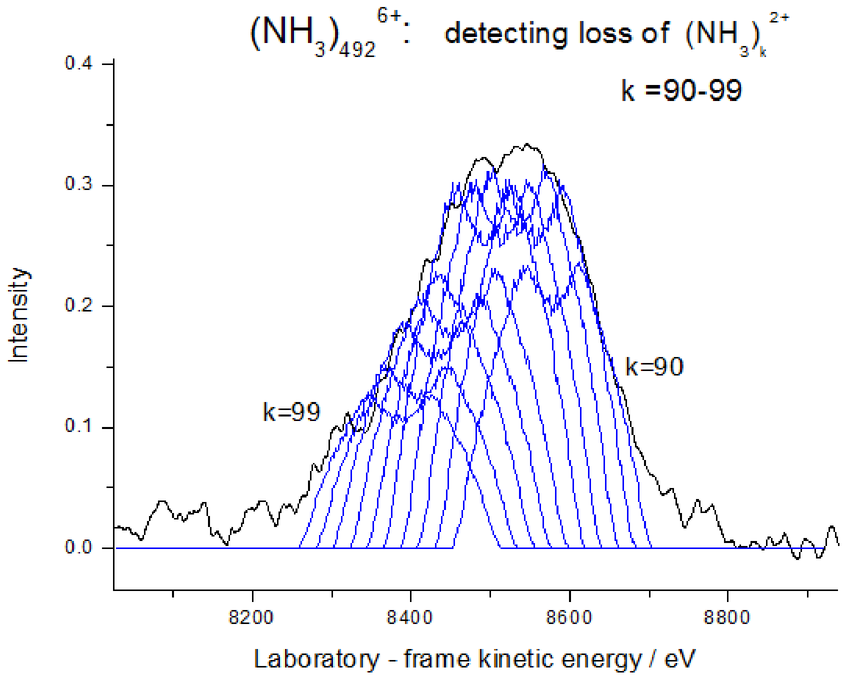

Figure 5.24: An expanded view of the MIKE spectrum showing the coulomb fission of $(NH_3)_{492}^{6+}$ into the fragments shown overlain with the simulated peaks for the pathways

Precursor cluster	Fragment channel	$< KER >$ /eV	$U_{\max}$ /eV
$(NH_3)_{492}^{6+}$	$k=90^{2+}$	3.92	4.02
	$k=91^{2+}$	3.92	4.02
	$k=92^{2+}$	3.92	4.02
	$k=93^{2+}$	3.92	4.02
	$k=94^{2+}$	3.92	4.01
	$k=95^{2+}$	3.92	4.01
	$k=96^{2+}$	3.92	4.01
	$k=97^{2+}$	3.92	4.01
	$k=98^{2+}$	3.92	4.01
	$k=99^{2+}$	3.92	4.00

Table 5.8: Table showing the values of $< KER >$ and U_{max} for the pathway shown in figure 5.24

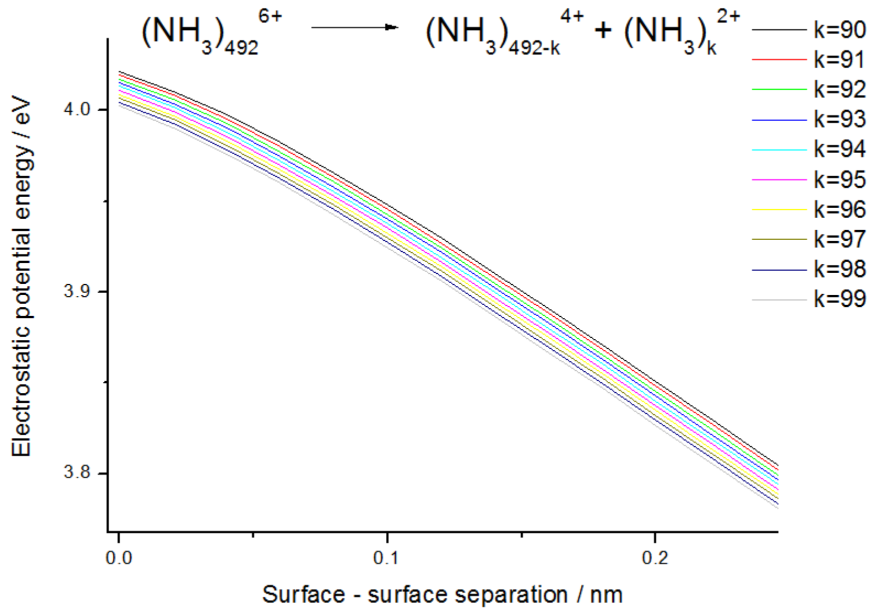

Figure 5.25: Solution to the dielectric particle model for the fragmentation pathways shown in figure 5.18

5.7 Sevenfold Charged Ammonia Clusters

The observation of fragmentation from sevenfold charged ammonia clusters is observed using the MIKE scanning technique. As before, intense singly charged precursor peaks in the mass spectrum were used for mass selection. These peaks will contain components from all charged species above the relevant critical size for the charge state. This leads to the observation of fragmentation from sixfold charged precursors in the same MIKE spectra as fragmentation from sevenfold charged precursors. This observation is similar to the preceding section and is attributed to the large critical range for six-fold charged ammonia clusters. However, the magnitude of the characteristic MIKE signal arising from coulomb fission is reduced in intensity. This may be explained by the increase in the total ionisation energy required to remove 7 electrons from ammonia (65 eV) which is converging on the limits of the electron energy of the ion source of the mass spectrometer (100 eV). Alternatively, it might be that during the cluster formation step, a reduced number of neutral clusters larger than the critical size are being formed by the supersonic expansion. Therefore, either the ‘neutral precursors’ are not present in great enough numbers, or that during the ionisation process neutral molecules are lost in great enough numbers to take the ionised cluster below the critical size and therefore will undergo coulomb fission on a shorter timescale..

Figure 5.26 shows an overlay of MIKE spectra obtained from sitting on a singularly charged peak in the mass spectrum, containing a component of both six and sevenfold charged clusters, and incrementally changing the size of the precursor. The black profile in figure 5.26 shows signals from the coulomb fission of $(NH_3)_{540}^{6+}$ and $(NH_3)_{630}^{7+}$. By following the profiles from back to front in the figure, the number of molecules in the precursor increases by a magnitude equal to Z_p, the charge state of the precursor, the characteristic signal from 6+ clusters at around 8700 eV decreases evenly from size n=540 until the stable size $n_{stab}(6) = 564$ is reached and the signal disappears. Concurrently, the signal from the component 7+ fission, around 8000 eV rises above the critical size of n_{crit} = 630, until at a size of $(NH_3)_{658}^{7+}$ the feature resembles a broad profile similar to what has been seen previously.

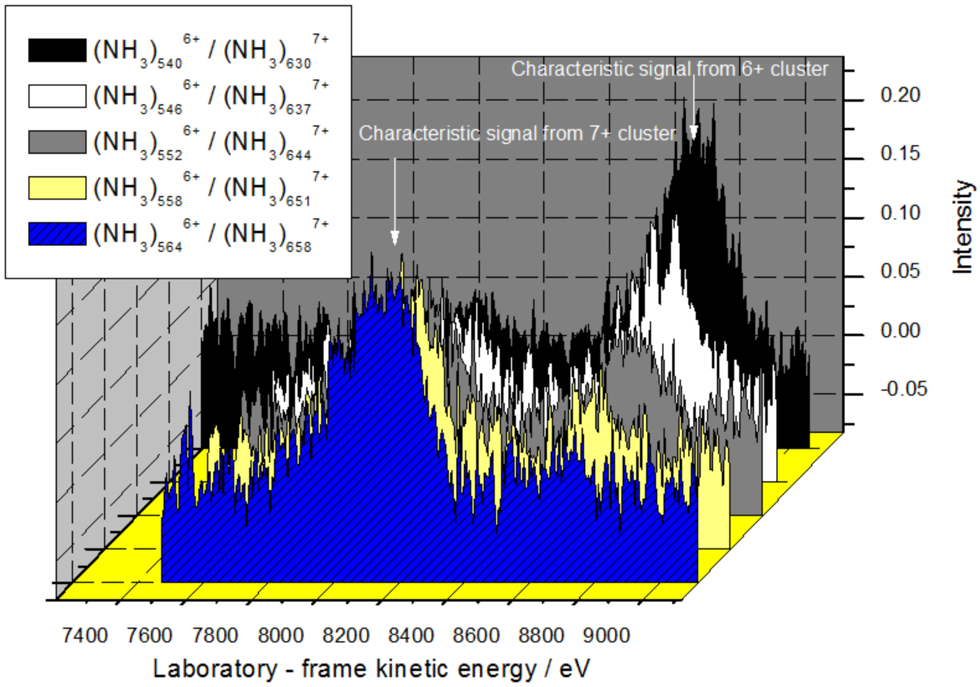

Figure 5.26: An overlay of MIKE spectra showing the simultaneous onset of 7+ clusters beyond $n_{crit}(7) = 630$ and the progression towards the stable size of 6+ clusters at $n_{stab}(6) = 564$

Figure 5.27 shows a collection of MIKE spectra for the coulomb fission of four sevenfold ammonia clusters. It is seen there is a tendency for a slight asymmetric in the profile shape with a tailing-off at the low energy side of the feature. This feature may be an artefact feature, an unavoidable concern in double focussing experiments [11], or the result of fission from different mechanisms. Fission from a precursor ion with charge state $Z_p = 7$ can produce a range of charge states for the detected fragment, and charge states of $Z_f = 6, 5, 4 +$ are, in theory, possible. Using eq. 2.10 for energy value at the centre of the features, the size of the fragments for the possible charge states Z_f are calculated. In the case of the $(NH_3)_{679}^{7+}$ precursor it is possible for a large 6+ charged fragment to be detected with the loss of a small singly charged cluster containing up to 14 molecules. The range of fragments is not broad enough to account for the full experimental width, but may account for the asymmetric shape towards the low energy side of the peak. This is illustrated in Figure 5.28.

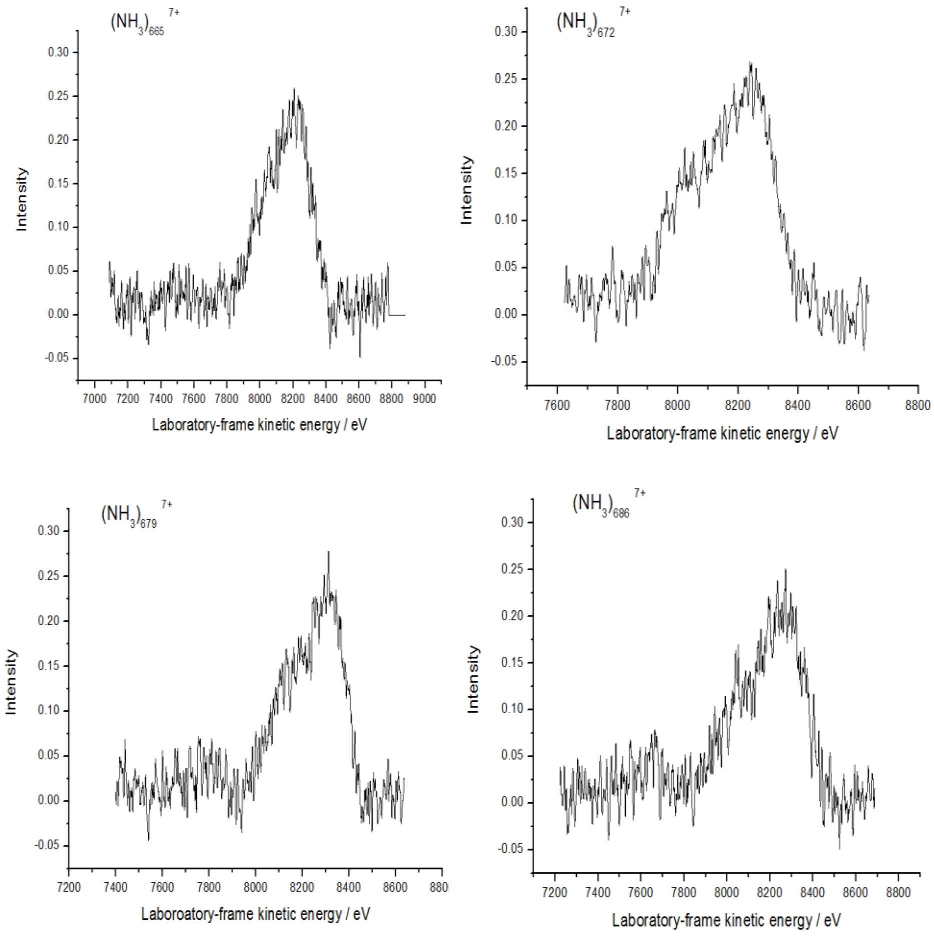

Figure 5.27: Four examples of MIKE spectra from sevenfold charged precursor ions showing degrees of asymmetry towards the low energy side of the peak.

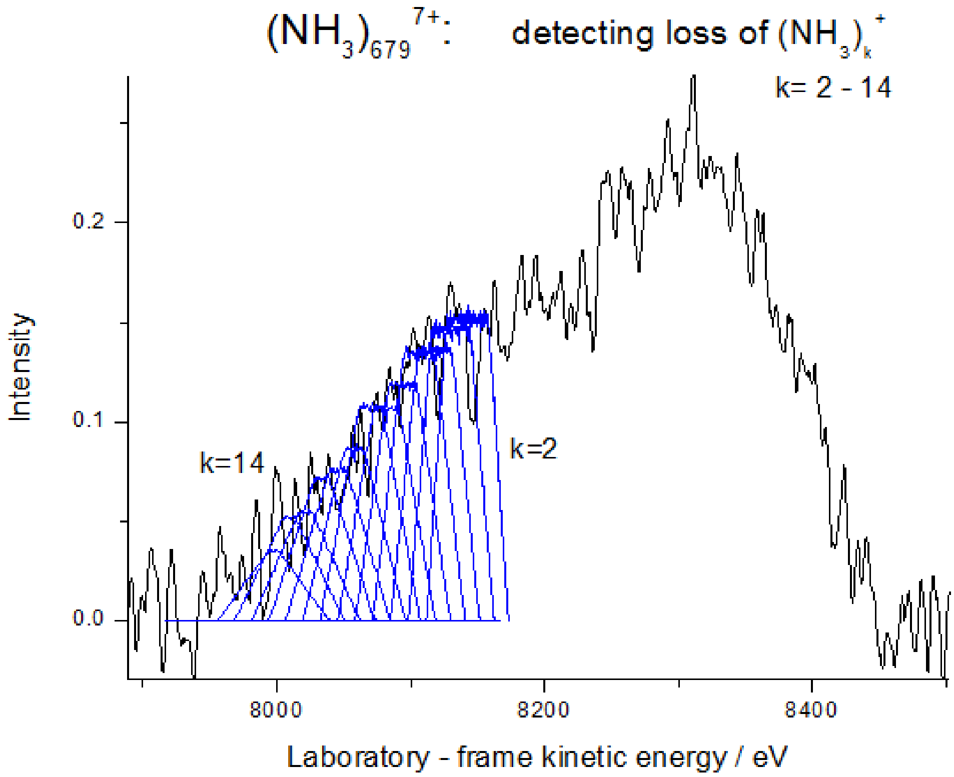

Figure 5.28: MIKE spectra for $(NH_3)_{679}^{7+}$ cluster ions overlain with the simulated peaks for the 6+/1+ fission mechanism

Precursor cluster	Fragment channel	$< KER >$ / eV	$U_{\max}$ /eV
$(NH_3)_{679}^{7+}$	k=2+	3.33	3.27
	k=3+	3.33	3.27
	k=4+	3.33	3.27
	k=5+	3.33	3.27
	k=6+	3.33	3.26
	k=7+	3.33	3.26
	k=8+	3.33	3.26
	k=9+	3.33	3.25
	k=10+	3.33	3.25
	k=11+	3.33	3.24
	k=12+	3.33	3.24
	k=13+	3.33	3.23
	k=14+	3.33	3.23

Table 5.9: Values for $< KER >$ and $U_{\max}$ for the simulated peaks in figure 5.28

The second type of fragmentation possible is the fission into 5+/2+ charged fragments. Figure 5.29 shows an example of how the width of the experimental spectrum of $(NH_3)_{679}{}^{7+}$ can be accounted for with 20 simulated peaks from the 5+/2+ coulomb fission mechanism. Table 5.10 gives the values for the energetics of the pathways.

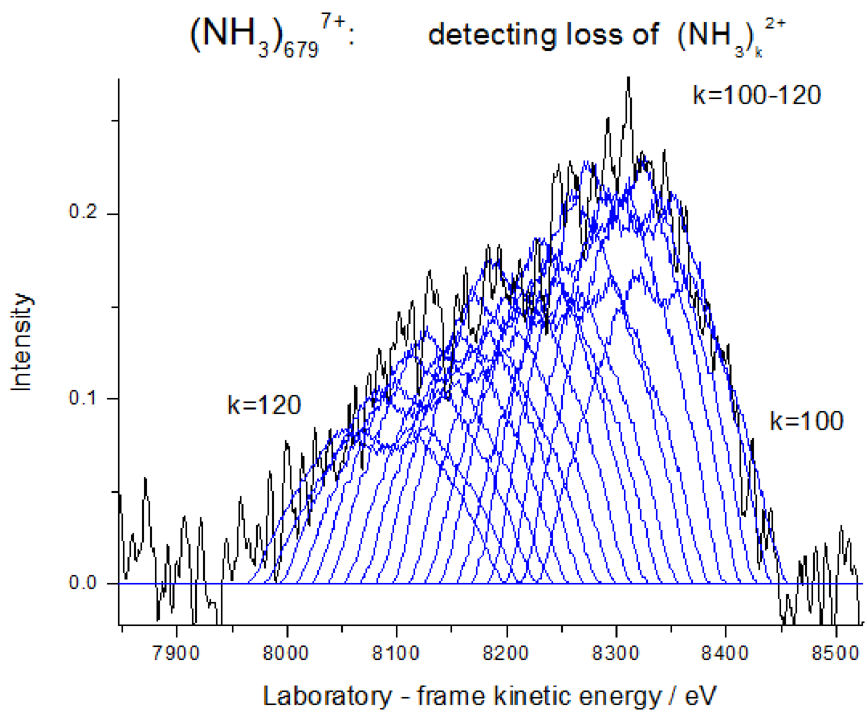

Figure 5.29: MIKE spectrum showing the fission of $(NH_3)_{679}{}^{7+}$ cluster ions. The simulated peaks for fragments are shown

Precursor cluster	Fragment channel	$< KER >$ / eV	$U_{\max}$ /eV
$(NH_3)_{679}^{7+}$	k=100^{2+}	4.67	4.62
	k=101^{2+}	4.67	4.62
	k=102^{2+}	4.67	4.62
	k=103^{2+}	4.67	4.61
	k=104^{2+}	4.67	4.61
	k=105^{2+}	4.67	4.61
	k=106^{2+}	4.67	4.61
	k=107^{2+}	4.67	4.60
	k=108^{2+}	4.67	4.60
	k=109^{2+}	4.67	4.60
	k=110^{2+}	4.67	4.60
	k=111^{2+}	4.67	4.59
	k=112^{2+}	4.67	4.59
	k=113^{2+}	4.67	4.58
	k=114^{2+}	4.67	4.58
	k=115^{2+}	4.67	4.58
	k=116^{2+}	4.67	4.57
	k=117^{2+}	4.67	4..57
	k=118^{2+}	4.67	4.57
	k=119^{2+}	4.67	4.57
	k=120^{2+}	4.67	4.56

Table 5.10: Values of $< KER >$ and $U_{\max}$ for the pathways shown on figure 5.29

The third possible fission mechanism is the fission into 4+/3+ fragments. The simulated peak shape is noticeably wider and more dished due to the relative lightness of the detected fragment and the high KER of the process as predicted by the value of U_{max}. This is shown by the blue peak in figure 5.30. It is clear that the single peak is not wide enough to account for the full width of the profile. The additional width on the low energy side of the peak could come from an artefact feature that has followed the same fission mechanism. The most likely cause of an artefact peak appearing in a MIKE spectrum is the transmission of an ion one molecule smaller than precursor of interest through the magnet and for that ion to undergo coulomb fission in the 2nd *ffr*. This instance would require the evaporation of one molecule in the 1st *ffr*, and as the binding energy decreases the potential for this to occur increases as the cluster gets larger. The value of the binding energies is small enough to allowing a number of clusters that have lost one or more molecules to form in the 1st *ffr*. The transmission of the fragments through the magnet will occur at mass $m^* = {m_d}^2/m_f$ where m_f and m_p are the masses of the fragment and precursor ions respectively. Solving this for the metastable fragment $(NH_3)_{678}{}^{7+}$ from the precursor ion $(NH_3)_{679}{}^{7+}$ reveals a difference in nominal mass of 5 amu, which under the reduced resolving power of the magnet required for the observation of coulomb fission is small enough for the transmission of both ions simultaneously. If this metastable fragment undergoes coulomb fission in the 2nd *ffr* to produce the $(NH_3)_{454}{}^{4+}$ and $(NH_3)_{223}{}^{3+}$ fragments, which is of the same order of symmetry of fragmentation as previously observed, then the remainder of the peak width is accounted for. This example is shown in figure 5.30 and 5.31 with the fragments resulting from the fission of the metastable artefact coloured in dashed red. It is seen from tables 5.11 and 5.12 that the values of $< KER >$ and U_{max} for the pathways correspond well for the precursor fission and the artefact fission.

Set out above are all the theoretically possible mechanisms for coulomb fission from sevenfold charged ammonia clusters. With reference to the points made in section 5.6 regarding the formation of a single detectable fragment following coulomb fission, one might consider discounting the 4+/3+ pathway as a possibility. It is seen that the body of the peak can be accounted for using only the peaks from the 5+/2+ mechanism. It is possible that the tailing off effect comes from the fragments resulting from the 6+/1+ fission mechanism. Therefore, it is assumed that both mechanisms are present in the fission of sevenfold charged precursors.

The the electrostatic potential energy curves for these two mechanisms are presented in Figure 5.32 and 5.33. Comparison of the two highlights the balance between the electrostatic repulsion and the induced attractive forces brought about by polarisation. An asymmetry in charge density in the fragments will favour the polarisation of the larger of the two fragments by the smaller, assuming the larger fragment is polarisable enough. This is evident in figure 5.33, where the curves show varying degrees of this effect. In the range of k=1-14 the magnitude of the short range attractive region of the curve at 0-0.2 nm separation decreases from 0.6 eV to 0 as asymmetry decreases. Analysis of the trend in U_{max} (table 5.9) points to the fact that even though the fragments are experiencing polarisation forces, electrostatic repulsion still dominates. The trend is for the most asymmetric fragmentations to have the largest U_{max}. This is due to the increase effectiveness of electrostatic repulsion from the smaller fragment. The curves for the 5+/3+ mechanism all show this effect. The curves are all repulsive in nature, with the magnitude of U_{max} determined by the effectiveness of the repulsion.

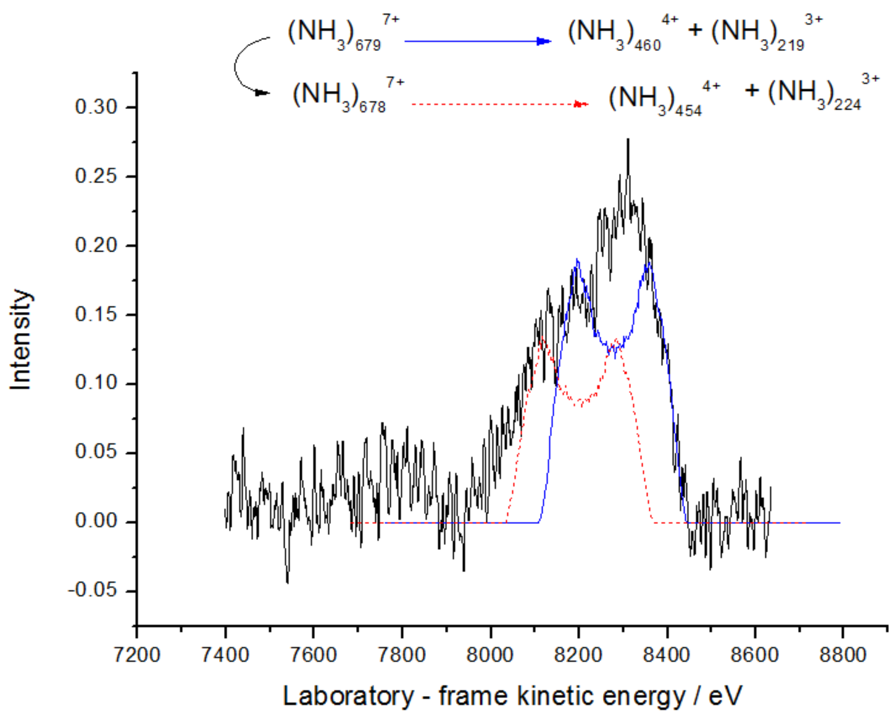

Figure 5.30: MIKE spectrum showing the coulomb fission of $(NH_3)_{679}{}^{7+}$ cluster ions. The simulated peak in blue is for coulomb fission into the fragments shown; in red is the simulated peak from the coulomb fission of the artefact precursor into a fragment of same symmetry

Precursor cluster	Fragment channel	$< KER >$ / eV	U_{max} /eV
$(NH_3)_{679}^{7+}$	k=219^{3+}	5.07	5.19
Artefact:			
$(NH_3)_{678}^{7+}$	k=224^{3+}	5.07	5.19

Table 5.11: Values of $< KER >$ and U_{max} for the pathways shown on figure 5.29

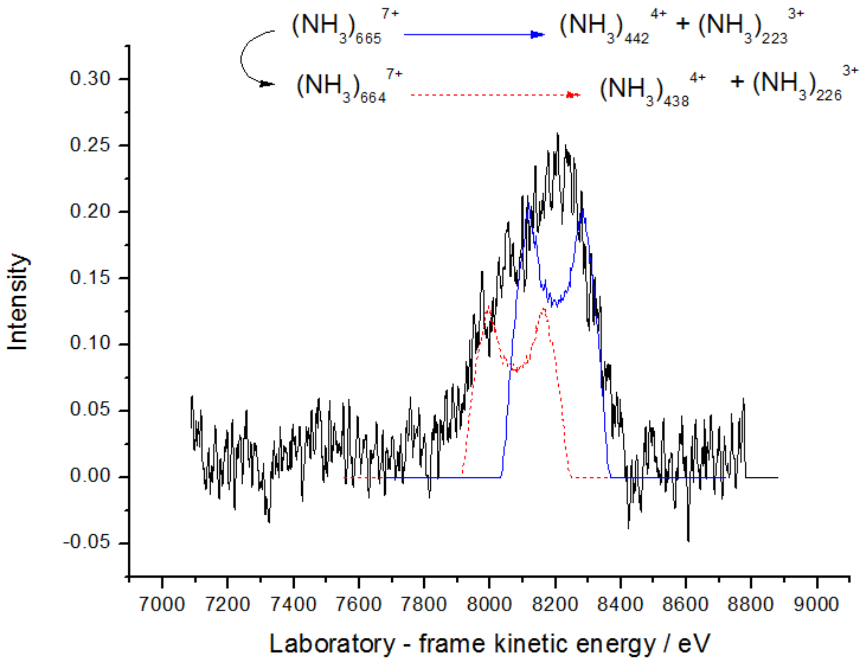

Figure 5.31: MIKE spectrum showing the coulomb fission of $(NH_3)_{665}^{7+}$ cluster ions. The simulated peak in blue is for coulomb fission into the fragments shown; in red is the simulated peak from the coulomb fission of the artefact precursor into a fragment of the same symmetry.

Precursor cluster	Fragment channel	$< KER >$ / eV	U_{max} /eV
$(NH_3)_{665}^{7+}$	k=223^{3+}	5.23	5.07
Artefact:			
$(NH_3)_{664}^{7+}$	k=226^{3+}	5.07	5.23

Table 5.12: Values of $< KER >$ and U_{max} for the pathways shown on figure 5.30

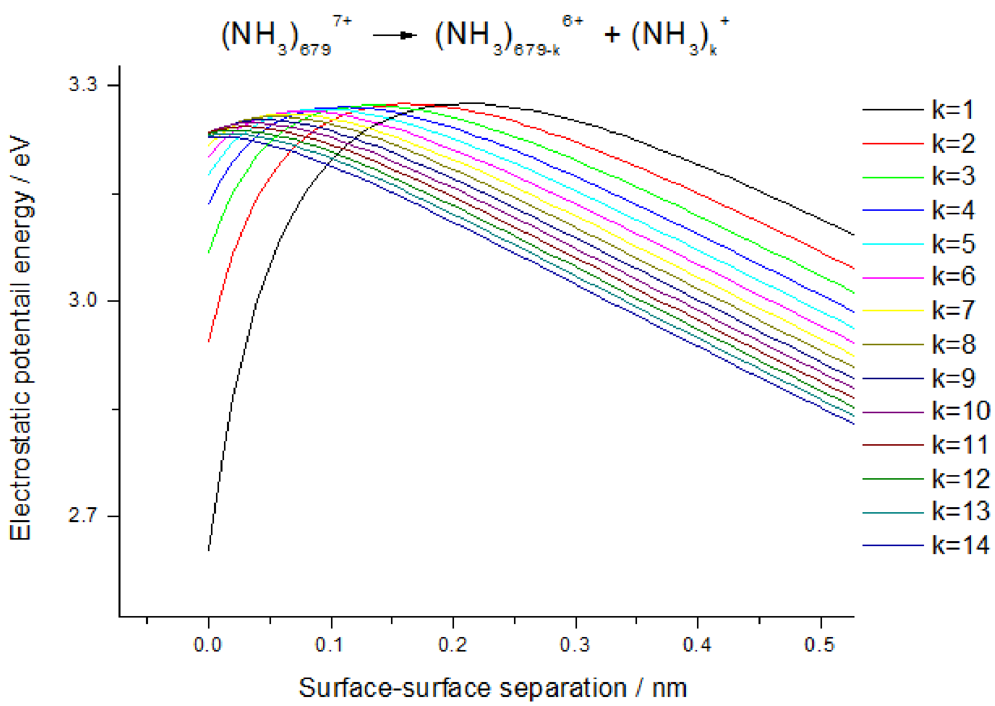

Figure 5.32: Electrostatic potential energy curve following coulomb fission of $(NH_3)_{679}^{7+}$ into 6+/1+ charged fragments

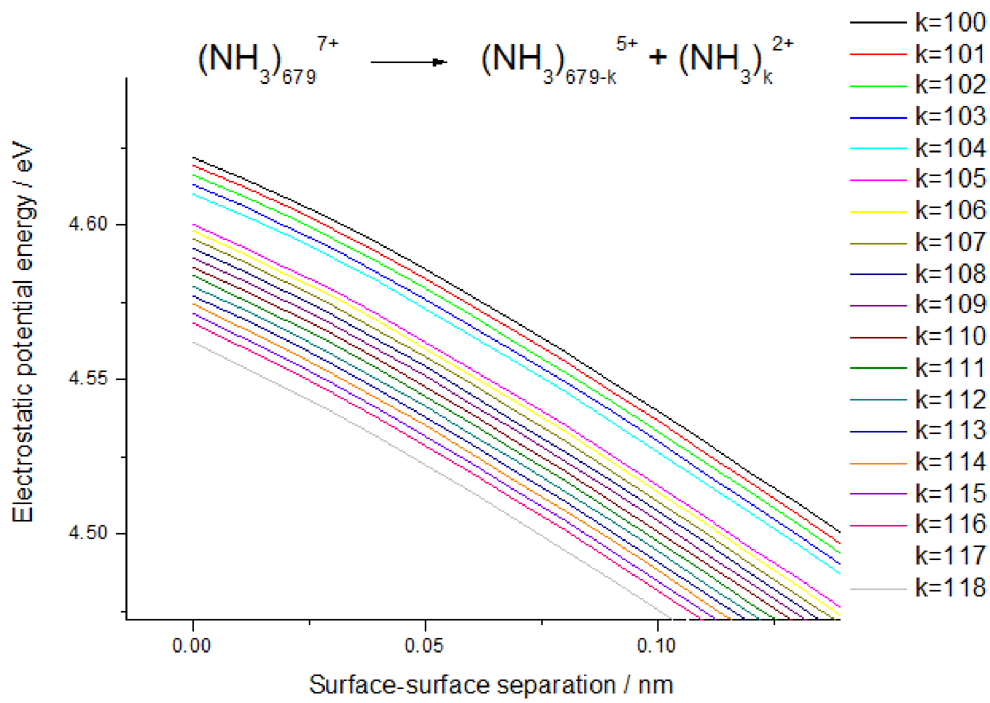

Figure 5.33: Electrostatic potential energy curve following coulomb fission of $(NH_3)_{679}^{7+}$ into 5+/2+ charged fragments

5.8 Eightfold Charged Ammonia Clusters

MIKE spectra following the coulomb fission from eight-fold charge ammonia clusters is presented. The identification and analysis of these data is hampered by generally poor signal sensitivity making the composition of peaks somewhat difficult to interpret. Following on from the argument made in the previous section accounting for the reduced signal intensities, the total ionisation potential (74.3 eV) for the removal of eight electrons from ammonia is closer to the limit of the mass spectrometer of 100 eV. Figure 5.34 shows the progression of the signal intensities towards a full profile as the size of cluster increases. At the same time, the intensities of the signal originating from fission of sevenfold charged ammonia clusters is seen to diminish when converging on the stable size.

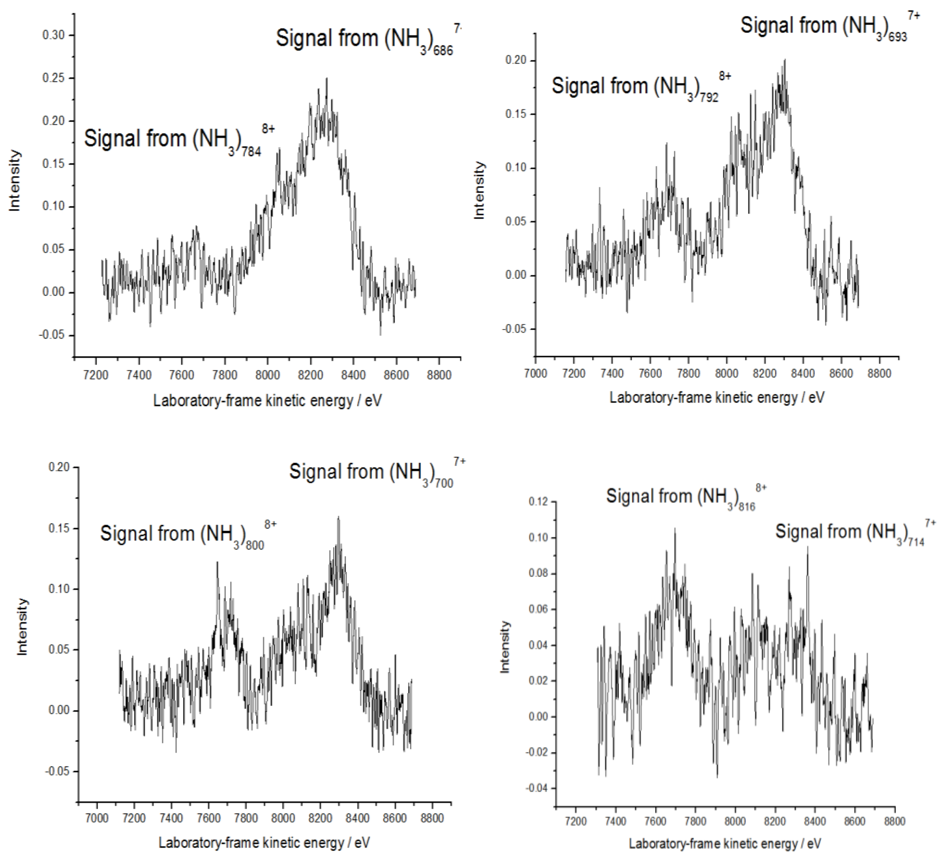

Figure 5.34: MIKE spectra showing an onset of a characteristic signal originating from eightfold charged ammonia clusters with a simultaneous decrease in intensity in sevenfold charged clusters as the stable size is reached

For a body containing 8 charges 4 possible types of fission are possible; 7+/+, 6+/2+, 5+/3+ and 4+/4+. Figure 5.33 shows the simulated peaks calculated for the fragment at the centre of the peak, approximately E_d = 7700 eV. A cursory look can discount 5+/3+ and 4+/4+ as fission mechanisms, as the simulated peaks are much too wide, which leaves 7+/+ and 6+/2+ as possibilities. The single peak simulated for 7+/+ is much narrower than the profile seen in the MIKE spectrum but a range of fragments is possible, filling the whole of the experimental width. Contrast to the 6+/2+ peak which takes up nearly the whole width of the experimental spectrum. This may confirm the identity of the fragment causing the MIKE peak as $(NH_3)_{680}^{6+}$. However, referring back to arguments made previously against the formation of a single fragment, differences in a single monomer unit on the lifetime of the fragmentation pathway will be marginal. Hence, it would be expected for more than one 6+ peak to be resolved. Therefore it is highly likely that the experimental feature is comprised solely from 7+ fragments.

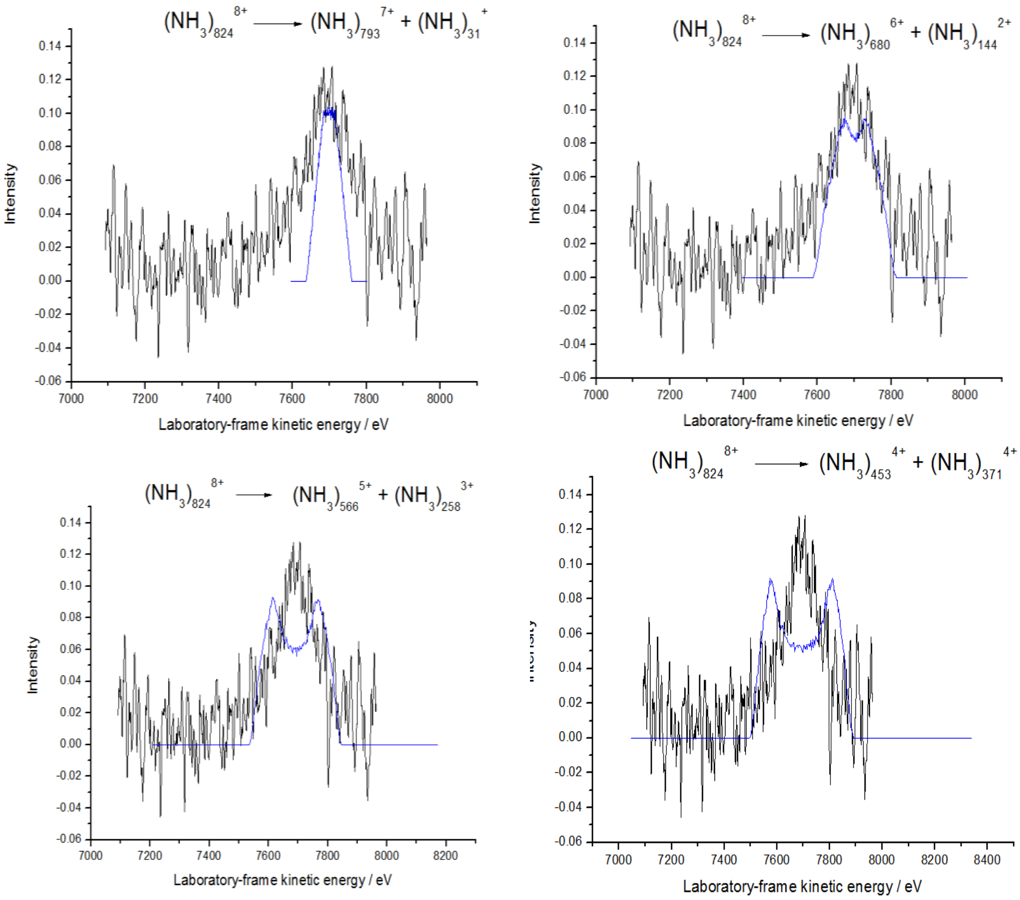

Figure 5.35: The MIKE spectra for the fission of the $(NH_3)_{824}{}^{8+}$ overlain with the simulated peaks for the potential fates of the cluster

Precursor cluster	Fragment channel	$< KER >$ / eV	$U_{\max}$ /eV
$(NH_3)_{824}{}^{8+}$	$k=31^{+}$	3.33	3.43
	$k=144^{2+}$	5.25	5.13
	$k=258^{3+}$	6.27	6.13
	$k=371^{4+}$	6.27	6.40

Table 5.13: Values of $< KER >$ and $U_{\max}$ for the pathways shown on figure 5.26

5.9 Stability of Multiply Charged Ammonia Clusters

A benefit of collecting the data on stability in the preceding sections is that it is possible to test the liquid drop model for molecular clusters for systems of a charge up to $z = 8$. This corresponds to cluster containing a maximum of approximately 800 molecules, corresponding to a radius of approximately 2 nm. It is informative to be able to study a system that is approaching the size of larger clusters as it is the size regime the original liquid drop theory is applied to. Figure 5.36 shows the values of the critical sizes $n_{crit}(z)$ determined by experiment (blue line) and also the values that are predicted by the liquid drop model (red line, eq. 1.1), both as a function of increasing charge. As can be seen from table 5.14 the general agreement is good, within 5% for all charge states. The Rayleigh equation for the liquid drop model below is shown below (Equation 1.1):

$$n_{crit}(z) = \frac{(ze)^2}{64\pi^2\gamma\varepsilon_0 {r_m}^3}$$

Where charge ze is the charge state multiplied by the elementary charge constant, γ is the surface tension, ε_0 is the permittivity of free space and r_m is the molecular radius. Previous theoretical calculations have been performed by Echt *et al.* [9] up to charge state 4+ using a modified method which aims to take account of size-dependant properties of the charged clusters in question. That data is included on figure 5.37, and as can be seen the agreement with experimental results available up to 4+ is not as good as the predicted by the Rayleigh equation. If one was to extend the calculations up to 8+ it is reasonable to assume that the divergence from what is seen experimentally would become increasingly large.

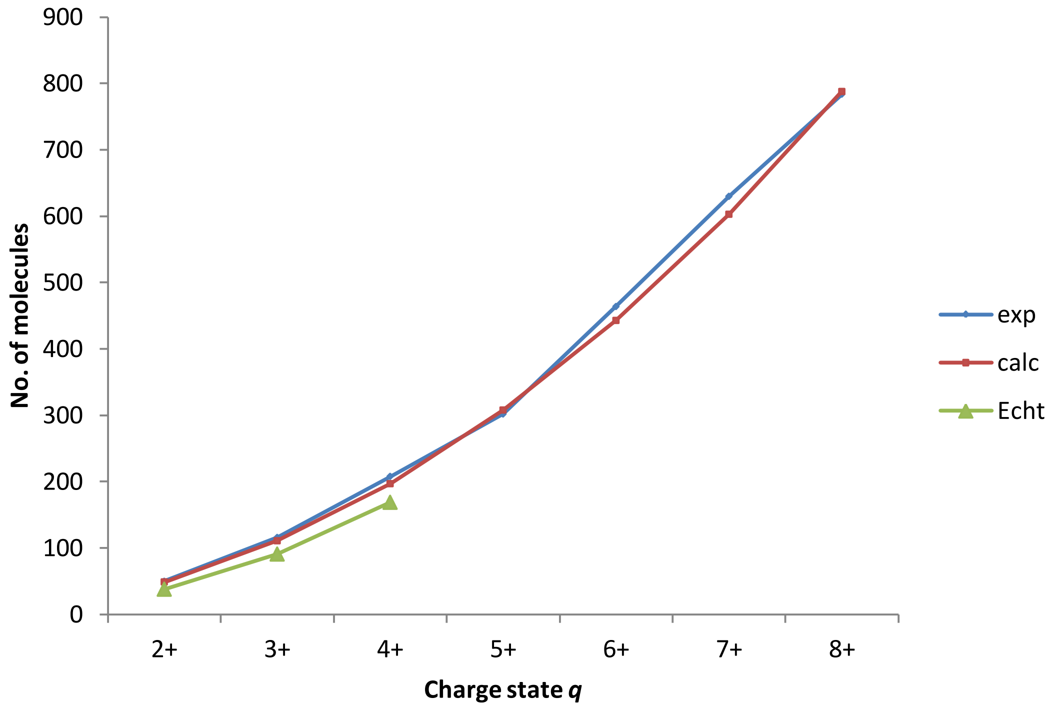

Figure 5.36: Comparison of the calculated and experimentally determined values of the critical sizes $n_{crit}(z)$

Charge state z	Experimental $n_{crit}(z)$	Calculated $n_{crit}(z)$	% difference
2+	50	49	2
3+	116	111	4
4+	208	197	5
5+	302	308	2
6+	464	443	4
7+	630	603	4
8+	784	788	1

Table 5.14: Values of experimentally determined and calculated $n_{crit}(z)$

There are several potential reasons why divergence between what is predicted by the model and what is seen experimentally might occur. In charge states above the fourfold charged system the presence of the multiply charged precursor is deduced by the observation of a characteristic MIKE profile and the critical size assigned as the size of cluster below which there is no observable signal. It is likely that in the case of low fragment signal from a precursor close to the critical size, that the cluster is undergoing fission before the 2nd *ffr* due to the short lifetime brought about by a vanishingly small barrier to fission ($\Delta E_{barrier}$). This becomes influential in the assignment of the critical size, and could potentially lead to an experimental assignment that is too large. Additionally, only ions with mass spectral signals coincident with singularly charged ions were scanned. At the exact m/z all z-fold-charged clusters above $n_{crit}(z)$ are able to pass though the magnet, this ensures exact m/z characterisation of the precursors and is useful in the 'cross-over' scans. However, in this method of determining the critical size the precursor clusters that exist between the singularly charged peaks are missed, adding a degree of uncertainty to the experimental values.

5.10 Conclusions

The promising early work on the identification of multiply charged ammonia clusters and the analysis of coulomb fission has been extended to the limits of the experimental set-up. The failure to observe ninefold charged species is attributed to the ionisation potential (83 eV) being close enough to the limits of the ion source in the mass spectrometer. It is likely that a portion of the extra incident energy from the ionising electrons is used to drive additional processes in the clusters which takes the ninefold appearance potential above the 100 eV limit. Generally it is found that the quality of the experimental data decreases as the charge state of the precursor cluster increases, which might suggest that a portion of the energy that is supplied to the clusters from the ionising electrons is increasingly partitioned into other modes.

In previous work on the dication ammonia cluster system the *KER* of the processes was calculated from an estimation of the FWHM of the experimental feature in the MIKE spectrum, assuming a Gaussian distribution. In this particular instance that method is not accurate because a) the signals of the MIKE peaks are small and therefore subject to poor signal-to-noise ratio and b) the fragments are close together in energy, to the extent that the peaks overlap. This makes accurate assignment of the FWHM subject to a degree of uncertainty. The peak simulation methodology addresses this by matching a peak with a calculated value of <*KER*> and overlaying it on the experimental feature. For a particular pathway, this has been shown to produce, in general, well fitted peaks with values of <*KER*> closer to the predicted barrier heights. The improvements to the experimental setup detailed in Chapter 2 have enabled better quality data to be collected for the dication system and has allowed the collection of data for higher order charged systems.

Triply charged ammonia clusters have been identified by an onset of peaks in the mass spectrum. The value of the critical size was determined by observation of coulomb fission signals from precursor clusters below this size. As put forward in the text, the reason for the observation of $n_{crit}(3)$ = 116 (previous value = 121) could be attributed to differences in the experimental apparatus. The coulomb fission profiles for triply charged ammonia clusters are characteristically weak, with the identification and analysis of them appearing to be obfuscated by the multitude of processes that can happen in the same time-frame which originate from multiple forms of protonated ammonia clusters. As noted in the text, the potential energy curves show a degree of attenuation by attractive potentials at the extreme of charge asymmetry, not enough to lower the barrier height relative to the surrounding pathways.

In the case of four-fold charged ammonia clusters, the identification of the critical size was achieved by using the MIKE scanning technique to find the smallest size cluster that shows a characteristic MIKE profile from coulomb fission. As noted in the text, all of the precursor clusters in the critical range produced qualitatively similar profiles with a broad profile roughly 400 eV wide. Confidence is given to the assignment of these MIKE profiles as from fourfold precursors as the intensity is seen to diminish and disappear close to the predicted critical size of the liquid drop model. One can discount the possibility of coulomb fission from coincident doubly or triply charged clusters as the corresponding sizes of these clusters will exceed the relevant stable sizes, i.e. the size at which fission ceases to be observed in the apparatus. This technique was used instead of mass scanning for detecting the onset of precursor signals due to the congestion and the decreasing resolution of the peaks in the mass spectrum. Using the methodology set out in the text, the simulated peaks for both 2+/2+ and 3+/1+ fission mechanisms were fitted to the MIKE spectra. For both fission mechanisms the experimental MIKE profile can be reproduced from a number of simulated peaks. This is keeping with a lifetime model explaining the relative intensities of the peaks relative to the neighbouring pathways, but suggests a deviation from the non-continuous trend of 3+/1+ fragmentations seen from other fourfold charged precursors presented in this work. Due to the fact that the peak simulation methodology is shown to accurately reproduce the individually resolvable experimental peaks in the dication system, it is treated as reliable for assigning the pathways and energetics of the peaks that make up the experimental features. The dielectric model predicts a dominating effect of the electrostatic repulsion over the induced potentials for the 3+/1+ mechanism. This is evidenced by the shape of the potential energy curves show little to no characteristic effect of the attenuation of the electrostatic repulsion seen in other examples. The values of U_{max} for the 2+/2+, less asymmetric pathways are consistently larger in magnitude. The most asymmetric pathway has the lowest magnitude of U_{max} and a crossover of the potential energy ordering of the pathways is seen as the induced potentials lose effectiveness. Compared to the curves predicted for the 3+/1+ mechanism, this shows that an increase in the charge on the smaller fragment can induce polarisation of the larger fragment despite the 2+ large fragment being smaller than the 3+.

The critical range of four-fold charged ammonia cluster that will undergo coulomb fission is 83 molecules, significantly larger than the critical ranges seen lower ordered charged clusters (up to approximately 10 molecules depending on the system). This can be explained with regards to the increase in surface area of the cluster as it grows. Each extra layer of molecules on the surface of the cluster will contain an increasing number of molecules. Therefore, increases in the inter-charge distance required to reach the stable size in multiply charged clusters will require increasing numbers of molecules.

Fivefold charged ammonia clusters were identified in the same manner as the four-fold charged examples. A characteristic profile from the MIKE spectra was identified as originating from five-fold charged ammonia cluster with the critical size identified from the deterioration and eventual loss of the profile below a certain size. In theory, Z_f for the fission can either be 4 or 3, but by using Equation 2.10, Z_f = 4 is ruled out as this fragment would exceed the size of the precursor. Barrier heights of magnitude of around 3 eV are predicted. Using this value as a guide, 9 simulated peaks are required to reproduce the experimental spectrum. It is interesting to note that this is the same number of pathways observed in the fission of four-fold charged clusters into 3+/1+ fragments and considerably more than the number observed for either triply, or doubly charged systems. This can be partially explained by using the predicted barrier heights of the pathways. The difference in barrier height for five-fold fission into 3+ fragments is of the order of 0.001 eV, making the differences in the barrier to fission ($\Delta E_{barrier}$) for the range of pathways negligible. The knock-on effect of this is that more pathways will have a lifetime which is comparable with the experimental constraints.

Six-fold charged ammonia clusters were observed using the same methodology as above. Again, the characteristic profile is observed over an energy range distinct from the fission signal from fivefold charged clusters, which makes the stepwise growth/death of signals originating from 6+ and 5+ precursor clusters observable. As seen in figures 5.23 there is a possibility that the signal can arise from the detection of only one 3+ fragment, at odds with the lifetime model. A potential reason for this might be a special stability of the $(NH_3)_{300}^{3+}$ or $(NH_3)_{192}^{3+}$ fragments, however, there are no recorded example of magic numbers in ammonia at this size regime. A qualitative measure of stability of a cluster is sometimes performed by observing the intensity of the signal in a mass spectrum relative to neighbouring signals. Unfortunately, this is not possible in this system as the resolution is not sufficient at large m/z values to resolve beyond 3+ cluster peaks close to $n_{crit}(3)$. It is much more likely that the profile that is observed is coming from multiple pathways of the 4+/2+ fission mechanism, consistent with the lifetime model and as observed in other systems.

Sevenfold charged clusters show a tendency to produce a profile with a degree of asymmetry at the low energy side of the peak. This observation can possibly be assigned to a strong artefact component in the feature resulting from the loss of one molecule before the magnetic sector followed by coulomb fission in the 2nd *ffr*. However as previously discussed, the formation of a single detectable fragment is unlikely to occur. The entire width of the feature can be reproduced by fragment peaks from the 5+/2+ mechanism and the 'step down' feature may be a result from additional fission processes from the 6+/1+ mechanism.

Eightfold charged clusters can undergo fission into either a 7+ or 6+ charged fragment, the other possible fragments are ruled out due to the simulated width of the peak exceeding the width of the experimental feature. In this case, like lower ordered charged clusters, it is determined that the profile is comprised of a range of 7+ fragments, rather than a single 6+ fragment..

Table 5.15 shows the values for some of the characteristic properties of multiply charged clusters over the range of charge states studied. For every case a range of fragments is determined to be the most probable outcome, over a single detectable fragment. The reasons for such a determination have been set out previously. The critical range, i.e. the range of clusters between $n_{crit}(z)$ and $n_{stab}(z)$ that undergo fission, is shown to increase with charge state. Fluctuations are due to the stated difficulties of assigning exact sizes for $n_{crit}(z)$ and $n_{stab}(z)$.

Evidence for the influence of the dielectric constant on the polarisation of the fragment clusters is seen in the trend in observed *KER* against the value of total charge, *q1.q2*. This is plotted in figure 5.37 and it can be seen that the values of the *KER* diverges strongly from the *KER=q1.q2* curve which is shown in red. For point charges the magnitude of the repulsive energy or *KER* will be proportional to the value of *q1.q2* as there is no polarising dielectric medium supporting the charges. In the case of ammonia clusters the magnitude of the dielectric constant ($\varepsilon_r = 22$) is shown to attenuate the purely repulsive effect of the repelling charges. Therefore, the experimental *KER* falls increasingly below the $q_1.q_2$ curve.

Charge State z_p	Critical range	Most probable pathways	No. Of pathways	Approx. *KER* / eV
2+	4	1+/1+	4	1.0
3+	8	2+/1+	3	1.4
4+	29	3+/1+, 2+/2+	9, 4	2.2, 2.5
5+	105	3+/2+	9	2.9
6+	94	4+/2+	10	3.9
7+	112	5+/2+	21	4.7
8+	72	7+/1+	~32	3.3

Table 5.15: Values for the critical range, most probable pathway, number of pathways and average KER over the available pathways for multiply charge ammonia clusters

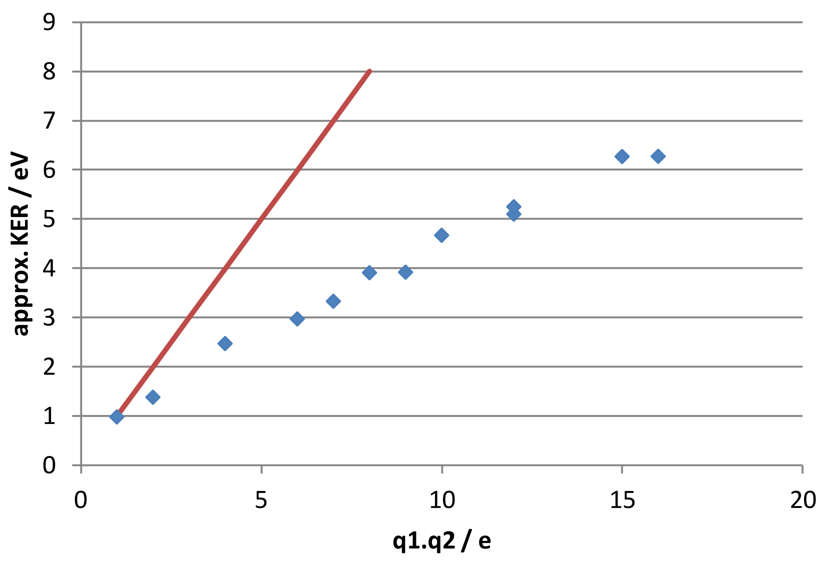

Figure 5.37: A graph showing the relationship of average KER to the magnitude of the total charge (q1.q2). In red is the curve av. KER = q1.q2.

References

1. G. H. Wu, X. J. Chen, A. J. Stace, P. Linse, *Journal of Chemical Physics* **134**, 4 (2011).
2. X. Chen, E. Bichoutskaia, A. J. Stace, *The journal of physical chemistry. A* **117**, 3877 (2013).
3. M. T. Coolbaugh, W. R. Peifer, J. F. Garvey, *Chemical Physics Letters* **156**, 19 (1989).
4. W. R. Peifer, M. T. Coolbaugh, J. F. Garvey, *Journal of Physical Chemistry* **93**, 4700 (1989).
5. P. Linse, *Journal of Chemical Physics* **128**, (2008).
6. E. Bichoutskaia, A. L. Boatwright, A. Khachatourian, A. J. Stace, *Journal of Chemical Physics* **133**, (2010).
7. H. Shinohara, N. Nishi, N. Washida, *Journal of Chemical Physics* **83**, 1939 (1985).
8. J. F. Garvey, R. B. Bernstein, *Chemical Physics Letters* **143**, 13 (1988).
9. O. Echt *et al.*, *Physical Review A* **38**, 3236 (1988).
10. R. G. Keesee, A. W. Castleman, *Journal of Physical and Chemical Reference Data* **15**, 1011 (1986).
11. P. G. Lethbridge, (1989).
12. E. Bruzzie, R. Parajuli, A. J. Stace, *Int. J. Mass Spectrom.* **345**, 160 (2013).

Chapter 6 : Multiply Charged Tetrahydrofuran Clusters

6.1 Introduction

Multiply charged tetrahydrofuran (THF) clusters have been produced as described by the experimental procedure in Chapter 2. Unimolecular coulomb fission reactions have been studied with respect to gaining understanding of the behaviour of these metastable species around the critical size. THF is a polar, cyclic ether with the empirical formula C_4H_8O and a dielectric constant of 7.52. Around two hundred thousand tonnes of THF are produced annually for use in industrial and other processes. Due to the polar nature of the molecule and large liquid range it is widely applied as a solvent for various processes [2]. Under strong acid THF polymerises to give polytetramethylene oxide which is used in the production of spandex [3]. Presented are the first observations of coulomb fission of multiply charged clusters of THF. Charge states of Z_p= 2–4 are isolated and the fragmentation from coulomb fission is analysed. The energetics of the processes is evaluated in the same fashion as in previous chapters. Using the dielectric particle model the barrier heights to fission (U_{max}) are calculated and are compared to the average kinetic energy release ($< KER >$) from fitted simulated peaks. Additionally, using the experimental data on the identification of precursors, comparison is made with the liquid drop predictions on the size of the cluster required to stabilise the contained z charges.

6.2 Doubly Charged THF clusters

Presented are the first direct experimental measurements on the stability and coulomb fission of doubly charged THF clusters. The onset of doubly charged THF clusters can be observed in a mass spectrum above a critical size of $n_{crit}(2)$ = 24 which lies underneath the much larger and coincident singularly charged $(C_4H_8O)_{12}^+$ peak. The presence of $(C_4H_8O)_{24}^{2+}$ is revealed by performing a MIKE scan by mass selecting the components of the large peak and detecting the fragments from the $(C_4H_8O)_{24}^{2+}$ precursor. A mass spectrum showing the onset of doubly charged peaks is shown in figure 6.1. Beyond n=24 a series of non-integer peaks are observed to rise above the baseline, corresponding to doubly charged THF clusters. The presence of background peaks complicates the spectrum. There is a peak 18 amu above a main cluster ion, this is characteristic of the pick-up of water by the cluster giving $(C_4H_8O)_n(H_2O)^+$ ions. This could be from either from contamination of the solvent sample or pick-up of residual water in the apparatus.

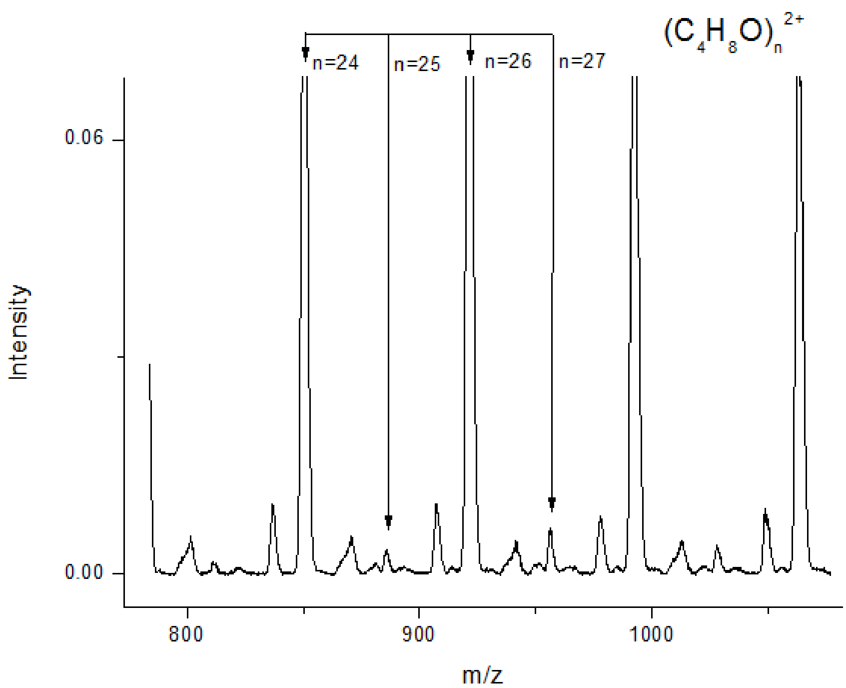

Figure 6.1: Mass spectrum showing the onset of $(C_4H_8O)_n^{2+}$ ion peaks

Figure 6.2 show the MIKE spectrum of $(C_4H_8O)_{24}{}^{2+}$, as in all examples of MIKE spectra presented, only the larger of the two ions are detected. It is observed that the fragment peaks are increasing in intensity towards total mass symmetry of the two fragments. This indicates a strong agreement of the lifetime of these pathways with the timeframe constraints of the apparatus. The peaks all show a degree of dishing, including even the most symmetric peaks, indicating fission is the ultimate step in the process. The peak profiles are accurately reproduced by the peak simulation model and the values for $< KER >$ are close to the barrier heights U_{max} in magnitude (table 6.1) and for the most part the degree of dishing in the peaks is simulated correctly, especially the k=11 pathway. The peak for the k=12 pathway shows the correct amount of dishing but the high energy side of the experimental data is diminished relative to the low energy side and the simulated peak. This most probably is due to an aberration in the experimental measurement and not an error in the simulation.

What is notable is that the calculated barrier heights for all the fission channels are, to two decimal places, equal. This differs from the calculations using the dielectric particle model on dication benzene clusters, the closest cluster in terms of molecular mass and dielectric constant. In benzene (Chapter 3), the large size difference between fragments and the low value for the dielectric constant leads to changes in the interactions of the fragments, and hence, U_{max} varies between pathways. THF has a smaller molecular size by only 3% compared to benzene, so is not sufficient to explain why there is only minor difference in the energetics of the pathways in THF. A possible explanation might be that the value of the dielectric constant for THF (ε_r=7.52) is large enough to attenuate the electrostatic repulsion by allowing sufficient ion-induced interactions from the polarisation of the larger fragment, but not to the extent that the changes in the charge density of the smaller fragment will bring the barrier down significantly. Figure 6.3 shows the electrostatic potential energy curves for the observed pathways at short surface-surface separations. It can be seen that the most asymmetric k=10 pathway has the lowest energy at separation=0, and if the scale was extended to beyond 0.3 nm separation a switch in ordering is be observed and the k=10 pathway will show the largest potential energy of the three pathways. This is evidence that at longer separations the influence of the short range induced potentials on the overall interaction between the fragments is diminished, with the electrostatic repulsion now dominating.

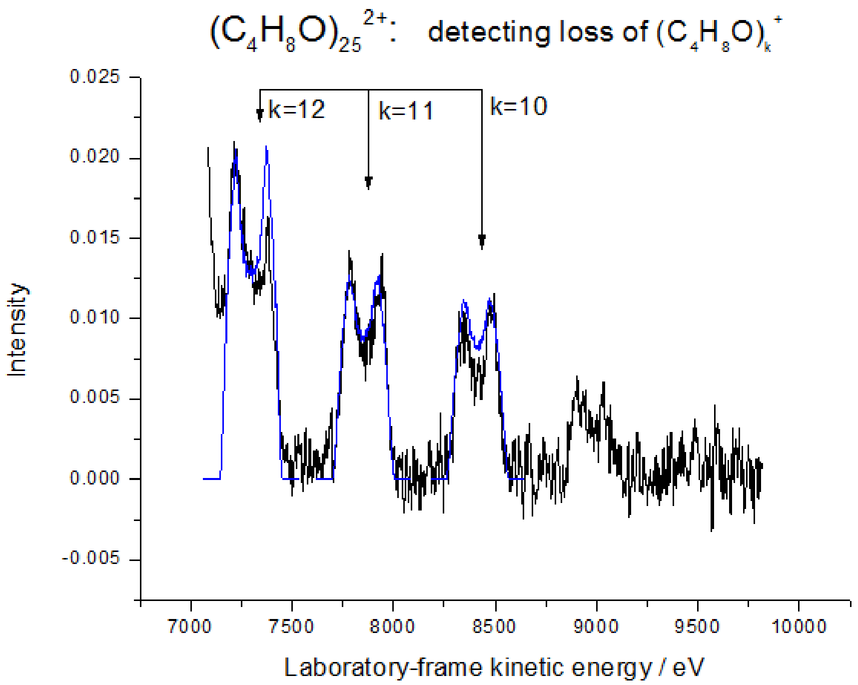

Figure 6.2: MIKE spectra of $(C_4H_8O)_{25}^{2+}$ overlain in blue by the simulated peaks

Precursor cluster	Fragment pathway	U_{max} / eV	$< KER >$ / eV
$(C_4H_8O)_{25}^{2+}$	k=10	0.89	0.78
	k=11	0.89	0.78
	k=12	0.89	0.86

Table 6.1: The barrier heights and the <KER> for the fragments detected in figure 6.2

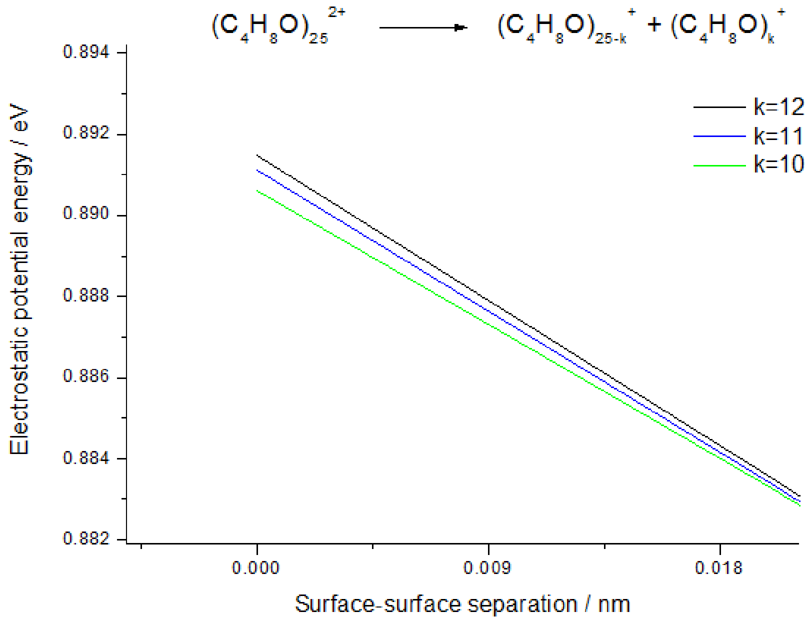

Figure 6.3: Potential energy curves for the fragmentation pathways shown in figure 6.1 at very short separations

6.3 Triply Charged THF Clusters

Triply charged THF clusters are detected by using the mass scanning technique. The critical size is found to be $(C_4H_8O)_{51}^{3+}$, located underneath the singularly charged $(C_4H_8O)_{17}^{+}$ peak. Figure 6.4 shows the mass spectrum, with the strong onset of the triply charged species clearly visible. Additional feature are seen in the mass spectrum (figure 6.4) including a peak from the addition of water to the doubly charged cluster ions, appearing 9 amu above the doubly charged n-mer: $(C_4H_8O)_n(H_2O)^{2+}$.

Figure 6.5 shows the coulomb fission of $(C_4H_8O)_{53}^{3+}$ ions in the 2nd *ffr*. Applying Equation 2.10, energy values for these peaks in the resultant MIKE spectra show that the fission mechanism is the ejection of small singly charged clusters from the precursor cluster ion with the larger of the two fragments retaining approximately 80% of the initial mass. six pathways are shown, corresponding to the loss of a singularly charged cluster containing between 7 and 12 molecules. The most intense channels are in the k=9-11 region with a dip in intensity for k=10. In most cases in this work the coulomb fission of triply charged clusters shows a finite range of peaks with the intensity tend indicative of how well the lifetime of the particular fission pathway agrees with the experimental constraints. This is evidenced by the intensity trend in the MIKE peaks with the peak with maximum intensity in the middle of the range of peaks. It would follow from this that the k=10 pathway would have the most agreeable lifetime and hence, expected to form the most intense peak. It is noted with respect to figure 6.5 that odd-numbered fragments have an increased intensity which could be a reflection an increase of stability in odd-numbered fragments relative to even-numbered. It is more likely, however, that this observation is due to an aberration in the experimental measurement of the k=10 fragment peak resulting in an unfortunate loss of sensitivity, otherwise the overall trend of the profile would agree with the intensity trends predicted by the lifetime model. The simulated peaks are overlain in blue and are show good fitting. A small deviation is seen in the predicted degree of dishing, the simulated peaks showing increasing amounts of dishing as the fragment reduces in size and undergoes more divergence following coulomb fission. This is not matched by the peaks in the MIKE spectra, possibly because the predicted increase in dishing is too slight to be picked up by the apparatus which is set up to maximise sensitivity with the inevitable detriment of resolution. The values for U_{max} and <*KER*> for the observed channels are given in Table 6.2 and close agreement is seen in all cases

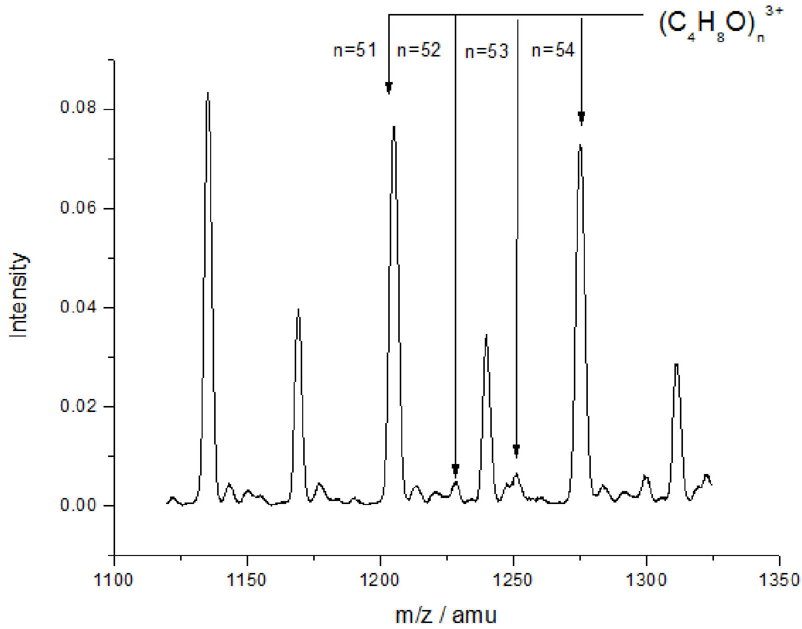

Figure 6.4: A mass spectrum showing the critical region of triply charged THF clusters

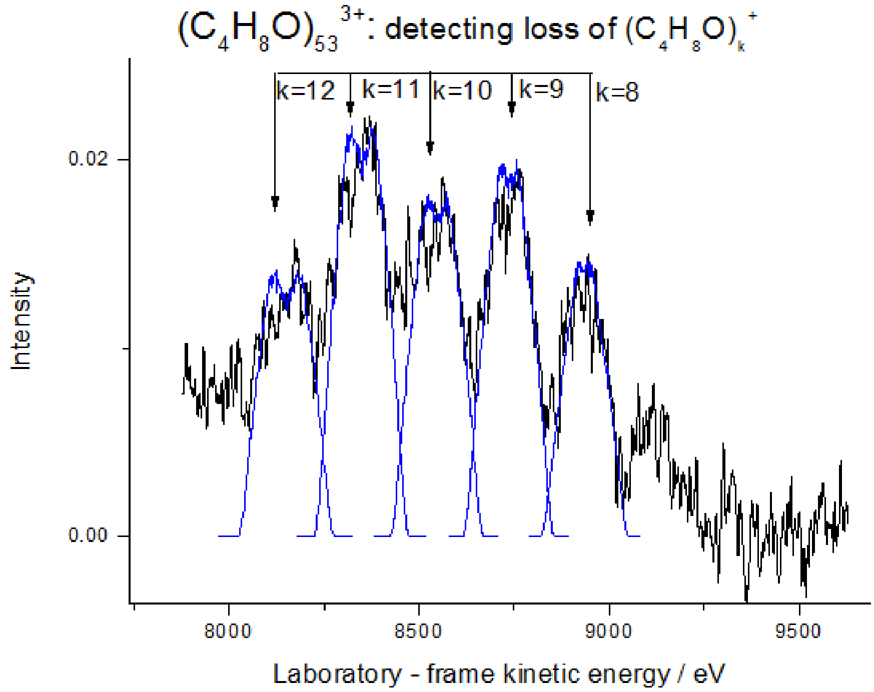

Figure 6.5: MIKE scan showing the fragmentation for the fission of $(C_4H_8O)_{53}^{3+}$.overlain in blue are the simulated peaks

Precursor cluster	Fragment	U_{max} / eV	<KER> / eV
$(C_4H_8O)_{53}^{3+}$	k=8	1.48	1.46
	k=9	1.47	1.55
	k=10	1.46	1.55
	k=11	1.46	1.55
	k=12	1.45	1.54

Table 6.2: The calculated values of barrier height and <KER> for the $(C_4H_8O)_{53}^{3+}$ cluster fission

Figure 6.6 shows the potential energy curves calculated for the pathways observed for the fission of $(C_4H_8O)_{53}^{3+}$. It can be seen that the curves are purely repulsive, with the asymmetric k=8 pathway showing the largest potential energy over all separations. Although the smaller of the two fragments has roughly the same charge density and the larger of the two fragments is much larger than in the 1+/1+ dication fission, the increase of total charge to 3+ leads the electrostatic repulsion to dominate the interaction. This means that the most asymmetric k=8 pathway shows the largest potential energy over all separations, this is due to the increased effectiveness of the repulsion from the more charge dense smaller fragment.

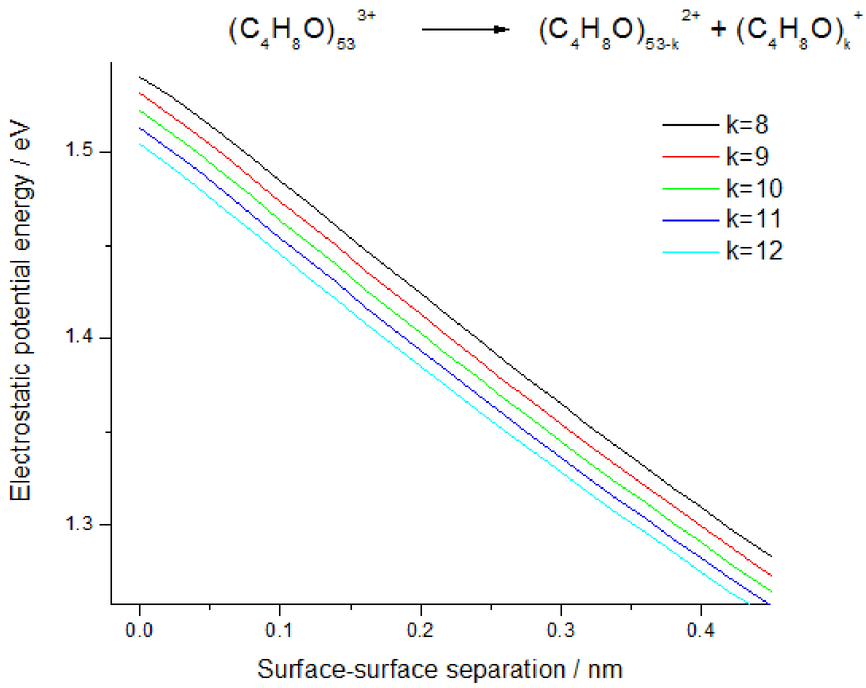

Figure 6.6: Potential energy curves for the interaction between the fragments for the pathways shown in figure 6.5

6.4 Fourfold Charged THF Clusters

The detection of fourfold charged THF clusters was achieved using the MIKE scanning technique. The ideal method of using the mass scanning technique to identify non-integer peaks was complicated by the presence of background signals and existing multiply charged peaks in the spectrum, making the resolution of discrete 4+ peaks difficult. To circumvent this it is noted that fourfold charged clusters above the critical size will exist underneath doubly charged cluster peaks of ½ the mass. Therefore, it is possible to use the MIKE scanning technique to search for the fragments of a known fourfold precursor by using the strong signal from a coincident cluster ion for mass selection. The neutral loss channel of the fourfold charged cluster was monitored as a function of size above the predicted critical size $n_{crit}(4)$ from the liquid drop model. Once a signal is detected it can be tuned to, and monitored as a function of decreasing size until it disappears completely. Figure 6.7 shows two MIKE scans around the critical region for fourfold charged THF. Figure 6.7a show 4 peaks originating from $(C_4H_8O)_{119}^{4+}$ and additional close lying precursor ions $(C_4H_8O)_{89}^{3+}$ and $(C_4H_8O)_{30}^{+}$, close to the cluster in terms of m/z. The high energy peak around 7000 eV is the precursor and the identities of the fragments are identified by using equation 2.10. The first peak lower in energy from the precursor corresponds to the loss of a single neutral monomer from the $(C_4H_8O)_{119}^{4+}$. This is followed by two peaks from the loss of a neutral molecule from the close-lying triply and singly charged precursor ions. These features are resolved as it is necessary to maximise the signal sensitivity at the detector by reducing the focusing of the ion beam around the magnet and hence the mass resolution. This allows ions that do not satisfy the nominal m/z constraints of the magnet to pass through. Ions with a value of m/z close to $(C_4H_8O)_{119}^{4+}$ can follow the curvature of the magnet and undergo fragmentation producing the additional peaks seen in figure

6.8a. The peak at approximately 6925 eV corresponds to a fragment of $(C_4H_8O)_{89}^{3+}$ that has lost a neutral molecule and the peak at approximately 6800 eV corresponds to the precursor $(C_4H_8O)_{30}^{+}$ losing one molecule. Figure 6.7b shows the MIKE spectrum of the imaginary fourfold charged precursor '$(C_4H_8O)_{105}^{4+}$' which is shown to be below the critical size and is coincident with the $(C_4H_8O)_{27}^{2+}$ ion. Applying the same methodology as above, both fragment peaks are determined to be fragments from the $(C_4H_8O)_{27}^{2+}$ ion. The peak at approximately 6890 eV is the loss of one neutral monomer and the peak at approximately 6750 eV is the loss of two monomers. The absence of a fourfold charged fragment from the '$(C_4H_8O)_{105}^{4+}$' ion which (predicted to be at approximately 6933 eV) indicates that the critical size $n_{crit}(4)$ is above n=105. Further observations on the signals resulting from coulomb fission lead to an assignment of $n_{crit}(4)$ = 107.

Figure 6.8 shows the result of performing a MIKE scan for the detection of charged fragments following coulomb fission of mass selected $(C_4H_8O)_{110}^{4+}$ ions. Three large peaks are observed with the centres of the peaks roughly 200 eV apart, this is a similar observation to fourfold benzene clusters and acetonitrile clusters, so it might be expected that the coulomb fission is following the same mechanism and forming the same charge states 3+ /1+. Applying equation 2.10 with Z_f = 3 gives calculated fragment sizes of 96, 98, 100, using this information the barrier heights for these channels are calculated and the peaks are simulated, these are shown in figure 6.9. The values for the barrier height and $<KER>$ for each pathway is given in table 6.3. As seen, using the values of U_{max} as a guide, well fitted peaks are produced with values of $< KER >$ closely matching the predicted energies. The alternative possibility can be examined using the same methodology. Figure 6.10 shows the simulated peak for the fission into two doubly charged fragments corresponding to the central feature in the MIKE spectrum. The peak is wide with a large degree of dishing which is due to the relative lightness of the fragment making it more susceptible to divergence and the resultant instrumental discrimination. It can be readily seen that even though the magnitude of $< KER >$ closely matches U_{max}, the resultant peak does not resemble any of the experimental features in either width or degree of dishing. Therefore, only the 3+/1+ mechanism is considered.

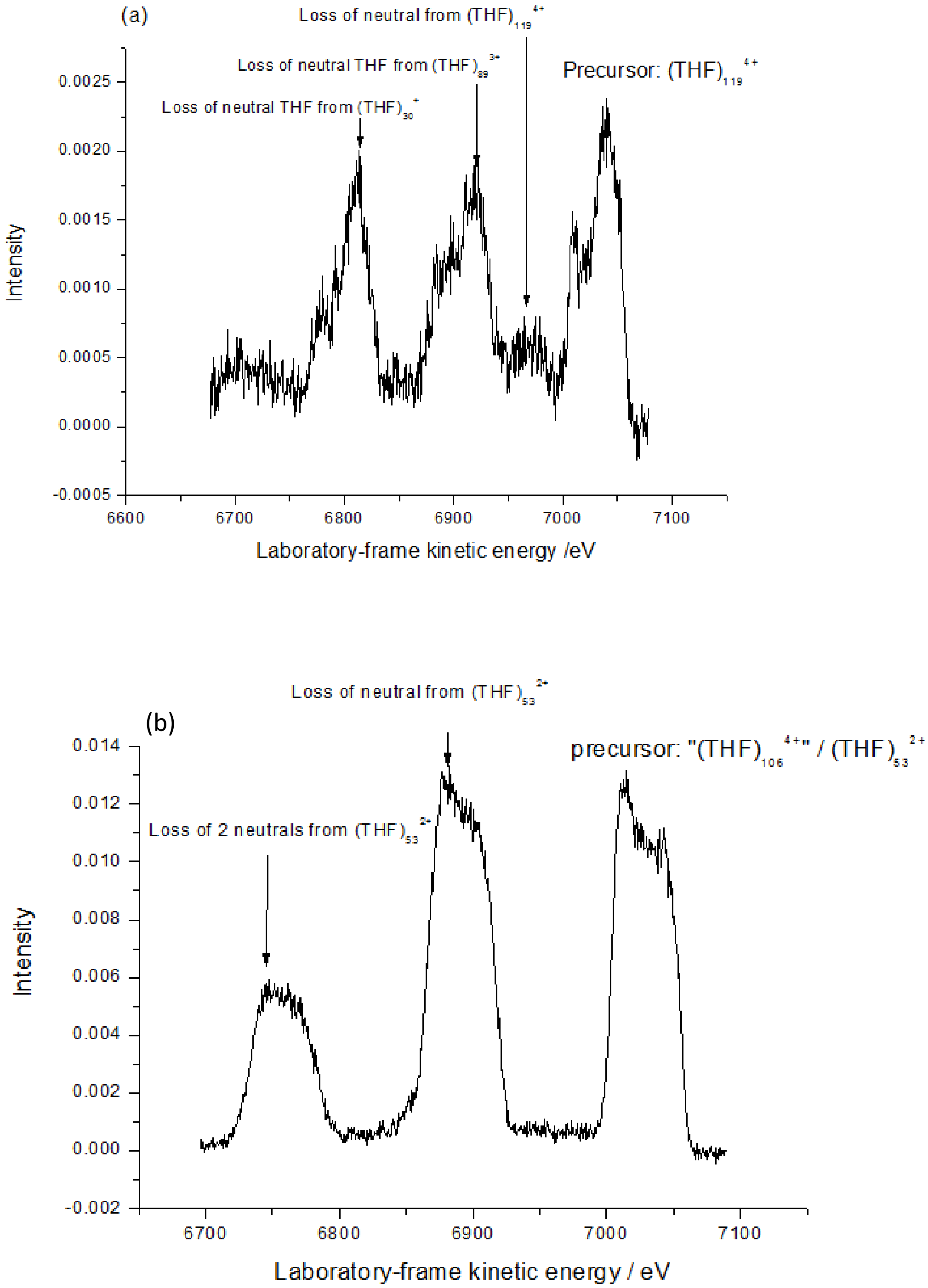

Figure 6.7: MIKE spectra showing fragments resulting from (a) $(C_4H_8O)_{119}^{4+}$ and (b) $(C_4H_8O)_{53}^{2+}$

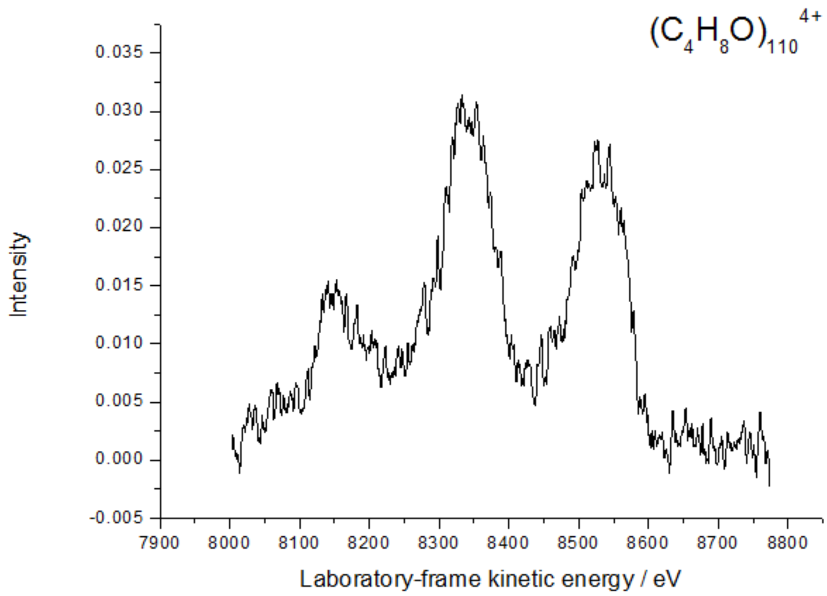

Figure 6.8: MIKE spectra showing fission from the precursor ion $(C_4H_8O)_{110}^{4+}$

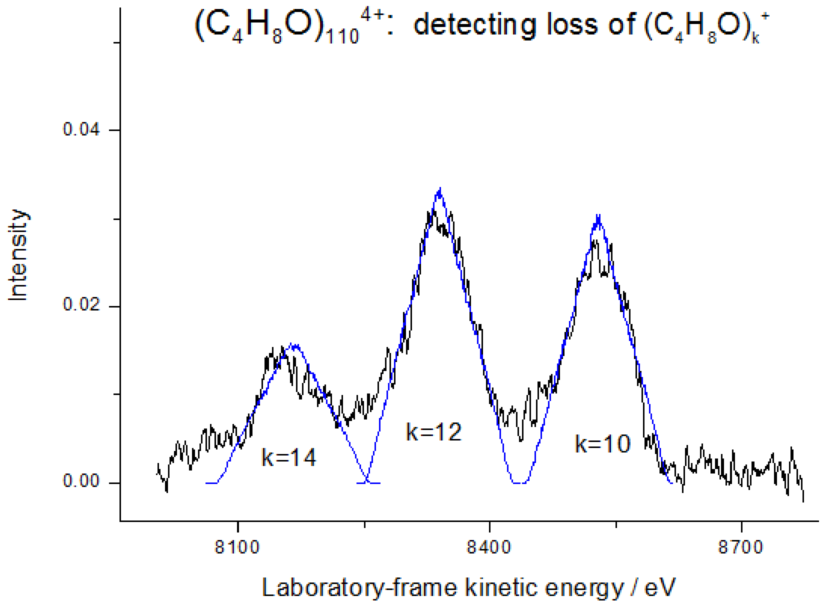

Figure 6.9: Figure 6.9 overlain with the fitted simulated peaks from the fragmentation into 3+/1+ fragments

Precursor cluster	Fragmentation pathway	U_{max} / eV	$< KER >$ / eV
$(C_4H_8O)_{110}^{4+}$	$K=10^+$	1.83	1.66
	$K=12^+$	1.81	1.66
	$K=14^+$	1.79	1.65

Table 6.3: The calculated values of U_{max} and $< KER >$ for the pathways shown in figure 6.9

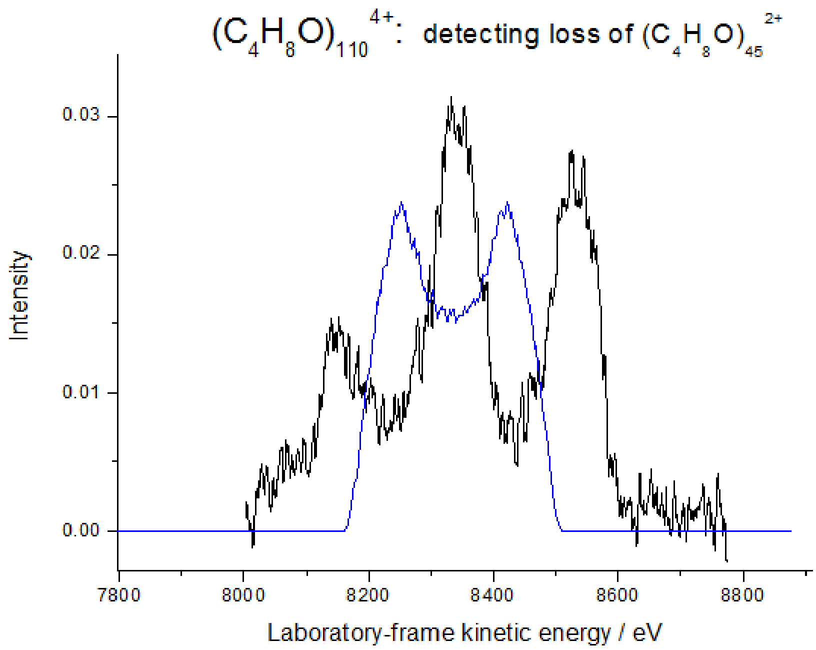

Figure 6.10: Figure 6.7 overlain with the simulated peak for the fission into 65^{2+} and 45^{2+} fragments

Precursor cluster	Fragmentation pathway	U_{max} / eV	$< KER >$ / eV
$(C_4H_8O)_{110}^{4+}$	$K=45^{2+}$	2.17	2.17

Table 6.4: The calculated values of U_{max} and $< KER >$ for the pathway shown in figure 6.10

6.5 Stability of Multiply Charged THF Clusters

Due to the first assignment of critical sizes for a charge range of Z_p= 2 - 4 in THF clusters there is an opportunity to compare experimental data on stability to what is predicted by existing theory. Table 6.5 and Figure 6.11 shows comparison with critical size values that were determined in the preceding sections compared against what is predicted by the Rayleigh equation (equation 1.1):

$$n_{crit}(z) = \frac{(ze)^2}{64\pi^2\gamma\varepsilon_0 {r_m}^3}$$

Where z is the charge state of the precursor, e is the elementary charge constant, γ is the surface tension ε_0 is the permittivity of free space and r_m is the molecular radius. Agreement is good for Z_p = 2, 3 with the two sets of data agreeing to within approximately 4%, however, there is a divergence in the sets of data at Z_p = 4 with the two values agreeing only to 20%. This is similar to the observation for the benzene and acetonitrile systems. It would seem that either the experimental determination is incorrect, or, the liquid drop model is not adequately describing the stability of these larger clusters. Taking the first presumption, the critical size determination was carried out by running MIKE scans over a range of fourfold charge clusters, monitoring the neutral loss channel. Although characteristically not as small as coulomb fission signals, these signals will still be small around the critical size, and hence, difficult to pick up at detection. However, Figure 6.7b shows a reasonably clean baseline for what would be $(C_4H_8O)_{106}{}^{4+}$ in the region where fragmentation is expected. Assuming the liquid drop model is correct for THF ($n_{crit}(4) = 86$), a size increase of 20 molecules should be great enough to yield large enough ion signals at $(C_4H_8O)_{106}{}^{4+}$ to be detected. It may be that the fourfold charged clusters in this size range size do not possess a barrier to fission ($\Delta E_{fission}$) great enough to stabilise it against inter-charge repulsion in the correct timeframe. In this instance most precursor clusters will undergo fission before the magnetic sector and hence no evidence of that precursor from fragmentation will be observed at detection.

If the nature of the cluster deviates significantly from the assumptions of the liquid drop model then it is possible that the model will not be able to adequately describe the stability of the system. A major assumption is that the shape of the cluster is spherical. However, the shape of the final cluster is determined by the orientation of the molecules relative to each other as the cluster grows during the cluster growth phase in the supersonic expansion. There are no strong directional hydrogen bonds in THF clusters that can allow for the growth of the cluster in three dimensions. This has been shown to produce spherical structures for ammonia [4] and water clusters [5]. Small benzene crystals have been shown to exhibit stacking characteristics due the overlap of the π – systems and increased geometrical efficiency [6]. Although THF lacks a ring of π – electrons it does possess a 5 atom ring structure with a strongly δ^- oxygen atom which could influence a stacking configuration, in which the O atoms are positioned at opposite ends at every layer to minimise the repulsion between δ^- atoms. On the scale of size that the fourfold clusters exhibit, this would lead to a very large and non-spherical shaped cluster. The deviation from a spherical shape can have implications for the overall stability of the cluster. As mentioned previously, a spherical geometry minimises the surface energy of the cluster, whilst keeping the total charge uniformly spaced on the surface of the cluster. The loss of spherical shape can have an effect on the proximity of the surface charge and it is possible that the charges will be closer together, increasing the overall energy of the cluster. These factors would necessitate the addition of molecules beyond the predicted size to stabilise the cluster.

As mentioned, there is a degree uncertainty in the assignments of critical sizes due to experimental constraints. By definition the critical size is the smallest possible number of molecules needed to stabilise a given number of charges. This intrinsic stability is predicated by the presence of an energy barrier that gives the charged clusters a lifetime great enough to be detected, in other words, it becomes metastable. It might be that the onset of the barrier to fission is only very small in the case of fourfold charged clusters compared to lower ordered examples, perhaps due to the geometry of the cluster. This would mean a range of clusters above the critical size that are not stable enough to be detected as they will undergo fission before entering the 2nd *ffr* or will not be present in a great enough number in the ion beam to produce a detectable signal.

It should be noted that the geometric constraints of the dielectric particle model require the fragment clusters to be spherical. The close agreement in the values of $< KER >$ to the values of U_{max} for the fitted 3+/1+ profiles suggest that this is the case. However, as stated previously, there is doubt as to whether THF cluster are spherical. In the examples shown of the fourfold cluster $(C_4H_8CN)_{110}^{4+}$ breaking into 3+/1+ fragments, the singularly charged smaller fragment does not exceed a size of 14 molecules. It is possible at this size that the fragment has not deviated in terms of function from ideal spherical shape. Indeed it is still acting on the larger cluster in the same fashion, as a source of an electric field, applied to a much bigger body.

Charge state z_p	Experimental $n_{crit}(z)$	Calculated $n_{crit}(z)$	% Difference
2	24	22	8
3	51	48	6
4	107	86	20

Table 6.5: Values for the experimental and calculated critical sizes

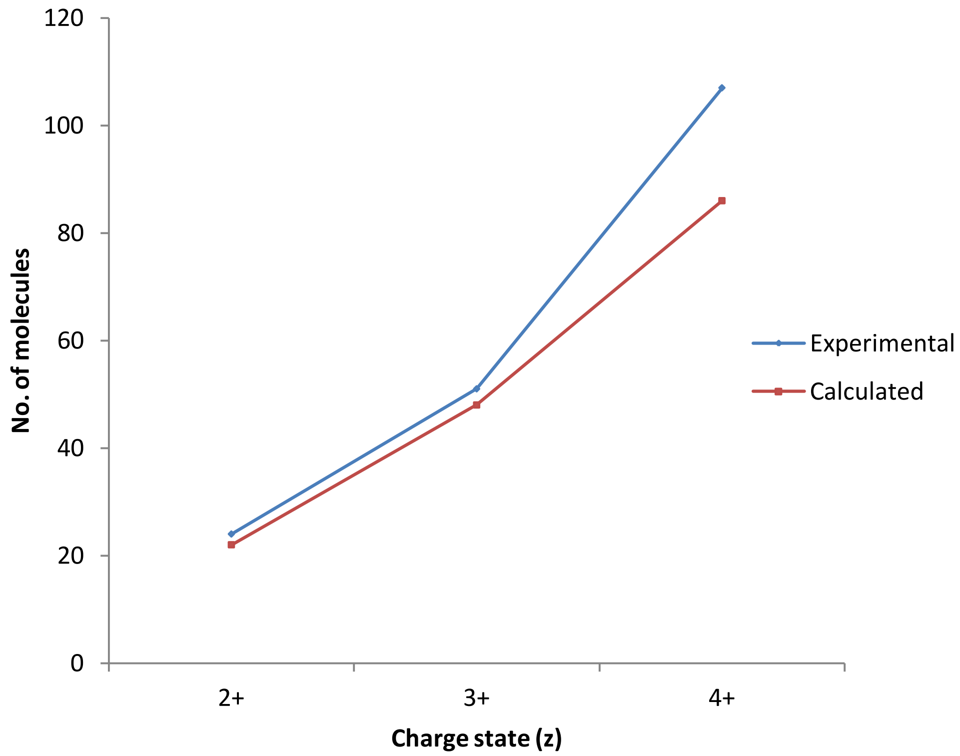

Figure 6.11: A plot of the experimental and critical sizes as a function of charge z

6.6 Conclusions

First measurements on multiply charged THF clusters have allowed the study of the stability and coulomb fission reactions around the onset of instability. A combination of mass scanning and MIKE scanning techniques have been used to accomplish this. The fission of doubly charged THF clusters is found to proceed in a similar fashion to the other systems studied in this work. A range of dish-shaped peaks are observed and correspond to incremental change in the size of the fragment. The range of fragments observed is dependent on the range of lifetimes of the fragments being in agreement to the experimental constraints. For the case of THF clusters the increase in intensity towards the fragment peak of maximum symmetry is unusual with respect to the other systems studied which all show a greater degree of asymmetry in the profiles observed. Additionally, the barrier heights (U_{max}) do not differ to 2 d.p. so a very similar lifetimes are expected between fragments with one molecule difference. From a qualitative perspective asymmetric fragmentation should be favoured as the ejection of a small ion from the precursor minimises the number of bonds needed to be broken. The reason for symmetric fragmentation may be that the critical shape of the precursor immediately before the fission event may be symmetric. This could be a result of the directed vibrational energy into the collective symmetric mode. This will also result in an increase in total surface energy.

Fission from triply charged THF clusters produced a range of detectable fragments, similar to what is seen in other systems. Values of U_{max} are used to simulated fragment peaks which match the experimental features well in terms of width. The calculated <*KERs*> agree with the U_{max} predictions. The electrostatic potential energy curves are shown to be repulsive, due to the small value of the dielectric constant.

The identification of fourfold charged THF clusters is achieved by using the MIKE scanning technique to follow the neutral loss pathway over a size range covering the critical size $n_{crit}(4)$. This is subject to a degree of uncertainty due to the fact that only the clusters coincident with more intense singularly and doubly charged ions are measured, to ensure correct mass selection. Above the critical size coulomb fission is shown to follow the mechanism forming 3+/1+ charged fragments. The <*KER*s> of the fitted simulated peaks give accurate account of the barrier heights, however, the range of fragments is non-sequential, with only even numbered fragments detected. This is could be due to the structural geometry providing special stability to the even numbered fragments.

References

1. L. K. W. J. Piel, *Ethers*. Kirk-Othmer Encyclopedia of Chemical Technology (John Wiley and Sons, Inc, 2004).
2. H. Muller, *Tetrahydrofuran*. Encyclopedia of Industrial Chemistry (2002).
3. G. Pruckmayr, P. Dreyfuss, M. P. Dreyfuss, *Polyethers, Tetrahydrofuran and Oxetane,* Kirk-Othmer Encyclopedia of Chemical Technology (John Wiley & Sons, inc. , 1996).
4. T. A. Beu, U. Buck, *Journal of Chemical Physics* **114**, 7848 (2001).
5. T. James, D. J. Wales, J. Hernandez-Rojas, *Chemical Physics Letters* **415**, 302 (2005).
6. M. L. Glowka, D. Martynowski, K. Kozlowska, *Journal of Molecular Structure* **474**, 81 (1999).

Chapter 7 : Multiply Charged Water Clusters

7.1 Introduction

Water is the most abundant compound on earth, covering the majority of the planet and present in the atmosphere. It is sometimes termed 'nature's solvent' because of the prominent role it plays in the sustenance of life on the planet. The anomalous physical properties of water have played a significant role in the evolution of life [1]. It is therefore no surprise that water is among the most commonly studied materials. The motivation to study water clusters is partly because the evolution of the physical properties that make it so interesting a species can be observed in the size regime that clustering provides [1]. Water clustering has been linked with the formation of acid rain in clouds [2] and the nucleation of rain droplets [3]. The large dipole moment in the O-H bond informs a large polarisability of the molecule and the consequent dielectric constant of the bulk species ($\varepsilon_r = 80$).

Multiply charged water clusters are observable in a mass spectrum. Early recorded examples were presented by Stace [4] that showed the onset of multiply charged cluster peaks for precursors up to $Z_p = 3$. The work of Chen *et al.* [5] presented direct observations of the charged fragments from coulomb fission of dication water clusters. The *KER* determined from the FWHM of the experimental peaks was found to be in good agreement with the predicted barrier heights from the dielectric particle model. Due to the large dielectric constant of water and the consequent polarisability of the fragments the potential energy curves were found to be attractive at short distances. This provides evidence that under certain conditions the formation of water droplets from like charged constituents may indeed be possible. A mechanism has been presented previously to explain the phenomena of like charge attraction and binding [6]. The work presented shows updated analysis on the previously studied dication water clusters. Utilisation of the peak simulation methodology allows for assignment of the average kinetic energy release (<*KER*>) of the fission processes that more accurately describes the energy releases contained in the experimental features. This is carried forward with the study of the stability and coulomb fission for higher order charged systems.

7.2 Doubly Charged Water Clusters

Doubly charged water clusters are observed from the onset of non-integer peaks in the mass spectrum corresponding to $(H_2O)_n^{2+}$ clusters. Figure 7.1 shows an example where beyond a size of n=35 peaks corresponding to doubly charged water clusters are observed. The strength of the signal increases rapidly with size until n=39 where the signal is roughly half the intensity of the singularly charged peaks. Improvements in resolution may reveal individual peaks that result from the intra-cluster ion-molecule reaction that results in protonated forms of the cluster. These reactions have been studied by Stace [4] who was able to identify two peaks and assign them as the un-protonated and doubly protonated forms of the cluster as a result of an intra-cluster protonation reaction.

$$H_2O^+ + H_2O^+ \;\rightarrow\; H_3O^+ + OH$$

Therefore, the cluster ion $(H_2O)_{37}H_2^{2+}$ can be re-written as: $(H_2O)_{35}.(H_3O)^+_2$. Improvements in the resolution of the mass spectrum would reveal the relative intensities of the non-protonated to the doubly protonated cluster peaks.

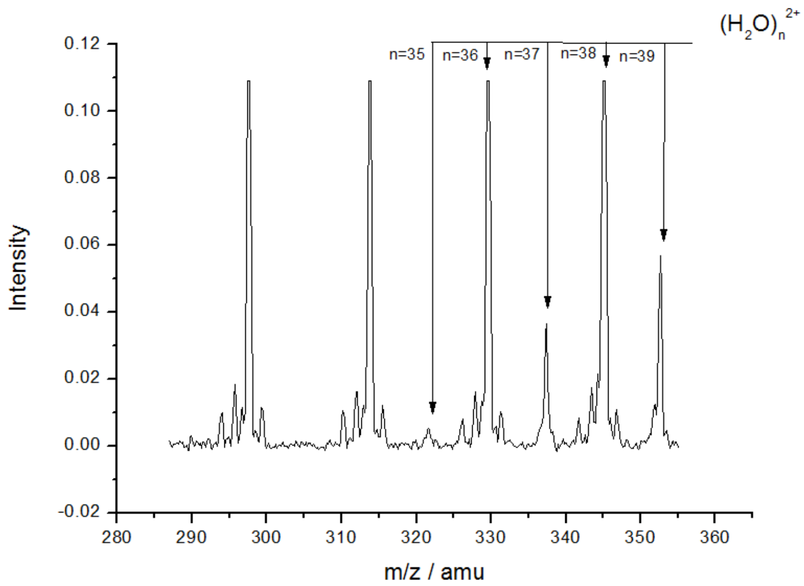

Figure 7.1: Mass spectrum showing the onset of doubly charged water clusters

Figure 7.2 shows the MIKE spectrum following coulomb fission of the $(H_2O)_{37}^{2+}$ ion into singly charged fragments [5,7]. Overlain in blue are the simulated peaks calculated by the peak simulation model. For the purposes of calculation only the non-protonated forms of cluster are considered; the difference in size of one proton will not have a significant effect on the value of U_{max} or the divergence from the main ion beam, and therefore the peak shape. It can be seen that the experimental peak shape is accounted for by the model with the value of $< KER >$ from the distribution of allowed values corresponding well to the predicted barrier height U_{max}. Table 7.1 shows a comparison of the values taken for the KER using the old methodology and it is seen that by using the new methodology closer agreement to the predicted barrier heights is achieved, roughly 97% compared to 80%.

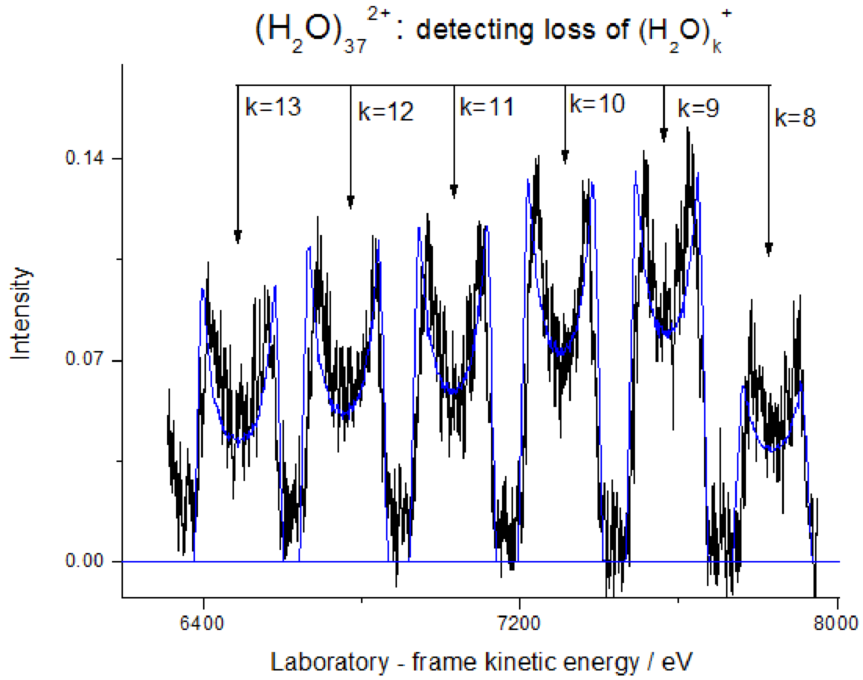

Figure 7.2: MIKE spectrum showing the fragments formed from coulomb fission of the $(H_2O)_{37}^{2+}$ ion [7]. Overlain are the simulated peaks from the peak simulation model

Precursor cluster	Fragment channel	$< KER >$/eV	KER	U_{max} /eV
$(H_2O)_{37}^{2+}$	K=8⁺	1.17	0.94	1.19
	K=9⁺	1.17	0.97	1.20
	K=10⁺	1.17	0.99	1.20
	k=11⁺	1.17	0.91	1.21
	k=12⁺	1.17	0.96	1.22
	k=13⁺	1.17	1.00	1.22

Table 7.7.1: Values of $< KER >$ from the fitted peaks and U_{max} for the fragmentation channels shown in figure 7.2. Included for comparison are values of KER calculated using the old methodology [7]

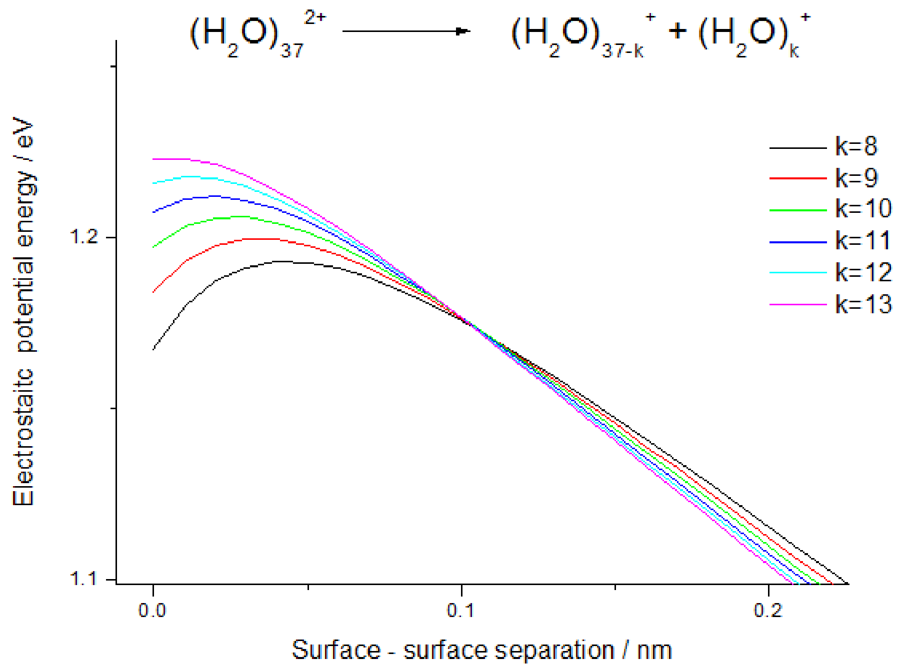

Figure 7.3: The potential energy curves calculated for the separating fragments for the pathways shown in figure 7.2

Figure 7.3 shows the electrostatic potential energy curves for the separating cluster fragments post coulomb fission for the pathways observed in figure 7.2. It is seen that in the cases of high mass asymmetry the curves are seen to rise to maximum values of potential energy (U_{max}) at surface-surface separation greater than 0. This is due to the strong attenuation of the electrostatic repulsion by induced attractive potentials brought about by the polarisation of the larger of the fragments by the charge-dense smaller fragment. The polarisability is directed by the value of the dielectric constant, which in the case of water is relatively large (ε_r = 80), this accounted for in the model with large attractive terms. Beyond a separation of approximately 0.1 nm the induced potentials lose the influence on the calculation and the curves are seen to switch over. This indicates that the electrostatic repulsion, which is more effective in cases of high asymmetry, now dominates the calculation. The smaller sphere in cases of high asymmetry will have a higher charge density and therefore will result in stronger repulsion.

7.3 Triply Charged Water Clusters

Triply charged water clusters of the form $(H_2O)_n^{3+}$ have been observed in a mass spectrum. Taking a range that includes the critical size $n_{crit} = 84$ an onset of a series of peaks is observed that correspond to triply charged water species. Water can undergo a protonation reaction to produce either singularly or triply protonated forms of the triply charged cluster. These species were studied by Stace [4]. As noted, this is at slight variance with ammonia (Chapter 5) in that the doubly protonated form is not observed. This has been attributed to the difference in exothermicity between the reactions in the cluster systems [8]. Figure 7.4a shows a mass spectrum in the region of the onset of triply charged clusters beyond the critical size. As can be seen from the spectrum, the peaks grow in intensity rapidly as the cluster size increases, until they are approximately half the peak height of the neighbouring doubly charged peaks. Figure 7.4b shows an expanded view of the spectrum, the different protonated forms are labelled. It is perhaps more accurate to re-write the observed $(H_2O)_nH_3^{3+}$ ion as $(H_2O)_{n-3}(H_3O^+)_3$. The presence of the $(H_2O)_{n-3}(H_3O^+)_3$ ion can be explained by considering that the form of the dimer ion $(H_2O)_2^+$ takes the form of a proton transfer complex (H_3O^+.....OH). Extending this to the triply charged, singularly protonated cluster ion ($(H_2O)_nH^+$) gives the form $(H_2O)_{n-5}(H_3O^+....OH)_2 \cdot H_3O^+$. The lack of observation of the $(H_2O)_nH_2^{3+}$ ion suggests that the presence of $(H_3O^+....OH)_2$ is required to stabilise the structure, adding to the hydrogen bonding network. It is apparent that the un-protonated form is not detected in the mass spectrum. This is probably due to the mentioned exothermicity of the protonation reaction driving the reaction at each charge centre leaving a diminished number of un-protonated clusters in the ion beam at detection. It is assumed at the high level of resolving power in the mass spectrum the peaks separation of 1/3 amu between the un-protonated and singularly protonated cluster would be resolvable, revealing the existence of the un-protonated cluster if it existed.

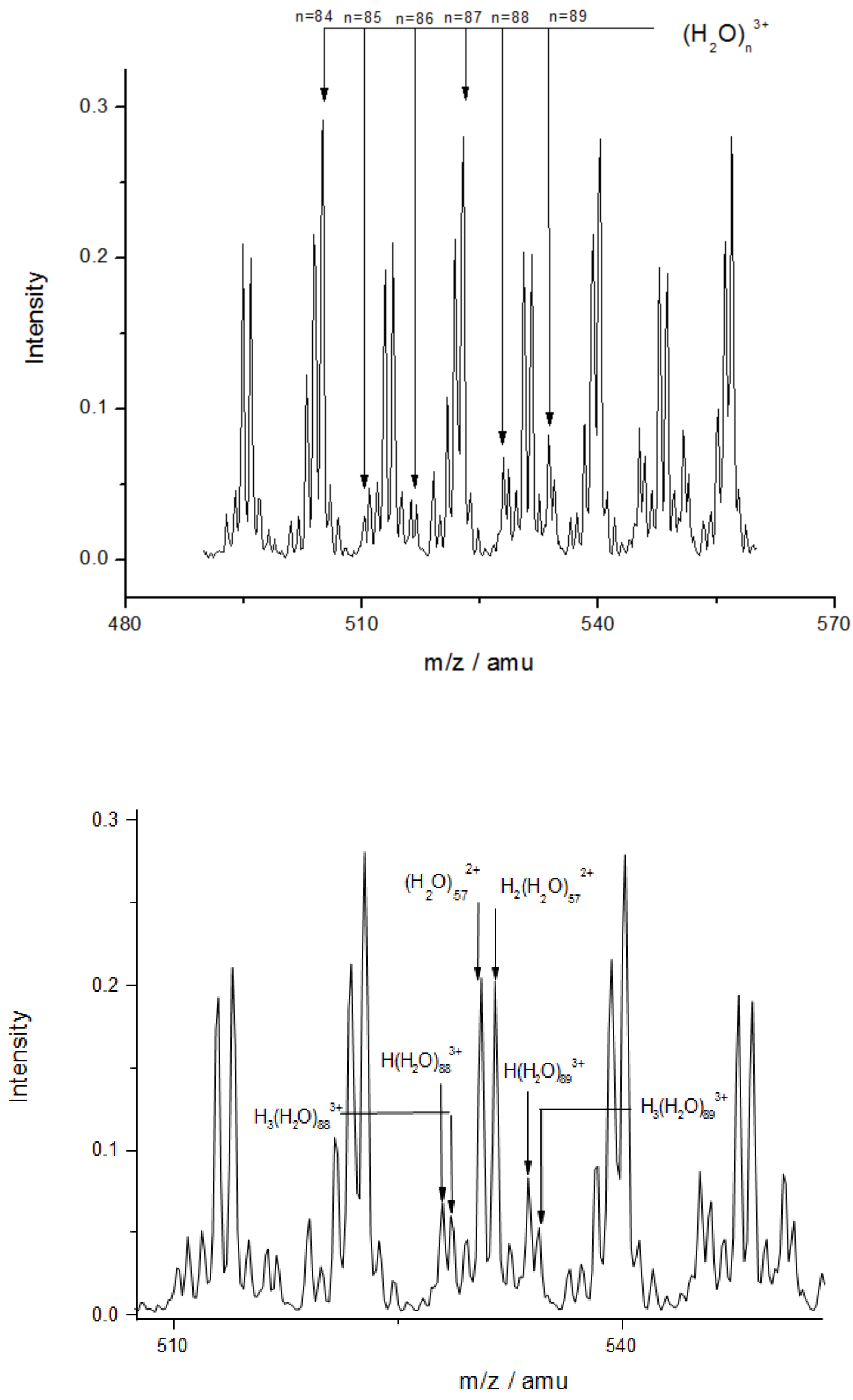

Figure 7.4: a) Mass spectra showing the region of onset of triply charged water clusters. b) An expanded view showing the peaks that make up the feature.

When performing a MIKE scan to search for the charged fragments from coulomb fission, to perform analysis it is necessary to maximise signal sensitivity to the detriment of mass resolution through the magnetic sector in order to obtain signal levels great enough for a fully formed peak to be resolved. This has the effect of allowing the multiple protonated forms of triply charged clusters to pass through the curvature of the magnet and into the 2nd *ffr.* The resultant fragmentations produce a MIKE spectrum that is complicated by components from the fission of precursors with mass difference of 2/3 amu into doubly charged fragments that can contain either none or two protons in the system. This effect can be visualised by applying Equation. 2.10 to the potential fragments, shown in figure 7.5. A MIKE spectrum of the fission of $H_x(H_2O)_{86}^{3+}$ is overlain with nominal values for the energies for the centres of the peaks; the added width to the peaks from the fission from and to the various possible protonated forms of the charged ammonia clusters can be visualised. The loss of resolution in the MIKE spectrum is an unfortunate consequence of the congestion of pathways, but some analysis can still be performed.

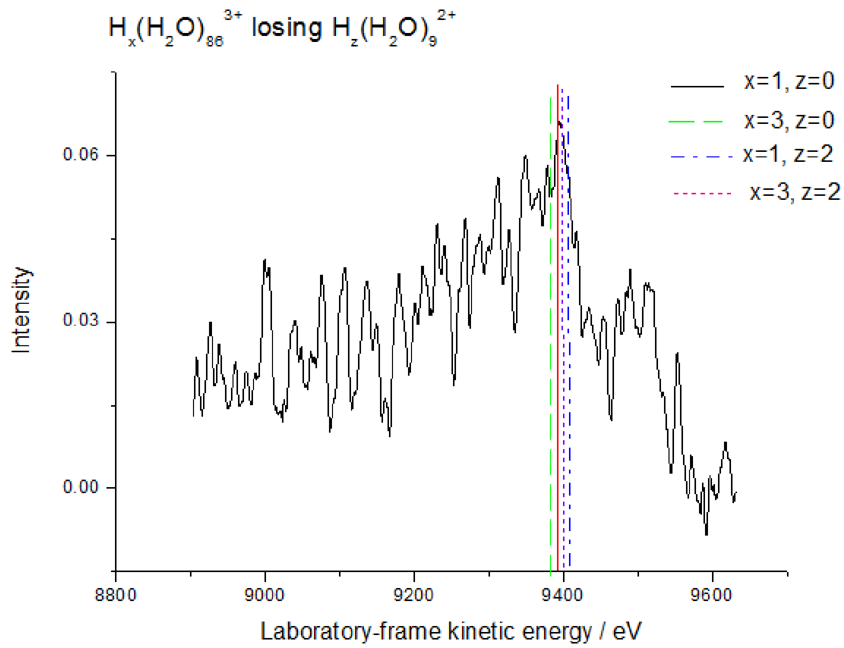

Figure 7.5: MIKE spectrum in the region of coulomb fission for forms of the $H_x(H_2O)_{86}^{3+}$ precursor. Overlain are the locations of the predicted energies for potential protonated forms of the 2+ charged fragment

Figure 7.6 shows the MIKE spectrum with the simulated peaks for the fragmentation pathways k=8-10 overlain. For ease of calculation only the theoretically non-existent un-protonated forms of the cluster have been considered. The difference of one proton to the overall mass of the system will be negligible in the calculation of the potential energy and the simulation of the distribution of allowed *KER*s that make up the metastable peaks. This is consistent with other simulations performed in this work where the 'bare' clusters are the only systems considered. Table 7.2 shows the predicted barrier heights and the values for $< KER >$ from the simulated peaks; the agreement is good but the simulated peaks cannot be regarded as 'fitted'. It would appear that the centres of the simulated peaks do not match the centres of the experimental features. With reference to the predicted values in figure 7.5, this might be a confirmation that the fission mechanism is proceeding with protonated forms of the cluster making up the precursor and the fragments. The energies of which are shown to fall within the maximum of the feature corresponding to the k=9 pathway. Additionally, the shapes of the features are not accounted for by the simulations. However, this could be explained by the relative weakness of the signal profile in general and so the shapes of the experimental peaks are not fully formed.

Figure 7.6 shows the potential energy curves for the fragmentation pathways shown in figure 7.5. A short range barrier to fission is present in all the curves, however increasing asymmetry does not result in a lowering of the value of U_{max}, only an increase in the magnitude of the barrier at separation > 0 nm. This could be due to the increased effectiveness of electrostatic repulsion balancing the improvement in the polarisability of the system at short separations, resulting in values of U_{max} that are similar.

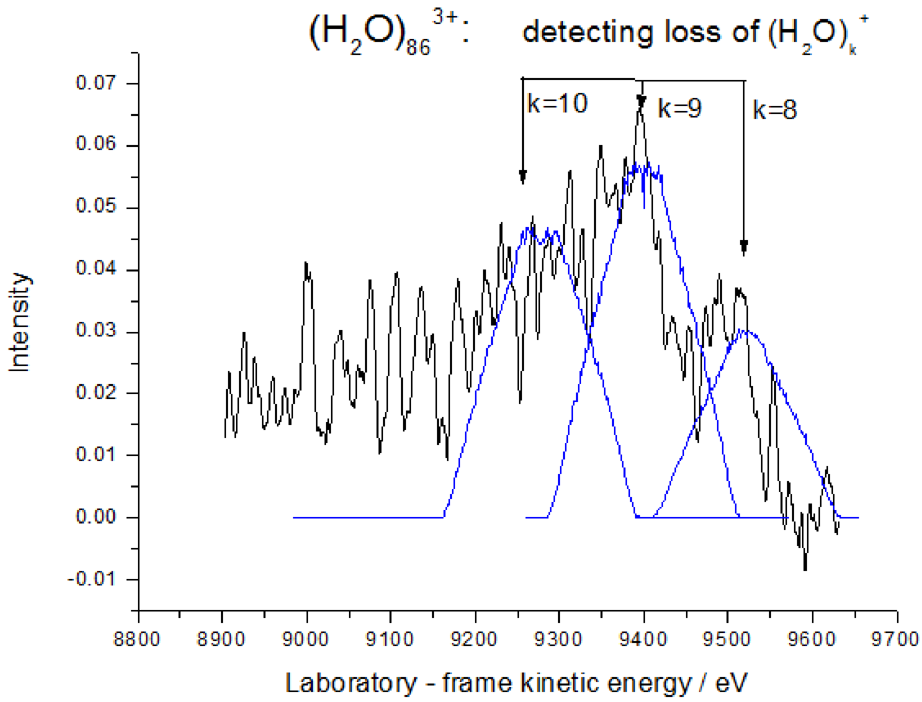

Figure 7.6: MIKE spectra showing the fission of $(H_2O)_{86}^{3+}$ overlain with the simulated peaks

Precursor cluster	Fragment channel	$< KER >$/eV	U_{max} /eV
$(H_2O)_{86}{}^{3+}$	$K=8^+$	1.97	1.20
	$K=9^+$	1.97	1.20
	$K=10^+$	1.97	1.19

Table 7.2: Values for the $< KER >$ for the simulated peaks and U_{max} for the pathways shown

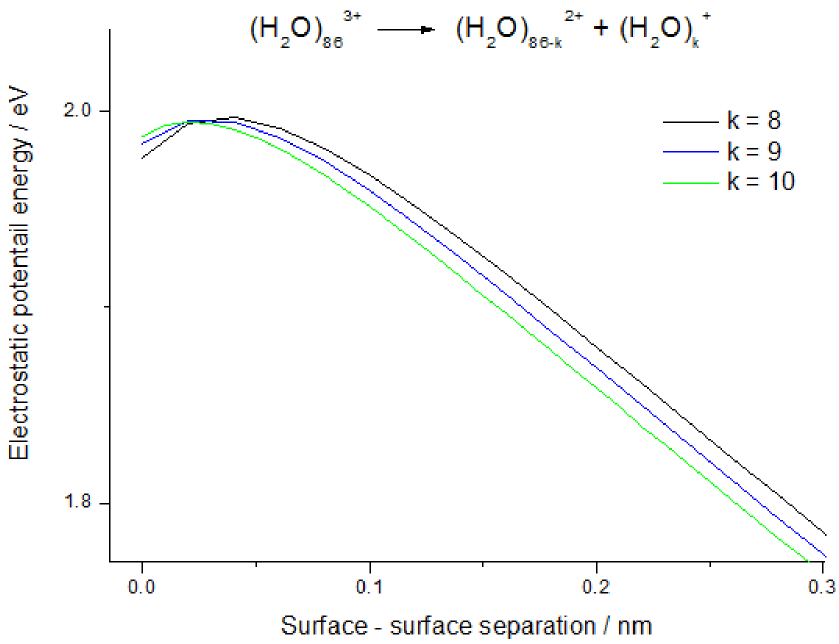

Figure 7.7: potential energy curves for the fragmentation pathways shown in figure 7.6

7.4 Fourfold Charged Water Clusters

The identification of fourfold charged precursor clusters could not be achieved by the mass scanning method. Under the experimental conditions, the resolving power of the magnet was not great enough to distinguish between the 3+ features (seen in figure 7.4) and the m/z values where distinct 4+ cluster peaks are expected. It was found that following the neutral loss pathway using the MIKE scanning technique, over a size range close to an expected critical size, revealed an onset of fragments originating from fourfold charged precursors. In order to minimise interference but guarantee sitting on the correct ion, the doubly charged ion peak corresponding to a cluster of half the mass was selected using the magnet. Above the critical size $n_{crit}(4)$ there will only be components from doubly and fourfold charged precursors under these peaks. Following a stepwise change in the size of the fourfold precursor cluster and monitoring the magnitude of the resultant MIKE peaks can assist in determining the critical size. Figure 7.8 shows an overlay of MIKE spectra from the fourfold charged cluster of size n. There are three main features present, the precursor peak at around 7000 eV and associated artefacts, a second feature around 6900 eV which corresponds to the fragment from the loss of one water molecule from the doubly charge component of the precursor ion signal. The third feature which is seen to evolve at 6950 eV is from the loss of one water molecule from the fourfold charged precursor:

$$(\mathrm{H_2O})_\mathrm{n}{}^{4+} \rightarrow (\mathrm{H_2O})_{\mathrm{n-1}}{}^{4+} + \mathrm{H_2O}$$

The third feature is seen to grow beyond a precursor size of n=150 to an intensity where it is a discernible peak. From this observation a critical size of $n_{crit}(4) = 150$ is assigned.

Following the suppositions of Stace [4] it is expected that a fourfold charged water clusters will have stable protonated forms of $(H_2O)_nH_2{}^{4+}$ and

$(H_2O)_nH_4^{4+}$ as well as the unprotonated $(H_2O)_n^{4+}$ ion. It would be inconceivable to expect to filter ions with a m/z difference of ½ amu with the experiment under normal MIKE scanning settings, therefore it is expected that the ion beam entering the 2nd *ffr* will contain components from all possible precursor forms.

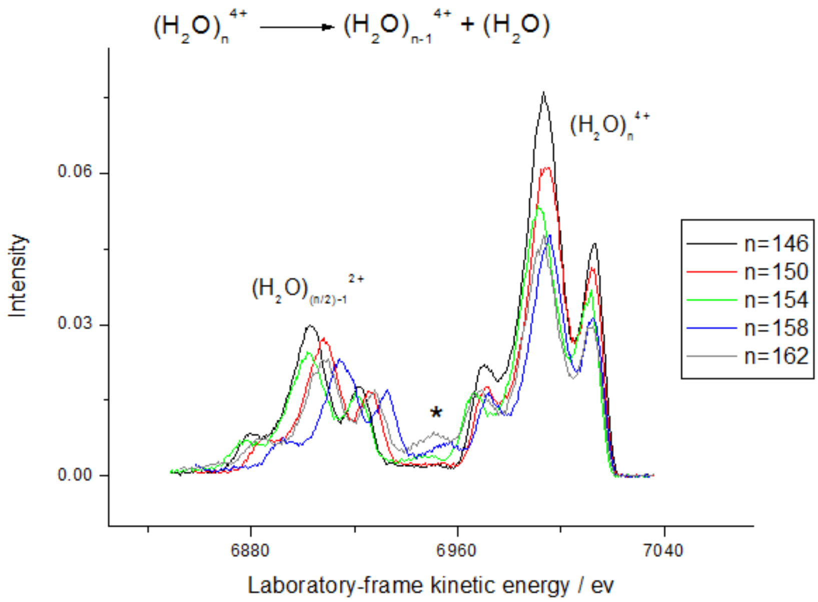

Figure 7.8: An overlay of MIKE spectra monitoring the neutral loss pathway for fourfold charged precursors at around 6940 eV. Asterisk denotes 4+ fragment

Figure 7.9 shows the MIKE spectra of the coulomb fission of $(H_2O)_{158}^{4+}$ precursor ions. When considering the potential pathways from a fourfold charged precursor, it can either fission into 3+/1+ fragments or 2+/2+ fragments. Application of equation 2.10 to the centre of the feature in Figure 7.8 reveals the detection of fragments in the order of either $(H_2O)_{99}^{2+}$ or $(H_2O)_{148}^{3+}$. It is possible to use the peak simulation methodology to simulate the peaks from the potential fragments to determine which fission mechanism is being followed. The values of the barrier heights U_{max} are used to help determine whether the resultant values of <*KER*> are appropriate.

Figure 7.10 shows the MIKE spectrum overlaid with the simulated peak for the detection of the doubly charged fragment $(H_2O)_{99}^{2+}$. Generally speaking the shape of the simulated peak matches the shape of the experimental feature, with a degree of simulated dishing originating from experimental discrimination. This is not seen in the experimental data, however this may be due to subsequent loss of neutral molecules which have a lower associated KER and so will not have significant divergence from the main beam at the focussing slit. From Table 7.3 the magnitude of the average kinetic release (2.15 eV) is significantly smaller than the predicted barrier (3.03 eV). This magnitude of disagreement is not seen in other systems studied in this work.

Figure 7.11 shows the same spectrum overlain with the simulated peaks for the detection of 3+ charged fragments of the 3+/1+ fission pathway. Due to the larger mass and smaller KER associated with the fragments, the shapes of the simulated peaks are more narrow and 'filled-in'. The experimental MIKE feature can be accounted for by six peaks. The agreement in the values of U_{max} and $< KER >$ is much closer than the example from the 2+/2+ fission mechanism.

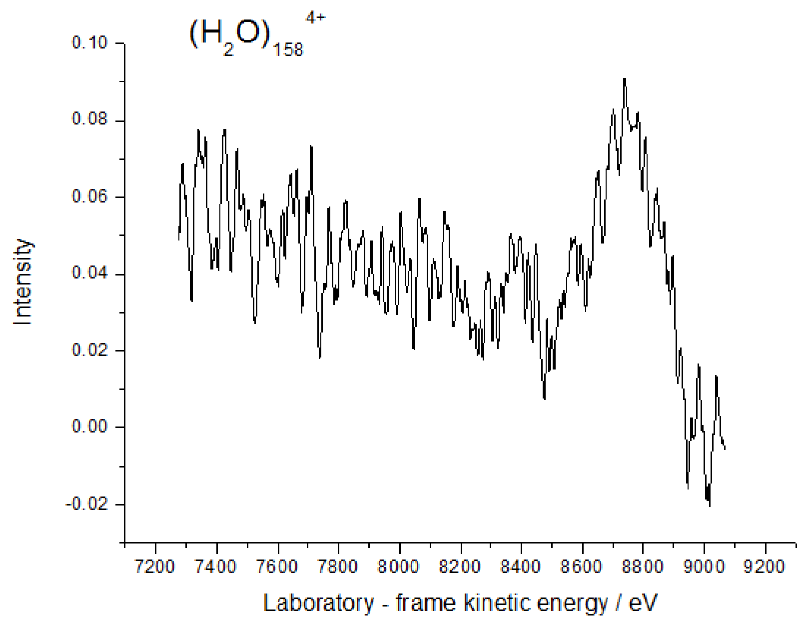

Figure .7.9: MIKE spectrum for the coulomb fission of $(H_2O)_{158}^{4+}$

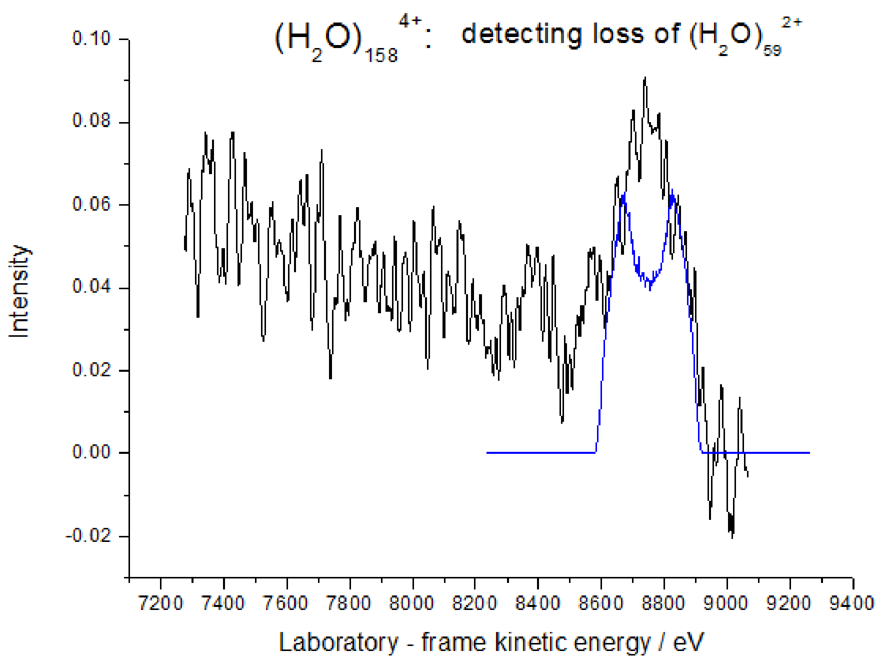

Figure .7.10: Figure 7.8 overlain with the predicted peak for the formation of the $(H_2O)_{99}^{2+}$ fragment

Precursor cluster	Fragment channel	$< KER >$/eV	U_{max} /eV
$(H_2O)_{158}^{4+}$	$K=59^{2+}$	2.15	3.03

Table 7.7.3: The values of $< KER >$ and U_{max} for the pathways shown in figure 7.10

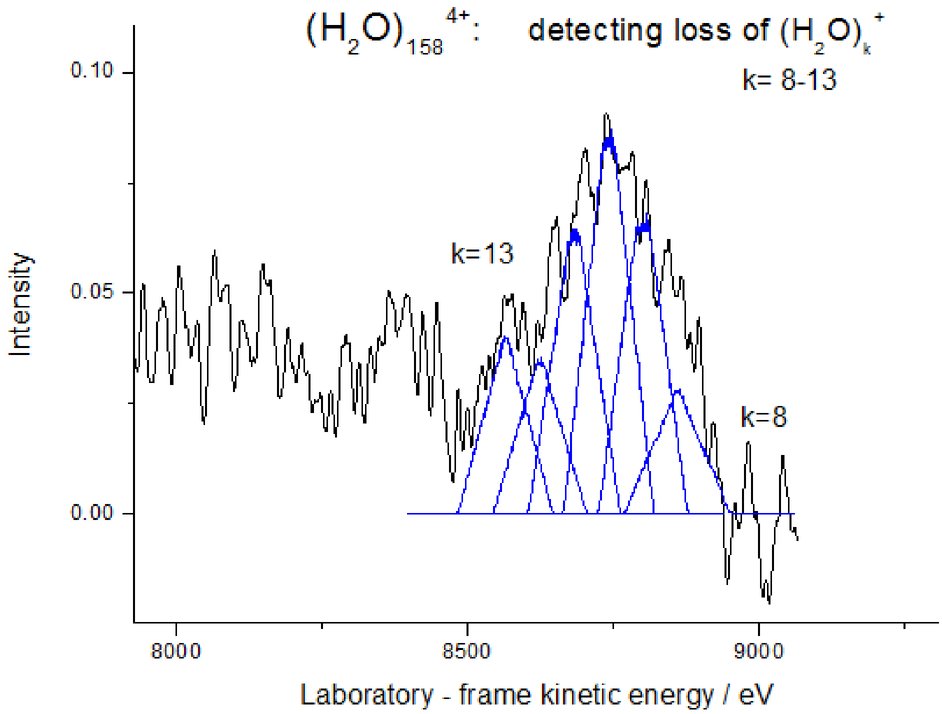

Figure 7.11: The MIKE spectrum of $(H_2O)_{158}^{4+}$ overlain with simulated peaks for the coulomb fission into 3+ charged fragments

Precursor cluster	Fragment channel	$< KER >$ /eV	U_{max} /eV
$(H_2O)_{158}^{4+}$	$k=8^+$	1.60	1.63
	$k=9^+$	1.60	1.63
	$k=10^+$	1.60	1.63
	$k=11^+$	1.60	1.63
	$k=12^+$	1.59	1.63
	$k=13^+$	1.59	1.63

Table 7.7.4: Values for $< KER >$ and U_{max} for the pathways shown in figure 7.11

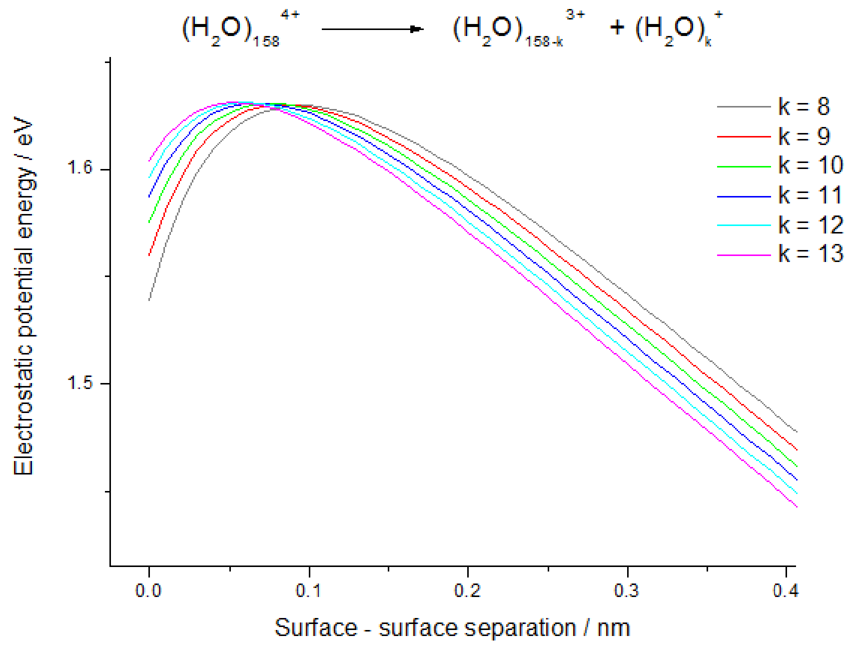

Figure 7.12: Potential energy curves for the fragments formed from the coulomb fission of $(H_2O)_{158}^{4+}$ into 3+/1+ fragments

Figure 7.12 shows the electrostatic potential energy curved for the fission of $(H_2O)_{158}^{4+}$ into 3+/1+ fragments for the pathways shown in figure 7.10. A relatively large short range barrier to fission is observed for all pathways at < 0.1 nm separation, increasing with increasing asymmetry. This is due to the high charge asymmetry between the fragments and the high value for the dielectric constant for water. The curves all reach a maximum of around 1.6 eV approximately 0.1 nm from separation = 0. Beyond this point the short range induced potentials that result in attractive forces between the spheres become less influential and the electrostatic repulsion from the charges dominates. This is seen in the crossing of the curves where the most asymmetric pathway (k=8) now has the largest potential energy as the fragments separate.

7.5 Fivefold Charged Water Clusters

The critical size determination for fivefold charged water clusters has been achieved via observation of a characteristic feature in the MIKE spectra, it is possible to follow this feature over a size range of precursor ions. Below the critical size the feature disappears completely and when the size of the precursor is increased an onset is observed. With further incremental increases in precursor size, the full characteristic feature is resolved. It was found that at n=240 and below none of the characteristic signal remains, whereas at a precursor size of n=250 a clear profile feature is resolved. Therefore, a tentative assignment of $n_{crit}(5)$ = 245 is made for water.

Figure 7.13 shows the MIKE spectrum for the coulomb fission of the $(H_2O)_{250}^{5+}$ precursor ion. The most charge asymmetric fragmentation pathway would be the coulomb fission into 4+/1+ charged fragments. However, taking the centre of the feature and applying Equation 2.10 reveals that in this hypothetical case the fragment would exceed the size of the precursor. Considering the low energy side of the feature, this would correspond to a fragment: $(H_2O)_{256}^{4+}$. Therefore the 3+/2+ mechanism is the only remaining possibility to be considered. Figure 7.14 shows a range of simulated peaks encompassing the experimental feature and the full width of the feature is accounted for with six peaks. The jump in intensity at 7915 eV that resembles a narrow peak on top of the main feature is not accounted for in the simulations, it is likely that this is caused by noise at the detector. Table 7.5 gives the energy values for the analysis in figure 7.14; it confirms that the values of U_{max} and $< KER >$ of the fitted peaks are in close agreement.

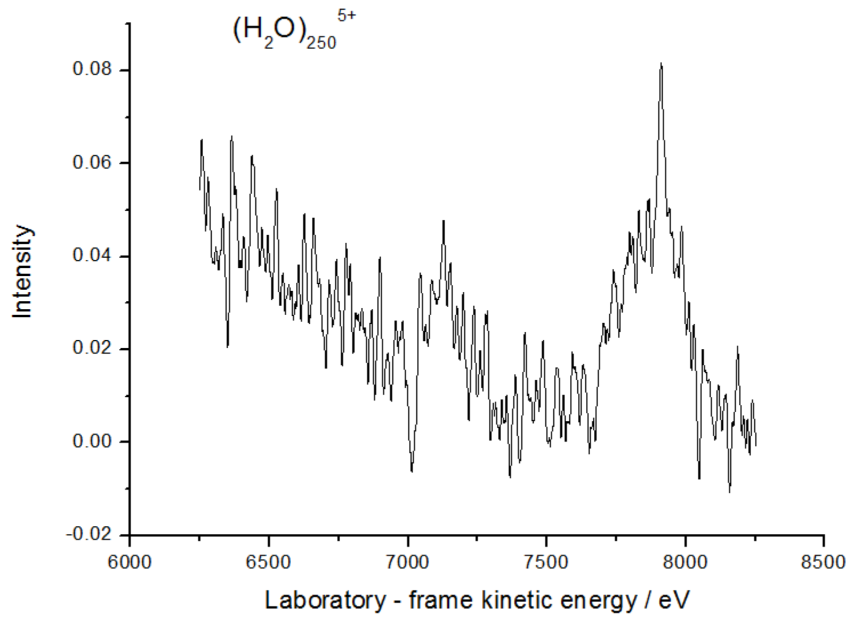

Figure 7.13: MIKE spectrum showing the coulomb fission of the $(H_2O)_{250}{}^{5+}$ ion

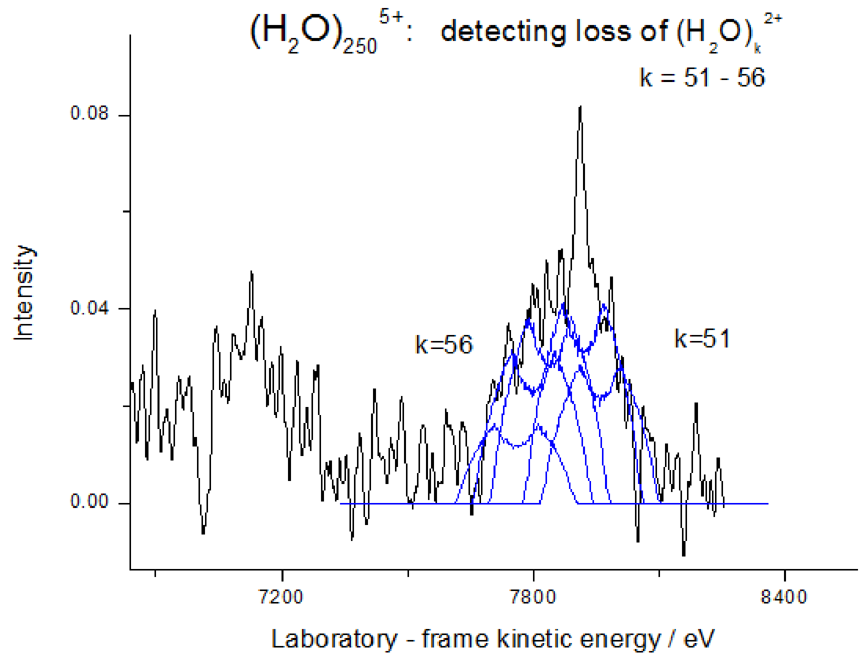

Figure 7.14: Figure 7.13 overlain with the simulated peaks for a range of 3+/2+ fragmentation pathways

Precursor cluster	Fragment channel	$< KER >$ /eV	U_{max} /eV
$(H_2O)_{250}^{5+}$	$k=51^{2+}$	4.00	4.03
	$k=52^{2+}$	4.00	4.03
	$k=53^{2+}$	4.00	4.03
	$k=54^{2+}$	4.00	4.03
	$k=55^{2+}$	4.00	4.03
	$k=56^{2+}$	4.00	4.03

Table 7.7.5: Values for $< KER >$ and U_{max} for the pathways shown in figure 7.14

7.6 Stability of Multiply Charge Water Clusters

With the collection of critical size data over the range of charge states studied in this work it is possible to compare that data to the Rayleigh equation of the liquid drop model.

$$n_{crit}(z) = \frac{(ze)^2}{64\pi^2\gamma\varepsilon_0 {r_m}^3}$$

Where charge ze is the charge state multiplied by the elementary charge constant, γ is the surface tension, ε_0 is the permittivity of free space and r_m is the molecular radius. Shown in Figure 7.15 are the values for the critical size at charge state z ($n_{crit}(z)$) (red line) and the values predicted by the liquid drop model (blue line). These values are tabulated in Table 7.6.

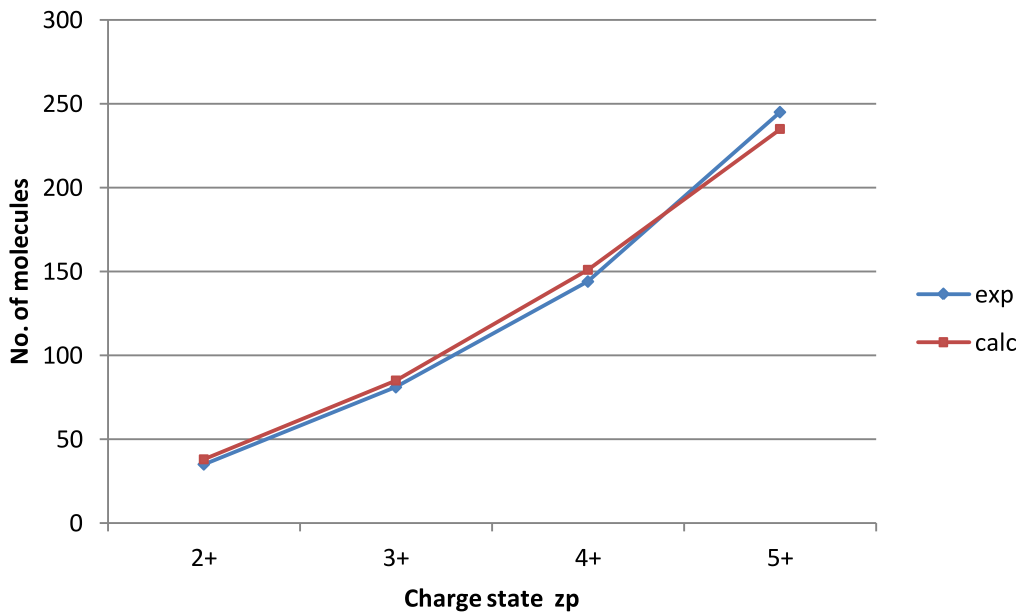

Figure 7.15: Comparison of the experimentally determined critical sizes and the values predicted by the liquid drop model

Charge state z_p	Experimental $n_{crit}(z)$	Calculated $n_{crit}(z)$	% Difference
2	35	38	8
3	84	85	1
4	144	151	5
5	245	235	4

Table 7.7.6: Values for the experimentally and theoretically determined critical sizes

The general agreement is good as the results are consistently within 5%. What is apparent, with the exception of $z_p = 5$, is that the model consistently overestimates the values of the critical sizes seen experimentally. It seems unlikely that this is due to experimental failings, the mass spectral onset for $z_p = 2$ (Figure 7.1) is especially clear. Taking the case of Figure 7.1, the onset in the intensity of the 2+ peaks is very rapid and the 2+ peaks surrounding the $(H_2O)_{36}^{2+}$ cluster peak have an intensity approaching half that of the singularly charged peak. The size corresponding to the onset of mass spectral peaks, however, should really be treated as an upper limit of the critical size, as the apparatus cannot take account of smaller precursor species that are metastable but do not have a lifetime great enough to make it to the detector in great enough number density to register as a signal.

In the case of triply charged water, the experimental assignment of the critical size is obscured by peaks surrounding the 2+ and 1+ features in the mass spectrum. In this case it may be possible that the critical size lies below n=84 but is unresolvable due to the interference of the background peaks. Indeed, if this were the case, it would still follow the trend of the experimental value falling below the calculated values in magnitude.

For the fourfold charged clusters the critical size was deduced from the fragments produced from the neutral evaporation pathway; a discrete signal is observed beyond a cluster size of n=144 which increases in intensity as a function of size. This is an indication of an increase in the number of precursor ions present in the 2nd *ffr* brought about by an increase in stability as charge separation increase in the precursor. That there are enough precursor ions present to produce a fragment signal would indicate that it is some way beyond the critical size. This method of determining the stable size is perhaps less precise than the mass scanning methodology usually employed. The dependency on precursor number for a discernible fragment signal at detection will likely result in framgnetation from precursor clusters close to the true critical size being cut out from the measurement. However, the experimental critical size of n=144 is still below the calculated value of n=151

In the case of fivefold charged clusters the critical size of $n_{crit}(5) = 245$ was deduced from a loss of a characteristic coulomb fission profile at a size n=240, the next observed signal was made at size n=250. It is noted that the absence of a signal from coulomb fission does not mean an absence of precursor ions and that it is likely that there is degree of uncertainty, as previously discussed, in using fragment signals to assign critical sizes.

To account for the apparent stability of the multiply charged water clusters compared to what is predicted by the liquid drop model. It is possible that the water cluster ions are gaining additional stability from somewhere. One potential reason could be that the comparatively large dielectric nature of water results in the electrostatic repulsion being effectively attenuated inside the cluster. That this effect is only seen in water might be evidence of a failing in the liquid drop model to account for stability in highly dielectric materials.

7.7 Conclusions

The measurements on stability and coulomb fission of multiply charger water clusters have been extended up to the precursor charge state $z_p = 5$. The identification of the critical sizes has been identified through mass spectral and MIKE scanning techniques and good agreement is seen with accepted theory. Previous work on dication clusters has been built on by employing the new peak simulation methodology to accurately determine the <*KER*> associated with each fission pathway. That the shape of the peak including the degree of dishing can be reproduced is an illustration of the validity of this method. The values of $< KER >$ from the distributions of allowed *KER*s that make up the peaks are found to be in closer agreement to the calculated barrier heights U_{max} than the values calculated by the old methodology. Close agreement is also seen for higher order charged clusters.

High resolution mass spectra are produced that show an onset of triply charged water clusters. The peaks showing the products of the protonation reactions are resolved showing the various protonated forms of the precursor clusters. This observation is helpful when identifying un-resolved protonated precursors for higher order charged clusters. The fragmentation profiles seen in the MIKE spectra for coulomb fission all show poor resolution of features. However, using the peak simulation methodology fragments can be identified and values of $< KERs >$ are assigned.

The critical size of fourfold charged clusters is identified by an onset of a MIKE signal which energy corresponds to the loss of one water molecule from the cluster. Allowing for a margin of error in assignment due to the technique employed the agreement of 5% is still very good. Two pathways are possible from this precursor: 2+/2+ and 3+/1+, it is determined that the experimental feature is made up of fragments from the 3+/1+ mechanism.

With reference to Figure 7.10, the centre of the peak corresponds to the $(H_2O)_{99}^{2+}$ fragment, the neighbouring fragments ($(H_2O)_{98}^{2+}$, $(H_2O)_{100}^{2+}$) would be 89 eV away in energy, well outside the limits of the experimental feature. Additionally, to accurately reproduce the experimental feature a distribution has to be simulated which has a value of $< KER >= 2.15$ eV, 30% off the predicted barrier height. For comparison, fitted peaks presented in this work fall within 10% of the predicted values. This would also be at odds with the lifetime theory, where a range of fragments is expected to be detected, at intensities corresponding to the agreement with experimental constraints. The width of the feature can be accounted for by a range of 6 simulated peaks for the 3+/1+ pathway, all of which possess a value of $< KER >$ close to the barrier height U_{max}. The critical size $n_{crit}(5) = 245$ was roughly assigned from the absence of coulomb fission signal. The experimental feature can be simulated by a range of peaks from the 3+/2+ fission pathway.

Also notable is the divergence of the magnitude of the *KER* data from the theoretical value of *KER = q1.q2*. Taking charge state $Z_p = 5$ the magnitude of the energy is predicted to be *KER* = 3*2 = 6 eV. For the fission of $(H_2O)_{250}^{5+}$, values of $< KER >= 4.00$ eV and U_{max} = 4.03 eV are recorded for all pathways. This provides an indication of the role that the attractive potentials from the polarisation play in the energy between fragments as they separate.

References

[1] R. Ludwig, *Angew. Chem.-Int. Edit.* **40** (2001) 1808.

[2] C.E. Kolb, J.T. Jayne, D.R. Worsnop, M.J. Molina, R.F. Meads, A.A. Viggiano, *Journal of the American Chemical Society* **116** (1994) 10314.

[3] H.R. Carlon, *Journal of Physics D-Applied Physics* **17** (1984) 1221.

[4] A.J. Stace, *Physical Review Letters* **61** (1988) 306.

[5] X. Chen, E. Bichoutskaia, A.J. Stace, *The journal of physical chemistry. A* **117** (2013) 3877.

[6] A.J. Stace, A.L. Boatwright, A. Khachatourian, E. Bichoutskaia, *Journal of Colloid and Interface Science* **354** (2011) 417.

[7] X. Chen, University of Nottingham, 2011.

[8] W.R. Peifer, M.T. Coolbaugh, J.F. Garvey, *Journal of Physical Chemistry* **93** (1989) 4700.

Chapter 8 : Conclusions and Future Work

The work presented in this thesis represents the first direct experimental measurements of the stability and unimolecular coulomb fission of molecular clusters in charge states of 3+ to 8+. This encompasses a precursor size range of approximately 60 molecules to approximately 800 molecules. By application of the experimental techniques the onset of stability of multiply charged clusters under electrostatic repulsion is monitored, and the fission into charged fragments is detected. In addition to the experimental measurements, the energetics and mechanisms of coulomb fission of these systems are explored using a combination of the dielectric particle model and the peak simulation model. By application of this new methodology, the identities of the fragments from coulomb fission can be assigned, even when there is ambiguity arising from more than one possible fragmentation mechanism. An additional benefit of using this methodology is that a more precise average kinetic energy release ($< KER >$) is determined which in turn, more closely matches the predicted barrier height from the dielectric particle model (U_{max}), for dication species when compared to previous measurements [1]. The simulated peaks for the fission of the majority of doubly and triply charged clusters presented are well fitted to the discrete peaks in the MIKE spectrum. The $< KERs >$ from the fitted peaks are within good agreement with U_{max}. This could serve as a template for future investigations in the area. The agreement of the data sets is seen as a validation of the dielectric particle model [2] as a means to describe the movement of charge and resulting interactions in separating charged dielectric fragments post coulomb fission. The potential energy solutions calculated by the model show sensitivity to total charge, charge density and polarisability (modelled by the dielectric constant) of the fragments. Taking the water system as an example, the attenuation of the electrostatic repulsion is shown to bring down the magnitude of U_{max} the most for pathways with the most asymmetry between fragments for dication clusters (Figure 7.3). When the total charge is increased to 3, there is still an attractive barrier at short separations, but the increase in the electrostatic repulsion results in a reversal in the trend in the values of U_{max} (Figure 7.7), indicating that electrostatic repulsion has an increased influence on the potential energy. A similar effect is observed for the interaction for the 3+/1+ mechanism in fourfold charged water clusters (Figure 7.12) .

Measurements on the critical sizes of the molecular cluster systems studied follow the predictions of the liquid drop model proposed by Rayleigh [3]. It is noted that the agreements are better for systems that have a strong hydrogen bonded network (ammonia and water) and less so for systems that may undergo stacking (THF, acetonitrile and benzene). This may be due to the spherical nature of the clusters, resulting from the hydrogen bonding network, more closely matching the constraints of the liquid drop model. Potential shortcomings in the experiential identification of the critical size have been identified as possible reasons for the disagreement. Table 8.1 gives a complete list of all the experimentally determined critical sizes presented in this work.

Molecular Cluster	Charge State Z_p						
	2+	3+	4+	5+	6+	7+	8+
$(C_6H_6)_n^{z+}$	17	43	96	-	-	-	-
$(CH_3CN)_n^{z+}$	28	66	161	-	-	-	-
$(NH_3)_n^{z+}$	50	116	208	302	464	630	784
$(C_4H_8O)_n^{z+}$	24	51	107	-	-	-	-
$(H_2O)_n^{z+}$	35	81	144	225	-	-	-

Table 8.1: Tabulation of the experimentally determined critical sizes of the systems studied

Comparison to a simple point charge model of electrostatics shows a distinction in how the charged molecular cluster fragments behave. Comparing the measured <*KER*> to the total charge $(q_1.q_2)$ of the system reveals a strong divergence from the <*KER*> = $(q_1.q_2)$ curve (see Figure 5.36 for an example from the ammonia system). This shows the effect of the polarisation of the dynamic free charge of the fragments, located on the surface of the fragments, as per the dielectric particle model, has in the interaction between clusters. If the charge was non-dynamic and stationary the interaction between the fragments would closely follow the point-charge trend due to the loss of attractive interactions resulting from the polarisation processes. As seen, as the total charge increases the degree of divergence increases, indicating that the magnitude of the total charge dictates the degree of polarisation and subsequent attenuation of the electrostatic repulsion.

Future work in this area would benefit from the further optimisation of the experimental setup. To achieve strong fragment signals without compromising the resolution in the MIKE spectra would be especially useful in the assignments of the fragments and the energetics of the processes, especially for higher order charged clusters. As seen in Chapter 5, precursors in charge states 3+ to 8+ all show a single broad feature in their MIKE spectra following coulomb fission. This profile, in isolation, cannot always be assigned to a particular fragmentation mechanism. Using the peak simulation methodology one can simulate MIKE peaks which reproduce the experimental feature. However, having direct experimental evidence showing the multiple peaks to confirm the predictions would be a significant step forward. Still unresolved is how to narrow and focus the ion beam, improving resolution and yet retain enough fragment signal at the detector to produce distinct, resolved peaks in the MIKE spectrum. One potential solution is to increase the number of multiply charged precursors entering the 2nd *ffr* and hence, the number of fission events occurring in the correct timeframe within the ion beam. Increasing the number of neutral clusters entering the ion source could be a first step. This has been achieved to a degree already in the current setup (see Chapter 2). By reducing the distance between the supersonic nozzle and the ion source the divergence of the ion beam is reduced significantly and hence, more neutral clusters make it into the ion source. There is still scope to reduce this distance even further by shortening the pieces connecting the nozzle chamber to the source chamber. This however would require quite a severe modification of several pieces that connect the two chambers together and the table on which the source chamber rests. This would have additional benefits in the accuracy of the assignments of the critical sizes. It has been shown that there can be a degree of discrepancy with the liquid drop model when using the MIKE scanning technique to determine the critical size via the identification of precursors by the observation of its fragments in a MIKE spectrum (see for acetonitrile, figure 4.10). This has been determined to be from the lack of the required signal at detection. Increasing the number of precursors should improve the assignments of the experimental critical sizes. The alternative to this would be to improve the mass resolution of the

ZAB to resolve the ion peaks in the mass spectrum. However, this becomes increasingly difficult as the mass of the precursor increases and resolution naturally decreases.

There is an apparent inconsistency in the treatment of the shape of the clusters under investigation. Across all systems presented in this work, the magnitude of the <*KER*> of the fitted peaks matched the predicted value for the U_{max} closely. This implies that the spheres follow the assumptions put forward by the dielectric particle model well, i.e. the clusters are polarisable spheres. However, as stated in the chapters on acetonitrile and tetrahydrofuran (Chapters 4 and 6) the divergence from the liquid drop model predictions on stability (which also assumes spherical symmetry) is marked, implying a potential for the clusters to be non-spherical. This can be accounted for by the very possible scenario where the experimental apparatus cannot accurately detect the critical size, and hence leads to an inaccurate measurement. However, it is highly likely that in some instances the clusters adopt a non-spherical shape due to stacking considerations in the minimisation of the energy of the cluster. What this indicates is that although the fragments may not be spherical in shape, they respond to the effects of an electric field in the same way a perfect sphere would. This would explain the observed agreements in U_{max} and <*KER*>.

References

[1] X. Chen, University of Nottingham, 2011.
[2] E. Bichoutskaia, A.L. Boatwright, A. Khachatourian, A.J. Stace, Journal of Chemical Physics 133 (2010).
[3] L. Rayleigh, Philos. Mag 14 (1882) 184.